Title

Radon Entry into Buildings: Effects of Atmospheric Pressure Fluctuations and Building Structural Factors

Author

Robinson, Allen L.

Publication Date

1996-05-01

LBNL-38843
UC-402

ERNEST ORLANDO LAWRENCE
BERKELEY NATIONAL LABORATORY

Radon Entry into Buildings: Effects of Atmospheric Pressure Fluctuations and Building Structural Factors

A.L. Robinson
Energy and Environment Division

May 1996
Ph.D. Thesis

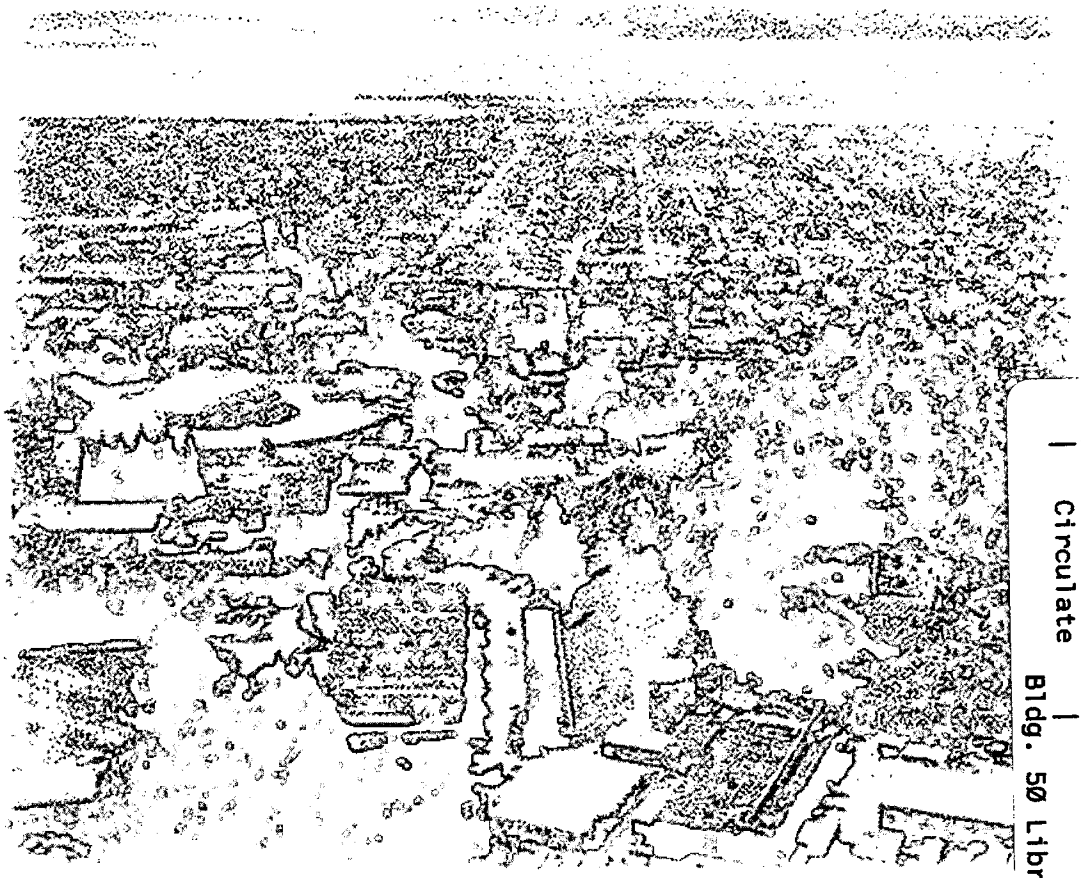

DISCLAIMER

LBNL-38843
UC-402

Radon Entry into Buildings: Effects of Atmospheric Pressure Fluctuations and Building Structural Factors

Allen Latham Robinson
Ph.D. Thesis

May 1996

Department of Mechanical Engineering
University of California at Berkeley

and

Indoor Environment Program
Energy and Environment Division
Lawrence Berkeley National Laboratory
University of California
Berkeley, CA 94720

This work was supported by the Director, Office of Energy Research, Office of Health and Environmental Research, Environmental Sciences Division, and by the Assistant Secretary for Energy Efficiency and Renewable Energy, Office of Building Technology of the U.S. Department of Energy (DOE), under Contract DE-AC03-76SF00098.

ABSTRACT

An improved understanding of the factors that control radon entry into buildings is needed in order to reduce the public health risks caused by exposure to indoor radon. This dissertation examines three issues associated with radon entry into buildings: 1) the influence of a subslab gravel layer and the size of the openings between the soil and the building interior on radon entry; 2) the effect of atmospheric pressure fluctuations on radon entry; and 3) the development and validation of mathematical models which simulate radon and soil-gas entry into houses.

Experiments were conducted using two experimental basements to examine the influence of a subslab gravel layer on advective radon entry driven by steady indoor-outdoor pressure differences. These basement structures are identical except that in one the floor slab lies directly on native soil whereas in the other the slab lies on a high-permeability gravel layer. Our measurements indicate that a high permeability subslab gravel layer increases the advective radon entry rate into the structure by as much as a factor of 30. The magnitude of the enhancement caused by the subslab gravel layer depends on the area of the openings in the structure floor; the smaller the area of these openings the larger the enhancement in the radon entry rate caused by the subslab gravel layer. A three-dimensional, finite-difference model correctly predicts the effect of a

subslab gravel layer and open area configuration on advective radon entry driven by steady indoor-outdoor pressure differences; however, the model underpredicts the absolute entry rate into each structure by a factor of 1.5.

Experiments were conducted in the structure with the subslab gravel layer to examine the importance of radon entry driven by atmospheric pressure fluctuations. Continuous measurements of soil-gas and radon entry driven by atmospheric pressure fluctuations were made for a range of steady indoor-outdoor pressure differences. In the absence of a steady indoor-outdoor pressure difference, atmospheric pressure fluctuations drive 1.5 times more radon entry into the experimental structure than diffusion. Pressurizing or depressurizing the interior of the structure diminishes the contribution of atmospheric pressure fluctuations to the long-term radon entry rate into the experimental structure.

To explain the effect of atmospheric pressure fluctuations on radon entry into houses, we present a detailed analysis of soil-gas flow driven by these fluctuations. A theoretical framework is developed to predict transient soil-gas entry into houses. Utilizing this framework, we examine and compare the measurements of soil-gas flow and the predictions of an analytical and a numerical model in both the time and frequency domains. Two scaling parameters are identified from a dimensional analysis of the analytical model to characterize how changes in water table depth, air-filled porosity, and soil permeability affect soil-gas flow driven by atmospheric pressure fluctuations. The

shorter the characteristic response time and the larger the capacitance of the soil, the larger the soil-gas flow rate caused by a given atmospheric pressure fluctuation.

Based on the results of our measurements and analyses of soil-gas and radon entry driven by atmospheric pressure fluctuations, we estimate an upper bound on the contribution of these fluctuations to the long-term, time-averaged radon entry rate. Over the long-term, atmospheric pressure fluctuations drive approximately the same amount of entry as diffusion; consequently, radon entry produced by these fluctuations will probably not cause long-term elevated indoor radon concentrations. However, for houses built in low permeability soils ($k \leq 10^{-11}$ m^2), atmospheric pressure fluctuations typically drive between 20% and 50% the total long-term radon entry. Therefore, in relative terms, atmospheric pressure fluctuations cause increased health risks for occupants of houses located at these sites.

to my Grandfather, Allen Latham Jr.

for the gift of education

TABLE OF CONTENTS

LIST OF FIGURES

CHAPTER 1

CHAPTER 2

CHAPTER 3

CHAPTER 4

CHAPTER 5

CHAPTER 6

APPENDIX A

APPENDIX B

APPENDIX C

APPENDIX D

LIST OF TABLES

CHAPTER 2

CHAPTER 3

CHAPTER 4

CHAPTER 5

CHAPTER 6

APPENDIX A

APPENDIX B

APPENDIX D

ACKNOWLEDGMENTS

I thank my advisers Ralph Greif, Bill Nazaroff and Rich Sextro for their guidance. Ralph Greif made sure I was well grounded in the fundamentals. The rigorous course work caused alot of "heartburn", but has paid handsomely. Bill Nazaroff reminded me of the big picture when I was lost in the minutia of my research. Most of all I want to thank Rich; for the past five years, he has truly been a mentor. His friendship and willingness to work side by side have helped me survive the rigors of graduate school.

A great deal of the intellectual development of this work was due to my close interaction with Karina Garbesi and Bill Riley. Karina patiently answered my numerous questions about the Small Structures and radon entry into buildings. My understanding of transient soil-gas and radon entry was developed through my many conversations with Bill Riley. I thank Karina and Bill for sharing their expertise, and I greatly value their friendship.

I am grateful to the Indoor Environment Program at Lawrence Berkeley National Laboratory for their generous financial support. Tim Nuzum, Claude Khalizadeh, and John Wooley provided valuable technical assistance for my experiments at the Small Structures. I thank Bill Riley, Bill Fisk, Yanxia Li, Marc Fischer, Karina Garbesi, and Steve Schery for reviewing drafts of papers which have evolved into the different chapters of my dissertation.

Special thanks go to all of my friends who have made graduate school such a special period of my life: especially, Tom Nordenholz for all the climbing trips to the Sierras and the pints of beer we drank at the Triple Rock, and my various house-mates, Brad Edgar, Brian Higgins and Jeff Muss, for making our apartments seem like home. Most of all, I thank Kathy Lachenauer for her love over the past five years.

Chapter 1

INTRODUCTION

The research reported in this dissertation was motivated by the serious health risks associated with human exposure to indoor radon. Between 13,000 and 16,000 lung cancer deaths a year in the United States are attributed to indoor exposure to radon and its decay products (Lubin and Boice, 1989). Of special concern are the large number of people who live in high radon houses, and therefore, incur greatly elevated risks of contracting lung cancer. The recent Environmental Protection Agency (EPA) Residential Radon Survey estimated that the average annual indoor radon concentration of approximately 6% of the U.S. housing stock (~ six million homes) exceeds the EPA recommended guideline of 150 Bq m^{-3} (Marcinowski et al., 1994).

Although two isotopes of radon have been studied with respect to their contributions to indoor radiation exposures, the ^{222}Rn isotope is believed to be primarily responsible for radon-associated lung cancer. Under certain circumstances, ^{220}Rn can also contribute to indoor exposures to radiation (Schery, 1990). However, its short half-life, ~55 s, generally limits the indoor concentration of ^{220}Rn and its decay products. This dissertation only considers ^{222}Rn, and the word radon is used to refer to that isotope.

The principal source of radon in most homes with elevated indoor concentrations is the radioactive decay of ^{226}Ra in the soil (Nero, 1988). Both ^{226}Ra and ^{222}Rn are decay products of the primordial radionuclide ^{238}U. The ^{238}U decay chain is shown in Fig. 1.1. Although there is some variation in the natural distribution of ^{238}U, this element and its decay products are ubiquitous in the earth's crust. In fact, radon can be found in all homes. In certain houses, building materials with high radium content (Stranden, 1988) and groundwater (Nazaroff et al., 1987) can also be important sources of radon.

Radon is a noble gas. Its lack of chemical activity has important implications on both the transport and ultimate fate of a radon atom. Because radon is chemically inert, radon atoms can migrate a substantial distance from the site of generation. However, radon's lack of chemical activity prevents it from accumulating in the lungs. This, in turn, reduces the direct contribution of radon atoms to the radiation dose associated with the exposure to indoor radon.

The radiation dose associated with exposure to indoor radon actually comes from the α-decay of ^{222}Rn's short-lived progeny, ^{218}Po and ^{214}Po. These species along with the intervening isotopes ^{214}Pb and ^{214}Bi are chemically reactive which enables them to deposit in the lungs when inhaled. Because of their relatively short half life, ~ 30 min, these species generally decay before they can be cleared from the lungs. Although chemical and physical transformations affect indoor concentrations of radon's decay products, common practice is to approximate their concentration from measurements or model predictions of the indoor concentration of radon.

FACTORS CONTROLLING INDOOR RADON CONCENTRATIONS

Reducing the public health risk associated with indoor radon requires thorough knowledge of the mechanisms that control indoor radon concentrations. The indoor concentration of radon depends largely on its entry rate and the building ventilation rate. Radioactive decay has little impact on indoor radon concentrations because radon's half-life, 3.8 days, is much longer than air exchange rate of typical buildings, ~ 1 hr^{-1}. Radon atoms do not undergo chemical transformations because radon is a noble gas.

A complex relationship exists between building ventilation rates and indoor radon concentrations. The indoor-outdoor pressure differences that drive building ventilation also drive advective radon entry (Nazaroff et al., 1988). However, a field study of more than 100 houses showed no correlation between indoor radon concentration and building ventilation (Nero et al., 1983; Doyle et al., 1984). This finding indicates that the radon entry rate is the dominant factor in determining indoor radon concentrations.

This dissertation focuses on the factors that control radon entry into buildings. Specifically, it examines the mechanisms which drive radon entry into buildings and the influence of soil properties and substructural characteristics on this entry. The research described in this dissertation is part of a larger study known as the Small Structures Project being conducted in the Indoor Environment Program of the Lawrence Berkeley National Laboratory (Fisk et al., 1989; Fisk et al., 1992; Garbesi, 1993). The broad aims of the Small Structures Project are to improve our understanding of radon entry into houses under different environmental conditions and for different types of basements, and to validate mathematical models for radon entry into houses. To pursue these objectives, the Small Structures Project staff designed and constructed two room-sized experimental basements. These structures are located in the Santa Cruz mountains near Ben Lomond, California. The structures are essentially identical except the floor slab of one structure rests on a high-permeability subslab gavel layer whereas the other structure's floor slab rests on natural soil.

RADON ENTRY INTO BUILDINGS

Advective entry of radon-laden soil gas is the dominant transport mechanism of radon into most homes with elevated indoor concentrations (Bruno, 1983; Åkerblom et al., 1984; Nero and Nazaroff, 1984; Nazaroff et al., 1985; Nazaroff, 1992). Advective entry refers to the transport of radon from soil into a building by the bulk flow of soil gas. Since concrete is essentially impermeable to air, soil gas flows into a house primarily through cracks, gaps, holes, and other penetrations through the building's foundation. Although diffusion plays a role in the transport of radon through the soil pore space, its contribution to the total entry rate of radon into houses with elevated indoor concentrations is small because of the low diffusivity of radon in concrete.

Small, but persistent indoor-outdoor pressure differences, typically 1 to 5 Pa, are thought to be primarily responsible for advective radon entry into buildings (Nazaroff, 1992). In the context of radon entry, indoor-outdoor pressure differences refer to the pressure differences between the indoor air and the soil gas at the level of the basement floor. A number of different mechanisms create these pressure differences: indoor-outdoor temperatures differences, wind interaction with the building superstructure, and the operation of heating, ventilation and air conditioning (HVAC) systems (Nazaroff et al., 1988). Although these mechanisms vary in time, most analyses approximate advective radon entry driven by indoor-outdoor pressure differences as a steady-state process.

Although advective radon entry driven by indoor-outdoor pressure difference has been accepted as the most important radon entry mechanism, many of the details of the effect of building design and soil properties on this entry are still unresolved. Improved understanding of how a building interacts with its soil environment, and how this interaction, in turn, affects radon entry rates is required to design effective radon-mitigation systems, and establish construction guidelines that minimize indoor-radon concentrations.

Detailed studies of radon entry into buildings have traditionally relied on mathematical models because of the difficulties associated with measuring radon entry in real houses. Many of the predictions of these theoretical studies have never been validated because of the lack of accurate radon entry measurements. The relatively few experimental studies that have measured radon entry rates do so indirectly by monitoring indoor radon concentrations and building ventilation rate. In addition, it is frequently difficult to draw detailed conclusions from these studies because of large uncertainties in the substructural characteristics of buildings and in the soil properties.

Revzan and Fisk (1992) used a mathematical model to study the effect of structural factors on radon entry driven by steady indoor-outdoor pressure differences. Of all the factors examined, the addition of a high permeability gravel layer had the most dramatic effect on the advective radon entry rate, increasing it by as much as a factor of 5. This finding has important implications for the design of houses in high-radon areas. Many local building codes require a subslab gravel layer to prevent the concrete floor slab from coming into contact with wet soil. In addition, the new residential building code proposal (EPA, 1994) requires the installation of a subslab gravel layer in conjunction with a passive subslab ventilation system in houses built in high radon areas. If this mitigation system is not operating correctly, the predictions of Revzan and Fisk (1992) suggest that the presence of a subslab gravel layer could substantially increase indoor radon concentrations.

RADON ENTRY DRIVEN BY ATMOSPHERIC PRESSURE FLUCTUATIONS

Although advective radon entry driven by steady indoor-outdoor pressure differences is believed to be primarily responsible for elevated indoor radon concentrations, several field studies have observed elevated indoor radon concentrations during periods when these pressure differences were small (Hernandez et al., 1984; Holub et al., 1985; Turk et al., 1989; Hintenlang and Al-Ahmady, 1992). Advective radon entry driven by atmospheric pressure fluctuations represents a possible explanation for these observed but unexplained elevated indoor radon concentrations. A recent theoretical study by Tsang and Narasimhan (1992) indicates that cyclical changes in atmospheric pressure can drive advective radon entry into buildings without sustained indoor-outdoor pressure differences.

Unlike entry driven by indoor-outdoor pressure differences, advective radon entry caused by atmospheric pressure fluctuations is fundamentally a transient phenomenon. Transient entry driven by atmospheric pressure fluctuations may explain some of the observed temporal variations in indoor radon concentrations. For example, Fig. 1.2 shows measurements of indoor radon concentration and atmospheric pressure made in a slab-on-grade house in Albuquerque, New

Mexico (Turk, 1990). Transient radon entry probably accounts for part of the factor of the large spikes in indoor radon concentration shown in Fig. 1.2 because building ventilation rates typically vary by less than a factor of 5 (Knutson, 1988). A comparison between the spikes in indoor radon concentration with the changes in atmospheric pressure shown in Fig. 1.2 suggests that these spikes may be correlated to large semi-diurnal fluctuations in atmospheric pressure.

The theoretical study by Tsang and Narasimhan (1992) is the most persuasive evidence for radon entry driven by atmospheric pressure fluctuations. Their results suggest that sinusoidal changes in atmospheric pressure may drive significant radon entry into buildings for certain combinations of soil types, basement types and atmospheric pressure signals. For example, they showed that decreasing the soil permeability increased the relative importance of radon entry driven by an oscillation in atmospheric pressure in comparison to entry driven by steady indoor-outdoor pressure differences.

The reported experimental evidence for radon entry driven by atmospheric pressure fluctuations is based on the correlation of changes in atmospheric pressure with measured indoor radon concentrations or indoor-subslab pressure differences. Hernandez et al. (1984) found a strong correlation between the measured basement radon concentration of a house in New Jersey and the time-rate-of-change of atmospheric pressure. Hintenlang and Al-Ahmady (1992) correlated measured indoor-subslab pressure differences with diurnal oscillations in atmospheric pressure. They hypothesized that advective entry driven by these pressure differences caused a sharp peak in indoor radon concentration at neutral pressure conditions (no indoor-outdoor pressure difference) observed in a research house in Florida.

Although these studies provide some empirical evidence for radon entry driven by atmospheric pressure fluctuations, neither study simultaneously measured indoor radon concentration and the building ventilation rate. Therefore, their results provide little insight on the magnitude of radon entry driven by atmospheric pressure fluctuations. No direct measurements of soil-gas radon entry driven by fluctuations in atmospheric pressure have been reported. In addition, field studies by Nazaroff and Doyle (1985) and Nazaroff et al. (1985) suggest that atmospheric pressure fluctuations have little or no effect on radon entry and indoor radon concentrations.

Many studies have examined the effect of changes in atmospheric pressure on the flux of radon from uncovered soil (Clements and Wilkening, 1974; Edwards and Bates, 1980; Schery and Gaeddert, 1982; Schery et al., 1984; Owczarski et al., 1990). However, the results of these studies provide little insight into the effect of atmospheric pressure fluctuations on radon entry into buildings. The low concentration of radon in the soil gas near the surface of an uncovered soil limits the advective flux of radon driven by atmospheric pressure fluctuations. In contrast, the radon concentration of soil gas immediately underneath a concrete slab is typically orders of magnitude larger than indoor radon concentrations because of the low diffusivity of radon in concrete.

OBJECTIVES AND OVERVIEW OF RESEARCH

To improve our understanding of radon entry into buildings detailed measurements of soil-gas and radon entry were made in two experimental basement structures. These measurements were used to validate the predictions of theoretical models for radon entry. These models were then used to examine the influence of changes in soil properties and substructural configuration on radon entry into buildings.

Chapter 2 examines the influence of a high-permeability subslab gravel layer and of the size of the openings between the soil and a building interior on radon entry. To pursue these objectives, measurements of soil-gas and radon entry driven by steady indoor-outdoor pressure differences made in two experimental structures are compared to predictions of a steady-state finite-difference model.

Chapters 3-6 examine the effect of atmospheric pressure fluctuations on radon entry into buildings. Measurements of soil-gas and radon entry and atmospheric pressure driven by atmospheric pressure fluctuations are reported. The measurements of soil-gas entry are compared to predictions of an analytical model and a transient, finite-element model. These models are used to examine the effect of soil properties and substructural configuration on soil-gas and radon entry driven by atmospheric pressure fluctuations.

OUTLINE OF DISSERTATION

Chapter 2 examines the influence of a subslab gravel layer and the area of the openings in a basement floor on radon entry driven by steady indoor-outdoor pressure differences. Measurements made in two room-sized, experimental basement structures are compared for a range of indoor-outdoor pressure differences and open areas. The structures are essentially identical except the floor slab of one structure rests on a high-permeability subslab gravel layer whereas the other structure's floor slab rests on natural soil. The detailed measurements of soil-gas and radon entry and the soil-gas pressure field are compared to predictions of a finite-difference model.

Chapter 3 reports measurements of soil-gas flow driven by atmospheric pressure fluctuations into and out of the experimental structure with a subslab gravel layer. These measurements depend critically on the effect of a high-permeability subslab gravel layer on soil-gas entry described in Chapter 2. An analytical model is derived to predict gas flow between a building and the underlying soil in response to atmospheric pressure fluctuations. A public-domain, transient, finite-element model called RN3D (Holford, 1994) is adapted to simulate soil-gas flow into houses driven by atmospheric pressure fluctuations.

Spectral analysis is used to examine the measurements of soil-gas flow and to compare them to the predictions of the analytical and the finite-element model.

Chapter 4 describes a parameteric investigation into the effects of soil properties, water table depth, and the presence of a high-permeability subslab gravel layer on soil-gas flow into and out of a house in response to atmospheric pressure fluctuations. Two scaling parameters are identified through dimensional analysis of the analytical model derived in Chapter 3. These scaling parameters describe how changes in water table depth, air-filled porosity, and soil permeability affect soil-gas flow driven by atmospheric pressure fluctuations. The effect of these parameters on transient soil-gas entry driven by atmospheric pressure fluctuations is demonstrated using predictions of the finite-element model.

Chapter 5 reports measurements of radon entry driven by atmospheric pressure fluctuations into the experimental basement structure with the subslab gravel layer. To examine how atmospheric pressure fluctuations affect radon entry driven by steady indoor-outdoor pressure differences, measurements were made for a range of indoor-outdoor pressure differences. These results provide a basis for evaluating the importance of atmospheric pressure fluctuations as a mechanism for driving radon entry.

Chapter 6 examines the contribution of atmospheric pressure fluctuations to the long-term radon entry rate. A model is derived to estimate the long-term, time-averaged radon entry rate into a prototypical basement for a range of soil properties and water table depths. The model accounts for radon entry driven by diffusion, steady indoor-outdoor pressure differences, and atmospheric pressure fluctuations. The chapter concludes with a brief discussion of the effect of atmospheric pressure fluctuations on building ventilation.

Chapter 7 summarizes the findings and discusses the implications of the results on radon entry into houses. It is pointed out that the results of this dissertation are directly applicable to entry of other gas-phase soil contaminants into buildings. Chapter 7 concludes with a brief discussion of future research directions.

REFERENCES

Åkerblom G., Anderson P. and Clavensjo B. (1984) Soil gas radon—A source of indoor radon daughters. *Radiation Protection Dosimetry* 7, 49-54.

Bruno R. C. (1983) Sources of indoor radon in houses: A review. *J. Air. Pollut. Control Assoc.* **33**, 105-109.

Clements W. E. and Wilkening M. H. (1974) Atmospheric pressure effects on ^{222}Rn transport across the earth-air interface. *J. Geophys. Res.* **79**, 5025-5029.

Doyle S. M., Nazaroff W. W. and Nero A. V. (1984) Time-averaged indoor Rn concentrations and infiltration rates sampled in four U.S. cities. *Health Phys.* **47**, 579-586.

Edwards J. C. and Bates R. C. (1980) Theoretical evaluation of radon emanation under a variety of conditions. *Health Phys.* **39**, 263-274.

EPA (1994) Model standards and techniques for control of radon in new residential buildings. *Federal Register Notices* **59**, 13402-13416.

Fisk W. J., Flexser S., Gadgil A. J., Holman H. Y., Modera M. P., Narasimhan T. N., Nuzum T., Revzan K. L., Sextro R. G., Smith A. R., Tsang Y. W. and Wollenberg H. A. (1989) Monitoring and modeling for radon entry into basements: A status report for the small structures project. LBL-27692, Lawrence Berkeley National Laboratory, Berkeley CA 94720.

Fisk W. J., Modera M. P., Sextro R. G., Garbesi K., Wollenberg H. A., Narasimhan T. N., Nuzum T. and Tsang Y. W. (1992) Radon entry into basements: Approach, experimental structures, and instrumentation of the small structures project. LBL-31864, Lawrence Berkeley National Laboratory, Berkeley CA 94720.

Garbesi K. (1993) Toward resolving model-measurement discrepancies of radon entry into houses. Ph.D. Dissertation, University of California at Berkeley. Also published as a technical report LBL-34244, Lawrence Berkeley National Laboratory, Berkeley CA 94720.

Hernandez T. L., Ring J. W. and Sachs H. M. (1984) The variation of basement radon concentrations with barometric pressure. *Health Phys.* **46**, 440-445.

Hintenlang D. E. and Al-Ahmady K. K. (1992) Pressure differentials for radon entry coupled to periodic atmospheric pressure variations. *Indoor Air* **2**, 208-215.

Holford D. J. (1994) RN3D: A finite element code for simulating gas flow and radon transport in variably saturated, nonisothermal porous media: User's manual, version 1.0. PNL-8943, Pacific Northwest Laboratory, Richland WA

99352.

Holub R. F., Droullard R. F., Borak T. B., Inkret W. C., Morse J. G. and Baxter J. F. (1985) Radon-222 and ^{222}Rn progeny concentrations measured in an energy-efficient house equipped with a heat exchanger. *Health Phys.* **49**, 267-277.

Knutson E. O. (1988) Modeling indoor concentration of radon's decay products. In Nazaroff W. W. and Nero A. V. (Ed.) *Radon and Its Decay Products in Indoor Air*, John Wiley and Sons, New York, 161-202.

Lubin J. H. and Boice J. D. (1989) Estimating Rn induced lung cancer in the United States. *Health Phys.* **57**, 417-427.

Marcinowski F., Lucas R. M. and Yeager W. M. (1994) National and regional distributions of airborne radon concentrations in United-States homes. *Health Phys.* **66**, 699-706.

Nazaroff W. W. (1992) Radon transport from soil to air. *Rev. Geophys.* **30**, 137-160.

Nazaroff W. W. and Doyle S. M. (1985) Radon entry into houses having a crawl space. *Health Phys.* **48**, 265-281.

Nazaroff W. W., Doyle S. M., Nero A. V. and Sextro R. G. (1987) Potable water as a source of airborne ^{222}Rn in U.S. dwellings: A review and assessment. *Health Phys.* **52**, 281-295.

Nazaroff W. W., Feustel H., Nero A. V., Revzan K. L., Grimsrud D. T., Essling M. A. and Toohey R. E. (1985) Radon transport into a detached one-story house with a basement. *Atmos. Environ.* **19**, 31-43.

Nazaroff W. W., Moed B. A. and Sextro R. G. (1988) Soil as a source of indoor radon: Generation, migration, and entry. In Nazaroff W. W. and Nero A. V.

(Ed.) *Radon and Its Decay Products in Indoor Air*, John Wiley and Sons, New York, 57-112.

Nero A. V. (1988) Radon and its decay products in indoor air: An overview. In Nazaroff W. W. and Nero A. V. (Ed.) *Radon and It's Decay Products in Indoor Air*, John Wiley and Sons, New York, 1-53.

Nero A. V., Boegel M. L., Hollowell C. D., Ingersoll J. G. and Nazaroff W. W. (1983) Radon concentrations and infiltration rates measured in conventional and energy-efficient houses. *Health Phys.* **45**, 401-405.

Nero A. V. and Nazaroff W. W. (1984) Characterizing the source of radon indoors. *Radiat. Prot. Dosim.* **7**, 23-39.

Owczarski P. C., Holford D. J., Freeman H. D. and Gee G. W. (1990) Effects of changing water content and atmospheric pressure on radon flux from surfaces of five soil types. *Geophys. Res. Let.* **17**, 817-820.

Revzan K. and Fisk W. (1992) Modeling radon entry into houses with basements: The influence of structural factors. *Indoor Air* **2**, 40-48.

Schery S. D. (1990) Thoron in the environment. *J. Air Waste Mange. Assoc.* **40**, 493-497.

Schery S. D. and Gaeddert D. H. (1982) Measurements of the effects of cyclic atmospheric pressure variation on the flux of ^{222}Rn from the soil. *Geophys. Res. Let.* **9**, 835-838.

Schery S. D., Gaeddert D. H. and Wilkening M. H. (1984) Factors affecting exhalation of radon from a gravelly sandy loam. *J. Geophys. Res.* **89**, 7299-7309.

Stranden E. (1988) Building materials as a source of indoor radon. In Nazaroff W. W. and Nero A. V. (Ed.) *Radon and Its Decay Products in Indoor Air*, John Wiley and Sons, New York, 113-130.

Tsang Y. W. and Narasimhan T. N. (1992) Effects of periodic atmospheric pressure variation on radon entry into buildings. *J. Geophys. Res.* **97**, 9161-9170.

Turk B. H. (1990) Barometric pumping of radon into buildings. Mountain West Technical Associates, 206 B Tano Rd., Santa Fe, NM 87501.

Turk B. H., Prill R. J., Sextro R. G. and Harrison J. (1989) Intensive radon mitigation research: Lessons learned. The 1988 International Symposium on Radon and Radon Reduction Technology. U.S. Environmental Protection Agency, Air and Energy Environmental Research Laboratory, Research Triangle Park NC 27711.

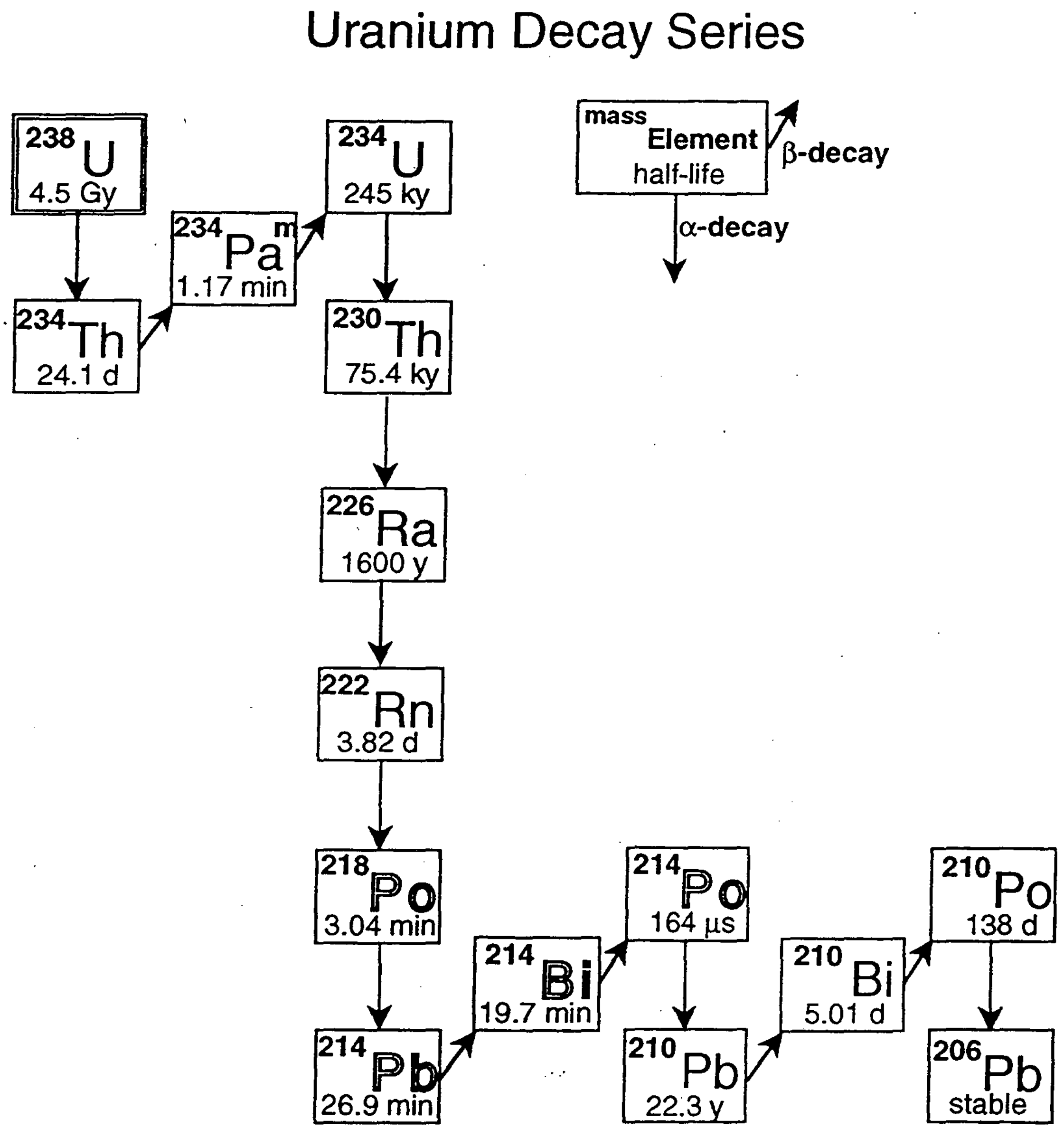

Fig. 1.1 Radioactive decay chain of ^{238}U. The radiation dose associated with exposures to indoor radon is mainly due to the α-decay of ^{218}Po and ^{214}Po.

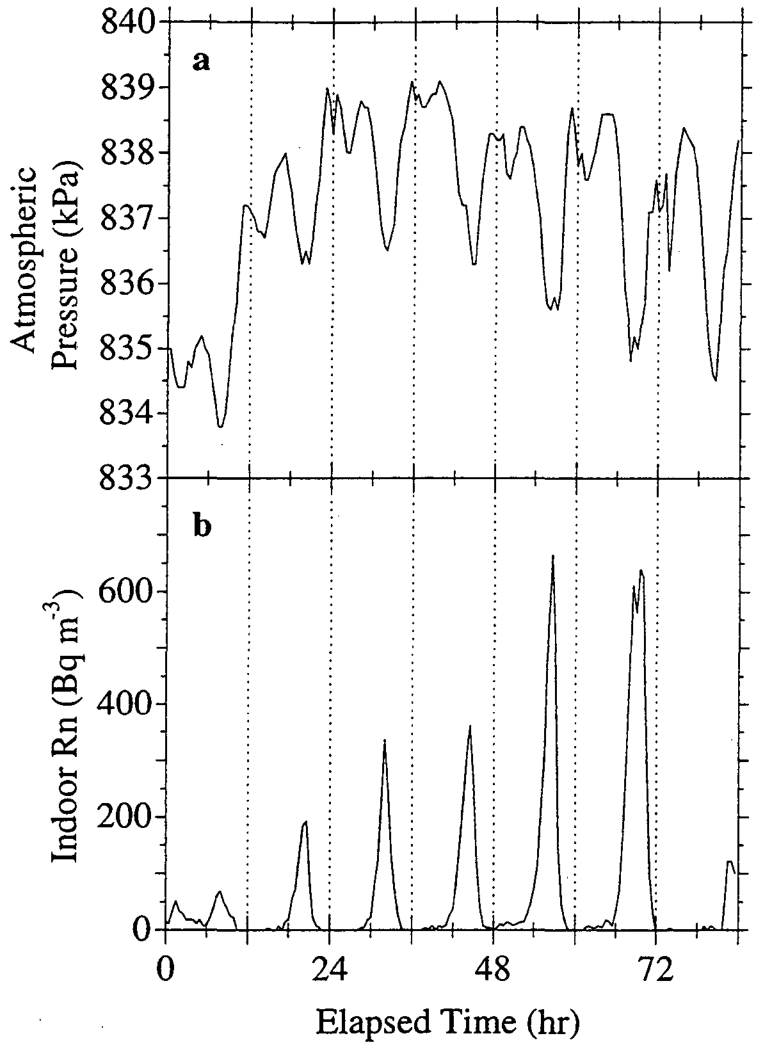

Fig. 1.2 Measurements of (a) atmospheric pressure and (b) indoor radon concentration made in a house in Albuquerque, New Mexico. These data were collected during a field study by Turk (1990). Zero hours elapsed time corresponds to midnight October 15, 1990.

Chapter 2

THE INFLUENCE OF A SUBSLAB GRAVEL LAYER AND OPEN AREA ON SOIL-GAS AND RADON ENTRY INTO TWO EXPERIMENTAL BASEMENTS*

ABSTRACT

Measurements of steady-state soil-gas and ^{222}Rn entry rates into two room-sized, experimental basement structures were made for a range of structure depressurizations (0 - 40 Pa) and open floor areas (0 - 165 x 10^{-4} m^2). The structures are identical except that in one the floor slab lies directly on native soil whereas in the other the slab lies on a high-permeability gravel layer. The subslab gravel layer greatly enhances the soil-gas and radon entry rate into the structure. The radon entry rate into the structure with the subslab gravel layer is four times greater than the entry rate into the structure without the gravel layer with an open floor area of 165 x 10^{-4} m^2; however the ratio increases to 30 for an open floor area of 5.0 x 10^{-4} m^2. The relationship between open area and soil-gas entry rate is complex. It depends on both the amount and the spatial distribution of the open area as well as the permeability of the soil near the opening. The entry rate into the experimental structures is largely determined by the presence or absence of a

---

* This chapter was taken from the published paper: Robinson A.L. and Sextro R. G. (1995) The influence of a subslab gravel layer and open area on soil-gas and radon entry into two experimental basements. *Health Phys.* 69, 367-377. Minor changes in wording were made.

subslab gravel layer. Therefore open area by itself is a poor indicator of radon and soil-gas entry into the structures. The extension of the soil-gas pressure field created by structure depressurization is a good measure of the radon entry. The measured normalized radon entry rate into *both* structures has the *same* linear relationship with the average subslab pressure coupling *regardless* of open area or the presence or absence of a subslab gravel layer. The average subslab pressure coupling is an estimate of the extension of the soil-gas pressure field. A three-dimensional finite-difference model correctly predicts the effect of a subslab gravel layer and different open area configurations on radon and soil-gas entry rate; however, the model underpredicts the absolute entry rate into each structure by a factor of 1.5.

INTRODUCTION

Advective flow of radon-laden soil gas is the dominant transport mechanism of radon into houses with elevated indoor radon concentrations (Bruno, 1983; Åkerblom et al., 1984; Nero and Nazaroff, 1984; Nazaroff et al., 1985; Nazaroff et al., 1988; Turk et al., 1990b). Since solid concrete is essentially impermeable to air (Rogers and Nielson, 1993), soil gas flows into a basement primarily through cracks, gaps, holes, and other penetrations through the building's foundation. Large gaps are commonly found around plumbing fixtures, utility penetrations, and the perimeter of a floor slab due to the shrinkage gap between the wall and a poured concrete slab. Smaller cracks are created by differential settling of the concrete slab (Scott, 1988). A typical basement with concrete wall and floor areas of 120-200 m^2 can have open areas up to a several hundred square centimeters (Scott, 1988). Open area is defined as the total cross-sectional area of all the macroscopic penetrations through a foundation. A field study done in Elliot Lake, Ontario, found that open area of the joints between the walls and the floor slab was typically around 0.03 m^2 (Eaton and Scott, 1984). In the extreme, cracks with a combined open area of 1.5 m^2 were found in a house in New Jersey (Turk et al., 1991a). In addition to flow through cracks, there may also be significant bulk soil-gas flow through basement walls constructed out of a high permeability material such as hollow concrete blocks (Garbesi and Sextro, 1989; Ruppersberger, 1991).

The importance of cracks as an advective soil-gas entry pathway led to the development of sealing as a radon mitigation technique. However, results from several radon mitigation studies indicate that sealing alone is often ineffective at reducing indoor radon concentrations (Henschel, 1988; Turk et al., 1991a; Turk et al., 1991b). The ineffectiveness of sealing as a mitigation technique has been attributed to a failure to seal a significant fraction of the total crack area, and therefore failing to significantly increase the resistance of the foundation to soil-gas flow with respect to the resistance of the soil. Sealing only becomes effective when the total substructure crack resistance approaches that of the soil (Mowris and Fisk, 1988).

Despite the role of cracks in soil-gas entry into houses and the apparent ineffectiveness of sealing as a radon mitigation technique, little work has been reported on the relationship between open area and soil-gas or radon entry. In a field study, Brennan et al. (1991) found that indoor radon concentrations were independent of changes in open area. They hypothesized that the failure of indoor radon concentrations to increase with increases in open area was caused by elevated soil-gas flow rates diluting the radon concentration of the soil gas. In a modeling study of the influence of different structural factors on radon entry, Revzan and Fisk (1992) found that radon entry rate was independent of opening width for soils with a permeability less than 10^{-10} m^2, and that the sizes and numbers of openings in the slab were relatively unimportant as long as the total open area is small in comparison to the slab area. That study concluded that the presence of a subslab gravel layer was the most important structural factor considered, with the potential to increase the radon entry rate by as much as a factor of five. Based on the predictions of an analytical model, Mowris (1986) found that cracks wider than 10^{-3} m created insignificant resistance to flow in comparison to the resistance of the soil.

This chapter reports on a soil-gas and radon entry study carried out at two experimental structures located in the Santa Cruz Mountains, California. These basement structures were designed and constructed to study the importance of structural and environmental factors on radon and soil-gas entry into houses. The two structures are identical except for the presence of a high-permeability gravel layer underneath the floor of one of the structures. Inclusion of a subslab gravel layer is a customary construction practice in some areas to prevent the slab from coming into contact with wet soil. In addition, the new residential building code proposal (EPA, 1994) requires the installation of a subslab gravel layer in conjunction with a passive subslab ventilation system in houses built in high radon areas. In case an active (i.e. fan-powered) mitigation system is necessary, the gravel layer will greatly enhance its performance (Henschel, 1993).

The structures employed in this study were designed with a simple geometry and precisely defined soil-gas entry points to facilitate comparison with existing numerical models. Such models are a valuable tool for investigating soil-gas and radon entry into houses; however, comparison between measurements of radon entry into houses and predictions of these models have indicated significant discrepancies. Initial measurements in the structure with the gravel layer confirmed this discrepancy (Garbesi et al., 1993a). Further work has shown that a large portion of this difference is due to the scale-dependence of soil permeability (Garbesi et al., 1993b).

This chapter has three goals: 1) to examine the effect of a subslab gravel layer on radon entry rate, 2) to examine the relationship between open area and radon entry rate, and 3) to compare predictions of a three-dimensional finite-difference model with these detailed measurements of radon and soil-gas entry. The experiments use constant depressurization of the structure, in the range of 10 to 40 Pa below atmospheric pressure. The open area is varied by opening or sealing a series of holes and precisely machined slots located in the structure's floor. The results of these experiments can be extrapolated to the few Pa depressurizations experienced by real houses under ordinary operating conditions, because soil-gas flow into the structures is governed by Darcy's law, where flow is a linear function of pressure.

MATERIALS AND METHODS

Structure Design and Instrumentation

Fig. 2.1 is a schematic drawing of one of the experimental structures. Each structure is a single chamber with floor dimensions of 2.0 x 3.2 m and a height of 2.0 m (inside dimensions); only about 0.1 m of the walls extend above grade. The two structures are identical except for the presence of a 0.1-m-thick gravel layer underneath the slab of one of the structures (Fisk et al., 1992). This structure will be referred to as the "gravel structure", and the structure which lies on native soil will be referred to as the "no-gravel structure".

A set of slots and holes have been installed in the floor of each structure to provide well-characterized openings through which soil gas can flow into the structure. Each structure has six smooth-walled slots to simulate the shrinkage gap that can develop at the floor-wall joint located at the perimeter of poured concrete floors in real houses. Each slot is 3.2×10^{-3} m wide, 0.86 m long and extends though the entire 0.15-m-thick slab. The open area of each slot is 27×10^{-4} m^2. As shown in Fig. 2.1 the slots are inset 0.34 m from, and run parallel to, each wall of the structures. There are two slots along each of the east and west walls, and one along each of the shorter north and south walls. These slots provide negligible resistance to soil-gas flow over the range of conditions considered in this study (Fisk et al., 1992). Each structure also has four 0.013-m-diameter circular holes drilled through its slab, one in the center of each quadrant of the structure floor. The open area of each hole is 1.3×10^{-4} m^2. There is also a 0.038-m-diameter circular hole in the center of the gravel structure floor, having an open area of 11×10^{-4} m^2. The total open area was varied by sealing the various slots and holes in the floor of the structures with aluminum plates and silicone sealant. Great care has been taken to seal all other cracks and other unintended openings between the structure and the soil environment so as to minimize uncharacterized soil-gas entry.

Thirty-two soil probes have been installed around each structure to measure soil-gas pressure disturbances, soil-gas radon concentrations, and soil permeability. As shown in Fig. 2.1, horizontal probes penetrate the walls at three different elevations, and vertical probes extend through the slab to monitor the subslab region. Table 2.1 summarizes the distribution and length of the soil probes around both structures. The probes are constructed out of 0.021-m-diameter steel pipe with a 0.15 m section of cylindrical well screen, for sampling, and a 0.04 m driving tip welded onto the end of the pipe (Fisk et al., 1992). A 5-m-long reference probe extends horizontally into the soil from each structure. The reference probe is at the level of the top of the structure floor slab.

Continuous radon monitors (CRM) are used to measure the ^{222}Rn concentration of the air in the structure, slots/holes, and soil. An oscillating fan continually mixes the air inside the structure to allow accurate sampling of the structure radon concentration from a single location. Air is also drawn from the bottom of all of the slab openings through 0.15-m-long needles, mixed into one sampling line, and delivered to a CRM. Soil-gas samples are multiplexed from the probes to one CRM. The method described by Thomas et al. (1979) was used to interpret the CRM data from the structure and slot CRMs. Since soil-gas samples are multiplexed, the algorithm developed by Busigin et al. (1979) was used to interpret the data from the probe CRM (Modera and Bonnefous, 1993).

Soil moisture and temperature, indoor and outdoor temperature, wind speed, wind direction, barometric pressure, rainfall, and water table depth are also monitored. A computer-controlled mass flow controller maintains the structure depressurization within ± 5% of the setpoint. The structure depressurization is the measured pressure difference between the interior of the structure and the reference probe. Further details of the design and instrumentation of the structures are found in Fisk et al. (1992) and Garbesi et al. (1993a).

Soil Properties

Table 2.2 reports the measured permeability of the gravel, backfill, and undisturbed soil at the structure site. The permeability of the undisturbed soil is scale dependent, increasing by more than an order of magnitude when the length scale increases from 0.1 to 3.5 m (Garbesi, 1993; Garbesi et al., 1996). High permeability flow paths such as old plant roots, animal burrows, and water leach pathways are thought to cause the scale dependence of the permeability of the undisturbed soil. The permeability of the undisturbed soil listed in Table 2.2 is the value measured at the 3 m scale because that is the characteristic length of a soil-gas flow path from the soil surface to an opening in the structure floor. The backfill region, shown in Fig. 2.1, was excavated during the construction of the structures. It was carefully refilled to minimize the disturbance of the native soil environment (Fisk et al., 1992). The careful packing of the backfill region is thought to have destroyed features which create the scale dependence observed in the undisturbed soil.

Table 2.3 summarizes measurements of soil-grain density, porosity, emanation fraction, and radium content at the structure site. Soil samples were taken from several bore holes, a soil trench, and the walls of the excavations for the structures. Further geological details of the structure site are described in Flexser et al. (1993) and Brimhall and Lewis (1992). Appendix A describes in more detail the results of soil permeability and porosity measurements made at the experimental site.

Pressure Field

The soil-gas pressure field created by depressurizing the interior of the structure drives advective soil-gas entry into the structure. The pressure field quantifies the field of influence of the structure and provides information on the advective soil-gas transport pathways. The soil-gas pressure field is reported in terms of the non-dimensional parameter pressure coupling (Nazaroff et al., 1987; Garbesi et al., 1993a). Given Darcy flow and negligible flow resistance though the openings relative to the soil, pressure coupling is independent of structure depressurization.

The pressure coupling at probe j is defined as

$$PC_j = \frac{\Delta P_{ref} - \Delta P_j - [\rho(T_{soil}) - \rho(T_{in})]\, g\, h_j}{\Delta P_{ref}}. \tag{2.1}$$

ΔP_{ref} is the measured pressure difference between the structure interior and the reference probe. ΔP_{ref} is corrected for any pressure coupling in the reference probe by comparing ΔP_{ref} with the time-averaged structure-to-outdoor pressure difference at the soil surface. ΔP_j is the measured pressure difference between the structure interior and probe j. The term $\left[\rho(T_{soil}) - \rho(T_{in})\right] g\, h_j$ is a small hydrostatic pressure correction which references PC_j to the floor slab level. The density, ρ, of the soil gas and the air inside the structure is calculated based on their respective temperatures, T_{soil} and T_{in}, and the molecular weight of dry air, 28.8 g mol^{-1}.

Radon and Soil-Gas Entry Rate

Experiments were conducted to determine the steady-state advective radon and soil-gas entry rates into each structure as a function of open area and structure depressurization. Each experiment lasted at least seven days to ensure that the structure and soil-gas radon concentrations had achieved steady-state. All of the experiments were conducted during relatively stable environmental conditions -- no large rainfall events or high winds (i.e. average windspeeds were less than 4 m s^{-1}). During each experiment the interior of the structure was held at a constant depressurization relative to the reference probe.

The total advective radon entry rate was computed using a steady-state mass balance

$$S_{adv} = I_{struc} Q_{exh} + I_{struc} \lambda V - S_{diff} \tag{2.2}$$

where S_{adv} is the total advective radon entry rate into the structure, I_{struc} is the steady-state activity concentration of radon inside the structure, Q_{exh} is the exhaust flow rate from the structure, λ is the radioactive decay constant of radon (2.1×10^{-6} s^{-1}), V is the volume of air inside the structure (13.4 m^3), and S_{diff} is the diffusive radon entry rate. The measured diffusive radon entry rate through the walls, floor, and openings into both structures, with no imposed structure depressurization, is 0.10 Bq s^{-1} (Garbesi et al., 1993a). The diffusive entry rate is assumed to be independent of structure depressurization and open area configuration because the measured soil-gas radon concentration field varied by less than 10% for the range of conditions considered in this study.

Although advective radon entry occurs primarily through the slots and holes, it must be corrected for entry through other, undetectable, unintentional openings to make valid comparisons with the numerical model and to study the influence of open area on radon entry. The uncharacterized radon entry rate was estimated by sealing all of the slots and holes in the floor of the structure and depressurizing the structure. The measured advective radon entry rate is then defined as the uncharacterized radon entry rate. This estimate is an upper bound on the uncharacterized radon entry rate because opening slots or holes changes the soil-gas pressure field around the structure, reducing the pressure drop across the structure walls which in turn decreases the flow through any unintentional openings. The uncharacterized radon entry rates are estimated to be 0.03 Bq s^{-1} Pa^{-1} and 0.06 Bq s^{-1} Pa^{-1} into the gravel structure and no-gravel structure respectively. The radon entry rate through the slots and holes (S_c) is then calculated by subtracting the estimate of the uncharacterized radon entry rate (S_u) from the total advective radon entry rate:

$$S_c = S_{adv} - S_u. \qquad (2.3)$$

In this chapter the term "radon entry rate" refers to the advective radon entry rate through the slots and holes, S_c, unless otherwise noted.

After calculating the radon entry rate through the holes and slots, the soil-gas entry rate into the structure is determined using a ^{222}Rn mass balance.

$$Q = \frac{S_c}{I_{open}}, \qquad (2.4)$$

where Q is the soil-gas flow rate into the structure through the characterized openings, and I_{open} is the measured ^{222}Rn concentration of the entering soil gas, averaged over all of the openings.

Numerical Modeling

A steady-state, three-dimensional, finite-difference model based on a code written by Loureiro et al. (1990) and modified by Revzan and Fisk (1992) was used to simulate the soil-gas pressure field around and the advective radon entry into the experimental structures. Garbesi et al. (1993a) made detailed comparisons between the predictions of this model and measurements made in the gravel structure to study the discrepancy between field measurements and predictions of numerical models.

The model assumes isothermal conditions and Darcy flow. Soil gas flows into the structure through openings defined in the floor of the simulated structure; the rest of the floor and the walls are treated as no-flow boundaries. To reduce storage and computational requirements, the model simulates flow in one-quarter of the soil block by assuming two planes of symmetry along the north-south and east-west centerlines of the structure (Loureiro et al., 1990).

Two types of openings are defined in the floor of the modeled structure: long slots with the same dimensions and locations as the slots in the experimental structures, and square holes with the same area and location as the circular holes in the floor of the experimental structure. The model assumes that the slots provide no resistance to soil-gas flow, i.e. that the slots provide negligible resistance to soil-gas entry in comparison to the soil. We accounted for pressure drop in the holes were made using a correlation developed by Shah (1978) which predicts the pressure drop in the inlet region of non-circular ducts. This correction was less than 5% of the total imposed pressure on the structure for the entire range of cases studied.

To simulate the soil-gas flow field, the modeled soil block was divided into three regions: undisturbed soil, backfill, and subslab region (Garbesi, 1993). The different soil regions are shown in Fig. 2.1 and are assigned the measured permeabilities reported in Table 2.2. The subslab region in the no-gravel structure is assigned the permeability of the undisturbed soil. The undisturbed soil was divided into layers to simulate the soil-gas radon concentration field (Garbesi, 1993). The depths and properties assigned to these different layers are listed in Table 2.3.

RESULTS AND DISCUSSION

Soil-Gas Entry as a Function of Structure Depressurization with Six Slots Open

Fig. 2.2 shows the measured soil-gas entry rate into the gravel and no-gravel structure as a function of structure depressurization. All of the measurements presented in Fig. 2.2 were made with six slots open, i.e. with a total open area of 165×10^{-4} m^2. As expected from Darcy's law and the negligible resistance of the slots to flow, the soil-gas entry rate is a linear function of structure depressurization. A linear regression of the soil-gas entry rate as a function of structure depressurization, weighted by the measurement uncertainties, yields slopes of $9.8 \times 10^{-6}\ m^3\ s^{-1}\ Pa^{-1}$ ($r^2 = 0.99$) for the gravel structure, and $2.5 \times 10^{-6}\ m^3, s^{-1}\ Pa^{-1}$ ($r^2 = 0.98$) for the no-gravel structure. Thus, with all six slots open, the measured soil-gas entry rate into the gravel structure is approximately four times greater than the measured soil-gas entry rate into the no-gravel structure. To verify the accuracy of determining the soil-gas entry rate with a radon mass balance, the soil-gas entry rate through the 0.038-m-diameter hole in the gravel structure was calculated with a radon mass balance and directly measured using a hot wire anemometer. The two measurements agreed to within 5% --- less than the experimental uncertainty. Fig. 2.2 shows that the model underpredicts the soil-gas entry rate into both the gravel and no-gravel structure by a factor of 1.5 and 1.4 respectively. Although the discrepancy for the no-gravel structure is slightly smaller than for the gravel structure, this difference in the discrepancies falls within the uncertainties of the permeability measurements used as inputs for the simulations and the soil-gas entry rate measurements.

Garbesi et al. (1993a) reported a soil-gas entry rate into the gravel structure of $1.7 \times 10^{-5}\ m^3\ s^{-1}\ Pa^{-1}$ based on a radon balance. The apparent reduction in soil-gas entry rate reported in this study is due to improved accuracy in the measurement of the radon concentration of the slot air. In the present study 0.15-m-long needles were used to sample air from the bottom of the slots. In the previous study 0.016-m-long needles were used to sample air from the slots; these shorter needles may have entrained air from the structure, diluting the slot air radon concentrations.

Pressure Coupling with Six Slots Open

Pressure coupling measurements made in the soil near both structures with six slots open are presented in Figs. 2.3, 2.4, and 2.5. As expected, the pressure coupling decreases as one moves away from the openings. The only exception is found in the mid-wall region of the no-gravel structure, shown in Fig. 2.5. However, these small values of pressure coupling have large experimental uncertainties associated with them. Figs. 2.3-2.4 indicate that the soil-gas pressure gradients are much larger in the subslab region (Fig. 2.3) than around the low and mid-wall probes (Figs. 2.4 and 2.5).

A comparison of the measured subslab pressure coupling underneath both structures, shown in Fig. 2.3, reveals the dramatic effect of a subslab gravel layer. The pressure coupling of 0.96 measured in the two 0.24-m-long subslab probes underneath the gravel structure indicates that the pressure in the gravel layer is essentially the same as the pressure inside the structure, and that the pressure gradient in the gravel immediately underneath the structure is relatively small. In contrast, the much smaller value of pressure coupling measured in the two 0.24-m-long probes underneath the no-gravel structure indicates that a large pressure gradient exists immediately underneath the no-gravel structure.

The effect of the gravel layer is clearly illustrated in the predicted pressure coupling fields around both structures. Fig. 2.6a shows that the soil-gas flow field converges uniformly into the gravel layer underneath the structure, indicating that the gravel layer acts as a plenum. Despite the large soil gas velocities caused by the convergence of the soil-gas flow field into the slots, the high-permeability gravel presents negligible resistance to soil gas flow in comparison with the low-permeability undisturbed soil. Consequently, the gravel layer effectively increases the area over which the soil-gas flow field converges, reducing the velocities in the low-permeability soil, and increasing the entry rate into the structure. In contrast, Fig 6b shows the soil-gas flow field converging into the slots in the floor of the no-gravel structure. Since no high-permeability layer exists underneath the no-gravel structure, large pressure gradients are required to drive the converging soil gas flow field into the narrow slots.

The performance of the numerical model can be assessed by comparing the model predictions and measurements of pressure coupling around both structures. Figs. 2.3, 2.4, and 2.5 show that the model underpredicts the pressure coupling around both structures at every probe location except the two 2.39-m-long probes in the no-gravel structure low-wall. Around the gravel structure, the model predictions of pressure coupling are more accurate in regions closer to the openings. Fig. 2.3 shows that the model underpredicts the pressure coupling measured in the 0.24 and 0.5-m-long probes in the subslab of the gravel structure by less than 10%. The accuracy of the model predictions in the region near the gravel layer indicates that the model correctly simulates the effect of a subslab gravel layer. However, the model fails to predict the horizontal extension of the soil-gas pressure field around the gravel structure. The model underpredicts the pressure coupling measured in all of the low-wall probes in the gravel structure by more than a factor of two, and in all of the mid-wall probes by more than a factor of three.

Around the no-gravel structure, Figs. 2.3, 2.4, and 2.5 show that the model underpredicts the pressure coupling by at least a factor of two at most probe locations, *including* the subslab. This general underprediction of the pressure coupling by the model suggests that it does not correctly simulate the soil-gas pressure field in the critical near-slot region. If the model overestimated the pressure gradient in the soil near the slots, it would then underpredict the pressure coupling in the rest of the soil block. Such an error could be caused by the value of permeability assigned to the subslab region of the modeled soil block being too small, or an incorrect definition of the interface between the soil and the bottom of the slab. The model assumes that a perfect interface between the soil and the bottom of the slab exists; however, settling could create air gaps under the slab of the no-gravel structure which would reduce the pressure gradient for a given flow compared to the model.

Pressure coupling measurements provide details of the soil-gas flow field created by the depressurization of the interior of the structure. The failure of the numerical model to correctly predict the *shape* of the pressure coupling field indicates that it does not accurately simulate the soil-gas flow field around the structures. Consequently, the factor of 1.5 discrepancy between the measured and modeled soil-gas entry rates into both structures is *not* caused by the permeability measurements used as inputs for the model being a factor of 1.5 too low. Simply increasing the permeability inputs into the model will *not* change the shape of the predicted pressure coupling and soil-gas flow fields. In fact, the comparison of the measurements and model predictions of pressure coupling suggests that the cause of this discrepancy may be different in each structure.

^{222}Rn Entry Rate as a Function of Open Area

Fig. 2.7 shows the measured and predicted radon entry rate into the structures as a function of open area. The radon entry rates have been normalized by structure depressurization. The measured radon concentration of the air in the openings varied by less than 8% over the entire range of pressures and open areas considered during these experiments; therefore, a linear relationship can be used to approximate the relationship between the radon entry rate and structure depressurization.

Fig. 2.7 shows the measured radon entry rate into the gravel structure rapidly increases with open area, reaching an asymptote approximately 0.8 Bq s^{-1} Pa^{-1} for open areas greater than 5 x 10^{-4} m^2. In contrast, the measured radon entry rate into the no-gravel structure gradually increases with open area for the entire range of open areas considered in this study. The slightly non linear response of the measured radon entry rate into the no-gravel structure to changes in open area indicates that there is some coupling between the openings in the floor of the no-gravel structure. However, this response also indicates that a high-permeability region does *not* exist underneath the no-gravel structure. During the construction of the no-gravel structure great care was taken to prevent the formation of any air gaps or regions of loosely packed soil underneath its slab. Consequently, the results from the no-gravel structure may not be representative of real houses.

Fig. 2.7 shows that the model accurately predicts the trend in the response of the radon entry rate into both structures to changes in open area, despite underpredicting the absolute entry rate into both structures by approximately a factor of 1.5. As expected, the model predicts that the soil-gas entry rate into the no-gravel structure will approach the entry rate into the gravel structure as the open area approaches the dirt floor limit, i.e. when no concrete slab is present.

The ratio of radon entry rate into the two structures varies with open area. For the base configuration of six-slots open (165 x 10^{-4} m^2), Fig. 2.7 shows that the measured radon entry rate into the gravel structure is four times greater than the entry rate into the no gravel structure -- the same as the ratio of the measured soil-gas entry rates with six slots open. However, with an open area of 5 x 10^{-4} m^2 the measured radon entry rate into the gravel structure is more than a factor of 30 greater than the entry rate into the no-gravel structure. To significantly reduce the radon entry rate into the gravel structure the open area must be much smaller than 2.5 x 10^{-4} m^2. This is similar to the results of a field study that concluded that the total open area of a basement must be very small in order to consider it radon resistant (Eaton and Scott, 1984).

The soil-gas and advective radon entry rate into the structures also depends on the spatial distribution of the open area. The spatial distribution of open area affects the pressure drop in the critical near-opening region of the soil, and the resistance of the opening itself to soil-gas flow.

Distributing the open area to reduce the soil gas velocities in the critical region of the soil near the openings increases the entry rate into the structure. For example, in the gravel structure, the measured soil-gas entry rate through the four 0.013-m-diameter holes is 30% *higher* than the entry rate through the 0.038-m-diameter hole in the center of the floor despite the four-hole configuration having a total open area of more than a factor of 2 *smaller* than the one-hole configuration. The single 0.038-m-diameter hole forces the soil-gas flow field to converge more sharply than the four-hole configuration. Spreading the open area in the floor of the gravel structure reduces the soil-gas velocity in the gravel near the mouth of the opening, thus reducing the pressure drop in this region. This more effectively depressurizes the gravel layer and increases the total soil-gas and advective radon entry rate into the structure. The distribution of open area similarly affects the radon entry rate into the no-gravel structure.

The resistance of the openings themselves to soil-gas flow also affects the advective radon entry rate into the structure. The relatively wide openings considered in this study cause negligible resistance to soil-gas flow in comparison with the soil. However, the geometry of the gaps and cracks in real houses may be such that the opening itself presents significant resistance to soil gas flow. Therefore, for a fixed open area, distributing the area to maximize the pressure drop in the openings, for example very thin cracks, may reduce the advective radon entry rate into the structure.

^{222}*Rn and Soil-gas Entry as a Function of Pressure Coupling*

Our results demonstrate that a complex relationship exists between open area and radon entry rate. Consequently, open area by itself is a poor indicator of radon entry potential. Even if the amount of open area can be measured, the radon entry into the structures depends strongly on the presence or absence of a subslab gravel layer as well as the spatial distribution of the open area.

A theoretical relationship between the soil-gas entry rate and the extension of the soil-gas pressure field can be derived using Darcy's law and the principle of conservation of mass. This analysis can be extended to the radon entry rate into the structures because the radon concentration of slot air was essentially constant during these experiments. By conservation of mass, the flow rate across any surface, S, which extends through the soil underneath the structure connecting the walls and enclosing the floor is equal to the soil-gas entry rate into the structure; an example of such a surface is the 0.1 pressure coupling contour around the gravel structure shown in Fig. 2.6a. Assuming incompressible flow and writing the soil-gas velocity in terms of Darcy's law, the soil-gas entry rate into the structure can be expressed as an integral over the surface S;

$$Q = \int_S \overline{u} \cdot \overline{n} dA = \int_S -\frac{k}{\mu} \nabla P \cdot \overline{n} dA \qquad (2.5)$$

where $\overline{u}$ is the soil-gas velocity, k is the permeability of the soil, μ is the dynamic viscosity of the soil-gas, ∇P is the pressure gradient across the surface S, and $\overline{n}$ is the unit normal vector to surface S. Assuming constant viscosity and defining the surface S such that $k\nabla P \cdot \overline{n}$ is constant, the soil-gas entry rate into the structure can be written as

$$Q = -\frac{k}{\mu} \nabla P \cdot \overline{n} \int_S dA = -\frac{k}{\mu} \nabla P \cdot \overline{n} A \qquad (2.6)$$

where A is the area of surface S. Eqn. (2.6) shows that for a given structure depressurization soil-gas entry rate into the structure is proportional to the area of a surface of constant $k\nabla P \cdot \overline{n}$.

Although soil-gas entry rate is proportional to the area of a surface of constant $k\nabla P \cdot \bar{n}$, such a parameter is not a practical predictor of soil-gas entry rate because the calculation of it requires exact knowledge of the soil-gas pressure field. However, the area of a surface of constant $k\nabla P \cdot \bar{n}$ is a measure of the extension of the soil-gas pressure field --- the greater the extension of the pressure field, the larger the area of such a surface, and the larger the region from which the structure draws radon-laden soil gas.

Individual measurements of pressure coupling indicate the extension of the soil-gas pressure field. Comparing measurements of pressure coupling made in the *same* location around each structure provides an estimate of the relative extension of the soil-gas pressure field around the structures. The effect of local soil-heterogeneity on an individual measurement of the extension of the pressure field can be reduced by averaging pressure coupling measurements made in several different probes.

In Fig. 2.8 the total advective radon entry rate normalized by structure depressurization is plotted as a function of average subslab pressure coupling, which is an average of the pressure coupling measurements made in all of the 0.24, 0.5, and 1.71-m-long subslab probes during each experiment. The open area of these experiments was varied between 0 and $165 \times 10^{-4}\ \mathrm{m}^2$. All of the measurements in Fig. 2.8 in the *gravel structure* with an entry rate less than

0.5 Bq s^{-1} Pa^{-1} were made with imperfectly sealed openings. Initially duct tape and Dux-seal were used to seal the openings in the structures; however, this seal did not eliminate entry through the openings. All of the measurements made in the *no-gravel structure* with an entry rate less than 0.1 Bq s^{-1} Pa^{-1} were made with an open area 5.0×10^{-4} m^2 or less.

Fig. 2.8 shows that the radon entry rate into *both* structures varies linearly with the average subslab pressure coupling *regardless* of subslab permeability and open area configuration. A linear regression of the radon entry rate into *both* structures as a function of average subslab pressure coupling yields a slope of 1.2 Bq s^{-1} Pa^{-1} per unit of pressure coupling and an intercept of -0.03 Bq s^{-1} Pa^{-1}, $r^2 = 0.97$. Despite incomplete knowledge of the soil-gas pressure field, a crude estimate of the extension of the pressure field is a good predictor of the radon entry rate into the structures. Estimating the extension of the pressure field with an average of the pressure coupling measurements made in a different set of probes, for example the mid-wall probes, does *not* change the linearity of the relationship between the radon entry rate and the extension of the pressure field. However using measurements made in a different set of probes to estimate the extension of the pressure field will change the slope of this relationship.

CONCLUSIONS

The results of this study demonstrate that a high permeability subslab gravel layer can substantially affect soil-gas and radon entry into houses. The measured radon entry rate into the gravel structure is four times greater than the entry rate into the no-gravel structure when the open area through the floor slab is 165 x 10^{-4} m^2. The ratio of the entry rates into the two structures increases as the open area is reduced; with an open area of 5.0 x 10^{-4} m^2 the entry rate into the gravel structure is factor of 30 greater than the entry rate into the no-gravel structure. The high permeability gravel layer couples the openings in the floor of the gravel structure together, enabling very small open areas to effectively depressurize the gravel layer to the same extent as the interior of the structure. Once this occurs, the radon entry rate through openings in the floor is maximized. In contrast, the openings in the floor of the no-gravel structure act relatively independently of each other. Consequently, an increase in open area in the floor of the no-gravel structures increases the radon entry rate.

The impact of a high permeability gravel layer on the soil-gas and radon entry rate underscores the importance of the permeability of the soil near an opening on determining the advective entry through that opening. Since the sharp convergence of the soil-gas flow field causes most of the pressure drop to occur in the soil near an opening, changing the permeability of the soil near an opening can dramatically affect the soil-gas entry rate through that opening. Increasing its permeability will increase the entry rate through the opening. Decreasing its permeability will decrease the entry rate through the opening.

The impact of a subslab gravel layer on radon and soil-gas entry depends on the permeability of the gravel layer and the surrounding soil. This study only considered the specific combination of soil permeabilities measured at the structure site (Table 2.2). However, the results of this study help validate the predictions of numerical models on the effect of different structural and soil parameters on radon and soil-gas entry rate into houses.

Open area is a poor indicator of radon or soil-gas entry rate into the experimental structures. A complex relationship exists between open area and radon and soil-gas entry rate. Although the amount and distribution of open area can affect the radon entry rate, entry into the experimental structures is largely determined by the subslab permeability. The results of this study demonstrate that the extension of the soil-gas pressure field created by depressurization of the structure interior is an excellent predictor of the radon and soil-gas entry into the experimental structures. The radon entry rate into *either* structure has the *same* linear relationship with average subslab pressure coupling *regardless* of open area or the presence or absence of a subslab gravel layer. The average subslab pressure coupling is a measure of the extension of the pressure field. Although a theoretical relationship exists between the extension of soil-gas pressure field and soil-gas entry rate, rigorous application of it requires detailed knowledge of the soil-gas pressure field. The success of the average subslab pressure coupling in predicting the radon entry rate into *both* structures indicates that a crude estimate of the extension of the pressure field may be a useful measure of the soil gas and radon entry potential for real houses without requiring precise knowledge of the physical characteristics of the building or the surrounding soil. Turk et al. (1990a) incorporated measurements of the soil-gas pressure field into a technique for assessing soil gas and radon entry potentials. However a simpler approach based on making pressure coupling and soil permeability measurements at several locations around a building may provide a good relative measure of soil gas entry within a set of similarly characterized buildings.

Comparison of measurements with predictions of a numerical model indicate that a finite-difference model based on Darcy's law with regionally-defined soil parameters accurately simulates the effect of different structure depressurizations, open areas, and subslab permeabilities on radon and soil-gas entry rate. However, the model underpredicts the soil-gas and radon entry rates into both structures by approximately a factor of 1.5. Comparison of the soil-gas pressure fields around both structures suggests that the source of this discrepancy may be different in each structure. The discrepancy in the case of the gravel structure may be caused by the failure of the model to predict horizontal extension of the pressure field.

However, in the case of the no-gravel structure the discrepancy appears to be caused by the model overestimating the pressure drop in the soil near the slots.

The results of this study also help to explain the ineffectiveness of sealing as a radon mitigation technique. In houses with a subslab gravel layer, one must seal essentially all of the openings to significantly reduce radon entry. In addition the results have implications for building codes which require the inclusion of a subslab gravel layer for homes constructed in high radon areas to improve the effectiveness of a passive subslab ventilation system (EPA, 1994). If the passive mitigation system is inadequate or if an active mitigation system is not installed or functioning properly the gravel layer can greatly enhance the radon entry rate, potentially increasing indoor radon concentrations.

REFERENCES

Åkerblom G., Anderson P. and Clavensjo B. (1984) Soil gas radon—A source of indoor radon daughters. *Radiat. Prot. Dosim.* 7, 49-54.

Brennan T. M., Clarkin M. E., Osborne M. C. and Brodhead W. P. (1991) Evaluation of radon resistant new construction techniques. The 1990 International Symposium on Radon and Radon Reduction Technology. Atlanta, GA, EPA.

Brimhall G. H. and Lewis C. J. (1992) Differential element transport in the soil profile at the Ben Lomond small structure radon site: A geochemical mass balance study. University of California at Berkeley, Dept. of Geology and Geophysics, Berkeley CA 94720.

Bruno R. C. (1983) Sources of indoor radon in houses: A review. *J. Air. Pollut. Control Assoc.* **33**, 105-109.

Busigin A., van der Vooren A. W. and Phillips C. R. (1979) Interpretation of the response of continuous radon monitors to transient radon concentrations. *Health Phys.* **37**, 659-667.

Eaton R. S. and Scott A. G. (1984) Understanding radon transport into houses. *Radiat. Prot. Dosim.* **7**, 251-253.

EPA (1994) Model standards and techniques for control of radon in new residential buildings. *Federal Register Notices* **59**, 13402-13416.

Fisk W. J., Modera M. P., Sextro R. G., Garbesi K., Wollenberg H. A., Narasimhan T. N., Nuzum T. and Tsang Y. W. (1992) Radon entry into basements: Approach, experimental structures, and instrumentation of the small structures project. LBL-31864, Lawrence Berkeley National Laboratory, Berkeley CA 94720.

Flexser S., Wollenberg H. A. and Smith A. R. (1993) Distribution of radon sources and effects on radon emanation in granitic soil at Ben Lomond, California. *Environ. Geol.* **22**, 162-177.

Garbesi K. (1993) Toward resolving model-measurement discrepancies of radon entry into houses. LBL-34244, Lawrence Berkeley National Laboratory, Berkeley CA 94720.

Garbesi K. and Sextro R. G. (1989) Modeling and field evidence of pressure-driven entry of soil gas into a house through permeable below-grade walls. *Environ. Sci. Technol.* **23**, 1481-1487.

Garbesi K., Sextro R. G., Fisk W. J., Modera M. P. and Revzan K. L. (1993a) Soil-gas entry into an experimental basement: Model-measurement comparisons and seasonal effects. *Environ. Sci. Technol.* **27**, 466-473.

Garbesi K., Sextro R. G., Fisk W. J. and Nazaroff W. W. (1993b) Toward resolving the model-measurement discrepancy of radon entry into houses: A study of the scale dependence of soil permeability to air. In Kalliokowski P., Jantunen M. and Seppänen O. (Ed.) Indoor Air' 93, Vol. 4: Particles, Microbes, Radon, Indoor Air '93, Helsinki, 575 - 580.

Garbesi K., Sextro R. G., Robinson A. L., Wooley J. D., Owens J. A. and Nazaroff W. W. (1996) Scale dependence of soil permeability to air: Measurement method and field investigation. *Wat. Resour. Res.* **32**, 547-560.

Henschel D. B. (1988) Radon reduction techniques for detached houses: Technical guidance (second edition). EPA/625/5-87/019, Research Triangle Park, NC: Air and Energy Engineering Research Laboratory.

Henschel D. B. (1993) Radon reduction techniques for existing detached houses: Technical guidance (third edition) for active soil depressurization systems. EPA/625/R-93/011, Research Triangle Park, NC: Air and Energy Engineering Research Laboratory.

Loureiro C. O., Abriola L. M., Martin J. E. and Sextro R. G. (1990) Three-dimensional simulation of radon transport into houses with basements under constant negative pressure. *Environ. Sci. Technol.* **24**, 1338-1348.

Modera M. P. and Bonnefous Y. (1993) Statistical uncertainties associated with multiplexed sampling with a continuous radon monitor. *Health Phys.* **64**, 291-299.

Mowris R. (1986) Analytical and numerical models for estimating the effect of exhaust ventilation on radon entry in houses with basements or crawl spaces. LBL-22067, Lawrence Berkeley National Laboratory, Berkeley CA 94720.

Mowris R. J. and Fisk W. J. (1988) Modeling the effects of exhaust ventilation on ^{222}Rn entry rates and indoor ^{222}Rn concentrations. *Health Phys.* **54**, 491-501.

Nazaroff W. W., Feustel H., Nero A. V., Revzan K. L., Grimsrud D. T., Essling M. A. and Toohey R. E. (1985) Radon transport into a detached one-story house with a basement. *Atmos. Environ.* **19**, 31-43.

Nazaroff W. W., Lewis S. R., Doyle S. M., Moed B. A. and Nero A. V. (1987) Experiments on pollutant transport from soil into residential basements by pressure-driven airflow. *Environ. Sci. Technol.* **21**, 459-466.

Nazaroff W. W., Moed B. A. and Sextro R. G. (1988) Soil as a source of indoor radon: Generation, migration, and entry. In Nazaroff W. W. and Nero A. V. (Ed.) *Radon and Its Decay Products in Indoor Air*, John Wiley and Sons, New York, 57-112.

Nero A. V. and Nazaroff W. W. (1984) Characterizing the source of radon indoors. *Radiat. Prot. Dosim.* **7**, 23-39.

Revzan K. and Fisk W. (1992) Modeling radon entry into houses with basements: The influence of structural factors. *Indoor Air* **2**, 40-48.

Rogers V. C. and Nielson K. K. (1993) Data and models for radon transport through concrete. The 1992 International Symposium on Radon and Radon Reduction Technology. Minneapolis, MN, EPA.

Ruppersberger J. S. (1991) The use of coatings and block specification to reduce radon inflow through block basement walls. The 1990 International Symposium on Radon and Radon Reduction Technology. Atlanta, GA, EPA.

Scott A. G. (1988) Preventing radon entry. In Nazaroff W. W. and Nero A. V. (Ed.) *Radon and Its Decay Products in Indoor Air*, John Wiley and Sons, New York, N.Y., 407-433.

Shah R. K. (1978) A correlation for the laminar hydrodynamic entry length solutions for circular and noncircular ducts. *J. Fluid Eng.* **100**, 177-179.

Thomas J. W. and Countess R. J. (1979) Continuous radon monitor. *Health Phys.*

36, 734-738.

Turk B. H., Harrison J., Prill R. J. and Sextro R. G. (1990a) Developing soil gas and ^{222}Rn entry potentials for substructure surfaces and assessing ^{222}Rn control diagnostic techniques. *Health Phys.* **59**, 405-419.

Turk B. H., Harrison J. and Sextro R. G. (1991a) Performance of radon control systems. *Energy Build.* **17**, 157-175.

Turk B. H., Prill R. J., Fisk W. J., Grimsrud D. T. and Sextro R. G. (1991b) Effectiveness of radon control techniques in fifteen homes. *J. Air Waste Mange. Assoc.* **41**, 723-734.

Turk B. H., Prill R. J., Grimsrud D. R., Moed B. A. and Sextro R. G. (1990b) Characterizing the occurrence, sources and variability of radon in Pacific Northwest homes. *J. Air Waste Mange. Assoc.* **40**, 498-506.

Table 2.1. Location of soil probes around both structures. As shown in Fig. 2.1, high-wall, mid-wall, and low-wall probes extend horizontally from the walls at the specified depth, and subslab probes extend vertically through the slab of each structure. Probe length is measured from the outside of the wall or floor slab to the middle of the sampling screen. The labels N,S,E,W identify one horizontal probe and the wall from which it extends -- North, South, East, or West.

		Probe Length (m)				
		0.24	0.5	1.11	1.71	2.39
Level Name	Depth Below Grade (m)	Number and Location of Probes				
High-wall	0.2	0	N,S,E,W	0	E,W	N,S
Mid-wall	0.8	0	N,S,E,W	0	E,W	N,S
Low-wall	1.6	0	N,S,E,W	0	E,W	N,S
Subslab (No-Gravel)	2	2	2	2	2	0
Subslab (Gravel)	2	2	2	0	3	1

Table 2.2. Measured soil and gravel permeability at structure site. Appendix A describes in more detail the results of permeability measurements made at the experimental site.

Soil Type	Horizontal Permeability (m^2)	Vertical Permeability (m^2)
undisturbed[a]	3.0×10^{-11}	1.8×10^{-11}
backfill[b]	3.5×10^{-12}	3.5×10^{-12}
gravel[c]	2.0×10^{-8}	2.0×10^{-8}

[a] (Garbesi, 1993; Garbesi et al., 1996)

[b] (Garbesi, 1993)

[c] (Fisk et al., 1992)

Table 2.3. Measured properties of the undisturbed soil at the structure site. Appendix A describes in more detail the results of porosity measurements made at the experimental site.

Depth of Layer (m)	Soil-grain Density[a] (kg m^{-1})	Radium Content[b] (Bq kg^{-3})	Air-filled Porosity[c]	Emanation Fraction[b]
0 - 1.4	2.80×10^3	30	0.45	0.31
1.4 - 2.25	2.80×10^3	30	0.45	0.45
2.25 - 6	2.80×10^3	30	0.3	0.31

[a] (Brimhall and Lewis, 1992)

[b] (Flexser et al., 1993)

[c] Appendix A

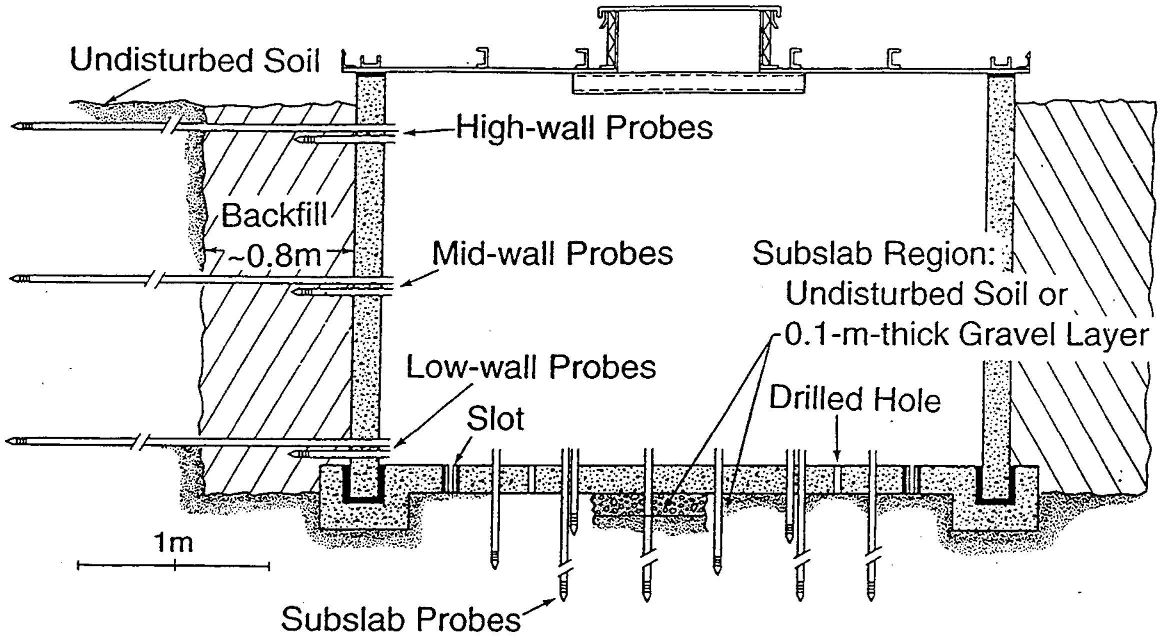

Fig. 2.1. Schematic diagram of north-south cross section of the experimental structures. Soil probes extend from all four walls of the structure, but some are omitted for visual clarity.

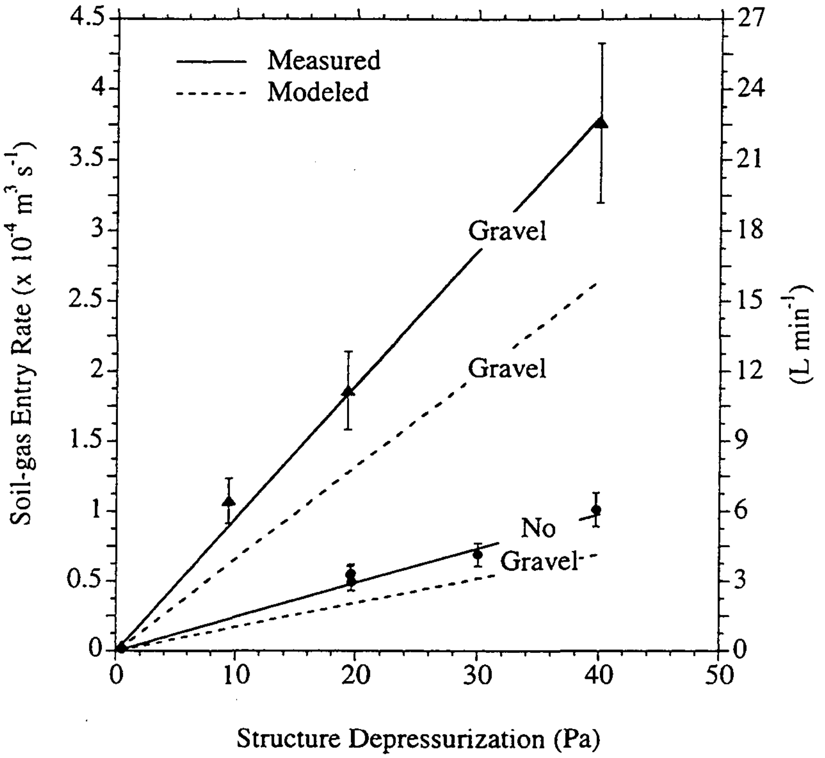

Fig. 2.2. A comparison of measured and predicted soil-gas entry rate into both structures as a function of structure depressurization. The lines through the measured points are linear regressions weighted by uncertainties. The regressions are constrained to pass through the origin. The vertical bars indicate measurement uncertainty.

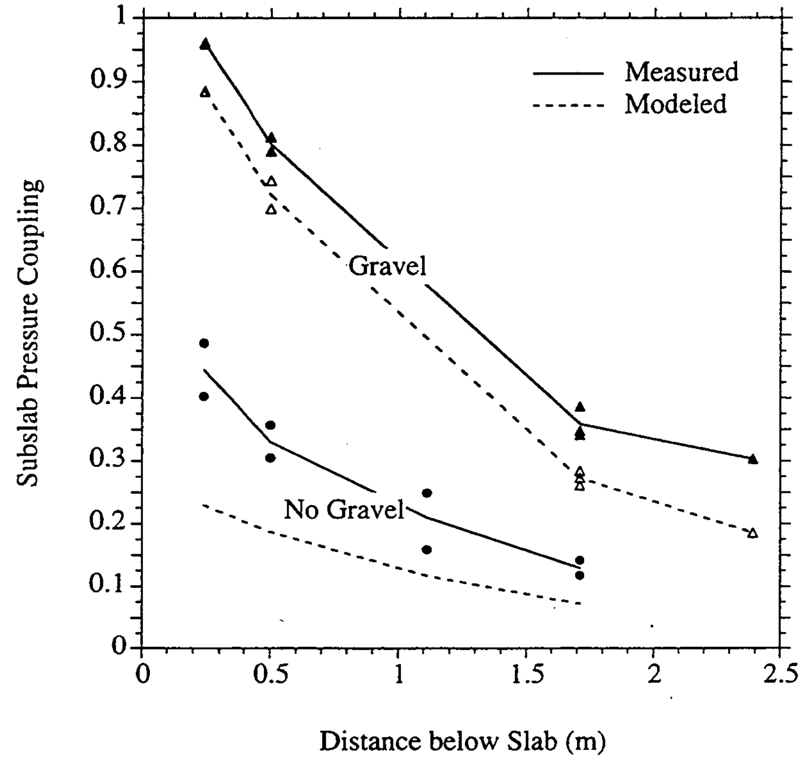

Fig. 2.3. A comparison of measured and modeled subslab pressure coupling underneath both structures with all six slots open. The lines connect average values for each probe length and are intended for visual guidance only. The measured values are indicated by solid symbols; the modeled values are indicated by open symbols. The maximum uncertainty in the measurements is ±0.03 in the gravel structure, and ±0.02 in the no-gravel structure. Note there are no 1.11-m-long probes underneath the gravel structure, and no 2.39-m-long probes underneath the no-gravel structure.

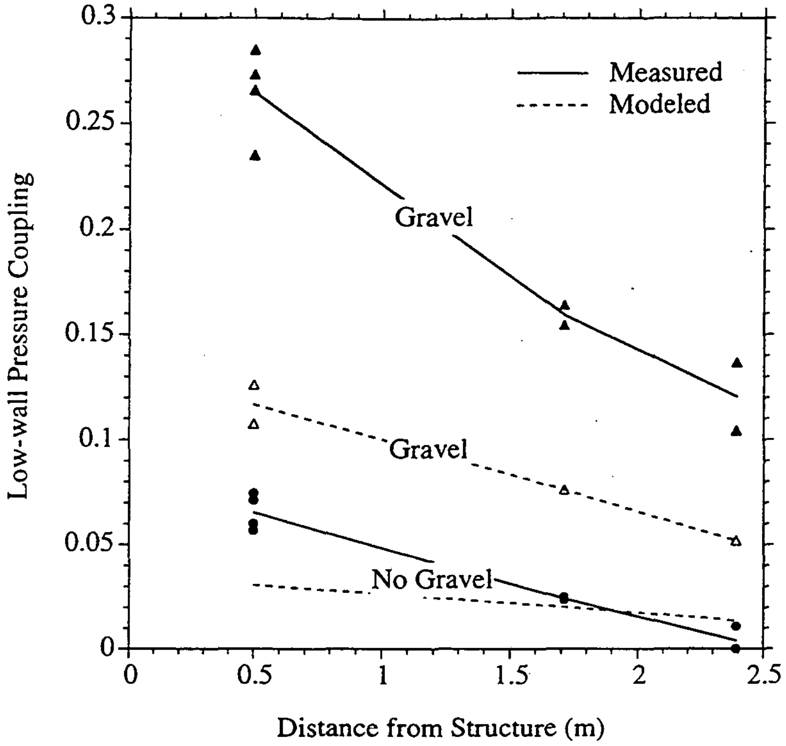

Fig. 2.4. A comparison of measured and modeled low-wall (1.6 m below grade) pressure coupling around both structures with all six slots open. Lines, symbols and uncertainties are the same as in Fig. 2.3.

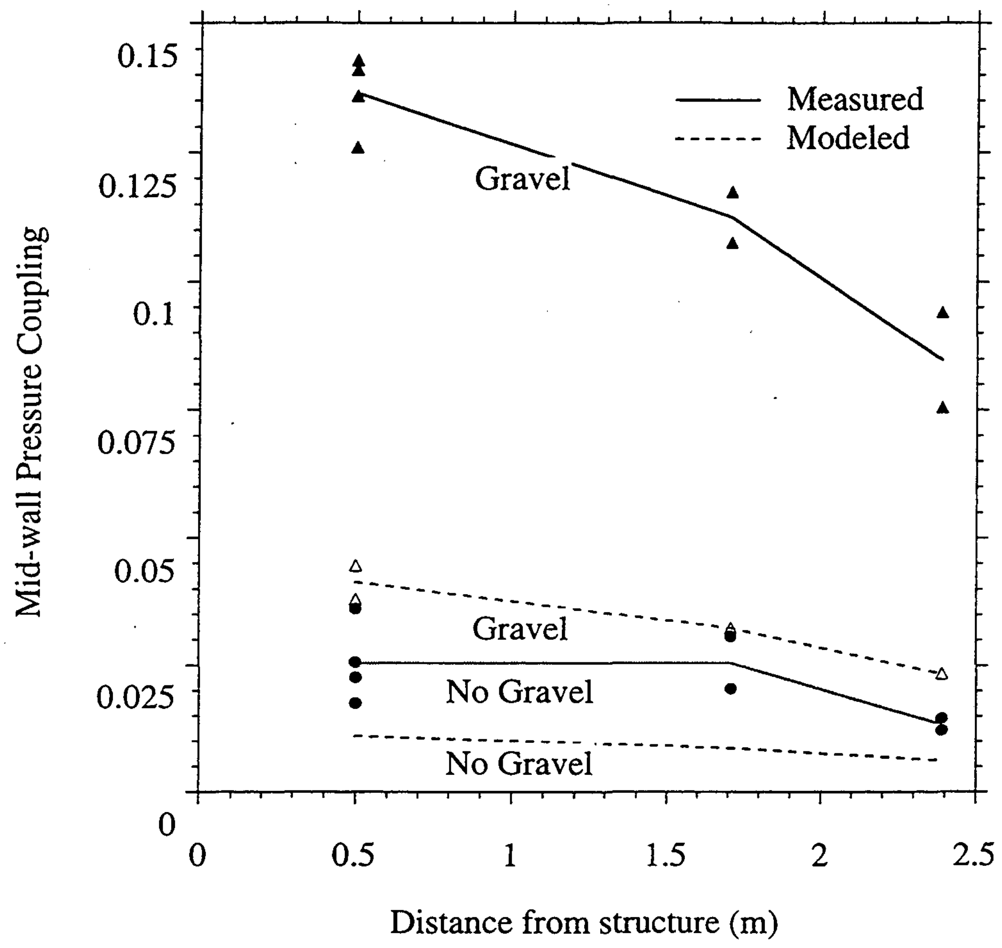

Fig. 2.5. A comparison of measured and modeled mid-wall (0.8 m below grade) pressure coupling around both structures with all six slots open. Lines, symbols and uncertainties are the same as in Fig. 2.3.

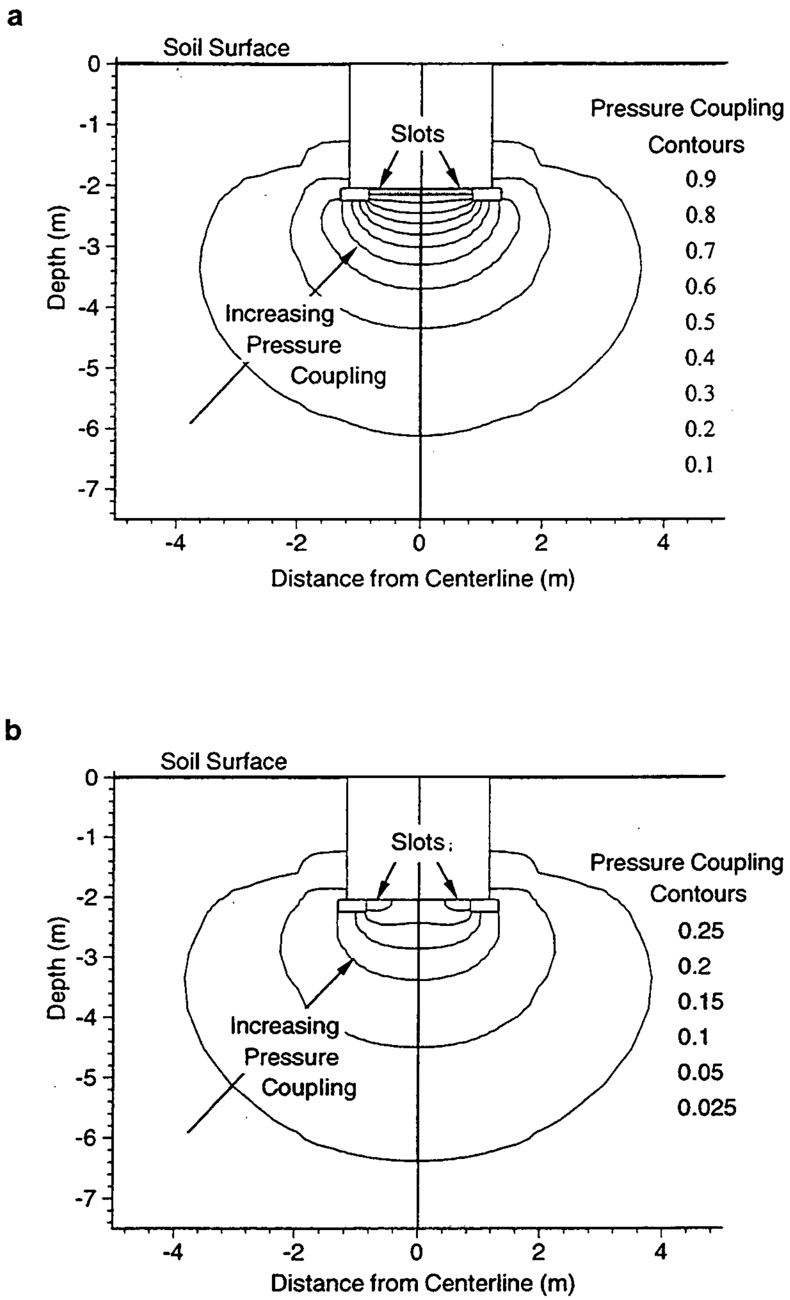

Fig. 2.6. Model prediction of the pressure coupling field in the east-west cross-section around the (a) gravel structure and (b) no-gravel structure with all six-slots open. Lines represent pressure coupling contours. The discontinuity in the 0.1 pressure coupling contour in (a) and the 0.025 pressure coupling contour in (b) corresponds to the the interface between the backfill and the undisturbed soil. The permeability changes by an order of magnitude at this interface (see Table 2.2). The vertical centerline represents the model's plane of symmetry.

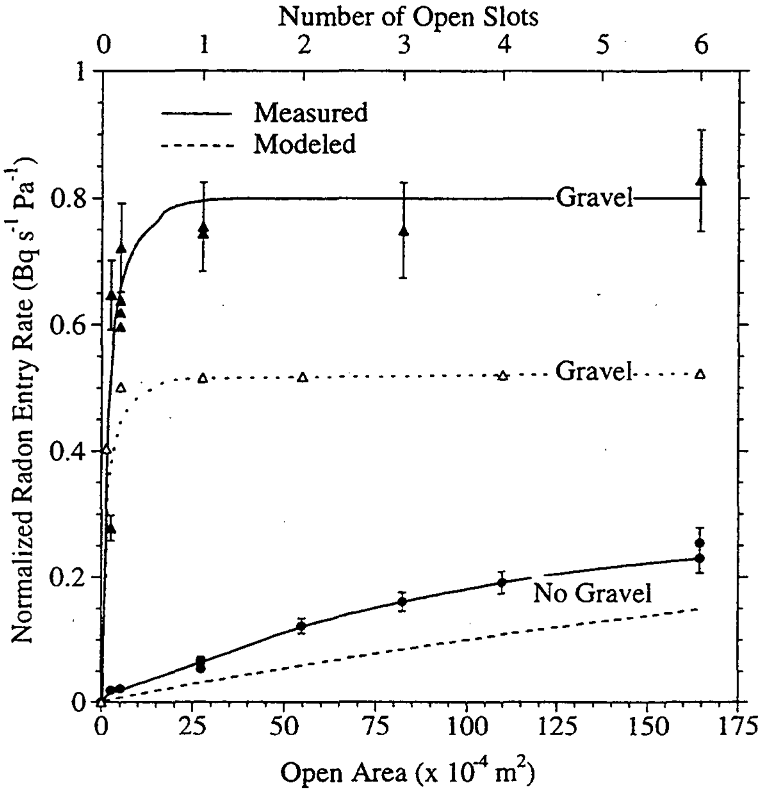

Fig. 2.7. A comparison of measured and modeled advective radon entry rate normalized by structure depressurization as a function of open area. Measured values are indicated by solid symbols, and modeled values are indicated by open symbols. Lines are intended for visual guidance only. The vertical bars indicate experimental uncertainty.

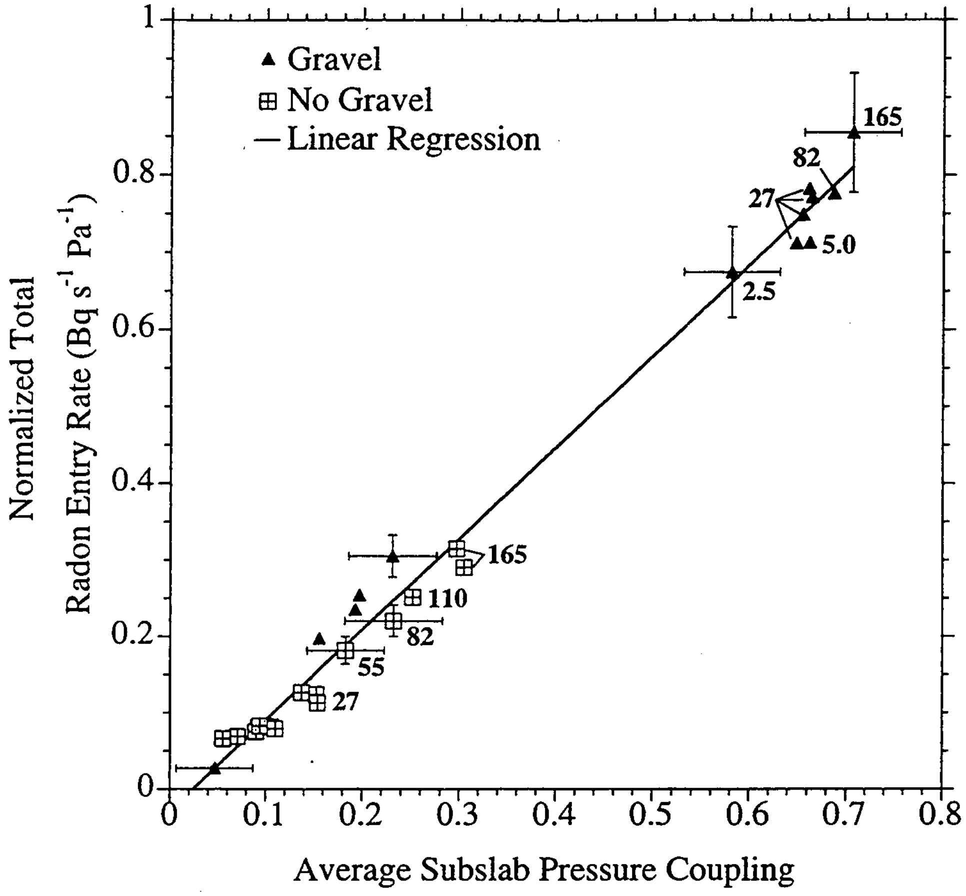

Fig. 2.8. Measured total advective radon entry rate into each structure normalized by structure depressurization as a function of average subslab pressure coupling. Numbers adjacent to symbols refer to open area in units of 10^{-4} m^2. Vertical bars indicate experimental uncertainty in the radon entry rate, a maximum of ±12%. Horizontal bars indicate the uncertainty of the average subslab pressure coupling, a maximum of ±0.05. Error bars omitted on some points for visual clarity.

Chapter 3

SOIL-GAS ENTRY INTO HOUSES DRIVEN BY ATMOSPHERIC PRESSURE FLUCTUATIONS: MEASUREMENTS, SPECTRAL ANALYSIS, AND MODEL COMPARISON[*]

ABSTRACT

To study the effect of atmospheric pressure fluctuations on the entry of radon and soil-gas contaminants into houses, we have simultaneously measured the gas flow rate into and out of an experimental basement structure and the changes in atmospheric pressure. Falling atmospheric pressure draws soil gas into the structure; rising atmospheric pressure drives air from inside the structure into the soil. The gas flow rate into and out of the structure depends on both the characteristic response time of the soil gas and the time-rate-of-change of the atmospheric pressure fluctuations. The larger the time-rate-of-change of a fluctuation in atmospheric pressure the larger the gas flow rate into the structure; a change in pressure must be sustained for a period comparable to several characteristic response times of the soil gas to maximize the soil-gas flow rate.

---

[*] A modified version of this chapter was submitted for publication to the journal Atmospheric Environment: Robinson A. L., Sextro R. G. and Fisk W.J. Soil-gas entry into houses driven by atmospheric pressure fluctuations, part 1 --- Measurements, spectral analysis, and model comparison. Preliminary results of this investigation were reported in the paper: Robinson A. L. and Sextro R. G. (1995) Direct measurements of soil-gas entry into an experimental basement driven by atmospheric pressure fluctuations. *Geophys. Res. Let.* 22, 1929-1932.

Spectral analysis reveals that diurnal and semi-diurnal oscillations in atmospheric pressure drive the largest components of the long-term gas flow rate into and out of the structure. Analytical and numerical model predictions are compared to the detailed measurements of gas flow in both the time and frequency domains. The finite-element model correctly predicts both the dynamics and the magnitude of the observed gas flow, while the analytical model correctly predicts its dynamics, but underpredicts the amplitude of the observed flow by a factor of ~ 2.3. Atmospheric pressure fluctuations may increase the long-term radon entry rate into the experimental structure by as much as 0.2 Bq s^{-1}. This entry rate is more than twice the total diffusive entry rate, and comparable to that induced by a sustained indoor-outdoor pressure difference of 0.4 Pa.

INTRODUCTION

Recent theoretical studies have shown that atmospheric pressure fluctuations can draw soil gas into houses (Narasimhan et al., 1990; Tsang and Narasimhan, 1992). We are interested in the different mechanisms which induce soil-gas flow because the advective entry of radon-bearing soil gas into houses is believed to be the dominant transport mechanism of radon into most homes with elevated indoor concentrations (e.g. Nazaroff, 1992). Advective soil-gas flow may also transport VOCs (volatile organic chemicals) from contaminated soils into buildings thereby contributing to indoor exposures to these contaminants (Wood and Porter, 1987; Hodgson et al., 1992; Little et al., 1992).

Soil-gas entry into houses is commonly associated with small but sustained indoor-outdoor pressure differences of the order of several Pa created by temperature effects, wind interaction with the building shell, and the operation of heating, ventilation and air-conditioning (HVAC) systems (Nazaroff et al., 1988). However, several field studies (Hernandez et al., 1984; Holub et al., 1985; Turk et al., 1989; Hintenlang and Al-Ahmady, 1992) have observed elevated indoor radon concentrations during periods when indoor-outdoor pressure differences were apparently small. Atmospheric pressure fluctuations can draw soil gas into a house *without* indoor-outdoor pressure differences because the response time of the interior of a house to a change in atmospheric pressure is generally several orders of magnitude shorter than the response time of the soil gas. Consequently, soil-gas entry driven by atmospheric pressure fluctuations represents a possible explanation for these observed but unexplained elevated indoor radon concentrations.

The reported experimental evidence for radon entry driven by atmospheric pressure fluctuations is based on the correlation of atmospheric pressure with measured indoor radon concentrations (Hernandez et al., 1984; Hintenlang and Al-Ahmady, 1992). Unfortunately, such studies provide little detailed insight into the effect of atmospheric pressure fluctuations on radon entry because indoor radon concentrations depend on both the entry rate and the building ventilation rate. Using a numerical model, Tsang and Narasimhan (1992) have investigated the effect of periodic atmospheric pressure oscillations on radon entry. Their results suggest that such oscillations may drive significant radon entry into houses for certain combinations of soil properties, basement configurations and atmospheric pressure signals.

In Chapters 3 and 4, we present a detailed examination of the gas flow between a building and the underlying soil in response to changes in atmospheric pressure. The goal of these chapters is to characterize the relationship between this flow, soil properties, and typical atmospheric pressure fluctuations. A thorough understanding of this transient gas flow is an important step towards understanding the complex effect of atmospheric pressure fluctuations on the entry of radon and other soil-gas contaminants into buildings.

In this chapter, we report measurements of gas flow and atmospheric pressure made in an experimental basement structure. We compare these measurements to predictions of both a finite-element and an analytical model. We employ spectral analysis to examine our measurements and to validate the predictions of these models. In the Chapter 4, these models are used to examine the sensitivity of the soil-gas entry into a house to changes in soil properties, water table depth, and the presence of a high-permeability gravel layer beneath the concrete floor slab.

EXPERIMENTAL AND COMPUTATIONAL METHODS

Experimental System

The measurements reported in this chapter were made in an experimental structure which was designed and constructed to study soil-gas and radon entry into houses (Fisk et al., 1992; Garbesi et al., 1993). Fig. 3.1 shows a schematic of the soil-structure system. The concrete structure is a single-chamber with interior dimensions of 2.0 x 3.2 m and a height of 2.0 m; only about 0.1 m of the walls extend above grade. The structure's floor slab rests on a 0.1-m-thick, high-permeability gravel layer. Two 1.25-cm-diameter holes located in one wall of the access hatch permitted the interior of the structure to rapidly respond to changes in atmospheric pressure. A companion structure exists at this experimental site which is essentially identical to the one used for this study except that its floor slab rests on undisturbed soil.

The atmospheric pressure was measured at 0.2 Hz using a pressure transducer connected to an outdoor omnidirectional static pressure tap located ~ 3 m from the structure (Paroscientific model 1015a). The response time, accuracy, and resolution of this pressure transducer are 1 s, ± 5 Pa, and 0.1 Pa, respectively. The pressure difference between the interior of the structure and the static pressure tap was measured at 30-s intervals using a differential pressure transducer (Validyne model DP103). We refer to this pressure difference as the indoor-outdoor pressure difference.

All openings between the structure interior and the soil are sealed except for a 3.8-cm-diameter hole in the center of the structure floor. Although this hole is not geometrically representative of the cracks and gaps which commonly exist in real houses (Scott, 1988), these experiments require such an opening in combination with a high-permeability subslab gravel layer to enable atmospheric pressure fluctuations to generate gas velocities greater than the detection limit of our flow sensor. Because of the high permeability of the subslab gravel layer, the soil-gas flow rate into the structure only weakly depends on the geometry of an opening if the opening does not provide significant resistance to flow. The effect of a gravel layer on steady-state soil-gas entry was examined in Chapter 2; its effect on transient entry is explored in the Chapter 4. Therefore, the measured gas flow rate through the hole is representative of the flow between the structure and the soil for more realistic opening configurations.

The gas flow rate through the 3.8-cm-diameter hole was measured using the flow sensor shown in Fig. 3.1. The 80-cm high sensor incorporates two omnidirectional hot-film velocity transducers (TSI model 8470) mounted in a U-shaped tube (1.9-cm ID) and measures the magnitude and direction of gas flows as small as 0.15 L min^{-1}. Two velocity transducers are required to determine the direction of the soil-gas flow. A hot-film velocity transducer determines the gas velocity by measuring the heat loss rate from a small sphere which is maintained at a constant temperature difference relative to the surrounding gas. At low velocities (low gas flow rates), the complex interaction between the slight flow induced by this temperature difference and the mean gas flow around the sphere causes this heat loss rate to depend on the orientation of the gas velocity with respect to gravity (Hatton et al., 1970). This effect enables us to determine the direction of the flow. At the same flow rate, the upward velocity reported by one transducer will be greater than the downward velocity reported by the other transducer. Although at flow rates in the sensor greater than 1 L min^{-1} this effect disappears, we assume that our sampling frequency of 0.2 Hz is much more rapid than the changes in flow direction, allowing us to record the direction of the lower velocities that accompany these changes. Because of the small size of the spherical sensing element, the slight flow induced by its elevated temperature does not affect our measurements of gas flow. The sensor was calibrated with a bubble flow meter. The response time, accuracy, and resolution of the flow sensor are 2 s, 5% of reading, and 0.02 L min^{-1} respectively. For the range of flows considered in this study, the resistance of the flow sensor tube varies linearly with flow and was measured in the laboratory to be 0.3 Pa L^{-1} min. Appendix B describes in more detail the theory, operation, and calibration of the U-shaped flow sensor.

Measured Soil Properties

Table 3.1 reports the measured permeability of the gravel, backfill, and undisturbed soil at the structure site. The permeability of the undisturbed soil is scale dependent, increasing by more than an order of magnitude when the measurement scale increases from 0.1 to 3.5 m (Garbesi et al., 1996). In Table 3.1 we report the values measured at the 3.5-m scale, the longest length scale at which measurements were made. Although the length scale of our system is ~ 6.5 m (defined by the depth of the water table below the structure floor slab), the measurements suggest that the horizontal permeability of the undisturbed soil approaches an asymptote of ~ 3×10^{-11} m^2 at length scales greater than 3 m (Garbesi et al., 1996). The backfill region, shown in Fig. 3.2, was excavated during the construction of the structure. It was carefully refilled to minimize the disturbance of the native soil environment (Fisk et al., 1992). The careful packing of the backfill region is thought to have destroyed the features which create the scale dependence observed in the undisturbed soil.

Measurements of the air-filled porosity of the soil at the structure site are summarized in Table 3.2. We calculated this porosity profile based on gravimetric analysis (Danielson and Sutherland, 1986) of soil cores taken by Flexser et al (1993). The change in porosity between 1.6 and 2.2 m corresponds to the transition between the organic surface soil and the underlying sapprolite. Further geological details of the structure site are described by Flexser et al. (1993) and Brimhall and Lewis (1992). Appendix A describes in more detail the results of soil permeability and porosity measurements made at the experimental site.

Spectral Analysis of Experimental Data

Atmospheric pressure and soil-gas entry data for spectral analysis were collected over a period of 30 days in the fall of 1994. This data set is continuous except for four ~ 1 hr periods during which data were downloaded. For this analysis, the data were broken into overlapping, equal length time blocks (Bendat and Piersol, 1986). To eliminate the influence of soil-gas flow driven by indoor-outdoor pressure differences on our estimates, time blocks were discarded in which the absolute value of the measured indoor-outdoor pressure differences were greater than 0.5 Pa. These periods occurred during storms when high winds (speeds greater than ~5 m s^{-1}) blowing over the open holes in the structure access hatch depressurized the interior of the structure relative to the outside. The application of this criterion resulted in data being drawn from approximately 21 non-sequential days of the measurements.

We employ the algorithms described by Bendat and Piersol (1986) to estimate 1) the atmospheric pressure, time-rate-of-change of atmospheric pressure, and soil-gas flow rate power spectra, and 2) the gain and phase functions of the soil-structure system. Briefly, the Hanning taper window was applied to the data in each time block to reduce leakage of power to adjacent frequency bins (Bendat and Piersol, 1986). The data were then transformed into the frequency domain using a fast Fourier transform. The Fourier transforms of the data within each time block were corrected for power loss due to the taper window, and then averaged to generate smooth, consistent spectral estimates of the various power spectra and gain and phase functions using the expressions described by Bendat and Piersol (1986). To minimize the effect of aliasing on our estimates, the highest 25% of the frequency ordinates of each periodogram were discarded.

We analyzed the reduced data set twice using different length time blocks. To increase the resolution of our estimates at low frequencies, 5-day-long blocks were used to calculate the various spectral functions at frequencies less than 200 day^{-1}. To decrease the variance of our estimates at higher frequencies, 24-hour-long blocks were used to estimate these functions at frequencies greater than 100 day^{-1}. These estimates were combined by averaging their respective values in overlapping frequency bins.

Theoretical Framework for Predicting Transient Soil-gas Flow

In this section we describe the equations which govern the transient flow of soil gas into houses. In subsequent sections we describe both an analytical and numerical model which we use to solve these equations and predict the gas flow rate into and out of the experimental structure in response to changes in atmospheric pressure.

Combining Darcy's law and the continuity equation, and considering soil air as a compressible ideal gas, the equation which predicts the propagation of a pressure fluctuation through a homogeneous porous medium is (see e.g. Massmann, 1989)

$$\frac{\partial p}{\partial t} = \frac{k}{\varepsilon\mu}\nabla(p\nabla p) \tag{3.1}$$

where p is the soil-gas disturbance pressure (Pa), k is the soil permeability to air (m^2), ε is the air-filled porosity (-), and μ is the dynamic viscosity of the soil gas (Pa s). Massmann (1989) shows that for small deviations from the mean pressure (< 5 %), eqn. (3.1) can be approximated with negligible error by the linear transient diffusion equation

$$\frac{\partial p}{\partial t} = D_p \nabla^2 p \qquad \text{where } D_p = \frac{k\bar{P}}{\varepsilon\mu} \tag{3.2}$$

where D_p is the pressure diffusivity ($m^2\ s^{-1}$), and $\bar{P}$ is the mean soil-gas pressure (Pa). Many authors (see e.g. Buckingham, 1904; Fukuda, 1955; Weeks, 1979) have used the transient diffusion equation to predict soil gas response to atmospheric pressure fluctuations. After eqn. (3.1) or (3.2) has been solved, the soil-gas velocity field, $\bar{v}$ ($m\ s^{-1}$), can be calculated with Darcy's law,

$$\bar{v} = \frac{-k}{\mu}\nabla p \tag{3.3}$$

Utilizing dimensional analysis, we can estimate a characteristic response time of the soil gas to a change in pressure. Such a response time, τ (s), can be derived from eqn. (3.2),

$$\tau = \frac{L^2}{D_p} \tag{3.4}$$

where L is the characteristic length scale of the system (m). Physically, τ characterizes the time for a pressure perturbation to propagate the distance L.

Since the equation which predicts the propagation of small pressure perturbations through a porous medium is linear, many powerful analysis tools can be used to investigate soil-gas flow driven by changes in atmospheric pressure. This transient flow can be equivalently characterized in both the time and the frequency domains (Chatfield, 1989). There are many advantages to examining this flow in the frequency domain because typical atmospheric pressure signals are dominated by large oscillations at two or three frequencies (Gossard, 1960). Several studies (Burkhard et al., 1987; Nilson et al., 1991; Neeper and Limback, 1994) have employed spectral techniques to analyze soil-atmosphere interactions.

In the time domain, the transient response of the soil gas to changes in atmospheric pressure is characterized in terms of the step-response function. The step-response function defines the soil-gas flow rate into the structure caused by a unit-step change in atmospheric pressure. Once this function is known, the soil-gas flow rate caused by *any* change in atmospheric pressure can be determined by convoluting the step-response function with the atmospheric pressure signal. In the study of heat conduction this convolution is known as Duhamel's theorem

(Carslaw and Jaeger, 1959). In the present context, Duhamel's theorem states that the soil-gas flow rate can be expressed as a function of either atmospheric pressure or the time-rate-of-change of atmospheric pressure. We will develop both formulations to compare and contrast these two ways at looking at the problem. Duhamel's theorem defines the gas flow rate into and out of the structure in response to changes in atmospheric pressure, q(t) ($m^3\ s^{-1}$), as

$$q(t) = \int_{-\infty}^{t} Q_{step}(t-\theta)\, P'_{atm}(\theta)d\theta, \text{ or} \tag{3.5a}$$

$$q(t) = \int_{-\infty}^{t} Q'_{step}(t-\theta)\, P_{atm}(\theta)d\theta \tag{3.5b}$$

where Q_{step} is the step-response function of the soil-structure system ($m^3\ s^{-1}\ Pa^{-1}$), Q'_{step} is the time derivative of the step-response function ($m^3\ s^{-2}\ Pa^{-1}$), P_{atm} is the atmospheric pressure (Pa), P'_{atm} is the time-rate-of-change of atmospheric pressure (Pa s^{-1}), and θ is a dummy variable indicating integration over time (s).

In the frequency domain, the transient response of the soil gas to changes in atmospheric pressure is characterized by the frequency-response function. The frequency-response function defines the amplitude and the phase of the soil-gas flow rate caused by a sinusoidal oscillation in atmospheric pressure. Because the equation which governs the propagation of a pressure perturbation through a porous medium is linear, a sinusoidal oscillation in atmospheric pressure will drive a sinusoidal oscillation of soil-gas flow at the *same* frequency (Chatfield, 1989). The frequency-response function can be defined as the Fourier transform of the step-response function:

$$\chi(\omega)=\int_0^\infty Q_{step}(\theta)\exp(-i\omega\theta)d\theta\text{, or} \tag{3.6a}$$

$$d\chi(\omega)=\int_0^\infty Q'_{step}(\theta)\exp(-i\omega\theta)d\theta \tag{3.6b}$$

where $i = \sqrt{-1}$, and ω is the circular frequency (radians s^{-1}).

We will report the complex valued frequency-response function in terms of the gain, $G(\omega)$, and phase, $\phi(\omega)$, functions (Chatfield, 1989),

$$G_{q,dp}(\omega)=|\chi(\omega)| \quad \text{and} \quad \phi_{q,dp}(\omega)=\arg(\chi(\omega)) \tag{3.7a}$$

$$G_{q,p}(\omega)=|d\chi(\omega)| \quad \text{and} \quad \phi_{q,p}(\omega)=\arg(d\chi(\omega)) \tag{3.7b}$$

where | | and arg( ) indicate the magnitude and argument of a complex number. $G_{q,dp}(\omega)$ (m^3 Pa^{-1}) and $\phi_{q,dp}(\omega)$ (radians) define the amplitude and phase of the soil-gas flow rate caused by an oscillation in the time-rate-of-change of atmospheric pressure as a function of frequency. $G_{q,p}(\omega)$ (m^3 s^{-1} Pa^{-1}) and $\phi_{q,p}(\omega)$ (radians) define the amplitude and phase of the soil-gas flow rate caused by a oscillation of atmospheric pressure as a function of frequency.

Description of the Analytical Model

In this section we derive analytical expressions for the step and frequency-response functions of an idealized structure based on an exact solution of eqn. (3.2). The model predicts the soil-gas flow underneath the structure by approximating this flow as one-dimensional in the vertical plane between the deep soil and the gravel layer. The flow underneath the structure is approximated as one-dimensional because: 1) the gravel layer acts as an isobaric plenum (see Chapter 2), and 2) atmospheric pressure fluctuations drive flow because of the compressibility of the soil gas. Although the flow within the gravel layer is not one-dimensional because of the convergence of the flow field into the hole in the concrete floor slab, we have assumed that this does not significantly affect the flow rate into the basement because the permeability of a gravel layer is almost 3 orders of magnitude larger than the permeability of the undisturbed soil. The analytical model assumes that the pressure within the gravel layer is uniform, and that the gas flow rate into and out of the structure is equal to the flow between the soil and the gravel layer.

With these assumptions, the step-response function of the soil-structure system can be approximated by solving eqn. (3.2) with the following initial and boundary conditions: initial condition, $p(z,0) = 0$ Pa for $0 \leq z \leq L$; boundary condition #1, $p(0,t) = 1$ Pa for $t > 0$ (unit step change in the disturbance pressure in the gravel layer defined at $z = 0$); boundary condition #2 $\partial p(L,t)/\partial z = 0$ Pa for $t > 0$ (a no flow boundary at the $z = L$; physically this boundary represents a water table, bedrock, or some other impermeable layer). The analytical model defines the interface between the gravel layer and the soil as $z = 0$. Assuming homogeneous soil, the solution of eqn. (3.2) for these boundary conditions is (Carslaw and Jaeger, 1959)

$$p(z,t) = -\frac{4}{\pi}\sum_{n=0}^{\infty}\frac{\sin\left[(2n+1)\frac{\pi}{2}\frac{z}{L}\right]}{(2n+1)}\exp\left[\frac{-t}{T_n}\right] \qquad \text{defined for } t \geq 0 \qquad (3.8)$$

where $T_n = \frac{1}{(2n+1)^2}\left(\frac{4}{\pi^2}\right)\left(\frac{L^2}{D_p}\right)$. Assuming that the gas flow rate into the structure is equivalent to the soil-gas flow into the gravel layer, we can obtain the structure's step-response function by applying Darcy's Law and eqn. (3.8):

$$Q_{step}(t) = \frac{k}{\mu}\frac{2}{L}A\sum_{n=0}^{\infty}\exp\left(\frac{-t}{T_n}\right) \qquad \text{defined for } t \geq 0 \qquad (3.9)$$

where A is the horizontal cross-sectional area of the gravel layer (m^2). Using eqns. (3.6a) and (3.9) we can derive an expression for the frequency-response function defined by the analytical model, $\chi_a(\omega)$,

$$\chi_a(\omega) = \frac{k}{\mu}\frac{8}{\pi^2}\frac{L}{D_p}A\sum_{n=0}^{\infty}\left(\frac{1}{(2n+1)^2}\right)\left(\frac{1-i\omega T_n}{1+(\omega T_n)^2}\right) \qquad \text{defined for } \omega > 0. \qquad (3.10)$$

Eqns. (3.8)-(3.10) indicate that application of the analytical model requires the evaluation of an infinite series. Fortunately, this series rapidly converges and only a small number of terms need be considered to accurately approximate the analytical solution. We considered the series converged when the relative error of neglecting an additional term was less than 10^{-8}. Values of the different soil and geometric properties used as inputs for the analytical model to simulate gas flow into and out of the experimental structure are listed in Table 3.3.

Description of Numerical Simulations

A transient, finite-element model was used to predict the gas flow rate into and out of the experimental basement structure. The model calculates this flow rate by solving eqns. (3.1) and (3.3) over the region shown in Fig. 3.2. The gas flow rate into and out of the structure is defined by the soil-gas velocity normal to the opening in the basement floor. The code is a modified version of the RN3D model written by Holford (1994). RN3D was developed to simulate gas flow and radon transport in variably saturated, non-isothermal porous media. The original code only simulates regularly shaped geometries; we have written a preprocessor to generate a two-dimensional mesh with an irregularly shaped boundary required for simulating soil-gas flow around a basement. Holford (1994) describes the mathematics, numerics, and physics of the model. Appendix C describes in more detail the modifications made to the RN3D.

Although the experimental structure has a rectangular floor plan, we simulated it as a cylindrical basement surrounded by a cylindrical soil block. The radius of the simulated gravel layer was defined to match the horizontal cross-sectional area of the gravel layer of the real structure, 5 m^2. By simplifying the problem into an axial-symmetric radial coordinate system we significantly reduce the computational requirements of the model while preserving the structure volume and floor area. In addition, by utilizing a cylindrical coordinate system we can accurately simulate the convergence of the soil-gas flow field into the hole in the center of the structure floor. We divided the model's soil block into the three regions shown in Fig. 3.2. The permeability values assigned to each region are listed in Table 3.1. The air-filled porosity of the soil block varied with depth as summarized in Table 3.2.

To examine the gas flow rate into and out of the structure driven by atmospheric pressure fluctuations, we used the finite-element model to simulate the step-response function. For this simulation the following initial and boundary conditions are used: initially ($t = 0$ s) the entire soil block was assigned a disturbance pressure of 1; for $t > 0$ s the soil surface (indicated as P1 in Fig. 3.2) and the mouth of the hole (indicated as P2 in Fig. 3.2) were assigned a disturbance pressure of 0 Pa. The disturbance pressure is the absolute soil-gas pressure corrected for hydrostatic effects; in other words, the disturbance pressure is the pressure that drives soil-gas flow. The mean soil-gas pressure at the experimental site is 92,200 Pa. As Fig. 3.2 indicates, the outside edge of the structure's concrete walls, floor, and footer are defined as no flow boundaries (the normal soil-gas velocity at each of these boundaries is zero). The bottom of the soil block is defined as a no flow boundary at the measured depth of the water table. The outside edge of the soil block is also defined as a no flow boundary. The radius of the soil block (15 m) was chosen such that outside edge of the soil block falls outside the domain of influence of the structure.

To simulate the step-response function, the finite-element model marches forward in time utilizing a fully-implicit time-discretization scheme until the soil-gas flow rate into the structure had fallen 7 orders of magnitude from its peak value. At this point, we assume that the soil gas and atmospheric pressure have reached equilibrium and the simulation is ended. We assumed that the atmospheric pressure is uniform across the entire surface of the soil, and that changes in atmospheric pressure are communicated instantaneously to the interior of the structure.

After determining the step-response function, we calculated the gain and phase functions by first numerically evaluating eqn. (3.6a) and then applying the definitions shown in eqns. (3.7a) and (3.7b). The gas flow rate into and out of the structure in response to different atmospheric pressure signals was determined by numerically evaluating eqn (3.5a). By indirectly calculating this flow using the step-response function, the computational time to simulate a particular atmospheric pressure signal is reduced by several orders of magnitude in comparison to directly simulating that pressure signal with the finite-element model. To examine the difference between the soil-gas flow rate calculated using the step-response function and the flow rate calculated directly by the finite-element model, we directly simulated 1 hr of atmospheric pressure data with the model. The maximum difference between the flow rate directly computed by the finite-element model and the flow rate calculated using the step-response function was less than 0.04 L min^{-1}; the average relative error was less than 0.5%.

An iterative procedure was used to incorporate the resistance of the flow sensor in the simulations. For each time step the pressure at the mouth of the hole was initially set equal to the pressure in the basement. The model then calculated the soil-gas flow rate into the basement. The pressure boundary condition at the bottom of the opening was adjusted to account for the resistance of the flow sensor and the flow rate into the structure was recomputed. This procedure was repeated until the flow rate had converged, defined as a relative flow change of less than 10^{-4} between iterations.

We also employed the finite-element model to simulate soil-gas entry driven by a steady-state indoor-outdoor pressure difference. For these calculations, the model solves the steady-state form of eqn. (3.1) with the following boundary conditions: soil surface (indicated as P1 in Fig. 3.2) is assigned a disturbance pressure of 1 Pa, and mouth of the opening (indicated as P2 in Fig. 3.2) is assigned a disturbance pressure of 0 Pa. As previously described, all of the other boundaries of the soil block are defined as no-flow.

RESULTS AND DISCUSSION

Since most investigations of soil-gas entry into houses have focused on entry driven by steady indoor-outdoor pressure differences, we briefly compare this entry to entry caused by changes in atmospheric pressure before presenting our measurements of gas flow and atmospheric pressure. A comparison of the flow field around the experimental structure created by an indoor-outdoor pressure difference to one induced by a change in atmospheric pressure highlights many of the differences between these two phenomena.

We employed the finite-element model to illustrate the nature of these flow fields. Fig. 3.3a shows the calculated soil-gas pressure and velocity fields caused by a constant time-rate-of-change of atmospheric pressure. The streamlines indicate that a change in atmospheric pressure drives approximately one-dimensional flow between the deep soil and the gravel layer underneath the structure. For comparison, predictions of the soil-gas pressure and velocity fields caused by steady indoor-outdoor pressure difference are shown in Fig. 3.3b. An indoor-outdoor pressure difference creates a more complex, three-dimensional flow field because the driving potential for flow exists between the interior of the structure and surface of the soil.

Although the different mechanisms which create indoor-outdoor pressure differences vary in time (Nazaroff et al., 1988), most analyses of soil-gas entry driven by these pressure differences assume that this entry can be approximated as a steady-state process in which the soil gas is treated as incompressible (e.g. Nazaroff 1992). Thus, the flow of soil gas into a basement driven by indoor-outdoor pressure differences is balanced by flow from the atmosphere into the soil. In contrast, soil-gas flow driven by changes in atmospheric pressure is fundamentally a transient phenomena where atmospheric pressure fluctuations drive gas flow because of the compressibility of the soil gas. A change in atmospheric pressure causes a net gas flow either into or out of the soil as the soil gas adjusts to the new pressure.

Atmospheric Pressure and Soil-gas Entry Measurements in the Time Domain

In Fig. 3.4, measurements of atmospheric pressure made during a 6-day experiment indicate that atmospheric pressure fluctuations occur at a variety of amplitudes and time scales. Several mechanisms, ranging from the diurnal heating of the earth to turbulent wind fluctuations, create changes in atmospheric pressure (Gossard and Hooke, 1975). The response of the soil-structure system to changes in atmospheric pressure depends on the characteristic response time of the soil gas to changes in pressure. Using eqn. (3.4) and values for L and D_p listed in Table 3.3, the characteristic response time of our soil-gas to a change in surface pressure is ~ 2 min --- much shorter than the time scale of the large atmospheric pressure fluctuations shown in Fig. 3.4.

Measurements of atmospheric pressure and the gas flow rate into and out of the experimental structure for a 1-hr period of the 6-day experiment are presented in Fig. 3.5. This 1-hr period was chosen because the large soil-gas flows clearly illustrate the dynamics of the soil-atmosphere interaction. Fig. 3.5a shows atmospheric pressure oscillations with a period of ~20 min and an amplitude of ~10 Pa. The calculated time-rate-of-change in atmospheric pressure, approximated using a central difference method, is shown in Fig. 3.5b. The measured gas flow rate into and out of the structure is shown in Fig. 3.5c. During this period, the average indoor-outdoor pressure difference was -0.02 Pa with a standard deviation of 0.25 Pa (approximately the resolution of the pressure transducer).

A comparison of the calculated time-rate-of-change of atmospheric pressure, shown in Fig. 3.5b, and the measured gas flow rate, shown in Fig. 3.5c, reveals that the soil-gas flow rate generally follows the time-rate-of-change of atmospheric pressure. Falling atmospheric pressure drives soil-gas entry into the structure; rising atmospheric pressure drives air from inside of the structure into the soil. The larger the time-rate-of-change of atmospheric pressure the larger the gas flow rate into or out of the structure. The soil-gas flow rate does not respond to the high frequency fluctuations in atmospheric pressure because the characteristic response time causes the soil to act as a high-frequency filter.

Model Predictions in the Time Domain

Predictions of the finite-element and the analytical model are compared to the measurements in Figs. 3.5c and 3.5d, respectively. The finite-element model correctly predicts both the amplitude and the temporal trends of the gas flow rate into and out of the experimental structure for this one hour period. The analytical model correctly predicts the temporal trends of the observed gas flow but underpredicts the magnitude of the entry by a factor of ~ 2.3.

The calculated soil-gas flow field shown in Fig. 3.3a suggests that the underprediction of the observed soil-gas flow rate by the analytical model may be due to its failure to account for the two-dimensional components of the flow field underneath the structure. Because the floor of the structure lies 2-m below the soil surface changes in atmospheric pressure propagate both vertically and horizontally away from the gravel layer.

Measured Atmospheric Pressure and Soil-gas Entry Power Spectra

To illustrate the spectral composition of a typical atmospheric pressure signal and the long-term soil-gas flow rate, power spectra estimated from more than 21 days of measurements are presented in Fig. 3.6. The large peaks in the atmospheric pressure power spectrum, shown in Fig. 3.6a, correspond to ~150 Pa diurnal and semi-diurnal oscillations in atmospheric pressure such as those shown in Fig. 3.4. The absence of any significant high-frequency spikes indicates that large, high-frequency pressure oscillations such as those shown in Fig. 3.5a occur only intermittently. The spectrum shown in Fig. 3.6a is consistent with previously reported estimates of the atmospheric pressure power spectrum (Gossard, 1960).

The calculated soil-gas flow and time-rate-of-change power spectra are shown in Fig. 3.6b. A comparison of these spectra reveals that the power distributions for soil-gas flow and the time-rate-of-change in atmospheric pressure match. The peaks at frequencies of 1 and 2 day^{-1} indicate large diurnal and semi-diurnal oscillations in the soil-gas flow rate. Approximately 3% of the total power of the soil-gas flow spectrum corresponds to a diurnal oscillation, and ~ 10% corresponds to a semi-diurnal oscillation. More than 60% of the total power of the soil-gas flow spectrum occurs at frequencies less than 100 day^{-1}.

Measured Gain and Phase Functions

By transforming our analysis into the frequency domain we can gain valuable insight into soil-gas flow driven by atmospheric pressure fluctuations. In the frequency domain, the gain and phase functions define the soil-gas flow rate caused by any change in atmospheric pressure. The estimates of these functions shown in Fig. 3.7 were calculated from 21 days of atmospheric pressure and gas flow measurements.

The estimate of $G_{q,p}(\omega)$ shown in Fig. 3.7a indicates the amplitude of the soil-gas flow rate caused by a 1 Pa oscillation in atmospheric pressure as a function of frequency. The shape of $G_{q,p}(\omega)$ reveals that low-frequency oscillations in atmospheric pressure require large amplitudes to drive significant gas flow into and out of the structure. For example, a diurnal oscillation in atmospheric pressure with an amplitude of 1 Pa drives only a 0.001 L min^{-1} diurnal oscillation in gas flow into and out of the structure. In comparison, a 1 Pa oscillation in atmospheric pressure with a frequency of 100 day^{-1} drives a 0.1 L min^{-1}, 100 day^{-1} oscillation in gas flow. Since the time-rate-of-change of a sinusoid varies linearly with its frequency, low-frequency atmospheric pressure oscillations require very large amplitudes to generate significant time-rates-of-change and soil-gas flows. This behavior underscores the utility of thinking about this phenomenon in terms of the time-rate-of-change in atmospheric pressure.

The shape of $G_{q,dp}(\omega)$, shown in Fig. 3.7b, illustrates the relationship between soil-gas flow and the characteristic response time of the soil gas to a change in pressure. Physically, we can interpret $G_{q,dp}$ as the amplitude of the soil gas flow caused by a 1 Pa min^{-1} oscillation in the time-rate-of-change of atmospheric pressure. The roll-off of $G_{q,dp}$ at a frequency of ~ 50 day^{-1} reveals that the soil acts as low pass filter. For a given amplitude, low-frequency oscillations in the time-rate-of-change atmospheric pressure will drive the largest soil-gas flow rates. The roll-off of $G_{q,dp}(\omega)$ occurs at the frequency at which the characteristic response time of the soil gas (τ ~ 2 min) limits the gas flow into and out of the structure.

The estimates of the phase functions shown in Fig. 3.7c further illustrate the relationship between the characteristic response time and the flow rate into and out of the structure. Physically, the phase function is the phase shift between the soil-gas flow rate and oscillations in atmospheric pressure. At frequencies less than 30 day^{-1}, $\phi_{q,dp}(\omega)$ indicates that the soil-gas flow rate and the time-rate-of-change are in phase --- the maximum soil-gas flow rate corresponds in time with the maximum time-rate-of-change of atmospheric pressure. As the frequency of the oscillations increases, the gas flow lags behind the time-rate-of-change of atmospheric pressure because of the finite response time of the soil gas.

The coherence of the measurements of gas flow and atmospheric pressure is shown in Fig. 3.8. The coherence indicates the linear correlation between the soil gas flow rate and the changes in atmospheric pressure as a function of frequency. The coherence varies between 0 and 1; the closer the coherence is to 1 the stronger the correlation (Chatfield, 1989). The coherence is greater than 0.85 for frequencies between 2 and 200 day^{-1} indicating a strong correlation between the observed gas flow and changes in atmospheric pressure. At very low frequencies, the coherence falls off because the frequency of the estimate approaches the spectral resolution of our analysis, ~ 0.17 day^{-1}. At high frequencies, we hypothesize that the coherence falls off because the size of both the atmospheric pressure and gas flow rate approach the resolution of our sensors. In addition, wind fluctuations may increase the experimental noise at these frequencies.

Comparison of Measured and Predicted Gain and Phase Functions

In Fig. 3.7, the gain and phase functions estimated from our measurements are compared to those predicted by both the analytical and numerical model. This comparison enables us to examine the predictions of these models over the entire range of possible atmospheric pressure fluctuations.

As expected from our analysis in the time domain, both models appear to correctly predict the dynamics of the observed soil-gas flow. Figs. 3.7a and 3.7b indicate that the finite-element model overpredicts by ~ 30% the magnitude of the gas flow rate driven by atmospheric pressure fluctuations with a frequency less than 100 day^{-1}. At frequencies greater than 100 day^{-1} the finite element model predicts the amplitude of the soil-gas flow rate to within 15%. Figs. 3.7a and 3.7b indicate that the analytical model underpredicts the amplitude of the observed gas flow rate by a factor of ~ 2.3 across the entire frequency band.

Comparing the measured and predicted phase functions in Fig. 3.7c indicates that both models correctly predict the phase lag between the soil-gas flow rate and oscillations in atmospheric pressure at frequencies less than 200 day^{-1}. However, the predicted and measured phase functions approach different high-frequency limits. We hypothesize that this discrepancy can be attributed to the magnitude of the high frequency changes in both the atmospheric pressure and the soil-gas entry rate approaching the resolution of our sensors. The coherence shown in Fig. 3.8 indicates that the correlation between the measured soil-gas entry rate and changes in atmospheric pressure falls off at high frequencies.

Considering the uncertainties associated with both our measurements of the gas flow rate and the soil properties used as inputs for the simulations, the predictions of the finite-element model are excellent. Our examination of the sensitivity of soil-gas flow to changes in soil properties presented in Chapter 4 suggests that the overprediction of the observed gas flow rate by the finite-element model for low-frequency oscillations in atmospheric pressure may be caused by the uncertainty in the air-filled porosity values used as inputs for the model. As Table 3.2 indicates, we assumed an air-filled porosity of 0.25 below 5.0 m; reducing the air-filled porosity in this region will decrease the gas flow into and out of the structure as calculated by the finite-element model.

Contaminant Entry Driven by Atmospheric Pressure Fluctuations

Although the time-averaged gas flow between the soil and the interior of the structure driven by atmospheric pressure fluctuations is zero, these fluctuations can produce a net entry rate of radon or other soil-gas contaminant because the radon concentration of the soil gas is generally orders of magnitude larger than indoor air. Unfortunately, detailed analysis of this entry process is complicated by the dilution of the radon concentration of the soil gas immediately underneath the structure by “fresh” air flowing out of the ventilated structure in response to increases in atmospheric pressure.

By ignoring the effects of dilution we can calculate an upper bound for the long-term radon entry rate caused by typical atmospheric pressure fluctuations. Atmospheric pressure fluctuations draw ~ 230 L of soil gas into the structure each day. Based on measurements presented in Chapter 2, the average radon concentration of the soil gas underneath the structure floor slab is ~ 90,000 Bq m^{-3}. If the radon concentration of the soil gas underneath structure’s floor slab was not diluted by the outflow of indoor air, atmospheric pressure fluctuations would increase the long-term radon entry rate into the structure by 0.2 Bq s^{-1}, more than twice the total measured diffusive entry rate into the structure. To compare this estimate with entry driven by steady indoor-outdoor pressure differences, we calculated an equivalent steady-state soil-gas entry rate. This equivalent steady-state entry rate is 0.15 L min^{-1} which corresponds to the entry rate caused by 0.4 Pa steady indoor-outdoor difference. A 0.4 Pa pressure difference is less than the average indoor-outdoor pressure differences found in real houses (Nazaroff, 1992).

CONCLUSIONS

Atmospheric pressure fluctuations can draw soil gas into buildings in the absence of the sustained indoor-outdoor pressure differences commonly associated with the advective entry of radon and other soil-gas contaminants. Consequently, atmospheric pressure fluctuations may represent an important mechanism for driving advective entry of radon and soil-gas contaminants into buildings.

The potential of an atmospheric pressure fluctuation for driving soil gas flow is determined by both its time-rate-of-change and the period over which it occurs. The larger the time-rate-of-change of an atmospheric pressure fluctuation the larger the soil-gas flow rate. However, changes in atmospheric pressure must be sustained to drive significant soil-gas flow. If a change is sustained for a period less than the characteristic response time of the soil gas to a change in pressure, this response time limits the flow rate into the structure --- effectively creating a low-pass filter. Changes in pressure must be sustained for a period comparable to several characteristic response times to maximize the soil-gas flow rate into or out of the structure.

Spectral analysis has revealed that diurnal and semi-diurnal oscillations in atmospheric pressure drive the largest component of the long-term gas flow rate into and out of the structure. These fluctuations are the most important because of their relatively large magnitude (~150 Pa) and their consistency. The largest observed soil-gas flow rates corresponded to relatively rapid (~20 min) and small (~15 Pa) fluctuations in atmospheric pressure. However, such high-frequency atmospheric pressure oscillations only occur intermittently and therefore do not significantly contribute to the long-term gas flow rate.

A transient finite-element model based on Darcy's law with regionally defined soil properties correctly predicts the observed gas flow rates into and out of the experimental structure. An analytical model based on a one-dimensional solution of the diffusion equation correctly predicts the dynamics of the gas flow, but underpredicts its magnitude by a factor of ~2.3. We hypothesize that this underprediction may be caused by the failure of the analytical model to account for two-dimensional components of the soil-gas flow field underneath the experimental structure.

Soil-gas flow into houses driven by atmospheric pressure fluctuations is fundamentally different than entry driven by sustained indoor-outdoor pressure differences. Indoor-outdoor pressure differences drive three-dimensional flow between the soil surface and openings in the building's substructure. In contrast, atmospheric pressure changes drive transient, largely one-dimensional flow between the basement and the deep soil. Because of these differences, we expect that the relationship between soil-gas entry, the properties of the soil, and the characteristics of a building's substructure will depend on whether this entry is driven atmospheric pressure fluctuations or indoor-outdoor pressure differences. In the Chapter 4, we examine the influence of soil properties, water table depth, and a high-permeability subslab gravel layer on soil-gas entry.

REFERENCES

Bendat J. S. and Piersol A. G. (1986) *Random Data: Analysis and Measurement Procedures.* Wiley-Interscience, New York.

Brimhall G. H. and Lewis C. J. (1992) Differential element transport in the soil profile at the Ben Lomond small structure radon site: A geochemical mass balance study. University of California at Berkeley, Dept. of Geology and Geophysics, Berkeley CA 94720.

Buckingham E. (1904) Contributions to our knowledge of the aeration of soils. *U.S. Dept. Agriculture Soils Bur. Bull.* **25**, 3-52.

Burkhard N. R., Hearst J. R. and Hanson J. M. (1987) Estimation of the bulk diffusivity of chimneys using post-shot holes. Proceeding of Fourth Symposium on Containment of Underground Nuclear Tests, Rep. LLNL-CONF-870961. Lawrence Livermore National Laboratory, Livermore CA 94550.

Carslaw H. S. and Jaeger J. C. (1959) *Conduction of Heat in Solids.* Clarendon Press, Oxford.

Chatfield C. (1989) *The Analysis of Time Series: An Introduction.* Chapman and Hall, London.

Danielson R. E. and Sutherland P. L. (1986) Porosity. In Black C. A. (Ed.) *Methods of Soil Analysis, Part 1. Physical and Mineralogical Methods*, American Society of Agronomy, Madison, WI, 443-450.

Fisk W. J., Modera M. P., Sextro R. G., Garbesi K., Wollenberg H. A., Narasimhan T. N., Nuzum T. and Tsang Y. W. (1992) Radon entry into basements: Approach, experimental structures, and instrumentation of the small structures project. LBL-31864, Lawrence Berkeley National Laboratory, Berkeley CA 94720.

Flexser S., Wollenberg H. A. and Smith A. R. (1993) Distribution of radon sources and effects on radon emanation in granitic soil at Ben Lomond, California. *Environ. Geol.* **22**, 162-177.

Fukuda H. (1955) Air and vapor movement in soil due to wind gustiness. *Soil Science* **4**, 249-256.

Garbesi K., Sextro R. G., Fisk W. J., Modera M. P. and Revzan K. L. (1993) Soil-gas entry into an experimental basement: Model-measurement comparisons and seasonal effects. *Environ. Sci. Technol.* **27**, 466-473.

Garbesi K., Sextro R. G., Robinson A. L., Wooley J. D., Owens J. A. and Nazaroff W. W. (1996) Scale dependence of soil permeability to air: Measurement method and field investigation. *Wat. Resour. Res.* **32**, 547-560.

Gossard E. E. (1960) Spectra of atmospheric scalars. *J. Geophys. Res.* **65**, 3339-3351.

Gossard E. E. and Hooke W. H. (1975) *Waves in the Atmosphere: Atmospheric Infrasound and Gravity Waves -- Their Generation and Propagation.* Elsevier, New York.

Hatton A. P., James D. D. and Swire H. W. (1970) Combined forced and natural convection with low-speed air flow over horizontal cylinders. *Journal of Fluid Mechanics* **42**, 17-31.

Hernandez T. L., Ring J. W. and Sachs H. M. (1984) The variation of basement radon concentrations with barometric pressure. *Health Phys.* **46**, 440-445.

Hintenlang D. E. and Al-Ahmady K. K. (1992) Pressure differentials for radon entry coupled to periodic atmospheric pressure variations. *Indoor Air* **2**, 208-215.

Hodgson A. T., Garbesi K., Sextro R. G. and Daisey J. M. (1992) Soil-gas contamination and entry of volatile organic compounds into a house near a landfill. *J. Air Waste Mange. Assoc.* **42**, 277-283.

Holford D. J. (1994) RN3D: A finite element code for simulating gas flow and radon transport in variably saturated, nonisothermal porous media: User's manual, version 1.0. PNL-8943, Pacific Northwest Laboratory, Richland WA 99352.

Holub R. F., Droullard R. F., Borak T. B., Inkret W. C., Morse J. G. and Baxter J. F. (1985) Radon-222 and ^{222}Rn progeny concentrations measured in an energy-efficient house equipped with a heat exchanger. *Health Phys.* **49**, 267-277.

Little J. C., Daisey J. M. and Nazaroff W. W. (1992) Transport of subsurface contaminants into buildings: An exposure pathway for volatile organics. *Environ. Sci. Technol.* **26**, 2058-2066.

Massmann J. W. (1989) Applying groundwater flow models in vapor extraction system design. *J. Environ. Eng.* **115**, 129-149.

Narasimhan T. N., Tsang Y. W. and Holman H. Y. (1990) On the potential importance of transient air flow in advective radon entry into buildings. *Geophys. Res. Let.* **17**, 821-824.

Nazaroff W. W. (1992) Radon transport from soil to air. *Rev. Geophys.* **30**, 137-160.

Nazaroff W. W., Moed B. A. and Sextro R. G. (1988) Soil as a source of indoor radon: Generation, migration, and entry. In Nazaroff W. W. and Nero A. V. (Ed.) *Radon and Its Decay Products in Indoor Air*, John Wiley and Sons, New York, 57-112.

Neeper D. A. and Limback S. P. (1994) Frequency domain analysis of subsurface barometric flows. *EOS*, Transactions, American Geophysical Union 1994 Fall Meeting **75**, Nilson R. H., Peterson E. W., Lie K. H., Burkhard N. R. and Hearst J. R. (1991) Atmospheric pumping: A mechanism causing vertical transport of contaminated gases through fractured permeable media. *J. Geophys. Res.* **96,** 21933-21948.

Scott A. G. (1988) Preventing radon entry. In Nazaroff W. W. and Nero A. V. (Ed.) *Radon and Its Decay Products in Indoor Air,* John Wiley and Sons, New York, N.Y., 407-433.

Tsang Y. W. and Narasimhan T. N. (1992) Effects of periodic atmospheric pressure variation on radon entry into buildings. *J. Geophys. Res.* **97**, 9161-9170.

Turk B. H., Prill R. J., Sextro R. G. and Harrison J. (1989) Intensive radon mitigation research: lessons learned. The 1988 International Symposium on Radon and Radon Reduction Technology. U.S. Environmental Protection Agency, Air and Energy Environmental Research Laboratory, Research Triangle Park NC 27711.

Weeks E. P. (1979) Barometric fluctuations in wells tapping deep unconfined aquifers. *Wat. Resour. Res.* **15**, 1167-1176.

Wood J. A. and Porter M. L. (1987) Hazardous pollutants in Class II landfills. *J. Air. Pollut. Control Assoc.* **37**, 609-615.

NOMENCLATURE

A	Horizontal cross-sectional area of structure gravel layer (m^2)
$\arg(\,)$	Argument of a complex number (-)
$d\chi(\omega)$	Frequency-response function defined by eqn. (3.6a) ($m^3\ s^{-1}\ Pa^{-1}$)
D_p	Pressure diffusivity of soil defined by eqn. (3.2) ($m^2\ s^{-1}$)
f_{dp}	Time-rate-of-change of atmospheric pressure power spectrum ($Pa^2\ s^{-1}$)
f_p	Atmospheric pressure power spectrum ($Pa^2\ s$)
f_q	Soil-gas flow power spectrum ($m^6\ s^{-1}$)
g	Acceleration of gravity ($9.8\ m\ s^{-2}$)
$G_{q,dp}(\omega)$	Gain function, amplitude of q(t) caused by a 1 Pa s^{-1} oscillation in the time-rate-of-change in atmospheric pressure ($m^3\ Pa^{-1}$)
$G_{q,p}(\omega)$	Gain function, amplitude of q(t) caused by a 1 Pa oscillation in atmospheric pressure ($m^3\ s^{-1}\ Pa^{-1}$)
i	$\sqrt{-1}$
k	Soil permeability to gas flow (m^2)
L	Vertical distance between bottom of gravel layer and water table (m)
n	Summation index (-)
p	Soil-gas disturbance pressure (Pa)
$\bar{P}$	Mean soil-gas pressure (Pa)
P1	Prescribed pressure boundary condition at soil surface (Pa)
P2	Prescribed pressure boundary condition at the mouth of the hole in structure floor (Pa)
$P_{atm}(t)$	Atmospheric pressure (Pa)
$P'_{atm}(t)$	Time derivative of atmospheric pressure (Pa)
$q(t)$	Gas flow rate into and out of the structure in response to changes in atmospheric pressure ($m^3\ s^{-1}$)
$Q_{step}(t)$	Step response function, soil-gas flow into structure caused by a 1 Pa step change in atmospheric pressure ($m^3\ s^{-1}\ Pa^{-1}$)
$Q'_{step}(t)$	Time derivative of step response function ($m^3\ s^{-2}\ Pa^{-1}$)
r	Radial coordinate (m)
t	Time (s)
T_n	Defined in text below eqn. (3.8) (s)

$\overline{v}$	Soil-gas velocity vector (m s^{-1})
z	Vertical coordinate (m)
$\chi(\omega)$	Frequency-response function defined by eqn. (3.6a) (m^3 Pa^{-1})
$\chi_a(\omega)$	Frequency-response function defined by analytical model defined by eqn. (3.10) (m^3 Pa^{-1})
ε	Air-filled porosity (-)
$\phi_{q,dp}(\omega)$	Phase function, phase shift between q(t) and oscillations in the time-rate-of-change of atmospheric pressure (radians)
$\phi_{q,p}(\omega)$	Phase function, phase shift between q(t) and oscillations in atmospheric pressure (radians)
μ	Dynamic viscosity of soil-gas (Pa s)
θ	Dummy variable used to integrate over time (s)
τ	Characteristic response time of soil-structure system to a change in atmospheric pressure (s)
ω	Circular frequency (radians s^{-1})
$\mid \; \mid$	Modulus of a complex number (-)

Table 3.1. Measured soil and gravel permeability at the structure site used as inputs for numerical simulations. Appendix A describes in more detail the results of soil permeability and porosity measurements made at the experimental site.

Soil Region	Permeability (m^2)
undisturbed[a]	3.0×10^{-11} (h) ; 1.8×10^{-11} (v)
backfill[b]	3.5×10^{-12}
gravel[c]	2.0×10^{-8}

[a] Horizontal permeability (h) based on measured permeability at 3.5-m length scale; vertical permeability (v) based on measured ratio of vertical to horizontal permeability (Garbesi et al., 1996).

[b] The average of single-point measurements taken around the basement structure (Garbesi et al., 1993).

[c] Based on laboratory measurements in a vertical column filled with a sample of the gravel used below the basement structure (Fisk et al., 1992)

Table 3.2. Measured air-filled porosity of the soil at the structure site used for numerical simulations. Appendix A describes in more detail the results of soil permeability and porosity measurements made at the experimental site. The depths are referenced to soil surface, not to the bottom of the subslab gravel layer.

Depth of layer (m)	ε, Air-filled porosity
0.0 - 1.6[a]	0.45
1.6 - 2.2[a]	Approximately linear decrease from 0.45 to 0.25
2.2 - 5.0[a]	0.25
5.0 - 8.5[b]	0.25 (inferred)

[a] Based on gravimetric analysis (Danielson and Sutherland, 1986) of soil cores taken by Flexser et al. (1993).

[b] We have extended the measured profile to 8.5 m, the measured depth of the water table below the soil surface.

Table 3.3. Soil and geometric properties used as inputs for the analytical model.

Property	Value
Soil permeability to air, k	3×10^{-11} m^2
Air-filled porosity of the soil, ε	0.40
Mean soil-gas pressure, $\overline{P}$	92 kPa
Dynamic viscosity of soil gas, μ	1.8×10^{-5} Pa s
Pressure diffusivity, D_p	0.39 m^2 s^{-1}
Horizontal cross-sectional area of gravel layer, A	5 m^2
Water table depth below structure, L	6.5 m

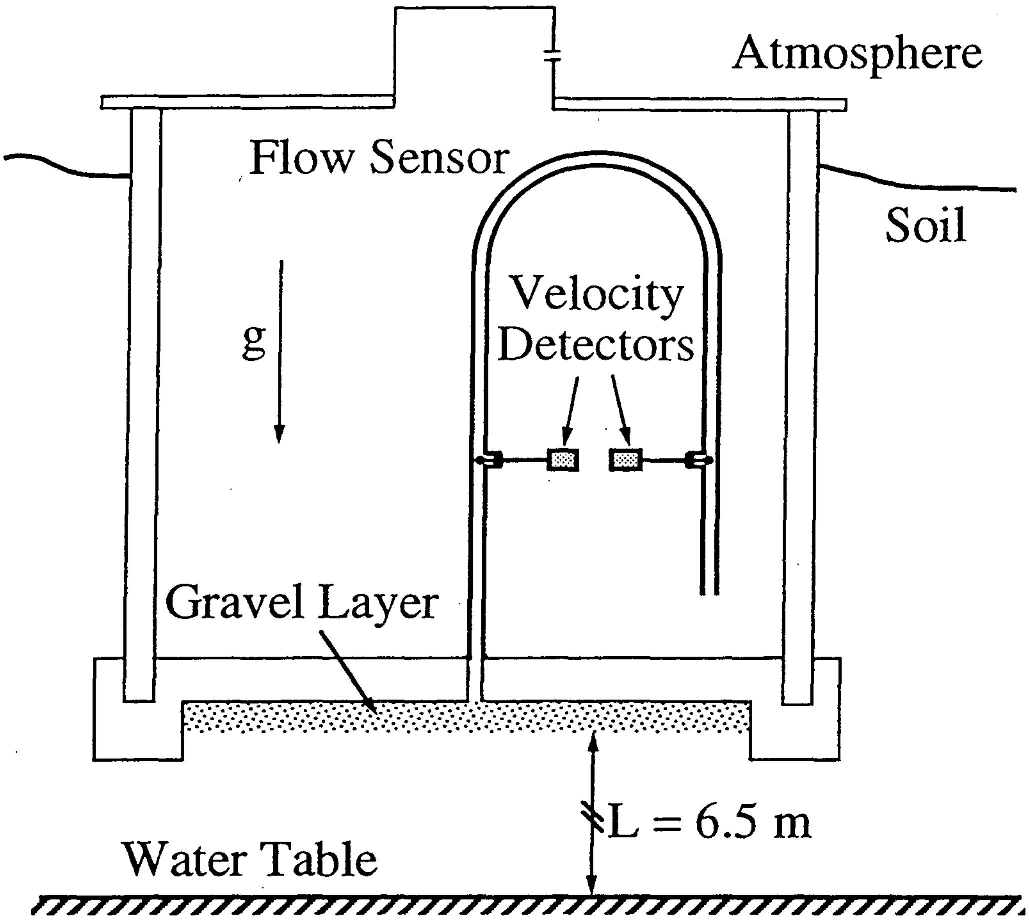

Fig. 3.1 Schematic of experimental structure and flow sensor. The figure is not drawn to scale.

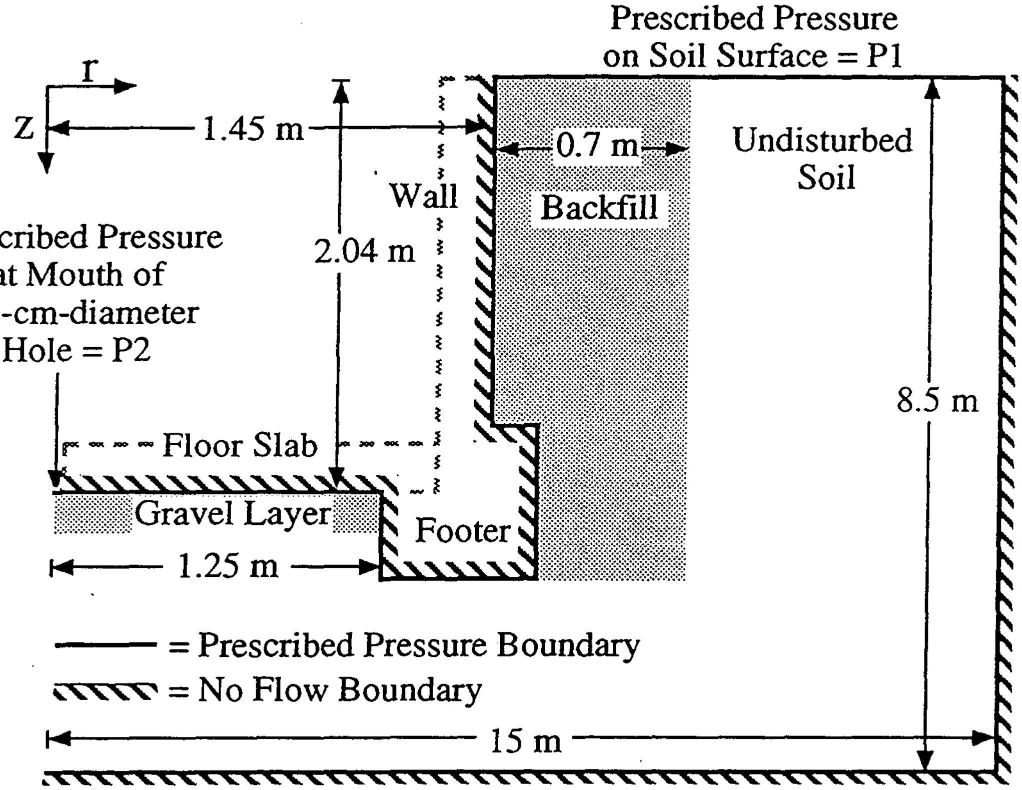

Fig. 3.2 Schematic of cylindrical structure and soil block simulated by finite-element model. Due to the axial-symmetry only half of the cylinder is shown. The finite-element model calculates the soil-gas pressure and velocity inside the region bound by the heavy black line. The dashed lines indicate the interior edge of the walls of the structure. These lines are intended for visual guidance only. The figure is not drawn to scale.

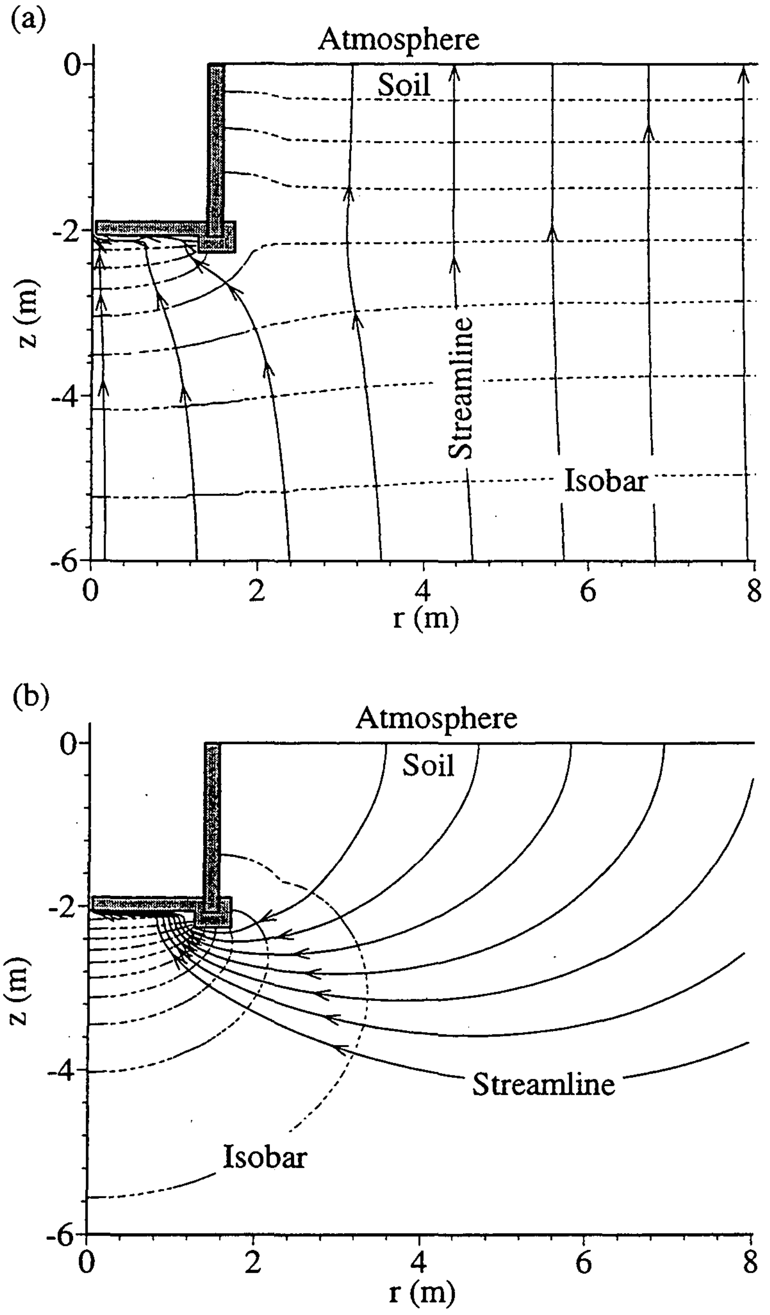

Fig. 3.3 Calculated soil-gas velocity and pressure fields: (a) caused by a constant negative time-rate-of-change in atmospheric pressure; (b) caused by a steady indoor-outdoor pressure difference. Solid lines indicate streamlines, and dashed lines indicate isobars. Soil-gas pressures have been corrected for hydrostatic effects to illustrate the pressure gradients that drive the flow.

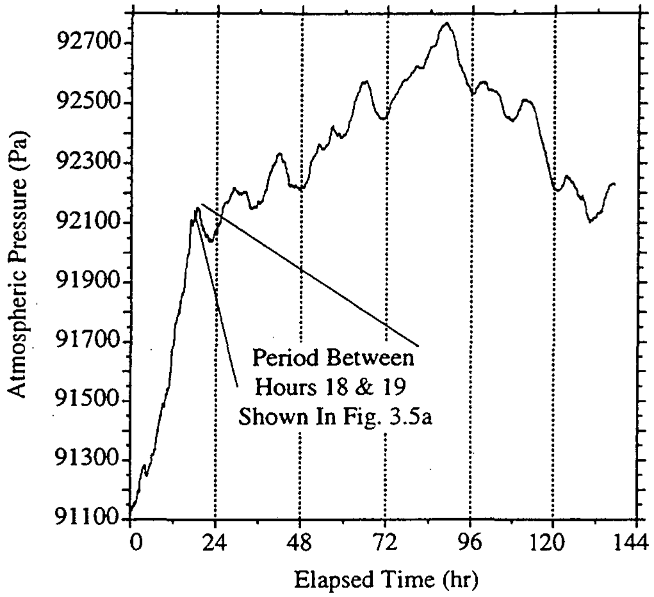

Fig. 3.4 Atmospheric pressure measured during a six-day experiment conducted in the fall of 1994. Between hours 0 and 16 a passing weather front caused a 1000 Pa change in atmospheric pressure.

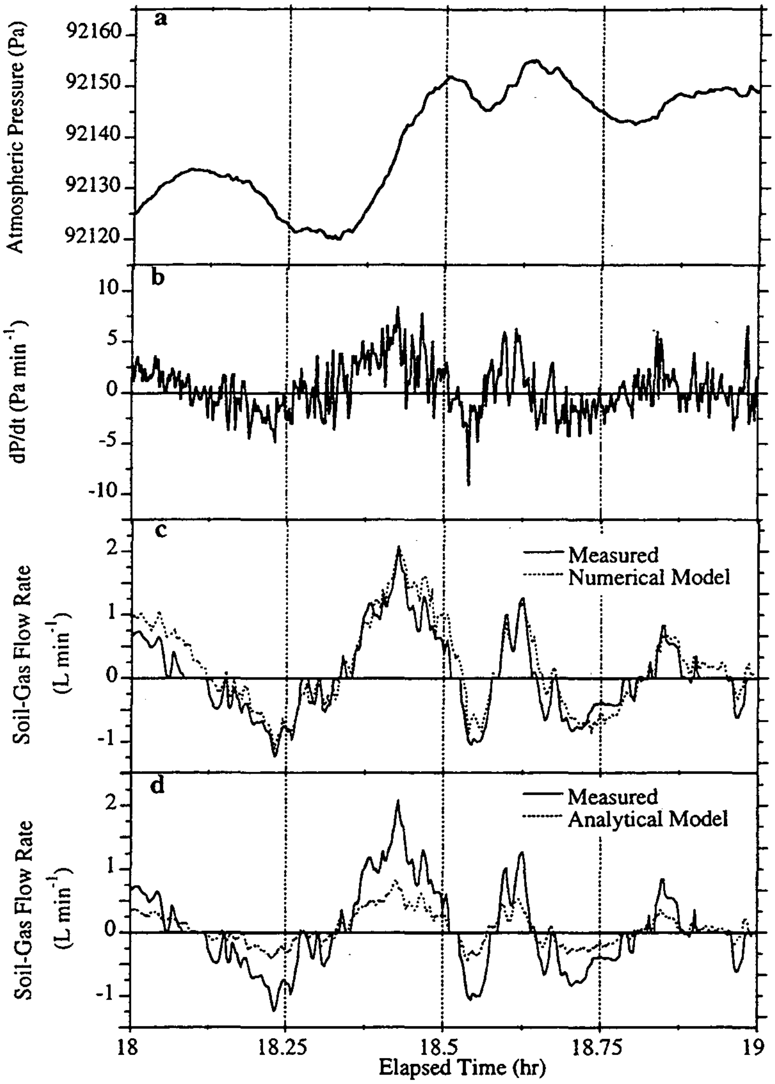

Fig. 3.5 Atmospheric pressure and the response of soil-structure system between hours 18 and 19 of the six-day experiment shown in Fig. 3.4: (a) measured atmospheric pressure; (b) time-rate-of-change of atmospheric pressure; (c) soil-gas flow rate (measured data represented by solid line, predictions of the numerical model shown by the dotted line); (d) soil-gas flow rate (measured data indicated by the solid line, predictions of the analytical model shown by the dotted line). Negative soil-gas flow indicates flow into the experimental structure. Uncertainty of the measured soil-gas flow rates is less than 5%.

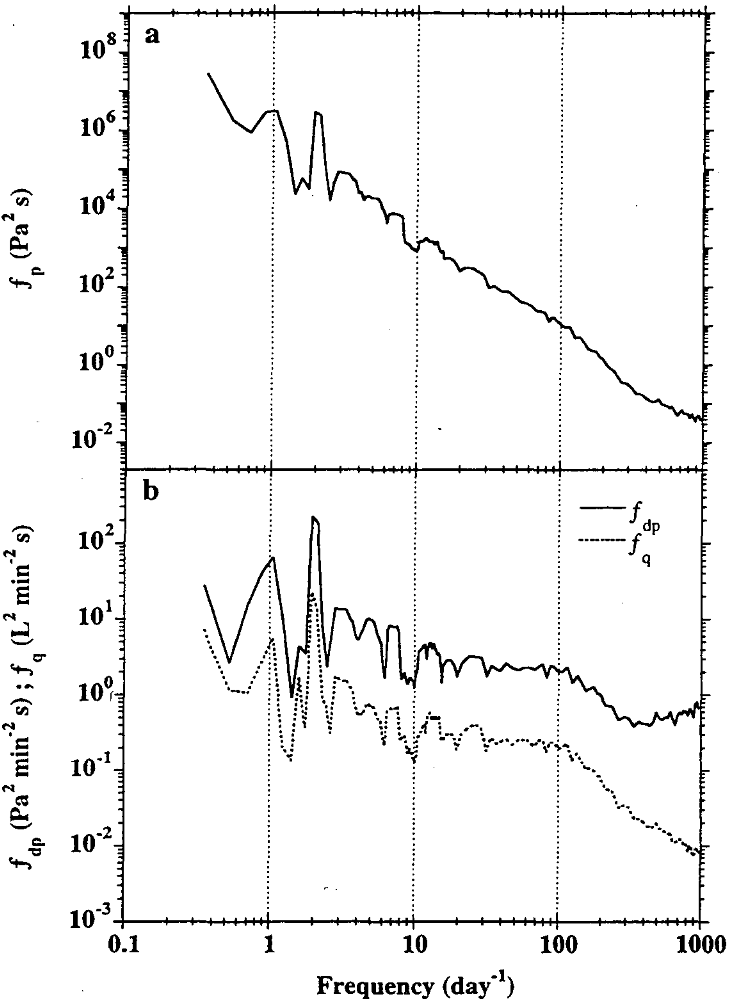

Fig. 3.6 Smoothed power spectra estimated from 21 days of experimental data: (a) f_p, atmospheric pressure; (b) f_{dp}, time-rate-of-change of atmospheric pressure, and f_q, soil-gas entry rate.

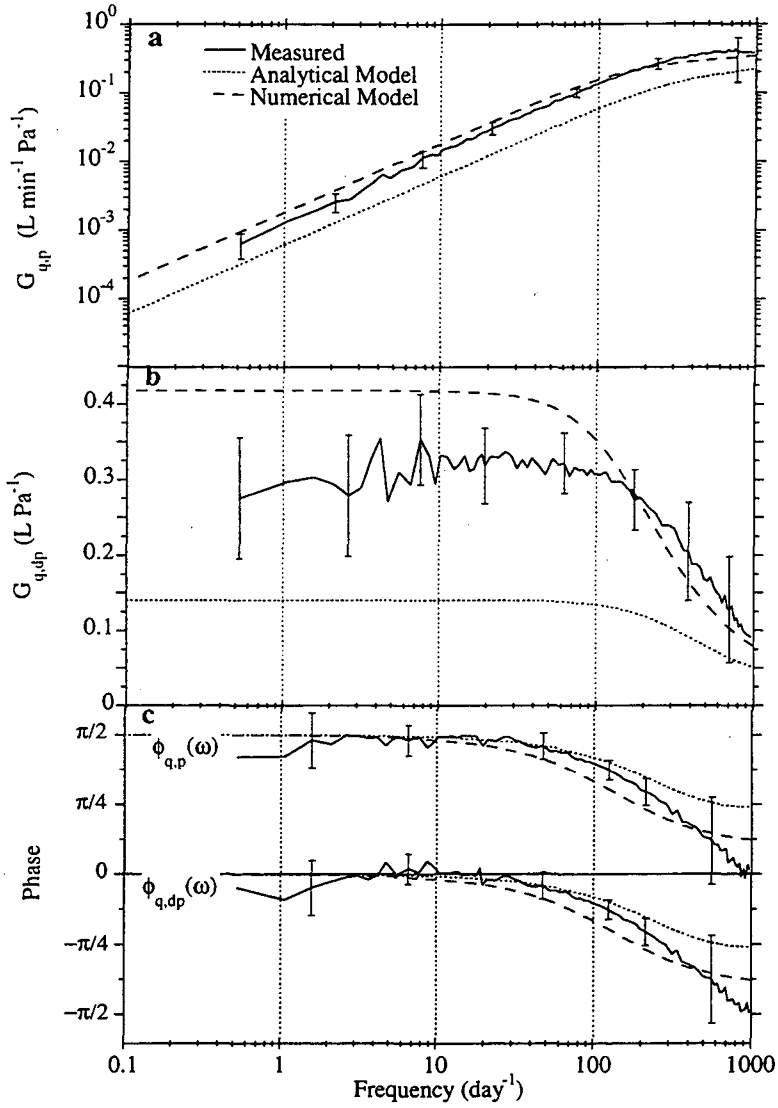

Fig. 3.7 Measured and predicted gain and phase functions: (a) $G_{q,p}(\omega)$, amplitude of the soil-gas entry rate caused by a 1 Pa oscillation in atmospheric pressure; (b) $G_{q,dp}(\omega)$, amplitude of the soil-gas entry rate caused by 1 Pa min^{-1} oscillation in the time-rate-of-change of atmospheric pressure; (c) $\phi_{q,p}(\omega)$, phase lag between the soil-gas entry rate and an oscillation in atmospheric pressure; $\phi_{q,dp}(\omega)$, phase lag between the soil-gas entry rate and an oscillation in the time-rate-of-change of atmospheric pressure. Vertical bars indicate measurement uncertainty.

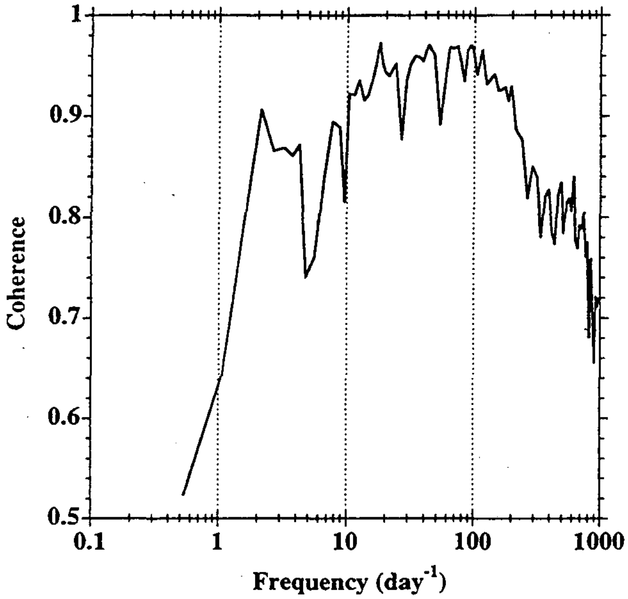

Fig. 3.8 Coherence between measured soil-gas flow and changes in atmospheric pressure.

Chapter 4

SOIL-GAS ENTRY INTO HOUSES DRIVEN BY ATMOSPHERIC PRESSURE FLUCTUATIONS: THE INFLUENCE OF SOIL PROPERTIES*

ABSTRACT

Atmospheric pressure fluctuations can draw soil gas into houses without the sustained indoor-outdoor pressure differences commonly associated with the advective entry of radon and other soil-gas contaminants. To investigate the influence of soil properties, water table depth, and a high-permeability subslab gravel layer on this phenomenon, we employ a finite-element model to simulate the soil-gas flow around a basement caused by changes in atmospheric pressure. The characteristic response time and the capacitance of the soil are used to characterize how changes in permeability, air-filled porosity, and water table depth affect this soil-gas flow. The shorter the characteristic response time and the larger the capacitance of the soil, the larger the soil-gas flow rate caused by a given fluctuation in atmospheric pressure. Relative to entry driven by steady indoor-outdoor pressure differences, contaminant entry driven by atmospheric

---

* This chapter has been published as a technical report: Robinson A. L., Sextro R. G. and Riley W. J. (1996) Soil-gas entry into houses driven by atmospheric pressure fluctuations, part 2 --- The influence of soil properties. LBL-38233, Lawrence Berkeley Laboratory, Berkeley CA 94720. It also has been submitted to the journal *Atmospheric Environment*.

pressure fluctuations will likely be most important in houses situated in a soil of low permeability ($< 10^{-12}$ m^2) and large air-filled porosity.

INTRODUCTION

Soil-gas entry into houses has been studied in relation to indoor exposures of humans to radon progeny and volatile organic chemicals (VOCs). Advective entry of radon-bearing soil gas is generally believed to be the dominant transport mechanism of radon into most homes with elevated indoor concentrations (Nazaroff, 1992). Advective soil-gas flow may also be an important transport mechanism of VOCs and methane into houses built near landfills or leaky gasoline storage tanks (Hodgson et al., 1992; Little et al., 1992).

Most investigations of soil-gas entry into houses have focused on entry driven by slight (a few Pa) but persistent indoor-outdoor pressure difference (Nazaroff, 1992). The phrase "indoor-outdoor pressure difference" refers to the pressure difference between the ambient atmosphere at the soil surface and the indoor air at an opening between the basement and the soil. Recent theoretical (Narasimhan et al., 1990; Tsang and Narasimhan, 1992) studies indicate that changes in atmospheric pressure can draw soil gas into a building in the absence of these persistent indoor-outdoor pressure differences.

In Chapter 3, we examined measurements of atmospheric pressure and gas flow into and out of an experimental basement structure. The characteristic response time of the soil and the time-rate-of-change of the atmospheric pressure signal play important roles in determining the soil-gas flow rate into the experimental structure. To build on this understanding, this chapter reports on a parametric investigation into the influence of soil properties, water table depth, and a high-permeability subslab gravel layer on soil-gas entry into houses. We derive a set of parameters which can be used to estimate the gas flow rate into and out of a building in response to changes in atmospheric pressure. We employ a transient finite-element model to demonstrate how these parameters influence this flow. In the Chapter 3, this finite-element model was shown to correctly predict the observed gas flow rate into and out of an experimental basement caused by changes in atmospheric pressure.

METHODS

We employ the following algorithm to examine the effect of typical atmospheric pressure fluctuations on gas flow into and out of a full-scale basement. First, we calculate the soil-gas flow into a prototypical basement caused by a unit-step change in atmospheric pressure using a finite-element model. These predictions are then transformed into the frequency domain and combined with an estimate of the long-term atmospheric pressure power spectrum to estimate the rate at which typical atmospheric pressure fluctuations pump gas into and out of a basement. Two scaling parameters derived from the analytical model described in Chapter 3 are used to interpret the calculated long-term soil-gas flow rates.

Spectral analysis of atmospheric pressure data

The atmospheric pressure data reported in this chapter have been collected in conjunction with an ongoing experimental investigation of soil-gas and radon entry into buildings (e.g. Fisk et al., 1992; Garbesi et al., 1993). To characterize typical atmospheric pressure fluctuations, we calculated the power spectra of the measured atmospheric pressure and time-rate-of-change of atmospheric pressure. For this analysis we employed the algorithm described by Bendat and Piersol (1986); a brief description of this algorithm is found in Chapter 3. To estimate the power spectrum at low-frequencies (< 50 day^{-1}), we analyzed 18-day-long blocks of continuous atmospheric pressure measurements made at 2-min intervals. These data were drawn from 108 days of non-sequential atmospheric pressure measurements collected in 1993. To estimate the power spectrum at high frequencies (> 25 day^{-1}), we analyzed 48-hour-long blocks of continuous atmospheric pressure data collected at 5-s intervals. These data were drawn from 15 days of non-sequential atmospheric pressure measurements collected in fall of 1994. These estimates were combined by averaging the values in the overlapping frequency bins.

House Substructure and Soil Properties

The geometry of the model basement shell and the surrounding soil is shown in Fig. 1. As Fig. 1a indicates, we have defined our prototypical basement as a cylinder surrounded by a cylindrical soil block. By defining such a basement and utilizing an axial-symmetric radial coordinate system we significantly reduce the computational requirements of the model while preserving the basement's volume and floor area. Although real houses have rectangular basements, we expect that the results of this study are directly applicable to real houses. Revzan et al. (1991) compared predictions of steady-state soil-gas entry using a cylindrical model with those generated with a three-dimensional Cartesian model and found no significant discrepancy for houses which are symmetric in the vertical plane. In the Chapter 3, the transient cylindrical model correctly predicted the observed gas flow into and out of a rectangular experimental basement in response to changes in atmospheric pressure.

Two different basement configurations were examined: a dirt floor, and a concrete slab with a perimeter crack. The perimeter crack is a 1-cm-wide gap around the edge of the slab floor. Such an opening simulates the shrinkage gap that can develop at the floor-wall joint located at the perimeter of the poured concrete floor in real houses. Although the opening considered in this study is wider than the shrinkage gap found in typical houses (Scott, 1988), we have used this opening size to eliminate crack resistance from the problem, which permits a focused analysis of the influence of soil properties on soil-gas entry. We expect that the impedance of the soil-structure system to soil-gas flow will largely be determined by the properties of the soil; therefore, more realistic crack configurations will probably not significantly affect on this flow.

Two different sets of simulations were run to examine the sensitivity of the soil-gas entry rate to changes in soil permeability, air-filled porosity, and water table depth. As Fig. 1b indicates, the water table depth is the vertical distance between the basement floor and the water table, bedrock, or some other impermeable layer. Tables 4.1 and 4.2 list the values of these properties used for each set of simulations. These values reflect the range of soils in which houses are commonly found (Bear, 1972; Nazaroff, 1992). For most of the cases studied we have assumed a homogeneous soil block. The only heterogeneity considered in this study is a high permeability subslab gravel layer. A subslab gravel layer is a common construction practice in many areas as a means of preventing the concrete floor slab from coming into contact with wet soil. It has been found to significantly increase soil-gas entry driven by steady indoor-outdoor pressure differences (Revzan and Fisk, 1992). We assigned the gravel layer an air-filled porosity of 0.3, and varied its permeability between 10^{-8} and 10^{-11} m^2.

Q_{RMS} as an Indicator for Contaminant Entry

Although the net long-term soil-gas entry rate driven by atmospheric pressure fluctuations is zero, transient gas flow into and out of a house can cause a net contaminant entry rate into a house because of the large difference between the concentration of a contaminant in indoor air and its concentration in the soil gas underneath a concrete floor slab (Tsang and Narasimhan, 1992). Unfortunately, the relationship between soil-gas flow driven by atmospheric pressure fluctuations and the transport of soil-gas contaminants into houses is unknown. Detailed analysis of this relationship is difficult due to dilution of contaminant concentrations in the soil underneath a basement by the outflow of low-concentration indoor air in response to rising atmospheric pressure.

To examine the effect of atmospheric pressure fluctuations on contaminant entry, we characterize the long-term gas flow rate into and out of a house in terms of the root-mean-square soil-gas flow rate, Q_{RMS} ($m^3\ s^{-1}$). Q_{RMS} is a measure of the volume of gas being pumped into and out of a building by changes in atmospheric pressure. We expect that the larger this volume the larger the contaminant entry rate; therefore, Q_{RMS} can act as a surrogate for contaminant entry.

The mean-square soil-gas flow rate, Q^2_{RMS} , is defined as

$$Q^2_{RMS} = \frac{1}{T}\int_0^T q^2(t)dt \tag{4.1}$$

where q(t) is the time-dependent gas flow rate into and out of a building driven by atmospheric pressure fluctuations ($m^3\ s^{-1}$). The period over which the average is taken, T (s), must be large enough so that the average soil-gas entry rate is zero. If T is much longer than the characteristic time of typical atmospheric pressure fluctuations then Q_{RMS} quantifies the average rate at which soil gas is being exchanged with indoor air. As T approaches infinity, we can use Parseval's Theorem to define Q_{RMS} in the frequency domain (Bendat and Piersol, 1986)

$$Q_{RMS}^2 = \lim_{T\to\infty} \frac{1}{T}\int_0^T q^2(t)dt = \int_0^\infty f_q(\omega)d\omega, \tag{4.2}$$

where $f_q(\omega)$ is the soil-gas flow power spectrum ($m^6\ s^{-1}$), and ω is the circular frequency (radians s^{-1}).

For this paper, we have evaluated Q_{RMS} in the frequency domain using eqn. (4.2). This evaluation requires an estimate of the soil-gas flow power spectrum, $f_q(\omega)$. Here, we briefly outline the approach used to calculate $f_q(\omega)$. A more complete description of the theory used to describe soil-gas flow driven by atmospheric pressure fluctuations can be found in Chapter 3.

Since the equation that governs soil-gas flow induced by changes in atmospheric pressure is linear, this flow can be characterized in either the time or the frequency domains. In the time domain, q(t) is defined in terms of the step response function,

$$q(t) = \int_{-\infty}^{t} Q_{step}(t-\theta)\, P'_{atm}(\theta)d\theta \tag{4.3}$$

where P'_{atm} is the time-rate-of-change of the atmospheric pressure (Pa s^{-1}), and θ is the dummy variable for integration over time (s). The step response function, $Q_{step}(t)$ (m^3 s^{-1} Pa^{-1}), defines the soil-gas entry rate caused by a 1 Pa step change in atmospheric pressure.

In the frequency domain, q(t) is characterized by the frequency response function, $\chi(\omega)$ (m^3 Pa^{-1}), which is defined as the Fourier transform of $Q_{step}(t)$

$$\chi(\omega) = \int_0^\infty Q_{step}(\theta)\, e^{-i\omega\theta} d\theta . \tag{4.4}$$

The complex-valued frequency response function is generally reported in terms of the gain and phase functions,

$$G_{q,dp}(\omega) = |\chi(\omega)| \tag{4.5a}$$

$$\phi_{q,dp}(\omega) = \arg(\chi(\omega)) \tag{4.5b}$$

where arg( ) and | | define the argument and modulus of a complex number, respectively. The gain function, $G_{q,dp}(\omega)$ (m^3 Pa^{-1}), defines the amplitude of q(t) caused by an oscillation in the time-rate-of-change of atmospheric pressure as a function of frequency. The phase function, $\phi_{q,dp}(\omega)$ (radians), defines the phase lag between q(t) and an oscillation in the time-rate-of-change in atmospheric pressure as a function of frequency.

By taking the Fourier transform of eqn. (4.3) and utilizing the definition of $\chi(\omega)$ we can express the soil-gas flow power spectrum, $f_q(\omega)$, as (Chatfield, 1989)

$$f_q(\omega) = G_{q,dp}^2(\omega)\, f_{dp}(\omega) \tag{4.6}$$

where $f_{dp}(\omega)$ is the time-rate-of-change of atmospheric pressure power spectrum ($Pa^2\ s^{-1}$).

Evaluating Q_{RMS} in the frequency domain using eqns. (4.2) and (4.6) requires substantially fewer calculations then an evaluation of Q_{RMS} in the time domain. To analyze different soil and basement configurations in the frequency domain requires that we determine the frequency response function for each configuration. Each of these frequency response functions can be combined with one estimate of $f_{dp}(\omega)$. In contrast, analysis in the time domain requires evaluation of several weeks of atmospheric pressure data for each of the different soil/basement configurations.

Description of Numerical Simulations

We employ a finite-element model to calculate $Q_{step}(t)$ and the steady-state soil-gas entry rate caused by a 1 Pa indoor-outdoor pressure difference for the different combinations of soil properties and basement configurations. The model calculates the soil-gas flow rate into the basement by simulating the soil-gas pressure and velocity fields in the region shown in Fig. 4.1b. This flow rate is determined by integrating the soil-gas velocity over the area normal to the opening in the basement floor. The finite-element code is based on the RN3D model written by Holford (1994). The model treats the soil gas as an ideal gas, and assumes that its flow is governed by Darcy's Law. More details on our use of this model are found in Chapter 3. Appendix C describes in more detail the modifications made to RN3D.

The following initial and boundary conditions are used to calculate $Q_{step}(t)$: initially (t = 0 s) the entire soil block is defined to have a disturbance pressure of 1 Pa; for t > 0 s the soil surface (indicated as P1 in Fig. 4.1b) and the mouth of the opening in the basement floor (indicated as P2 in Fig. 4.1b) are assigned a disturbance pressure of 0 Pa. The disturbance pressure is the absolute soil-gas pressure corrected for hydrostatic effects; in other words, the disturbance pressure is the pressure that drives soil-gas flow. The mean soil gas pressure is 10^5 Pa. As Fig. 4.1b indicates, the outside edge of the concrete walls, floor, and footer are defined as no-flow boundaries (the normal soil-gas velocity at each of these boundaries is zero). The bottom of the soil block is defined as a no-flow boundary which physically represents a water table, bedrock, or some other impermeable layer. The outside edge of the soil block is also defined as a no-flow boundary. The radius of the soil block (20 m) was chosen such that the outside edge of the soil block falls outside the domain of influence of the structure.

To evaluate $Q_{step}(t)$, the model predicts the evolution of the soil-gas pressure and velocity fields using a fully-implicit time discretization scheme. The simulation is ended when the flow rate into the basement has fallen 7 orders of magnitude from its peak value. At this point, we assume that the soil gas and atmospheric pressure have reached equilibrium. In addition, we assume that changes in atmospheric pressure are communicated instantaneously to the interior of the basement, that the atmospheric pressure is uniform across the entire soil surface, and that the opening in floor creates no resistance to gas flow. To evaluate Q_{RMS}, we transform $Q_{step}(t)$ into the frequency domain by numerically integrating eqn. (4.4).

To compare the soil-gas flow rate into a basement caused by a change in atmospheric pressure to the entry rate caused by a steady indoor-outdoor pressure difference, we also used the finite-element model to predict the steady-state soil-gas entry rate induced by a 1 Pa indoor-outdoor pressure difference, Q_{SS}. For this analysis, the model calculates the steady-state soil-gas pressure and velocity fields for the region shown in Fig. 4.1b in response to the following boundary conditions: the disturbance pressure at the soil surface (indicated as P1 in Fig. 4.1b) is defined as 1 Pa and the disturbance pressure at the mouth of the opening in the basement floor (indicated as P2 in Fig. 4.1b) is defined as 0 Pa. As previously described, all of the other boundaries of the soil block are treated as no-flow.

Description of Analytical Model

In this section we reproduce the analytical model derived in Chapter 3. We employ this model to interpret the predictions of the numerical model. The step response function, $Q_{step}(t)$, defined by the analytical model is

$$Q_{step}(t) = \frac{k}{\mu}\frac{2}{L}A\sum_{n=0}^{\infty}\exp\left(-\frac{t}{T_n}\right) \qquad \text{defined for } t \geq 0. \qquad (4.7)$$

The frequency response function, $\chi_a(\omega)$, defined by the analytical model is

$$\chi_a(\omega) = \frac{8}{\pi^2}\frac{L\varepsilon}{\overline{P}}A\sum_{n=0}^{\infty}\frac{1}{(2n+1)^2}\frac{1-i\omega T_n}{1+(\omega T_n)^2}, \qquad \text{defined for } \omega > 0. \qquad (4.8)$$

where k indicates soil permeability to air (m^2), μ is the dynamic viscosity of the soil gas (Pa s), A is the cross-sectional area of the floor slab (m^2), ε is the air-filled porosity (-), $\overline{P}$ is the mean soil-gas pressure (Pa), and $T_n = \frac{1}{(2n+1)^2}\left(\frac{4}{\pi^2}\right)\left(\frac{L^2\varepsilon\mu}{k\overline{P}}\right)$. L is the distance between the basement floor and the water table, bedrock or some other impermeable layer (m). For convenience, we will refer to L as the water table depth.

RESULTS AND DISCUSSION

Typical Atmospheric Pressure Fluctuations

To illustrate the magnitude and frequency of typical atmospheric pressure fluctuations, 24 days of continuous atmospheric pressure data are shown in Fig.

4.2. Diurnal heating of the earth's surface cause the prominent 200 Pa oscillations. Passing weather fronts can cause changes in pressure greater than 1000 Pa. Gossard and Hooke (1975) describe the variety of mechanisms that cause changes in atmospheric pressure.

The calculated time-rate-of-change of atmospheric pressure for this 24-day period is shown in Fig. 4.2b. Comparing Figs. 4.2a and 4.2b reveals that the largest time-rates-of-change correspond to relatively small, but rapid changes in pressure. The time-rates-of-change associated with the very large (> 1000 Pa) changes in atmospheric pressure are typically small because these changes generally occur over periods of days. The prominent diurnal and semi-diurnal oscillations shown in Fig. 4.2a cause ~ 1 Pa min^{-1} oscillations in the time-rate-of-change of atmospheric pressure.

The power spectra shown in Fig. 4.3a characterize typical changes in atmospheric pressure in the frequency domain. The long-term spectrum was calculated from 108 days of measured atmospheric pressure data and identifies the magnitude and frequency of typical fluctuations in atmospheric pressure. This spectrum is consistent with previously reported atmospheric pressure power spectra (Gossard, 1960). The short-term spectrum, indicated by the dashed line in Fig. 4.3a, was calculated from a 5-hour period of atmospheric pressure data. It characterizes the magnitude and frequency of the relatively small, but rapid pressure fluctuations which create the largest time-rates-of-change of atmospheric pressure. The associated power spectra for the time-rate-of-change of atmospheric pressure are shown in Fig. 4.3b.

The long-term power spectra shown in Figs. 4.3a and 4.3b reveal several important characteristics of typical atmospheric pressure fluctuations. The prominent spikes occurring at frequencies of 1 and 2 day^{-1} indicate that diurnal and semi-diurnal oscillations are the dominant oscillations in atmospheric pressure. In addition, more than 60% of the total power of the long-term time-rate-of-change spectrum occurs at frequencies less than 100 day^{-1}. Comparing the short-term and long-term power spectra shown in Fig. 4.3b indicates that high-frequency pressure fluctuations can substantially increase the total power of the time-rate-of-change of atmospheric pressure. The short-term spectrum has 6 times more power than the long-term spectrum. However, the absence of a high-frequency peak in the long-term spectrum reveals that such fluctuations only occur intermittently. These high-frequency fluctuations also temporarily shift the distribution of power from low-frequencies to high-frequencies. For example, only 40% of the power of the short-term spectrum shown in Fig. 4.3b is at frequencies less than 100 day^{-1}.

Scaling parameters

The gas flow rate between a building and the underlying soil can be understood in terms of two scaling parameters derived through dimensional analysis of the analytical model, eqns. (4.7) and (4.8). Despite the many assumptions required for the derivation of this analytical model, predictions of the finite-element model indicate that these two parameters describe how q(t) scales with changes in air-filled porosity, permeability, and water table depth.

The first scaling parameter is the capacitance of the soil block. It characterizes the volume of soil gas that flows into a house in response to a step change in atmospheric pressure. The capacitance, C (m^3 Pa^{-1}), can be defined as

$$C = \frac{L\varepsilon}{\overline{P}} A . \tag{4.9}$$

The second scaling parameter is the characteristic response time of the soil gas to changes in atmospheric pressure. Such a parameter can be defined based on the time for a pressure disturbance to propagate through a characteristic length of the system;

$$\tau = \frac{L^2}{D_p} = \left(\frac{L\varepsilon}{\overline{P}}\right)\left(\frac{L\mu}{k}\right) = C \cdot R \tag{4.10}$$

where D_p is the pressure diffusivity of the soil gas ($D_p = \overline{P}k/\mu\varepsilon$) ($m^2$ s^{-1}). The characteristic response time, τ (s), can be expressed as the product of the capacitance, C, and the resistance of the soil to gas flow, $R = L\mu/Ak$ (Pa s m^{-3}).

Values for these parameters for the different combinations of soil properties and water table depths considered in this study are listed in Tables 4.1 and 4.2.

The characteristic response time of typical soils varies from seconds to days; the capacitance of typical soils varies between 1 and $10\,\mathrm{L\,Pa^{-1}}$. Although the characteristic response time depends on the water table depth, air-filled porosity, and permeability, the calculations shown in Tables 4.1 and 4.2 indicate that the permeability determines the range of this response time because the permeability of common soils can span more than six orders of magnitude (10^{-9} - 10^{-15} $\mathrm{m^2}$) (Nazaroff, 1992). In contrast, the air-filled porosity and water table depth typically vary within an order of magnitude.

The results presented in Fig. 4.4 illustrate the relationship between q(t) and these scaling parameters in the time domain. Fig. 4.4a shows the measured atmospheric pressure data used as the boundary condition for this analysis. The time-rate-of-change of this atmospheric pressure signal is shown in Fig. 4.4b. We examined the measured gas flow rate into and out of an experimental basement structure in response to this one-hour atmospheric pressure signal in Chapter 3. The results shown in Figs. 4.4c and 4.4d were calculated using $Q_{step}(t)$ for a dirt floor basement and eqn. (4.3). $Q_{step}(t)$ was evaluated with the numerical model; the soil properties used for these simulations are listed in Table 4.1. A comparison of the flow rates shown in Fig. 4.4c reveals that the magnitude of q(t) scales with the capacitance of the soil block. Comparing the flow rates shown in

Fig. 4.4d indicates that a soil with a slow characteristic response time acts as a low-pass filter, dampening q(t) driven by high-frequency fluctuations.

The results shown in Fig. 4.4 only reveal qualitative aspects of the relationship between the scaling parameters and q(t). We can improve our understanding of this relationship by transforming our analysis into the frequency domain. The gain, $G_{q,dp}(\omega)$, and phase, $\phi_{q,dp}(\omega)$, functions shown in Fig. 4.5 describe q(t) as a function of the frequency of fluctuations in atmospheric pressure. $G_{q,dp}(\omega)$ defines the amplitude of q(t) caused by a 1 Pa $\min^{-1}$ oscillation in the time-rate-of-change of atmospheric pressure as a function of frequency --- the larger $G_{q,dp}(\omega)$, the larger q(t). $\phi_{q,dp}(\omega)$ defines the phase shift between an oscillation in the time-rate-of-change of atmospheric pressure and q(t). We calculated $G_{q,dp}(\omega)$ and $\phi_{q,dp}(\omega)$ by transforming the step response functions used for the analysis presented in Fig. 4.4 into the frequency domain.

The gain functions shown in Fig. 4.5a illustrate the effect of changing the capacitance of the soil on the magnitude of q(t) for a fixed value of the characteristic response time. As noted earlier, increasing the capacitance increases the volume of soil gas which is compressed and expanded with changes in atmospheric pressure. The estimates of $G_{q,dp}(\omega)$ shown in Fig. 4.5a indicate that the magnitude of q(t) scales linearly with the capacitance. If the characteristic response time of the soil is held constant, changing the capacitance does not affect the spectral composition of q(t).

The estimates of $G_{q,dp}(\omega)$ shown in Fig. 4.5b provide insight into the relationship between the characteristic response time of the soil and the filtering of high-frequency fluctuations in atmospheric pressure. These results were calculated by changing this response time while holding the capacitance fixed. The roll-off of the gain function occurs at the frequency where the finite response time of the soil gas begins to restrict the gas flow rate caused by high-frequency changes in atmospheric pressure --- the shorter the response time, the higher the roll-off frequency.

The phase lag between q(t) and the time-rate-of-change in atmospheric pressure further illustrates the relationship between the characteristic response time and q(t). In Fig. 4.5c we plot estimates of $\phi_{q,dp}(\omega)$. These estimates correspond to the gain functions shown in Figs. 4.5a and 4.5b. The phase shift only depends on the characteristic response time of the soil. Increasing this response time decreases the frequency at which the q(t) begins to lag the time-rate-of-change of atmospheric pressure.

The results in Fig. 4.5b suggest that for a fixed value of the capacitance, the gain function converges to the same value at low frequencies. This implies that q(t) driven by very low-frequency fluctuations in atmospheric pressure does not depend on the permeability of the soil. In light of the linear relationship between permeability and soil-gas entry driven by steady indoor-outdoor pressure differences this appears to be a surprising prediction. The low-frequency behavior of q(t) can be understood by examining the low-frequency limit of $\chi(\omega)$,

$$\lim_{\omega \to 0} \chi(\omega) = \int_0^\infty Q_{\text{step}}(\theta) d\theta. \tag{4.11}$$

Using eqns. (4.5a) and (4.5b) we can rewrite this limit in terms of the gain and phase functions,

$$\lim_{\omega \to 0} G_{q,dp}(\omega) = \int_0^\infty Q_{\text{step}}(\theta) d\theta, \text{ and} \tag{4.12a}$$

$$\lim_{\omega \to 0} \phi_{q,dp}(\omega) = 0. \tag{4.12b}$$

Eqn. (4.12a) reveals that the magnitude of q(t) driven by low-frequency fluctuations atmospheric pressure is defined by the volume of soil gas which flows into a basement in response to a step change in atmospheric pressure. At very low-frequencies, the period of the atmospheric pressure oscillations is many times longer than the characteristic response time of the soil, and the entire soil block completely responds to these fluctuations. For example, Fig. 4.5b indicates that for soils with a permeability greater than 10^{-11} m^2 the soil gas completely responds to changes in atmospheric pressure with a frequency less than 10 day^{-1}.

For a fixed water table depth, the two-scaling parameters derived from the analytical model predict exactly how changes in air-filled porosity and permeability interact to determine q(t). However, these parameters do not describe exactly how changes in water table depth affect q(t). We can examine this failure by plotting the low-frequency limit of $\chi(\omega)$ as a function of the capacitance. Ideally this relationship should be linear because eqn. (4.11) indicates that the low-frequency limit of $\chi(\omega)$ is a measure of the "true" capacitance (the capacitance characterizes the volume of soil gas which flows into a building in response to a step change in atmospheric pressure). Our expression for the capacitance, eqn. (4.9), does not exactly define this volume because the soil-gas flow around a basement in response to a change in atmospheric pressure is not one-dimensional (see streamline plot shown in Chapter 3, Fig. 3.3). Although Fig. 4.6 indicates that the low-frequency limit of $\chi(\omega)$ for a dirt floor basement does not scale linearly with capacitance, we can accurately approximate this relationship as linear. A linear regression of the low frequency limit of $\chi(\omega)$ as a function of the capacitance yields an R^2 greater than 0.999 for the range of water table depths considered in this study.

Effect of a high-permeability subslab gravel layer

In this section, we explore the effect of a high-permeability subslab gravel layer on q(t) using the numerical model. The gain functions shown in Fig. 4.7a indicate that the addition of a subslab gravel layer increases the magnitude of q(t) for a basement with a small perimeter crack by more than a factor 3. The size of the increase depends on the ratio of the permeability of the gravel layer to that of the rest of the soil block.

The effect of a high permeability subslab gravel layer can be understood by comparing the characteristic response time of the gravel layer to the response time of the soil block. Since the permeability of gravel is typically orders of magnitude larger than that of common soils, the response time of a gravel layer to a change in pressure is orders of magnitude shorter than the rest of the soil block. Therefore, the gravel layer will respond instantaneously to changes in atmospheric pressure relative to the rest of the soil, effectively creating an isobaric plenum underneath the basement. The gain and phase functions shown in Fig. 4.7 indicate that if the permeability of this gravel layer is more than 2 orders of magnitude greater than that of the surrounding soil, the basement will essentially interact with the surrounding soil as if it had a dirt floor. Consequently, we will focus our examination on the two extremes, a basement with and without a floor slab.

Comparing the roll-off of the gain functions shown in Fig. 4.7a indicates that the addition of a high-permeability subslab gravel layer has little effect on the characteristic response time of the system. An examination of the calculated soil-gas velocity field around the basement reveals that a subslab gravel layer dramatically increases the size of the region from which a building draws soil gas. This, in effect, increases the capacitance of the system. The size of this region depends on the two-dimensional nature of the soil-gas flow field (for example see streamline plot shown in Chapter 3, Fig. 3.3). Because it is derived from the analytical model, which assumes one-dimensional flow, our definition for the capacitance does not account for adjustments in the size of the region from which the basement draws soil gas due to the addition of a gravel layer. However, Fig. 4.6 reveals that the analytical model predicts the volume of this region to within a factor 2.

Soil-gas and contaminant entry driven by typical atmospheric pressure fluctuations

Table 4.2 lists values of Q_{RMS} calculated by combining predictions of the numerical model with the long-term estimate of f_{dp} shown in Fig. 4.3b. These results reveal how changes in soil properties, water table depth, and the presence or absence of an impermeable floor slab affect Q_{RMS}. As noted earlier, Q_{RMS} describes the rate at which gas is pumped into and out of a basement in response to typical changes in atmospheric pressure.

Table 4.2 shows that increasing the permeability of the soil block three orders of magnitude from 10^{-13} to 10^{-10} m^2 only increases Q_{RMS} by a factor of ~6 (case 1). In contrast, a more linear relationship exists between Q_{RMS} and both air-filled porosity and water table depth (cases 2 and 3). For all cases, removing the concrete slab increases Q_{RMS} by more than a factor of 3.5. However, the presence or absence of a concrete slab does not alter the relative relationship between Q_{RMS}

and the permeability, porosity, and water table depth. For example, Q_{RMS} scales nearly linearly with air-filled porosity in a basement both with and without the floor slab.

For comparison, the values of steady-state soil-gas entry rate driven by a steady 1 Pa indoor-outdoor pressure difference, Q_{SS}, are also listed in Table 4.2. An examination of these values reveals that Q_{SS} varies linearly with soil permeability (case 1), depends slightly on water table depth (case 3), and is independent of air-filled porosity (case 2). In comparison, the relationship between Q_{RMS} and these properties is much more complex. Q_{RMS} varies non linearly with soil permeability, linearly with porosity, and nearly linearly with water table depth.

Fundamentally, soil-gas flow driven by atmospheric pressure changes depends on the characteristic response time and the capacitance of the soil. In Fig. 4.8, we have plotted Q_{RMS} as a function of the characteristic response time for several different values of soil capacitance. These results were calculated using eqn. (4.8) and the long-term estimate of f_{dp} shown in Fig. 4.3b. The analytical model was used for this analysis because use of the numerical model would have required an enormous amount of computation time to evaluate so many different combinations of soil properties and water table depths. A comparison between the predictions of the analytical model and finite element model indicates that the analytical model correctly predicts the relationship between Q_{RMS}, the characteristic response time, and the capacitance of the soil. For the cases listed in Table 4.2, the values of Q_{RMS} calculated with the analytical model are within a factor of 2 of those based on predictions of the finite element model.

Fig. 4.8 reveals two important characteristics of soil-gas flow driven by atmospheric pressure fluctuations. First, the largest values of Q_{RMS} occur in buildings surrounded by soils with short characteristic response times and large soil capacitance. Second, Q_{RMS} is relatively insensitive to changes in τ if this response time is less than ~ 1000 s because more than 60% of the total power of the long-term time-rate-of-change of typical atmospheric pressure fluctuations occurs at frequencies less than 100 day^{-1}.

Using Q_{RMS} as a surrogate for the contaminant entry rate, the results presented in Table 4.2 and Fig. 4.8 provide insight into the influence of soil properties, water table depth, and a subslab gravel layer on contaminant entry driven by atmospheric pressure fluctuations. These results suggest that the largest contaminant entry rate driven by atmospheric pressure fluctuations will likely occur in a basement with a high-permeability subslab gravel layer surrounded by a soil with a short characteristic response time and a large capacitance. To possess these qualities a soil must have both a high permeability and a large air-filled porosity; the texture of such a soil might be described as sandy (USDA, 1975; Nielson and Rogers, 1990).

In addition to maximizing contaminant entry driven by atmospheric pressure fluctuations, a high-permeability soil will also maximize the entry rate driven by steady indoor-outdoor pressure differences. For such a soil, the results in Table 4.2 suggest that indoor-outdoor pressure differences will drive a much larger fraction of the total contaminant entry rate than atmospheric pressure fluctuations (case 1, $k = 10^{-10}$ m^2). However, these results also suggest that contaminant entry driven by typical atmospheric pressure fluctuations will likely be relatively more important than contaminant entry in a basement surrounded by a less permeable soil with a large capacitance. For example, a plot of case 1 shown in Fig. 4.9 illustrates how the non-linear relationship between Q_{RMS} and permeability affects the relative importance of contaminant entry driven by these two different mechanisms. Because of this non-linear relationship, Q_{RMS} and Q_{SS} intersect at a soil permeability of ~ 10^{-12} m^2. The texture of a less permeable soil with high porosity might be described as clayey (USDA, 1975; Nielson and Rogers, 1990).

Our estimates of contaminant entry based on Q_{RMS} are consistent with the calculations of radon entry driven sinusoidal oscillations of atmospheric pressure previously reported by Tsang and Narasimhan (Tsang and Narasimhan, 1992).

Our work has examined these effects in greater detail and provides additional physical insight into the phenomenon.

CONCLUSIONS

We have investigated the effects of atmospheric pressure fluctuations on soil-gas entry into houses. Because atmospheric pressure fluctuations can draw soil gas into a basement without the indoor-outdoor pressure differences commonly associated with the advective transport of radon and other soil-gas contaminants into houses, soil-gas flow driven by these fluctuations may represent an important mechanism for the transport of contaminants into houses.

Soil-gas flow driven by atmospheric pressure fluctuations can be described in terms of the characteristic response time and the capacitance of the soil. The response time characterizes the relaxation time of the soil gas to a change in atmospheric pressure, while the capacitance describes the volumetric change of the soil gas in response to a change in atmospheric pressure. If the period of an atmospheric pressure fluctuation is much longer than the characteristic response time, then the gas flow rate into and out of the soil depends only on its capacitance. As the period of these pressure fluctuations approach the characteristic response time of the soil, this response time restricts the gas flow rate into and out of the basement. Consequently, the shorter the characteristic response time and the larger the capacitance of the soil, the larger the gas flow rate into and out of building caused by a given change in atmospheric pressure.

Although atmospheric pressure fluctuations occur over a wide range of frequencies and magnitudes, relatively low-frequency (< 100 day^{-1}) oscillations in atmospheric pressure are the most important for driving long-term soil-gas entry into houses. The finite response time of the soil gas to a change in pressure restricts the entry caused high-frequency changes in atmospheric pressure. In addition, more than 60% of the total power of the time-rate-of-change of typical atmospheric pressure fluctuations occurs at frequencies less than 100 day^{-1}.

The presence of a high permeability subslab gravel layer can increase the soil-gas flow rate into a basement driven by atmospheric pressure fluctuations by more than a factor of 3. The size of this increase largely depends on the ratio of the permeability of the gravel to that of the rest of the soil. If the permeability of the gravel is 2 orders of magnitude larger than the rest of the soil, a basement with a small perimeter crack and a subslab gravel layer effectively acts as if it has an open dirt floor.

Although the dilution of the soil-gas underneath a basement slab by the outflow of indoor air driven by rising atmospheric pressure complicates the analysis of the contaminant entry rate, the results of this study suggest the maximum contaminant entry rate driven by atmospheric pressure fluctuations will occur into a basement with a high permeability subslab gravel layer surrounded by a high permeability soil with a large air-filled porosity. Relative to entry driven by steady indoor-outdoor pressure differences, contaminant entry driven by atmospheric pressure will likely be most important in houses surrounded by soil with low permeabilities and a large air-filled porosity and a large soil depths to an impermeable layer.

REFERENCES

Bear J. (1972) *Dynamics of Fluids in Porous Media.* Dover Publications Inc., New York.

Bendat J. S. and Piersol A. G. (1986) *Random Data: Analysis and Measurement Procedures.* Wiley-Interscience, New York.

Chatfield C. (1989) *The Analysis of Time Series: An Introduction.* Chapman and Hall, London.

Fisk W. J., Modera M. P., Sextro R. G., Garbesi K., Wollenberg H. A., Narasimhan T. N., Nuzum T. and Tsang Y. W. (1992) Radon entry into basements: Approach, experimental structures, and instrumentation of the small structures project. LBL-31864, Lawrence Berkeley National Laboratory, Berkeley CA 94720.

Garbesi K., Sextro R. G., Fisk W. J., Modera M. P. and Revzan K. L. (1993) Soil-gas entry into an experimental basement: Model-measurement comparisons and seasonal effects. *Environ. Sci. Technol.* **27**, 466-473.

Gossard E. E. (1960) Spectra of atmospheric scalars. *J. Geophys. Res.* **65**, 3339-3351.

Gossard E. E. and Hooke W. H. (1975) *Waves in the Atmosphere: Atmospheric*

Infrasound and Gravity Waves -- Their Generation and Propagation. Elsevier, New York.

Hodgson A. T., Garbesi K., Sextro R. G. and Daisey J. M. (1992) Soil-gas contamination and entry of volatile organic compounds into a house near a landfill. *J. Air Waste Mange. Assoc.* **42**, 277-283.

Holford D. J. (1994) RN3D: A finite element code for simulating gas flow and radon transport in variably saturated, nonisothermal porous media: User's manual, version 1.0. PNL-8943, Pacific Northwest Laboratory, Richland WA 99352.

Little J. C., Daisey J. M. and Nazaroff W. W. (1992) Transport of subsurface contaminants into buildings: An exposure pathway for volatile organics. *Environ. Sci. Technol.* **26**, 2058-2066.

Narasimhan T. N., Tsang Y. W. and Holman H. Y. (1990) On the potential importance of transient air flow in advective radon entry into buildings. *Geophys. Res. Let.* **17**, 821-824.

Nazaroff W. W. (1992) Radon transport from soil to air. *Rev. Geophys.* **30**, 137-160.

Nielson K. K. and Rogers V. C. (1990) Radon transport properties of soil classes for estimating indoor radon entry. *Indoor Radon and Lung Cancer: Reality of Myth?* Pacific Northwest Laboratory, Richland WA, Battelle Press.

Revzan K. and Fisk W. (1992) Modeling radon entry into houses with basements: The influence of structural factors. *Indoor Air* **2**, 40-48.

Revzan K. L., Fisk W. J. and Gadgil A. J. (1991) Modeling radon entry into houses with basements: Model description and verification. *Indoor Air* **1**, 173-189.

Scott A. G. (1988) Preventing radon entry. In Nazaroff W. W. and Nero A. V.

(Ed.) *Radon and Its Decay Products in Indoor Air,* John Wiley and Sons, New York, N.Y., 407-433.

Tsang Y. W. and Narasimhan T. N. (1992) Effects of periodic atmospheric pressure variation on radon entry into buildings. *J. Geophys. Res.* **97**, 9161-9170.

USDA (1975) *Soil taxonomy.* U.S. Department of Agriculture, Soil Conservation Service, Washington D.C.

NOMENCLATURE

A	Cross-sectional area of gravel layer or dirt floor (m^2)
arg( )	Argument of a complex number (-)
C	Capacitance of soil-structure system (m^3 Pa^{-1})
D_p	Pressure diffusivity of soil (m^2 s^{-1}) : $D_p = \frac{k\overline{P}}{\varepsilon\mu}$
$f_{dp}(\omega)$	Time-rate-of-change of atmospheric pressure power spectrum (Pa^2 s^{-1})
$f_p(\omega)$	Atmospheric pressure power spectrum (Pa^2 s)
$f_q(\omega)$	Soil-gas flow power spectrum (m^6 s^{-1})
$G_{q,dp}(\omega)$	Gain function, amplitude of q(t) caused by a 1 Pa s^{-1} oscillation in the time-rate-of-change in atmospheric pressure (m^3 Pa^{-1})
i	$\sqrt{-1}$
Im( )	Imaginary part of a complex number (-)
k	Soil permeability to gas flow (m^2)
L	Depth of the water table below the gravel layer or dirt floor (m)
n	Index for infinite summation (-)
$\overline{P}$	Mean soil-gas pressure (Pa)
P(t)	Atmospheric pressure (Pa)
P′(t)	Time derivative of atmospheric pressure (Pa s^{-1})
q(t)	Gas flow rate into and out of a basement driven by fluctuations in atmospheric pressure (m^3 s^{-1})
Q_{RMS}	Root-mean-square soil-gas entry rate (m^3 s^{-1})
$Q_{step}(t)$	Step response function, soil-gas flow into a house in response to 1 Pa step change in atmospheric pressure (m^3 s^{-1} Pa^{-1})
R	Resistance of soil to gas flow (Pa s m^{-3})
Re( )	Real part of a complex number (-)
t	Time (s)
T	Period over which a time average is taken (s)
T_n	Time for index n (s)

$\chi(\omega)$	Frequency response function (m^3 Pa^{-1})
$\chi_a(\omega)$	Frequency response function predicted by analytical model (m^3 Pa^{-1})
ε	Air-filled porosity (-)
$\phi_{q,dp}(\omega)$	Phase function, phase shift between q(t) and oscillations in the time-rate-of-change of atmospheric pressure (radians)
μ	Dynamic viscosity of soil-gas (Pa s)
θ	Dummy variable used to integrate over time (s)
τ	Characteristic response time of soil gas to a change in atmospheric pressure (s)
ω	Circular frequency (radians s^{-1})
$\lvert \ \rvert$	Modulus of a complex number (-)

Table 4.1 Soil properties used for simulations shown in Figs. 4.4 and 4.5.

Figure	k (m^2)	ε (-)	L (m)[a]	τ (s)[b]	C (L Pa^{-1})[c]
4.4c, 4.5a, 4.5b, 4.5c	10^{-11}	0.4	8	~ 460 s	2.50
4.4c, 4.5a, 4.5c	5×10^{-12}	0.2	8	~ 460 s	1.25
4.4d, 4.5b, 4.5c	10^{-10}	0.4	8	~ 46 s	2.50
4.4d, 4.5b, 4.5c	10^{-12}	0.4	8	~ 4,600 s	2.50

[a] L = distance between basement floor and water table

[b] calculated with $\overline{P}$= 100,000 Pa, and $\mu = 1.8 \times 10^{-5}$ Pa s

[c] calculated with $\overline{P}$= 100,000 Pa, and A = 78.5 m^2

Table 4.2 Soil properties used for simulations shown in Figs. 4.7 and 4.8. Calculated soil-gas entry rate, Q_{SS}, driven by a 1 Pa steady indoor-outdoor pressure difference, and the root-mean-square soil-gas entry rate, Q_{RMS}, caused by typical atmospheric pressure fluctuations.

						Dirt Floor		Perimeter Crack	
case	k (m^2)	ε (-)	L (m)[a]	τ (s)[b]	C ($L\ Pa^{-1}$)[c]	Q_{SS} ($L\ min^{-1}$)	Q_{RMS} ($L\ min^{-1}$)	Q_{SS} ($L\ min^{-1}$)	Q_{RMS} ($L\ min^{-1}$)
1	10^{-10}	0.4	8	46	2.5	8.6	0.53	2.7	0.14
1	10^{-11}	0.4	8	460	2.5	0.86	0.34	0.27	0.091
1	10^{-12}	0.4	8	4,600	2.5	0.086	0.20	0.027	0.052
1	10^{-13}	0.4	8	46,000	2.5	0.0086	0.088	0.0027	0.021
2	10^{-11}	0.2	8	230	1.25	0.86	0.20	0.27	0.055
2	10^{-11}	0.3	8	345	1.9	0.86	0.28	0.27	0.074
2	10^{-11}	0.4	8	460	2.5	0.86	0.34	0.27	0.091
2	10^{-11}	0.5	8	575	3.1	0.86	0.41	0.27	0.11
3	10^{-11}	0.4	3	65	0.9	0.70	0.18	0.25	0.053
3	10^{-11}	0.4	8	460	2.5	0.86	0.34	0.27	0.091
3	10^{-11}	0.4	13	1,220	4.1	0.88	0.45	0.27	0.12
3	10^{-11}	0.4	18	2,330	5.7	0.89	0.54	0.27	0.14

[a] L distance between basement floor and water table

[b] calculated with $\bar{P} = 100{,}000$ Pa, and $\mu = 1.8 \times 10^{-5}$ Pa s

[c] calculated with $\bar{P} = 100{,}000$ Pa, and $A = 78.5\ m^2$

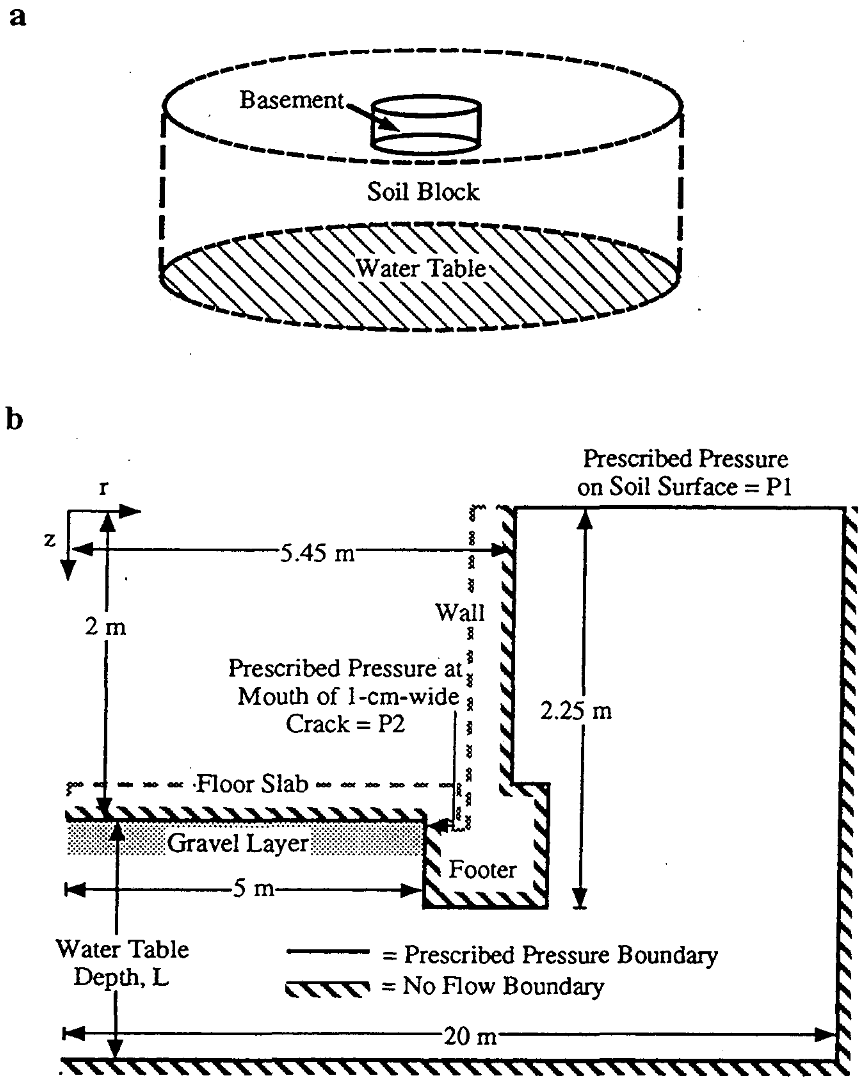

Fig. 4.1 Schematic of: (a) the cylindrical basement and soil block; (b) cross-section of model basement and soil block (due to axial-symmetry only half the cylinder is shown). The finite-element model calculates the soil-gas pressure and velocity inside the region bound by the heavy black line shown in Fig. (b). The dashed lines indicate the interior edges of the walls of the structure. These lines are intended for visual guidance only. Only the gravel layer with a perimeter gap configuration is shown in (b). For simulations of a basement with an open dirt floor the gravel layer is assigned the same properties as the rest of the soil block and the prescribed pressure boundary condition P2 is applied across the bottom of the entire floor slab. For simulations of a basement with a perimeter gap and a homogeneous soil block the gravel layer is assigned the same properties as the rest of the soil block. The figure is not drawn to scale.

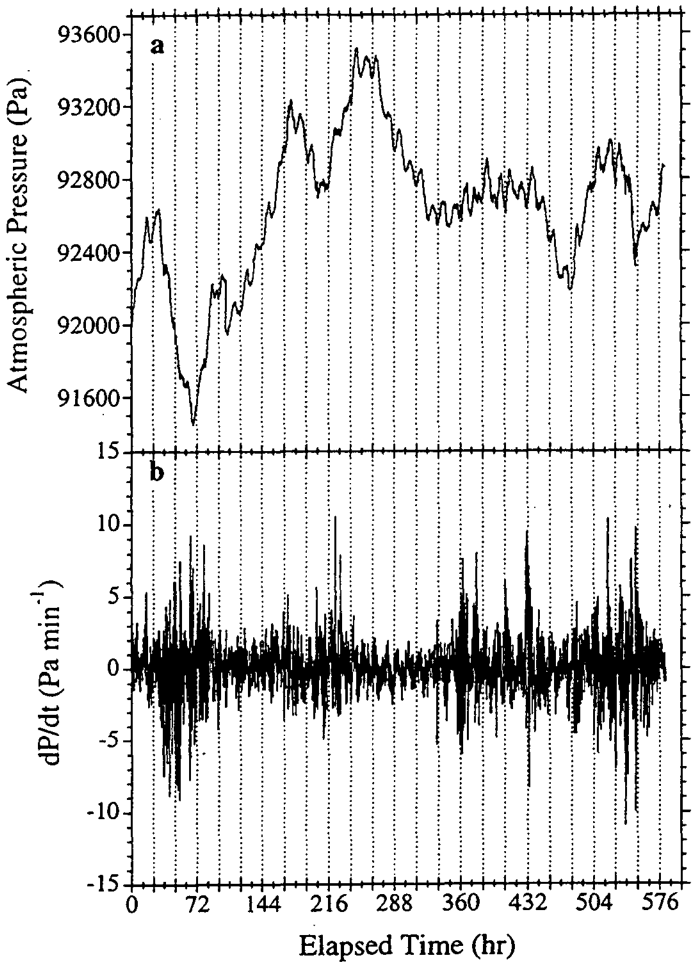

Fig. 4.2 (a) Atmospheric pressure measured during a 24-day experiment; (b) time-rate-of-change of atmospheric pressure, defined as the change in pressure over a two-minute time interval. These data were collected during the February and March of 1993.

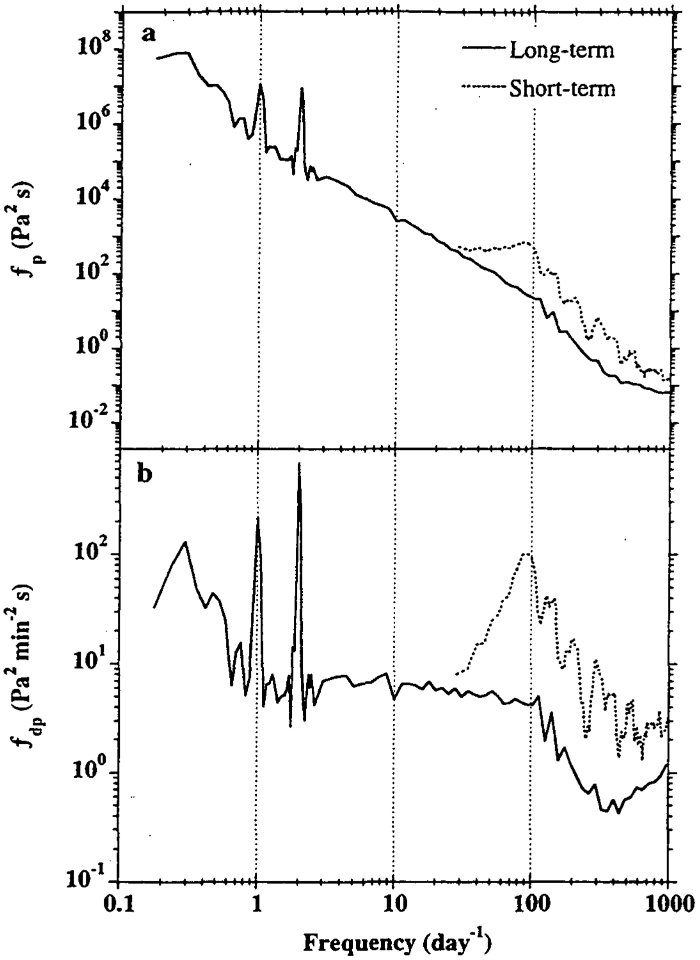

Fig. 4.3 Power spectra for (a) atmospheric pressure, and (b) time-rate-of-change of atmospheric pressure. The long-term spectra are based on more than 108 days of measured atmospheric pressure data, while the short-term spectra are based on 5 hours of data.

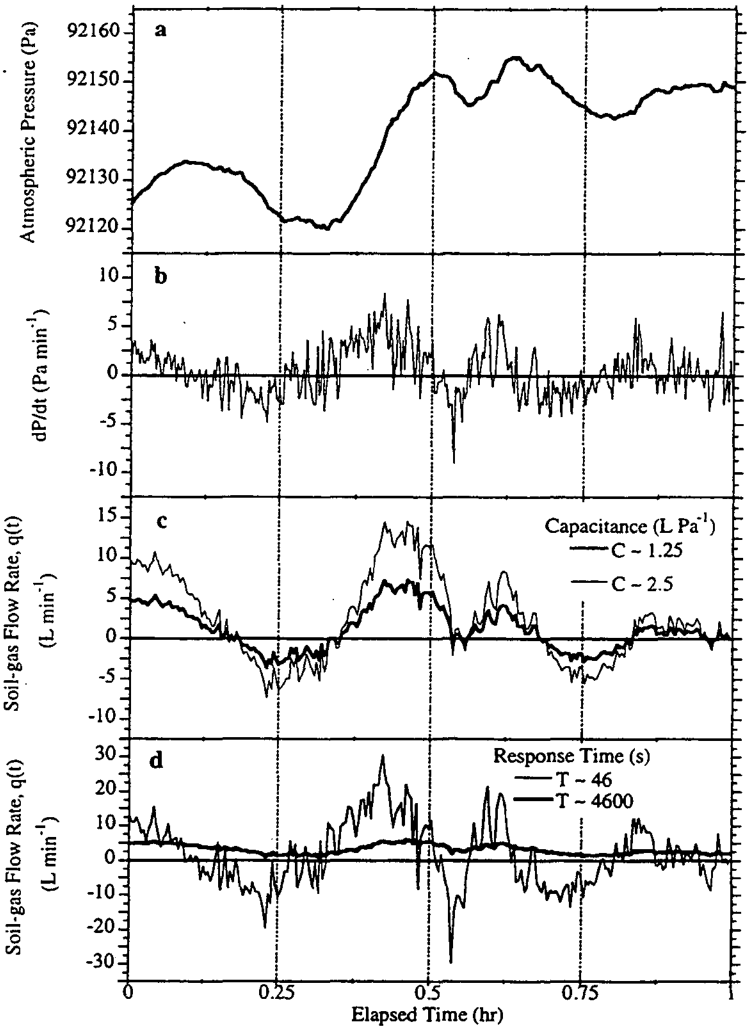

Fig. 4.4 Atmospheric pressure and calculated gas flow into and out of a basement with a dirt floor: (a) measured atmospheric pressure used as boundary condition for calculations; (b) time-rate-of-change in atmospheric pressure, defined as the change in pressure over a 15-s interval; (c) q(t) as a function of capacitance with the characteristic response time held constant ($\tau \sim 460$ s); (d) q(t) as function of characteristic response time with the capacitance held constant ($C \sim 2.5$ L Pa^{-1}). Negative flow rates indicate soil-gas flow into the basement. Soil properties used for these calculations are listed in Table 4.1.

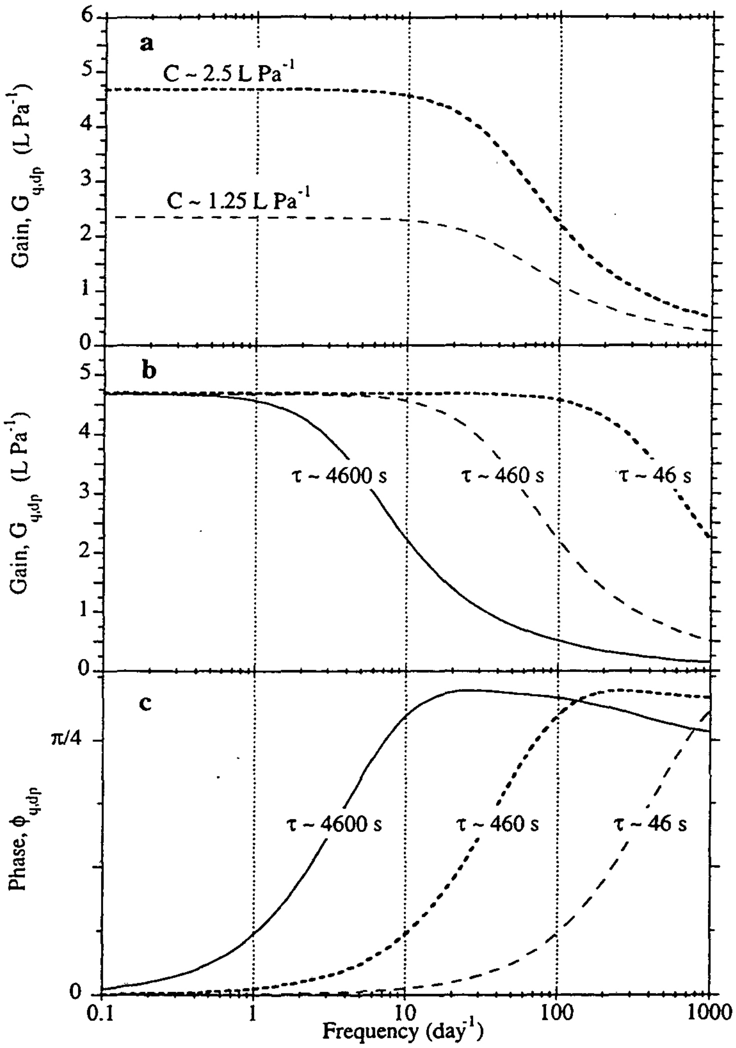

Fig. 4.5 Calculated frequency response function for a basement with a dirt floor: (a) gain, $G_{q,dp}(\omega)$, as a function of capacitance with the characteristic response time held constant (τ ~ 460 s); (b) gain, $G_{q,dp}(\omega)$, as a function of characteristic response time with the capacitance held constant (C ~ 2.5 L Pa^{-1}); (c) phase function, $\phi_{q,dp}(\omega)$. Soil properties are listed in Table 4.1.

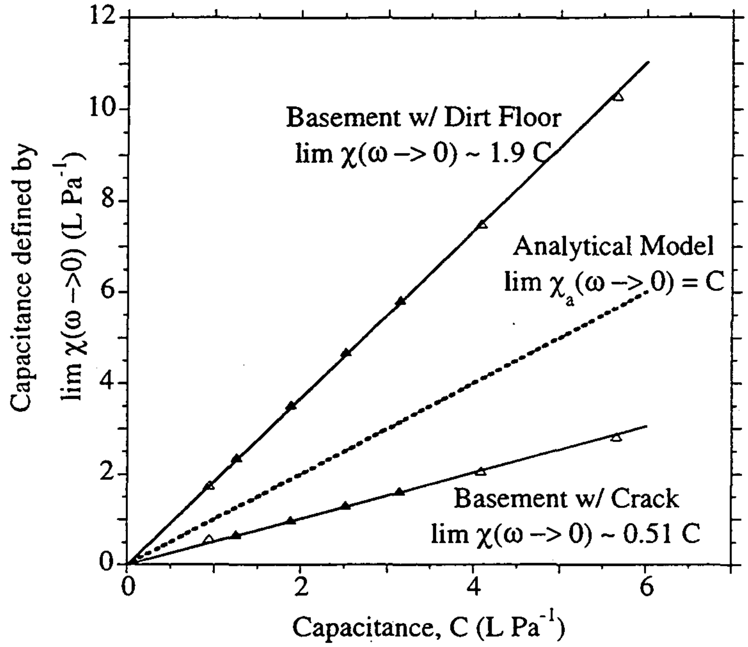

Fig. 4.6 Low-frequency limit of $\chi(\omega)$ as a function of the capacitance. The capacitance is varied by changing either the water table depth while holding the air-filled porosity fixed at 0.4 (open symbols) or the air-filled porosity while holding the water table depth fixed at 8 m (solid symbols). The values of the soil properties used for these calculations are listed as Cases 2 and 3 in Table 4.2. Solid lines indicate linear regressions, where $R^2 > 0.999$ in each case. The dashed line indicates low frequency limit of $\chi_a(\omega)$ defined by the analytical model.

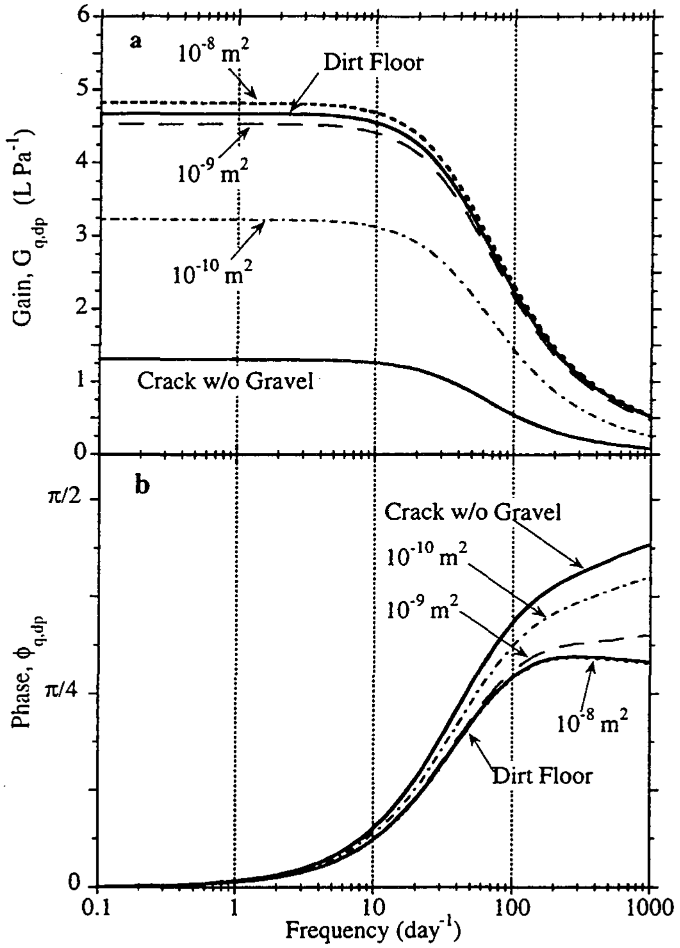

Fig. 4.7 Comparison of the frequency response function for a basement with a dirt floor and a basement with a perimeter crack: (a) gain, $G_{q,dp}(\omega)$; (b) phase, $\phi_{q,dp}(\omega)$. For the basement with a perimeter crack, the permeability of a 10-cm-thick gravel layer immediately underneath the slab was varied between 10^{-10} and 10^{-8} m^2. Numbers labeling curves indicate permeability of gravel layer. Other properties used for these simulations are water table depth L = 8 m, permeability of the soil (not including gravel layer) $k = 10^{-11}$ m^2, air-filled porosity of the soil (not including gravel layer) $\varepsilon = 0.4$.

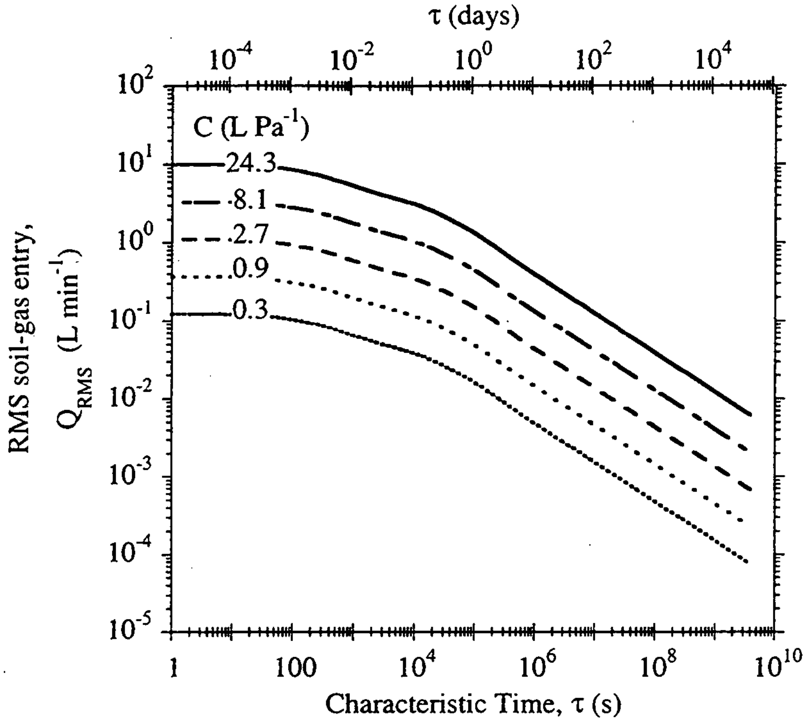

Fig. 4.8 Q_{RMS} as a function of characteristic response time and capacitance. For this analysis, we employed eqn. (4.8) and long-term spectrum shown in Fig. 4.3b.

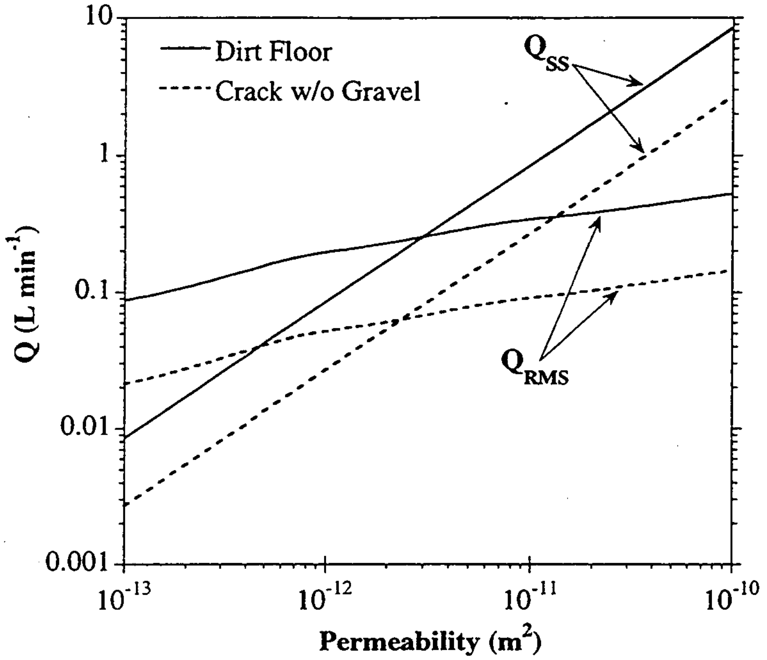

Fig. 4.9 Q_{RMS} and Q_{SS} as a function of soil permeability. Soil properties used for these simulations listed as Case 1 in Table 4.2.

Chapter 5

THE EFFECTS OF ATMOSPHERIC PRESSURE FLUCTUATIONS ON RADON ENTRY INTO HOUSES

ABSTRACT

To study the importance of radon entry into houses driven by atmospheric pressure fluctuations, we have simultaneously measured the radon entry rate into an experimental basement structure and the changes in atmospheric pressure. Although the net entry of soil gas driven by atmospheric pressure fluctuations is zero, the oscillating soil-gas flow created by these fluctuations drives radon entry because of the several order of magnitude difference between the radon concentration of the indoor air and that of the surrounding soil gas. In the absence of a steady indoor-outdoor pressure difference, atmospheric pressure fluctuations at the study site drive 1.5 times more radon entry than diffusion. Pressurizing or depressurizing the interior of the structure relative to the ambient atmosphere diminishes the contribution of entry driven by atmospheric pressure fluctuations to the long-term radon entry rate. When the structure is pressurized 0.5 Pa relative to the ambient atmosphere, fluctuations in atmospheric pressure increase the long-term radon entry rate by 30%. When the structure is depressurized 0.5 Pa relative to the ambient atmosphere, atmospheric pressure fluctuations increase the long-term radon entry rate by 10%. When the magnitude of sustained indoor-

outdoor pressure differences is greater than 1.5 Pa, atmospheric pressure fluctuations have essentially no effect on the long-term radon entry rate.

INTRODUCTION

Advective flow of radon-laden soil gas is primarily responsible for houses with elevated indoor radon concentrations (Nazaroff, 1992). This flow is commonly associated with small but sustained indoor-outdoor pressure differences created by temperature effects, wind interaction with the building shell, and the operation of heating, ventilation and air-conditioning (HVAC) systems (Nazaroff et al., 1988; Nazaroff, 1992). However, several field studies (Hernandez et al., 1984; Holub et al., 1985; Turk et al., 1989; Hintenlang and Al-Ahmady, 1992) have observed elevated indoor radon concentrations during periods when these pressure differences were small. Advective radon entry driven by atmospheric pressure fluctuations represents one possible explanation for these previously observed but unexplained elevated indoor radon concentrations. Atmospheric pressure fluctuations pump soil gas into and out of a house *without* indoor-outdoor pressure differences because the response time of the interior of a house to a change in atmospheric pressure is orders of magnitude shorter than the response time of the soil gas. The interior of a house typically responds to changes in atmospheric pressure on a time scale of milliseconds (Allen, 1984); whereas, common soils respond to changes in atmospheric pressure on a time scale ranging from minutes to days (Nazaroff et al., 1988).

The reported experimental evidence for radon entry driven by atmospheric pressure fluctuations is based on the observed correlation of atmospheric pressure with measured indoor radon concentrations (Hernandez et al., 1984; Hintenlang and Al-Ahmady, 1992). Unfortunately, these studies provide little detailed insight into the effect of atmospheric pressure fluctuations on radon entry because indoor radon concentrations depend on both the radon entry rate and the building ventilation rate. No direct measurements of radon entry into a building driven by atmospheric pressure have been reported.

Many researchers have examined the effect of atmospheric pressure fluctuations on the flux of radon across the soil surface (e.g. Clements and Wilkening, 1974; Edwards and Bates, 1980; Schery et al., 1984). Measurements indicate that cyclical changes in atmospheric pressure cause surface fluxes of radon to vary by more than a factor of 2; however, for a homogeneous soil, the long-term time-averaged flux is well approximated by a pure diffusion process (Schery et al., 1984; Nazaroff, 1992). Unfortunately, studies of surface flux provide little insight into the problem of radon entry into houses because the concentration of radon in the soil gas near the surface of an uncoverd soil surface is generally very low. This, in turn, limits the contribution of advective flow caused by atmospheric pressure fluctuations to the total radon flux across the soil surface. In contrast, the radon concentration of soil gas immediately underneath a concrete slab is frequently orders of magnitude larger than the concentration of indoor air because of the low diffusivity of radon in concrete.

The most persuasive evidence for radon entry into houses driven by fluctuations in atmospheric pressure is the theoretical study by Tsang and Narasimhan (1992). Their results suggest that sinusoidal oscillations in atmospheric pressure may drive significant radon entry into houses for certain combinations of soil properties, basement configurations and atmospheric pressure signals.

This chapter builds on the results presented in Chapters 3 and 4 by reporting measurements of radon entry driven by atmospheric pressure fluctuations made in an experimental basement structure. Experiments were conducted over a range of controlled indoor-outdoor pressure differences to examine the interaction of radon entry caused by atmospheric pressure fluctuations and that resulting from steady indoor-outdoor pressure differences. The goal of this chapter is to quantify the importance of atmospheric pressure fluctuations as a mechanism for generating radon entry into the experimental structure relative to entry resulting from steady indoor-outdoor pressure differences and from diffusion.

EXPERIMENTAL METHODS

Experimental System

The measurements reported in this study were made in an experimental structure which was designed and constructed to study soil-gas and radon entry into houses (Fisk et al., 1992; Garbesi et al., 1993; Robinson and Sextro, 1995). Fig. 5.1 shows a schematic of the soil-structure system. The concrete structure is a single-chamber with interior dimensions of 2.0 x 3.2 m and a height of 2.0 m; only about 0.1 m of the walls extend above grade. The structure's floor slab rests on a 0.1-m-thick, high-permeability gravel layer. Two 1.25-cm-diameter holes in one wall of the access hatch permitted the interior of the structure to rapidly respond to changes in atmospheric pressure. A companion structure exists at this experimental site which is essentially identical to the one used for this study except that its floor slab rests on undisturbed soil.

The atmospheric pressure was measured at 0.2 Hz using a pressure transducer connected to an outdoor omnidirectional static pressure tap located ~ 3 m from the structure (Paroscientific model 1015a). The response time, accuracy, and resolution of this pressure transducer are 1 s, ± 5 Pa, and 0.1 Pa, respectively. The pressure difference between the interior of the structure and the static pressure tap was measured at 30-s intervals using a differential pressure transducer (Validyne model DP103).

All openings between the structure interior and the soil were sealed except for a 3.8-cm-diameter hole in the center of the structure floor. Although this hole is not geometrically representative of the cracks and gaps which commonly exist in real houses (Scott, 1988), this study requires such an opening in combination with a high-permeability subslab gravel layer to enable atmospheric pressure fluctuations to generate gas velocities greater than the detection limit of our flow sensor. Because of the high permeability of the subslab gravel layer, the soil-gas flow rate into the structure depends only weakly on the geometry of an opening if the opening does not provide significant resistance to flow. Therefore, the measured gas flow rate through the hole is representative of the flow between the structure and the soil for more realistic opening configurations. A discussion of the effect of a high permeability subslab gravel layer on soil gas entry can be found in Chapters 2 and 4.

The gas flow rate through the 3.8-cm-diameter hole was measured using the flow sensor shown in Fig. 5.1. The 30-cm high sensor incorporates two omnidirectional hot-film velocity transducers (TSI model 8470) mounted in a U-shaped tube (1.9-cm ID). The velocity transducers can measure the magnitude and direction of gas flow down to 0.15 L min^{-1}. Appendix B describes in more detail the theory, calibration, and operation of the U-shaped flow sensor. The flow sensor used for this study is identical to the one described in Chapter 3 expect that the length of the U-shaped tube was shortened to reduce the resistance of the sensor tube to gas flow. The resistance of the flow sensor tube varies linearly with flow rate and was measured in the laboratory to be 0.1 Pa L^{-1} min. The gas flow rate through the sensor was measured at 5-s intervals.

A continuous radon monitor (CRM) was used to measure the radon concentration of the air inside the structure. An oscillating fan continually mixed the structure air to allow accurate sampling of the structure radon concentration from a single location. Counts from the structure CRM were interpreted using the method described by Thomas and Countess (1979).

Two low-volume, low flow rate CRMs were used to monitor the radon concentration of the air inside the U-shaped sensor tube, and the soil gas in the gravel layer. As indicated in Fig. 5.1, one CRM samples air from the top of the U-shaped tube, another CRM samples soil gas from the gravel layer ~ 15 cm from the hole in the center of the structure floor. Samples are drawn at a constant flow rate of 66 cm^3 min^{-1} and passed through a 33 cm^3 scintillation cell. To reduce the effects of ^{220}Rn on the measurements, the samples were drawn through an 11-m-long tube to provide a 3-min delay before being delivered to the CRM. Counts from each CRM were recorded at one-minute intervals and interpreted using the algorithm described by Busigin et al. (1979). These low-volume, low flow rate CRMs strike a balance between the conflicting objectives of minimizing the effect of sampling on our results while maximizing the temporal resolution of our measurements. The 66 cm^3 min^{-1} sampling flow rate creates much smaller flows in the sensor tube than the 500 to 1000 cm^3 min^{-1} flow rates caused by typical atmospheric pressure fluctuations. The high radon concentration of the soil gas underneath the structure, ~ 100,000 Bq m^{-3}, enables us to achieve acceptable levels of statistical uncertainty despite the small size of the scintillation cell. Appendix D describes in more detail the calibration and performance of these low-volume, low-flow CRMs.

Measured Soil Properties at the Structure Site

The soil at the structure site has been extensively characterized. Table 5.1 reports the measured permeability of the gravel, backfill, and undisturbed soil at the structure site. Measurements of the air-filled porosity, emanation fraction, and radium content of the soil at the structure site are summarized in Table 5.2. The change in porosity between 1.6 and 2.2 m corresponds to the transition between the organic surface soil and the underlying sapprolite. Further geological details of the structure site are described by Flexser et al. (1993) and Brimhall and Lewis (1992). Appendix A describes in more detail the results of soil permeability and porosity measurements made at the experimental site.

Measured Radon Entry Rate

Experiments were conducted to measure the advective radon entry rate into the structure as a function of steady indoor-outdoor pressure difference. Each experiment lasted approximately 7 days. The pressure of the interior of the structure was varied using a pump and a computer-controlled mass-flow controller. To depressurize the interior of the structure relative to the atmosphere, air was drawn from the structure at a constant flow rate. To pressurize the interior of the structure relative to the atmosphere, air was added to the structure at a constant flow rate. The magnitude of the indoor-outdoor pressure difference was varied by changing the set point of the mass-flow controller. To create neutral pressure conditions, a small flow rate of air was added to the structure to offset the slight indoor-outdoor pressure difference, ~ 0.15 Pa, created by the temperature of the soil gas next to the structure being 5 - 10 °C cooler than the temperature of the air inside the structure.

The advective radon entry rate through the 3.8-cm-diameter hole in the center of the structure floor, $S_A(t)$ (Bq s^{-1}), is defined as

$$S_A(t) = Q(t)\,I(t) \tag{5.1}$$

where Q(t) is the measured gas flow rate (m^3 s^{-1}), and I(t) is the measured radon concentration of the air inside the U-shaped pipe (Bq m^{-3}). When the magnitude of I(t) falls below the measurement uncertainty of the flow sensor CRM, we assume that the radon concentration of the air inside the sensor tube is equal to the measured indoor radon concentration. This occurs when indoor air is driven into the soil by rising atmospheric pressure. The uncertainty associated with our measurement of I(t), ~ ±7500 Bq m^{-3}, is similar in magnitude to the measured indoor radon concentration, but much smaller than the ~ 100,000 Bq m^{-3} radon concentration of the soil gas underneath the structure floor slab. The majority of the measurement uncertainty is due to counting statistics and the 1-min counting interval used to analyze the flow sensor CRM data.

To examine the effect of atmospheric pressure fluctuations on the long-term radon entry rate into the structure, data from each experiment were broken into 24-hour time blocks. Time blocks were discarded in which the standard deviation of the measured indoor-outdoor pressure difference exceeded 0.5 Pa. Large fluctuations in indoor-outdoor pressure typically occurred during storms when high winds blew over the open holes in the structure access hatch. For the remaining time blocks, we calculated the average radon entry rate and the average indoor-outdoor pressure difference. The results were then sorted by indoor-outdoor pressure difference. Time blocks with similar indoor-outdoor pressure differences were grouped together and averaged to estimate the long-term radon entry rate as function of indoor-outdoor pressure difference. Each data group used to estimate the long-term radon entry rate contained between 6 and 8 days of measurements.

RESULTS AND DISCUSSION

Radon entry driven by atmospheric pressure fluctuations

The time series data shown in Fig. 5.2 illustrate the relationship between atmospheric pressure fluctuations and radon entry into the structure. These measurements were made under neutral pressure conditions, i.e. no indoor-outdoor pressure difference. Fig. 5.2a shows the calculated time-rate-of-change of atmospheric pressure based on the change in pressure over a 15-s interval. The measured gas flow rate, Q(t), is shown in Fig. 5.2b. The measured radon concentration in the U-shaped pipe, I(t), is shown in Fig. 5.2c. The radon entry rate into the structure, calculated using eqn. (5.1), is shown in Fig. 5.2d. Table 5.3 lists the average indoor-outdoor pressure difference, volume of gas pumped into and out of the structure, average advective radon entry rate, no-dilution radon entry rate, and measured indoor radon concentration for this 2-hr period.

Fig. 5.2 indicates that falling atmospheric pressure draws high-concentration soil gas, ~ 80000 Bq m^{-3}, into the structure. Rising atmospheric pressure forces low-concentration indoor air, ~ 2600 Bq m^{-3}, back into the soil. Although approximately the same volume of gas is pumped into and out of the structure over this period (30 L pumped in vs. 32 L pumped out), the net effect of this pumping is to drive an average net advective radon entry rate of 0.23 Bq s^{-1} into the structure, more than two times the measured diffusive entry rate, 0.1 Bq s^{-1} (Garbesi, 1993).

The outflow of low-concentration indoor air dilutes the radon concentration of the soil gas immediately underneath the structure floor slab. This dilution, in turn, reduces the average radon entry rate driven by atmospheric pressure fluctuations. If the soil gas underneath the structure was not diluted by the outflow of indoor air, the average radon entry rate during the 2-hr period shown in Fig. 5.2 would have been 0.43 Bq s^{-1}, almost twice the actual average entry rate of 0.23 Bq s^{-1}.

The no-dilution radon entry rate is the product of the equivalent steady-state soil-gas entry rate and the undiluted radon concentration of the soil gas underneath the structure. The equivalent steady-state soil-gas entry rate is defined as the total volume of soil-gas drawn unidirectionally into the structure over a fixed period of time. For example, atmospheric pressure fluctuations drew 32 L of soil gas into the structure during the 2-hr period shown in Fig. 5.2, yielding an equivalent steady state soil-gas entry rate for this 2-hr period of 0.27 L min^{-1}. The undiluted radon concentration of the soil gas immediately underneath the structure is ~96,000 Bq m^{-3}. This value is the measured radon concentration of the air inside the flow sensor when the interior of the structure is depressurized a steady 5 Pa relative to the ambient atmosphere, a value at which atmospheric pressure fluctuations do not pump any low-concentration indoor air into the soil.

In addition to reducing the advective radon entry rate into the structure, the dilution of the soil gas underneath the structure floor slab complicates the analysis of radon entry driven by atmospheric pressure fluctuations. For example, compare the two spikes in radon entry rate immediately before hour 139 in Fig. 5.2d. Although these spikes are caused by equivalent soil-gas entry rates, ~ 1 L min^{-1}, the second spike in the radon entry rate is much smaller than the first because of the dilution of the soil gas underneath the structure. If there was no dilution of the soil gas underneath the structure then these two spikes in radon entry should have essentially the same magnitude.

Time-series data are shown in Figs. 5.3 and 5.4 to illustrate the interaction of fluctuations in atmospheric pressure and steady indoor-outdoor pressure differences. The results shown in Fig. 5.3 are from a period during which the interior of the structure was pressurized 0.9 Pa relative to the ambient atmosphere; the measurements shown in Fig. 5.4 were made during a period when the interior of the structure was depressurized 0.9 Pa relative to the ambient atmosphere. Figs. 5.3a and 5.4a show the time-rate-of-change of atmospheric pressure. Measured soil-gas flow rates are shown in Figs. 5.3b and 5.4b. Measured pipe radon concentrations are shown in Figs. 5.3c and 5.4c. The calculated radon entry rates are shown in Figs. 5.3d and 5.4d. Table 5.3 lists the average indoor-outdoor pressure difference, volume of gas pumped into and out of the structure, average advective radon entry rate, no-dilution radon entry rate, and average indoor radon concentration for the 2-hr periods shown in Figs. 5.3 and 5.4.

The measurements shown in Fig. 5.3 indicate that atmospheric pressure fluctuations drive advective radon entry into the structure even when the interior of the structure is slightly pressurized relative to the atmosphere. Sustained periods of rapidly falling atmospheric pressure overcome the slight positive indoor-outdoor pressure difference and drive soil-gas and radon entry into the structure. The average advective radon entry rate into the structure for the 2-hr period shown in Fig. 5.3 is 0.02 Bq s^{-1}, 20% of the diffusive entry rate. For this analysis, we assumed that the measured diffusive entry rate of 0.1 Bq s^{-1} was independent of indoor-outdoor pressure difference.

When the interior of the structure is pressurized relative to the atmosphere, the dilution of the soil gas underneath structure floor slab severely reduces the radon entry rate caused by fluctuations in atmospheric pressure. Fig. 5.3c shows peak pipe radon concentrations of ~ 25,000 Bq m^{-3} in comparison to the ~ 80,000 Bq m^{-3} peak concentrations observed under neutral pressure conditions (Fig. 5.2c). If the soil gas underneath the structure was not diluted, the average radon entry rate driven by atmospheric pressure for the period shown in Fig. 5.3 would have been 0.23 Bq s^{-1}, more than 10 times the actual entry rate.

If the interior of the structure is slightly depressurized relative to the atmosphere, atmospheric pressure fluctuations enhance the advective radon entry rate into the structure. The average advective radon entry rate for the 2-hr period shown in Fig. 5.4 is 0.58 Bq s^{-1}, 20% greater than the radon entry rate driven by -0.9 Pa steady indoor-outdoor pressure.

The radon entry rate driven by a steady indoor-outdoor pressure difference is defined by the steady-state soil-gas entry rate and the radon concentration of the undisturbed soil gas underneath the structure floor slab, ~ 96,000 Bq m^{-3}. The steady-state soil-gas entry rate depends on the resistance of the soil-structure system to soil-gas entry. We determined this resistance by measuring the gas flow rate through the U-shaped flow sensor for a range of steady indoor-outdoor pressure differences. A linear regression of these measurements yields the resistance of the soil-structure system to soil-gas entry, 0.35 L min^{-1} Pa^{-1}. Using the measured indoor-outdoor pressure difference we calculate the steady-state soil-gas entry rate into the structure. For example, the 0.9 Pa structure depressurization shown in Fig. 5.3 creates a 0.32 L min^{-1} steady-state soil-gas entry rate into the structure.

The results in Table 5.3 indicate that dilution of the soil gas in the gravel layer reduces the advective radon entry rate even when the interior of the structure is slightly depressurized relative to the atmosphere. The soil gas underneath the structure is diluted because sustained periods of rapidly rising atmospheric pressure overcome the steady structure depressurization and drive low-concentration indoor air into the soil. If the soil gas underneath the structure was not diluted, the average radon entry rate driven by atmospheric pressure for the period shown in Fig. 5.3 would have been 0.74 Bq s^{-1}, 30% more than the actual entry rate.

Long-term-average radon entry

Although the time series shown in Figs. 5.2-5.4 illustrate the dynamics of radon entry driven by atmospheric pressure fluctuations, these short time series provide little insight into the importance of atmospheric pressure fluctuations as a mechanism for driving long-term radon entry. Since occasional, high-frequency oscillations in atmospheric pressure can generate large soil-gas and radon entry rates, we must average more than the two hours of measurements shown in Figs. 5.2-5.4 to determine the long-term-average radon entry rate.

Fig. 5.5 summarizes the enhancement of the long-term-average radon entry rate into structure due to atmospheric pressure fluctuations. Each data point shown in Fig. 5.5 was determined by averaging 6 to 8 days of measurements. Since more than 99% of the total power of the time-rate-of change spectrum occurs at frequencies greater than 1 day^{-1}, the average entry rate over a 6 day period should represent the effect of typical atmospheric pressure fluctuations on the long-term-average radon entry rate.

The contribution of diffusion, steady indoor-outdoor pressure differences, and atmospheric pressure fluctuations to the long-term radon entry rate is shown in Fig. 5.5a. The enhancement or percent increase of the long-term radon entry rate due to fluctuations in atmospheric pressure is shown in Fig. 5.5b. When the structure is pressurized relative to the ambient atmosphere only diffusion and atmospheric pressure fluctuations drive radon entry. When the structure is depressurized, diffusion, steady indoor-outdoor pressure differences, and atmospheric pressure fluctuations drive radon entry.

At neutral pressure conditions, Fig. 5.5a indicates that the total radon entry rate into the structure is 0.25 Bq s^{-1} of which 0.1 Bq s^{-1} is due to diffusion. The remaining 0.15 Bq s^{-1} is caused by atmospheric pressure fluctuations. Therefore, atmospheric pressure fluctuations enhance the long-term radon entry by 150% at neutral pressure conditions.

As the interior of the structure is pressurized or depressurized relative to the outside, the contribution of fluctuations in atmospheric pressure to the total entry rate into the structure falls off. Fig. 5.5b indicates that when the interior of the structure is depressurized 0.5 Pa, atmospheric pressure fluctuations enhance the long-term radon entry rate by 10%. When the interior of the structure is pressurized 0.5 Pa, atmospheric pressure fluctuations enhance the long-term radon entry rate by 30%. When the magnitude of this pressure difference is greater than ~ 1.5 Pa, atmospheric pressure fluctuations have essentially no effect on the long-term radon entry rate.

Using the principle of superposition, we can separate the measured gas flow rate into a component driven by steady indoor-outdoor pressure differences and a component driven by fluctuations in atmospheric pressure. Steady indoor-outdoor pressure differences create an offset in the gas flow rate into the structure; the dashed line drawn in Fig. 5.3b indicates the steady flow rate caused by a 0.9 Pa pressurization of the interior of the structure relative to the atmosphere on the measured gas flow rate. The effect of atmospheric pressure fluctuations is then added to this steady flow.

By separating the effects of indoor-outdoor pressure differences and atmospheric pressure fluctuations on the gas flow rate we can improve our understanding of the contribution of these fluctuations to the long-term radon entry rate. Figs. 5.3 and 5.4 indicate that an offset in the soil-gas flow rate reduces the volume of gas pumped into and out of the structure by atmospheric pressure fluctuations. This, in turn, reduces the radon entry rate driven by these fluctuations. Increasing the indoor-outdoor pressure difference increases the offset in the soil-gas flow rate; when this offset is larger than the largest flow rate created by changes in atmospheric pressure, the atmospheric pressure fluctuations no longer contribute to the long term radon entry rate.

Dilution of soil gas

An estimate of the long-term radon entry rate assuming no-dilution of the soil gas underneath the structure is presented in Fig. 5.5. Comparing this estimate with the measured results shows that at neutral pressure conditions, dilution reduces the total long-term radon entry rate into the structure by a factor of ~2. Dilution also reduces the range of indoor-outdoor pressure differences at which atmospheric pressure fluctuations contribute to the long-term radon entry rate. For example, Fig. 5.5b indicates that when the interior of the structure is depressurized 1 Pa, atmospheric pressure fluctuations no longer contribute to the long-term radon entry rate. If the soil gas underneath the structure was not diluted by the outflow of low-concentration indoor air, atmospheric pressure fluctuations would enhance the long-term radon entry rate by ~20% when the structure was depressurized 1 Pa. The fact that the no-dilution estimate is not zero indicates that even when the interior of the structure is depressurized 1 Pa, some atmospheric pressure fluctuations are large enough to overcome the effect of this depressurization and to pump soil gas into and out of the structure. However, because of the effect of dilution, this pumping does not does not contribute to the long-term radon entry rate.

The effect of dilution on the long-term radon entry rate depends on the "recharge rate" of the soil. The phrase recharge rate refers to the rate at which the soil replenishes the radon concentration of the low-concentration indoor air flows which is driven into the soil during periods of rising atmospheric pressure. This recharge rate depends on both the production of radon through the decay of ^{226}Ra in the soil and the transport of radon through the soil pore space by diffusion and dispersion. In addition, the recharge rate will also depend on the building substructural characteristics such as the presence of a high permeability subslab gravel layer and the spatial distribution of leakage area.

Examining the typical period of time between reversals in flow direction caused by atmospheric pressure fluctuations provides insight into which physical process, generation or transport, controls the recharge rate of the soil gas immediately underneath the structure floor slab. Figs. 5.2-5.4 indicate that atmospheric pressure fluctuations cause reversals in the soil gas flow direction every 10 to 15 min. Since these fluctuations drive significant radon entry, the radon concentration of the soil gas must recharge on a time scale of minutes. The time scale for recharging the soil gas radon concentration based on generation of new radon atoms is ~ 3.8 days, the half-life of radon. Therefore, generation of radon in soil immediately underneath the gravel cannot recharge the indoor air on a time scale of minutes, and this recharge must be limited by the transport of radon through the soil pore space.

We can estimate the time scale of the recharge rate due to diffusive transport using dimensional analysis of the diffusion equation,

$$\tau_{\mathrm{diff}} \sim \frac{L^2}{D}, \tag{5.2}$$

where L is a characteristic length scale (m), and D is the interstitial diffusivity of radon ($m^2\ s^{-1}$). Defining L as the thickness of the gravel layer, 0.1 m, and using a value of $3 \times 10^{-6}\ m^2\ s^{-1}$ for the interstitial diffusivity of radon (Nazaroff, 1992), the characteristic time scale for the recharge rate due to diffusive transport is ~ 55 min.

CONCLUSIONS

Atmospheric pressure fluctuations drive advective radon entry into our experimental basement structure without requiring the sustained indoor-outdoor pressure differences commonly associated with advective entry of radon and other soil-gas contaminants into buildings. This phenomenon may explain previously reported higher-than-expected indoor radon concentrations observed under neutral pressure conditions (Hernandez et al., 1984; Holub et al., 1985; Turk et al., 1989; Hintenlang and Al-Ahmady, 1992).

Atmospheric pressure fluctuations have the largest effect on the long-term radon concentrations at neutral pressure conditions, where there is essentially no indoor-outdoor pressure difference. Under these conditions, atmospheric pressure fluctuations increase the long-term radon entry rate into the structure by 150%. As the interior of the structure is pressurized or depressurized in comparison with the ambient atmosphere, the relative contribution of atmospheric pressure fluctuations to the total radon entry rate into the structure diminishes. If the magnitude of these pressure differences is greater than ~ 1.5 Pa, atmospheric pressure fluctuations have essentially no effect on the long-term radon entry rate into the structure. Increasing the recharge rate of the soil-gas radon concentration may increase the range of indoor-outdoor pressure differences over which atmospheric pressure fluctuations drive radon entry.

The effect of atmospheric pressure fluctuations on long-term radon entry rate depends on the permeability and porosity of the soil surrounding a house. The soil surrounding the experimental basement is relatively permeable, 3×10^{-11} m^2. The relatively high permeabiltiy of this soil enables small indoor-outdoor pressure differences to drive significant soil-gas flow into the structure. This flow reduces the contribution of atmospheric pressure fluctuations to the total long-term radon entry rate into the structure.

The effect of atmospheric pressure fluctuations on the long-term radon entry rate is complex due to the dilution of the radon concentration of the soil gas underneath the structure floor slab. Rising atmospheric pressure drives low-concentration indoor air into the soil, diluting the soil-gas radon concentration immediately underneath the structure floor. This dilution reduces the radon entry resulting from atmospheric pressure fluctuations under neutral pressure conditions by a factor of 2. Although analyses which ignore the effect of dilution will overpredict the contribution of atmospheric pressure fluctuations to the long-term radon entry rate, they still indicate the qualitative trends of the relationship between atmospheric pressure fluctuations and long-term radon entry rate into the structure.

REFERENCES

Allen C. (1984) Wind pressure data requirements for air infiltration calculations. Technical Note AIC-13, Air Infiltration Center, Bracknell, Berkshire, Great Britain RG12 4AH.

Brimhall G. H. and Lewis C. J. (1992) Differential element transport in the soil profile at the Ben Lomond small structure radon site: A geochemical mass balance study. University of California at Berkeley, Dept. of Geology and Geophysics, Berkeley CA 94720.

Busigin A., van der Vooren A. W. and Phillips C. R. (1979) Interpretation of the response of continuous radon monitors to transient radon concentrations. *Health Phys.* **37**, 659-667.

Clements W. E. and Wilkening M. H. (1974) Atmospheric pressure effects on ^{222}Rn transport across the earth-air interface. *J. Geophys. Res.* **79**, 5025-5029.

Danielson R. E. and Sutherland P. L. (1986) Porosity. In Black C. A. (Ed.) *Methods of Soil Analysis, Part 1. Physical and Mineralogical Methods*, American Society of Agronomy, Madison, WI, 443-450.

Edwards J. C. and Bates R. C. (1980) Theoretical evaluation of radon emanation under a variety of conditions. *Health Phys.* **39**, 263-274.

Fisk W. J., Modera M. P., Sextro R. G., Garbesi K., Wollenberg H. A., Narasimhan T. N., Nuzum T. and Tsang Y. W. (1992) Radon entry into basements: approach, experimental structures, and instrumentation of the small structures project. LBL-31864, Lawrence Berkeley National Laboratory, Berkeley CA 94720.

Flexser S., Wollenberg H. A. and Smith A. R. (1993) Distribution of radon sources and effects on radon emanation in granitic soil at Ben Lomond, California. *Environ. Geol.* **22**, 162-177.

Garbesi K. (1993) Toward resolving model-measurement discrepancies of radon entry into houses. LBL-34244, Lawrence Berkeley National Laboratory, Berkeley CA 94720.

Garbesi K., Sextro R. G., Fisk W. J., Modera M. P. and Revzan K. L. (1993) Soil-gas entry into an experimental basement: Model-measurement comparisons and seasonal effects. *Environ. Sci. Technol.* **27**, 466-473.

Garbesi K., Sextro R. G., Robinson A. L., Wooley J. D., Owens J. A. and Nazaroff W. W. (1996) Scale dependence of soil permeability to air: Measurement method and field investigation. *Wat. Resour. Res.* **32**, 547-560.

Hernandez T. L., Ring J. W. and Sachs H. M. (1984) The variation of basement radon concentrations with barometric pressure. *Health Phys.* **46**, 440-445.

Hintenlang D. E. and Al-Ahmady K. K. (1992) Pressure differentials for radon entry coupled to periodic atmospheric pressure variations. *Indoor Air* **2**, 208-215.

Holub R. F., Droullard R. F., Borak T. B., Inkret W. C., Morse J. G. and Baxter J. F. (1985) Radon-222 and ^{222}Rn progeny concentrations measured in an energy-efficient house equipped with a heat exchanger. *Health Phys.* **49**, 267-277.

Nazaroff W. W. (1992) Radon transport from soil to air. *Rev. Geophys.* **30**, 137-160.

Nazaroff W. W., Moed B. A. and Sextro R. G. (1988) Soil as a source of indoor radon: Generation, migration, and entry. In Nazaroff W. W. and Nero A. V. (Ed.) *Radon and Its Decay Products in Indoor Air*, John Wiley and Sons, New York, 57-112.

Robinson A. L. and Sextro R. G. (1995) The influence of a subslab gravel layer and open area on soil-gas and radon entry into two experimental basements. *Health Phys.* **69**, 367-377.

Schery S. D., Gaeddert D. H. and Wilkening M. H. (1984) Factors affecting exhalation of radon from a gravelly sandy loam. *J. Geophys. Res.* **89**, 7299-7309.

Scott A. G. (1988) Preventing radon entry. In Nazaroff W. W. and Nero A. V. (Ed.) *Radon and Its Decay Products in Indoor Air*, John Wiley and Sons, New York, N.Y., 407-433.

Thomas J. W. and Countess R. J. (1979) Continuous radon monitor. *Health Phys.* **36**, 734-738.

Tsang Y. W. and Narasimhan T. N. (1992) Effects of periodic atmospheric pressure variation on radon entry into buildings. *J. Geophys. Res.* **97**, 9161-9170.

Turk B. H., Prill R. J., Sextro R. G. and Harrison J. (1989) Intensive radon mitigation research: lessons learned. The 1988 International Symposium on Radon and Radon Reduction Technology. U.S. Environmental Protection Agency, Air and Energy Environmental Research Laboratory, Research Triangle Park NC 27711.

Table 5.1. Measured soil and gravel permeability at the structure site. Appendix A describes in more detail the results of soil permeability measurements made at the experimental site.

Soil Region	Permeability (m^2)
undisturbed[a]	3.0×10^{-11} (h) ; 1.8×10^{-11} (v)
backfill[b]	3.5×10^{-12}
gravel[c]	2.0×10^{-8}

[a] Horizontal permeability (h) based on measured permeability at 3.5-m length scale; vertical permeability (v) based on measured ratio of vertical to horizontal permeability (Garbesi et al., 1996).

[b] The average of single-point measurements taken around the basement structure (Garbesi et al., 1993).

[c] Based on laboratory measurements using a vertical column filled with a sample of the gravel used below the basement structure (Fisk et al., 1992)

Table 5.2. Measured air-filled porosity, emanation fraction, and radium content of soil at the structure site. Appendix A describes in more detail the results of porosity measurements made at the experimental site.

Depth of Layer (m)	Soil-grain density[a] (kg m^{-3})	Radium content[b] (Bq kg^{-1})	Air-filled porosity	Emanation fraction[b]
0 - 1.6	2.80×10^3	30	0.45[c]	0.31
1.6 - 2.2	2.80×10^3	30	Approximately linear decrease from 0.45 to 0.25[c]	0.45
2.2 - 5	2.80×10^3	30	0.25[c]	0.31
5.0 - 8.5	2.80×10^3	30	0.25 (inferred)[d]	0.31

[a] (Brimhall and Lewis, 1992)

[b] (Flexser et al., 1993)

[c] Based on gravimetric analysis (Danielson and Sutherland, 1986) of soil cores taken by Flexser et al. (1993).

[d] We have extrapolated the measured profile to 8.5 m, the measured depth of the water table below the soil surface.

Table 5.3 Time-averages of soil-gas flow and radon entry measurements shown in Figs. 5.3-5.5.

Fig.	$Q_{SS}(\Delta P)$ (L min^{-1})	ΔP (Pa)	Volume of Gas In (L)	Volume of Gas Out (L)	Average Advective Rn Entry Rate (Bq s^{-1})	No-Dilution Rn Entry Rate (Bq s^{-1})	Indoor Rn (Bq m^{-3})
5.3	0	0	32	30	0.23	0.43	2600
5.4	0.3	0.9	15	52	0.02	0.21	1800
5.5	-0.3	-0.9	55	19	0.58	0.74	4900

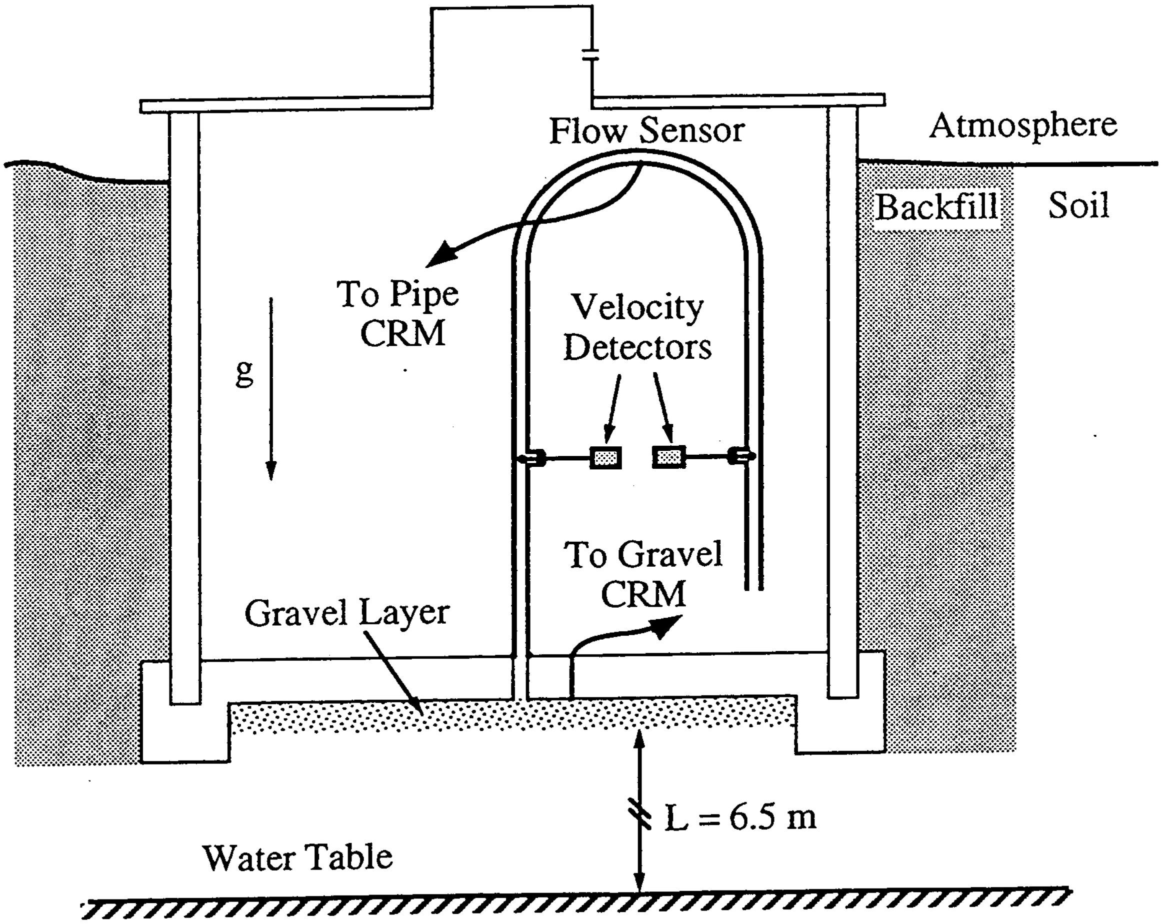

Fig. 5.1 Schematic of experimental structure and flow sensor. The figure is not drawn to scale.

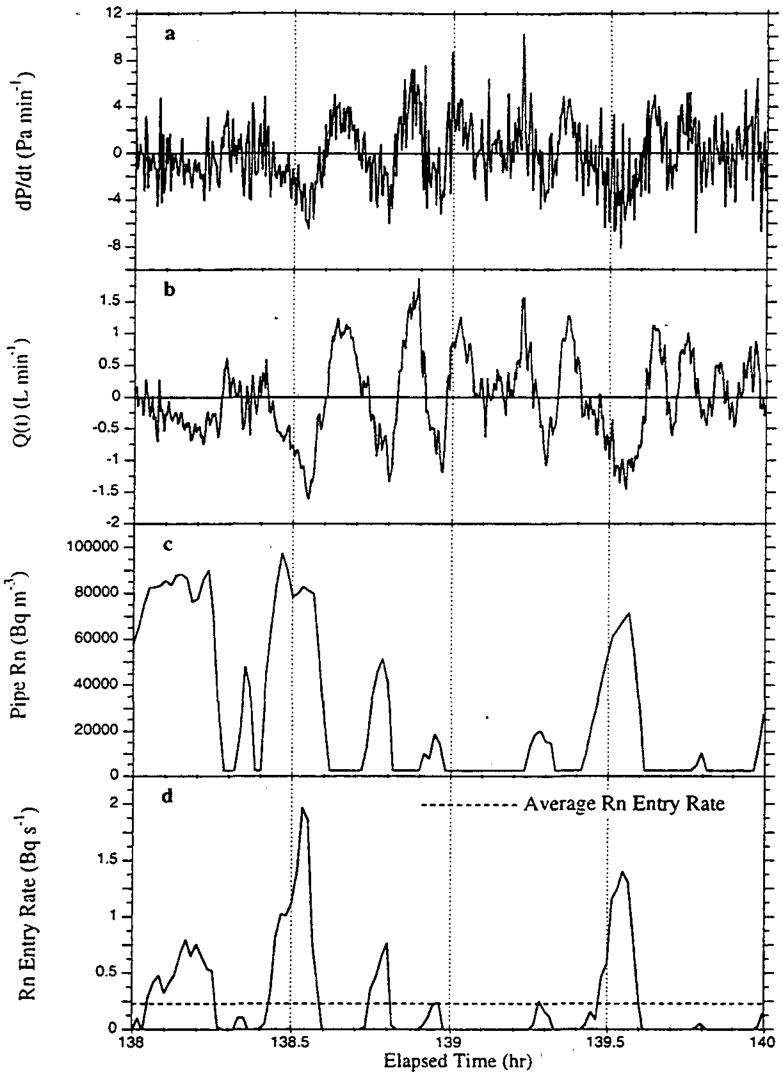

Fig. 5.2 Time series measurements made during neutral pressure conditions (no steady indoor-outdoor pressure difference): (a) time-rate-of-change of atmospheric pressure, (b) measured gas flow rate, (c) measured radon concentration in U-shaped pipe, and (d) calculated radon entry rate.

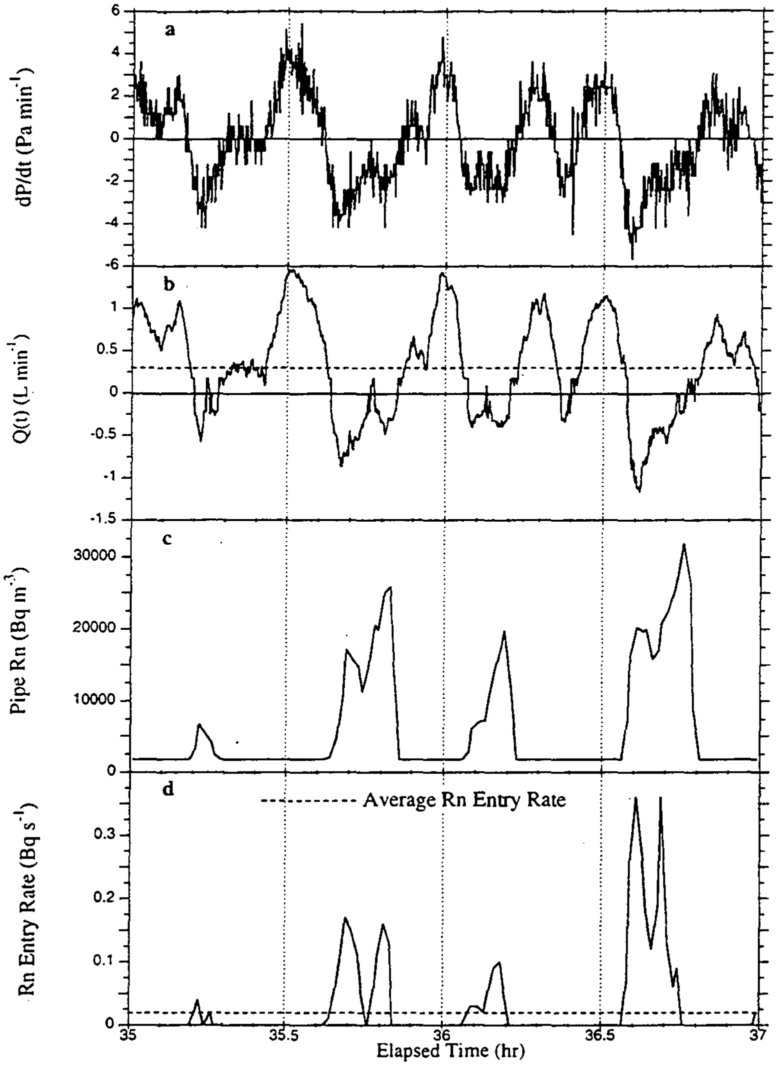

Fig. 5.3 Time series measurements made during a period when the interior of the structure was steadily pressurized 0.9 Pa relative to the ambient atmosphere: (a) time-rate-of-change of atmospheric pressure, (b) measured gas flow rate, (c) measured radon concentration in U-shaped pipe, and (d) calculated radon entry rate. The dashed line shown in (b) indicates the estimated gas flow rate out of the structure caused by a 0.9 Pa steady indoor-outdoor pressure difference.

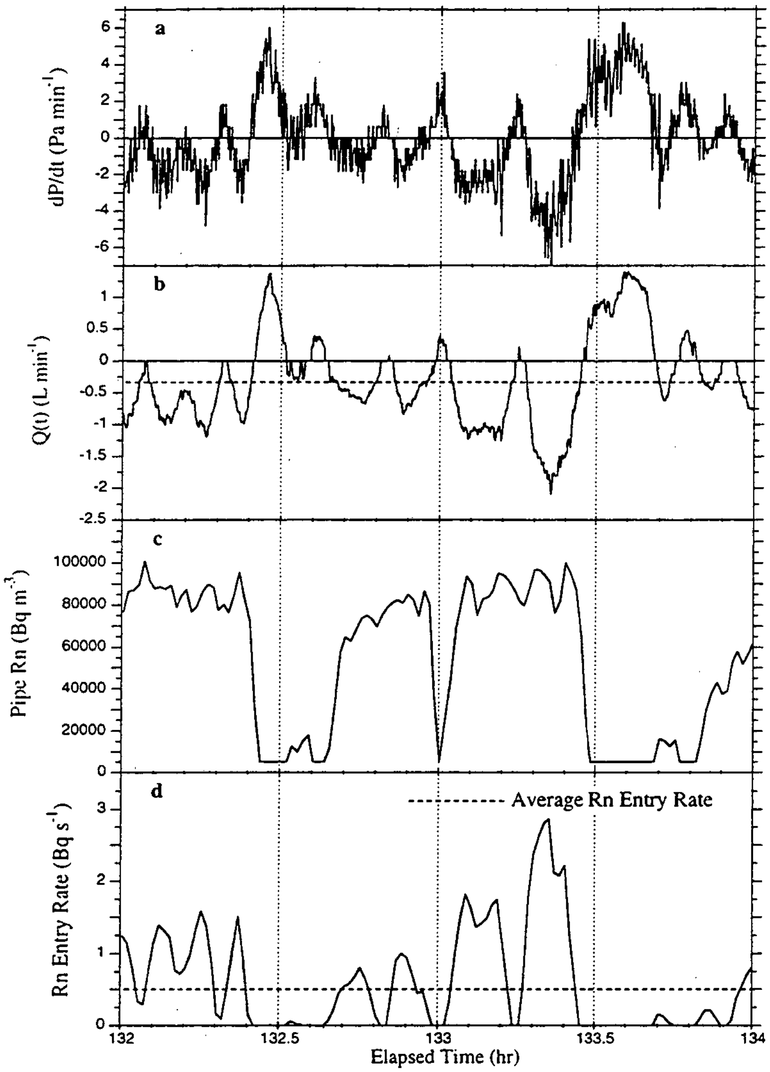

Fig. 5.4 Time series measurements made during a period when the interior of the structure was steadily depressurized 0.9 Pa relative to the ambient atmosphere: (a) time-rate-of-change of atmospheric pressure, (b) measured gas flow rate, (c) measured radon concentration in U-shaped pipe, and (d) calculated radon entry rate. The dashed line shown in (b) indicates the estimated soil-gas entry rate into the structure caused by a -0.9 Pa steady indoor-outdoor pressure difference (the negative sign indicates structure depressurized relative to atmosphere).

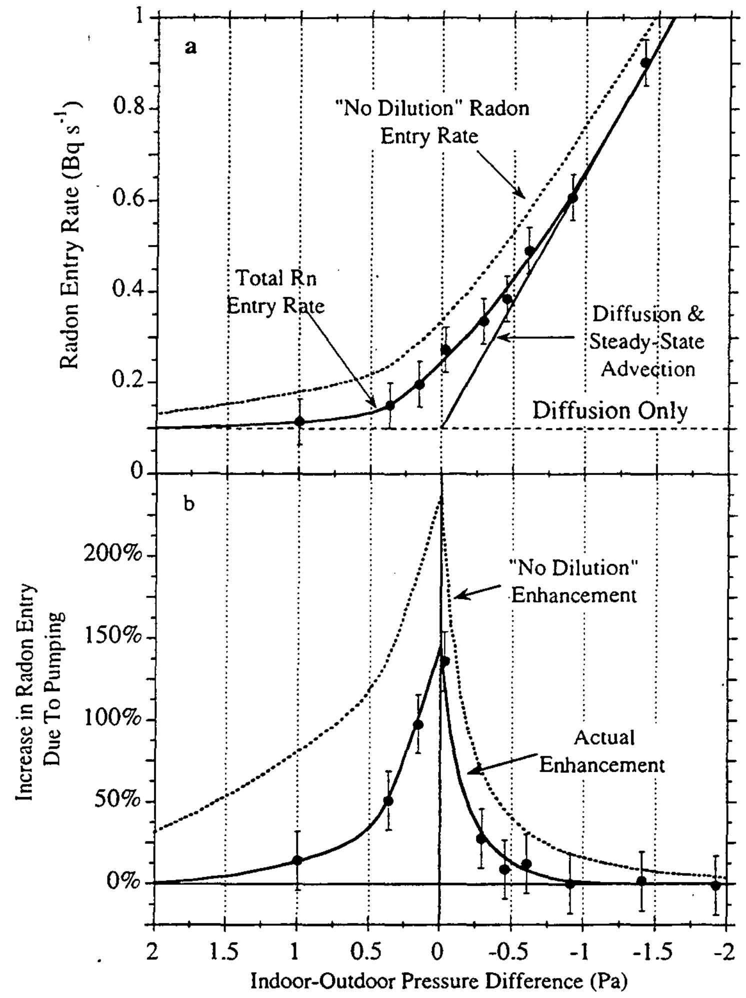

Fig. 5.5 (a) The total long-term-average radon entry rate as a function of steady indoor-outdoor pressure difference; (b) Enhancement of long-term radon entry rate due to atmospheric pressure fluctuations. An enhancement of 100% indicates that atmospheric pressure fluctuations drive the same amount of radon entry as both diffusion and indoor-outdoor pressure differences. In other words, such fluctuations increase the long-term radon entry rate by a factor of 2. Negative indoor-outdoor pressure indicates that the interior of the structure is depressurized relative to the ambient atmosphere. Radon entry under steady depressurization conditions is estimated based on the resistance of the soil-structure system, as described in the text. Only diffusion and atmospheric pressure fluctuations drive radon entry when the indoor-outdoor pressure difference is greater than or equal to zero.

Chapter 6

HOW IMPORTANT IS RADON ENTRY DRIVEN BY ATMOSPHERIC PRESSURE FLUCTUATIONS?

ABSTRACT

Atmospheric pressure fluctuations draw radon-laden soil gas into houses without requiring the indoor-outdoor pressure differences commonly associated with advective radon entry. To investigate the influence of soil properties, water-table depth, and a high-permeability subslab gravel layer on this phenomenon, we employ a model to estimate an upper bound on the contribution of these fluctuations to the long-term radon entry rate into a prototypical basement. The model combines results from numerical simulations of soil-gas flow with analytical expressions for the soil-gas radon concentration. The model accounts for entry driven by diffusion, steady indoor-outdoor pressure differences, and atmospheric pressure fluctuations. Under neutral indoor-outdoor pressure conditions, atmospheric pressure fluctuations can increase the radon entry rate into a basement built at a site with a high permeability soil by as much as factor of 5. However, neutral pressure conditions are relatively rare. Typical long-term indoor-outdoor pressure differences range from -1 to -5 Pa depending on the season. Accounting for these pressure differences, atmospheric pressure fluctuations typically cause between 20% and 50% of the long-term radon entry

rate at sites with a soil permeability less than $k = 10^{-11}$ m^2. Atmospheric pressure fluctuations generate the largest component (up to 50%) of the long-term radon entry rate at sites with a soil permeability of 10^{-12} m^2. However, the total magnitude of the long-term radon entry driven by atmospheric pressure fluctuations is comparable to that caused by diffusion.

INTRODUCTION

Atmospheric pressure fluctuations drive advective transport of radon-laden soil gas into houses. Measurements reported in Chapter 5 indicate that under neutral pressure conditions these fluctuations produce 1.5 times more radon entry than diffusion into an experimental basement. However, steady indoor-outdoor pressure differences dramatically diminish the relative contribution of atmospheric pressure fluctuations to the long-term radon entry rate. When the magnitude of the indoor-outdoor pressure difference is greater than 1.5 Pa, atmospheric pressure fluctuations have essentially no effect on the long-term radon entry rate into the experimental structure.

The measurements reported in Chapter 5 provide important experimental evidence for advective radon entry driven by atmospheric pressure fluctuations. However, these results only apply to one combination of soil properties and basement configuration. The theoretical analysis described in Chapter 4 indicates that changes in soil properties, water-table depth, and subslab permeability can dramatically affect the soil-gas entry rate caused by atmospheric pressure fluctuations. Therefore, the effect of all these factors must be examined in order to assess the importance of radon entry driven by atmospheric pressure fluctuations.

In this chapter, a model is developed to quantify the importance of atmospheric pressure fluctuations as a mechanism for driving radon entry. The model accounts for entry driven by diffusion, steady indoor-outdoor pressure differences, and atmospheric pressure fluctuations. Using this model, we conduct a parametric investigation into the influence of soil properties, water-table depth, and a high-permeability subslab gravel layer on radon entry driven by atmospheric pressure fluctuations.

The model ignores the effect of soil-gas dilution on the radon entry rate. Rising atmospheric pressure drives low concentration indoor air into the soil. This flow dilutes the soil-gas radon concentration immediately underneath the slab which, in turn, reduces the concentration of the soil gas advected into the basement. By ignoring this dilution, the predictions of the model are an upper bound on contribution of atmospheric pressure fluctuations to the long-term radon entry rate. Measurements described in Chapter 5 indicate that dilution reduces the contribution of atmospheric pressure fluctuations to the long-term radon entry rate by a factor of ~2.

To estimate the long-term rate entry, we must quantify typical indoor-outdoor pressure differences. These pressure differences drive advective radon entry, and reduce the contribution of atmospheric pressure fluctuations to the long-term radon entry rate. In this chapter, we employ a simplified version of the LBL infiltration model (Sherman, 1980) to estimate typical seasonal and annual average indoor-outdoor pressure differences for a prototypical house located in four different cities.

The chapter concludes with a brief discussion of the relationship between radon entry rate, building ventilation rate, and indoor radon concentration. Since the health risks associated with human exposure to indoor radon depends on long-term indoor concentrations, the importance of different mechanisms that drive radon entry must ultimately be evaluated based on the basis of their impact on these long-term concentrations.

METHODS

House Substructure and Soil Properties

The geometry of the model basement used for this study is identical to the one used for the analysis of soil-gas entry described in Chapter 4. By employing the same geometry, we ensure that the results reported here are directly comparable to those described in Chapter 4.

Fig. 6.1 shows a schematic of the model basement shell and the surrounding soil. As Fig. 6.1a indicates, we have defined our prototypical basement as a cylinder surrounded by a cylindrical soil block. Although real houses have rectangular basements, we expect that the results of this study are directly applicable to real houses. Revzan et al. (1991) compared predictions of steady-state radon entry using a cylindrical model with those generated with a three-dimensional Cartesian model and found no significant discrepancy for houses which are symmetric in the vertical plane.

Advective radon entry only occurs through a 1-cm-wide gap around the edge of the slab floor. Such an opening simulates the shrinkage gap that can develop at the floor-wall joint located at the perimeter of the poured concrete floor in real houses. Although the opening considered in this study is wider than the shrinkage gap found in typical houses (Scott, 1988), we have used this opening size to eliminate crack resistance from the problem, which permits a focused analysis into the influence of soil properties on advective radon entry.

Diffusive entry occurs through both the concrete walls and floor of the basement. This entry arises from radon generated in both the concrete and the soil. The values of the soil and concrete properties used to evaluate the diffusive entry rate and the radon concentration in the soil and the concrete are listed in Table 6.1. These values represent a typical concrete and soil (Nazaroff, 1992).

Two different sets of simulations were run to examine the sensitivity of the advective radon entry rate to changes in soil permeability, air-filled porosity, and water-table depth. As Fig. 6.1b indicates, the water-table depth is the vertical distance between the basement floor and the water table, bedrock, or some other impermeable layer. Table 6.2 lists the values of these parameters used for each set of simulations. These values reflect the range of soils in which houses are commonly found (Nazaroff, 1992). For the first set of simulations, we have assumed a homogeneous soil block. For the second set, we have included a high permeability subslab gravel layer. A subslab gravel layer is a common construction practice in many areas as a means of preventing the concrete floor slab from coming into contact with wet soil. As the results reported in Chapters 2 and 4 indicate, a high permeability subslab gravel layer can significantly increase soil-gas and radon entry into a basement. We assigned the gravel layer an air-filled porosity of 0.3, and a permeability of 10^{-8} m^2.

Model for Calculating Radon Entry

This section describes a theoretical model used to predict the radon entry rate into a basement. The model accounts for diffusive entry through the basement walls and floor, and advective entry through a 1-cm-wide perimeter gap. Both steady indoor-outdoor pressure differences and atmospheric pressure fluctuations drive advective radon entry.

For this analysis, we assume that the soil-gas radon concentration field around the basement only depends on radon generation and diffusion. Under certain circumstances, advective soil-gas flow can reduce the soil-gas radon concentration. This dilution reduces the radon entry rate into the basement by 1) changing the concentration gradients which drive diffusive entry, and 2) reducing the radon concentration of the soil-gas advected into the structure. Consequently, by ignoring the effects of advective soil-gas flow on the radon concentration field, our model estimates an upper bound on the radon entry rate.

Chapter 5 examines the effects of soil-gas dilution caused by atmospheric pressure fluctuations on the long-term radon entry rate. Under neutral pressure conditions, rising atmospheric pressure forces low concentration indoor air into the soil. This flow dilutes the radon concentration of the soil-gas immediately underneath a basement floor slab. This dilution reduces the contribution of atmospheric pressure fluctuations to the long-term radon entry rate into an experimental basement by a factor of ~2. Soil-gas dilution also shrinks the range of indoor-outdoor pressure differences over which atmospheric pressure fluctuations contribute to the long-term radon entry rate. For houses built in permeable soils ($k > 10^{-11}$ m^2), soil-gas flow created by large, steady indoor-outdoor pressure differences (Nazaroff and Sextro, 1989; Loureiro et al., 1990) and wind interaction with a building superstructure (Riley et al., 1996) can also dilute the soil-gas radon concentration.

The instantaneous radon entry rate, $S_T(t)$ (Bq s^{-1}), into the basement can be expressed as

$$S_T(t) = S_D + S_A(t, \Delta P) \tag{6.1}$$

Diffusive entry, S_D (Bq s^{-1}), is assumed to be steady and independent of the advective radon entry. Advective radon entry, $S_A(t,\Delta P)$ (Bq s^{-1}), is driven by steady indoor-outdoor pressure differences and atmospheric pressure fluctuations. Since the health risks associated with human exposure to indoor radon depends on long-term indoor concentrations, we time-average the instantaneous radon entry rate, $S_T(t)$, to quantify the importance of radon entry driven by atmospheric pressure fluctuations. We refer to this time-averaged radon entry rate as the long-term radon entry rate. To estimate the long-term radon entry rate we employ seasonal and annual average indoor-outdoor pressure differences, and 112 days of atmospheric pressure data.

Estimating the Soil-Gas Radon Concentration Field

This section describes a model to estimate the soil-gas radon concentration field around a basement. The soil-gas radon concentration field only depends on radon generation and diffusion. To estimate the radon concentration field, we divide the soil around a basement into two regions. As shown in Fig. 6.2, Region 1 includes the basement floor slab and the underlying soil; Region 2 consists of the soil adjacent to the basement walls. In each of these regions we assume: 1) the soil is homogeneous, 2) radon transport through soil only occurs in the vertical direction, 3) radon migrates solely by diffusion, and 3) the radon concentration field is steady. Under these conditions, the soil-gas radon concentration obeys the steady-state, one-dimensional radon diffusion equation (Nazaroff et al., 1988),

$$D_e \frac{\partial^2 I}{\partial z^2} - \lambda I + G = 0 \tag{6.2}$$

where D_e is the interstitial diffusivity of radon ($m^2\ s^{-1}$), λ is the radioactive decay constant of radon (s^{-1}), and I is the activity concentration of radon (Bq m^{-3}). G (Bq $m^{-3}\ s^{-1}$) is the radon generation rate,

$$G = \rho f A_{Ra} \lambda \frac{(1-\varepsilon)}{\varepsilon} \tag{6.3}$$

where ρ is the soil-grain density (kg m^{-3}), f is the emanation fraction (-), A_{Ra} is the radium content of the soil (Bq kg^{-1}), and ε is the air-filled porosity (-).

The soil-gas radon concentration field in region 1, $I_1(z)$, is determined by solving eqn. (6.2) with the following boundary conditions: $I(z=0)=0$ (z = 0 is the soil surface); and $\lim_{z \to \infty} I(z) = I_\infty$.

$$I_1(z) = I_\infty \left(1 - \exp\left(\frac{-z}{\Gamma}\right)\right) \tag{6.4}$$

where I_∞ is the deep soil radon concentration, $I_\infty = G/\lambda$, and Γ is the diffusion length of radon in the soil (m), $\Gamma = \sqrt{\frac{D_e}{\lambda}}$.

Region 2 consists of a concrete slab resting on top of an unbounded column of soil. In this region, radon is generated and diffuses through the concrete slab and the underlying soil. The concrete slab is assumed to have different properties than the soil. The thickness of the concrete slab is T. We estimate the radon concentration field in region 2, $I_2(z)$, by solving eqn. (6.2) with the following boundary conditions: $I(z=-T)=0$ (z = -T is the inside edge of the concrete slab); and $\lim_{z\to\infty} I(z) = I_\infty$. For region 2, z = 0 is defined as the interface between the concrete slab and the underlying soil.

$$I_2(z) = \frac{1}{\lambda}\left\{G_c\left[1-\cosh\left(\frac{T+z}{\Gamma_c}\right)\right]+B\sinh\left(\frac{T+z}{\Gamma_c}\right)\right\} \qquad \text{for } -T \le z \le 0 \quad (6.5a)$$

$$I_2(z) = \frac{G}{\lambda}\left[1-A\exp\left(\frac{-z}{\Gamma}\right)\right] \qquad \text{for } 0 \le z \le \infty \quad (6.5b)$$

where,

$$A = \frac{\varepsilon_c\Gamma_c}{\varepsilon\Gamma G}\left\{B\cosh\left(\frac{T}{\Gamma_c}\right)-G_c\sinh\left(\frac{T}{\Gamma_c}\right)\right\} \qquad (6.5c)$$

$$B = \frac{G+G_c\left\{\frac{\varepsilon_c\Gamma_c}{\varepsilon\Gamma}\sinh\left(\frac{T}{\Gamma_c}\right)+\cosh\left(\frac{T}{\Gamma_c}\right)-1\right\}}{\frac{\varepsilon_c\Gamma_c}{\varepsilon\Gamma}\cosh\left(\frac{T}{\Gamma_c}\right)+\sinh\left(\frac{T}{\Gamma_c}\right)}. \qquad (6.5d)$$

Eqn. (6.5a) gives the radon concentration in the concrete slab, and eqn. (6.5b) gives the soil-gas radon concentration underneath the floor slab. The subscript "c" denotes the properties of the concrete: ε_c is the air-filled porosity of the concrete (-), Γ_c is the diffusion length of radon in concrete (m), G_c is the radon generation rate in the concrete (Bq m^{-3} s^{-1}).

Using eqn. (6.5) we estimate the undisturbed soil-gas radon concentration immediately underneath the concrete floor slab, I_u. This is assumed to be the radon concentration of the soil-gas advected into the basement.

$$I_u = I_2(z=0) = \frac{1}{\lambda}\left\{G_c\left[1-\cosh\left(\frac{T}{\Gamma_c}\right)+B\sinh\left(\frac{T}{\Gamma_c}\right)\right]\right\} \qquad (6.6)$$

Diffusive Radon Entry

Radon can enter a building by diffusion through the walls and floor of the basement. The diffusive entry rate is determined by Fick's law and the radon concentration inside the concrete walls and floor of the basement.

To estimate the diffusive flux through the basement walls, we assume that the diffusive transport of radon through the walls does not affect the soil-gas radon concentration. This assumption is based on the diffusivity of radon in common soils being two orders of magnitude larger than the diffusivity of radon in common concretes (Nazaroff, 1992). Therefore, we can decouple the radon concentration of the soil gas adjacent to the basement walls to the radon flux through the walls. The soil-gas radon concentration is assumed to vary only with depth, while the radon flux through the concrete wall is approximated as one-dimensional in the horizontal direction. To estimate radon flux at the inside edge of the concrete wall, we first solve for the radon concentration profile in the wall. This profile is approximated by solving eqn. (6.2) with the following boundary conditions: $I(x = 0) = I_1(z)$ ($I(x=0)$ is the outside edge of the wall), and $I(x = -T) = 0$ ($x = -T$ is the inside edge of the wall).

$$I_w(x) = \frac{1}{\lambda}\left\{ G_c\left[1 - \cosh\left(\frac{x+T}{\Gamma_c}\right)\right] + \frac{\lambda I_1(z) + G_c\left[\cosh\left(\frac{T}{\Gamma_c}\right) - 1\right]}{\sinh\left(\frac{T}{\Gamma_c}\right)} \sinh\left(\frac{x+T}{\Gamma_c}\right)\right\} \quad (6.7)$$

Using eqn. (6.7) and Fick's law we estimate the diffusive flux through the concrete wall as a function of depth,

$$J^d_{\text{wall}}(z) = \frac{\varepsilon_c \Gamma_c}{\sinh\left(\frac{T}{\Gamma_c}\right)}\left\{ G_c\left[1 - \cosh\left(\frac{T}{\Gamma_c}\right)\right] - \lambda I_1(z)\right\} \quad (6.8)$$

Finally, combining eqn. (6.8) and (6.4) we calculate an average diffusive flux through the walls,

$$\bar{J}^d_{\text{wall}} = \frac{1}{d}\int_0^d \frac{\varepsilon_c \Gamma_c}{\sinh\left(\frac{T}{\Gamma_c}\right)}\left\{ G_c\left[1 - \cosh\left(\frac{T}{\Gamma_c}\right)\right] - G\left[1 - \exp\left(\frac{z}{\Gamma}\right)\right]\right\} dz \quad (6.9)$$

where d is the depth of the basement below the soil surface (m).

The diffusive flux at the inside edge of the floor slab can be derived from eqn. (6.5a) (Nazaroff, 1988)

$$J_{\mathrm{slab}}^{d} = \frac{\Gamma_c \varepsilon_c G_c \left[\frac{\Gamma_c \varepsilon_c}{\Gamma \varepsilon} \sinh\left(\frac{T}{\Gamma_c}\right) + \cosh\left(\frac{T}{\Gamma_c}\right) - 1 \right]}{\sinh\left(\frac{T}{\Gamma_c}\right) + \frac{\Gamma_c \varepsilon_c}{\Gamma \varepsilon} \cosh\left(\frac{T}{\Gamma_c}\right)} + \frac{\Gamma \varepsilon G}{\frac{\Gamma \varepsilon}{\Gamma_c \varepsilon_c} \sinh\left(\frac{T}{\Gamma_c}\right) + \cosh\left(\frac{T}{\Gamma_c}\right)} \tag{6.10}$$

Using eqns. (6.9) and (6.10) we estimate the diffusive entry rate into the basement,

$$S_D = A_{\mathrm{wall}} J_{\mathrm{wall}}^{d} + A_{\mathrm{slab}} J_{\mathrm{slab}}^{d} \tag{6.11}$$

where A_{wall} is the surface area of the wall (m^2), and A_{slab} is the surface area of the floor slab (m^2). The value of S_D for the different combinations of soil properties considered in this study are listed in Table 6.2.

Advective Radon Entry

We employ the finite-element model described in Chapters 3 and 4 to predict the transient flow of radon-laden soil gas into the basement. The finite-element model determines the magnitude of the flow. Eqn. (6.6) determines the radon concentration of the soil gas drawn into the basement.

Using the principle of superposition, we divide the total gas flow rate into the basement into a component caused by atmospheric pressure fluctuations and one driven by steady indoor-outdoor pressure differences,

$$Q(t,\Delta P)=Q_S(\Delta P)+Q_{APF}(t). \tag{6.12}$$

$Q_S(\Delta P)$ is the component of the total flow caused by steady indoor-outdoor pressure differences ($m^3\ s^{-1}$), and $Q_{APF}(t)$ is the component caused by atmospheric pressure fluctuations ($m^3\ s^{-1}$).

We employ the finite-element model described in Chapters 3 and 4 to evaluate $Q_S(\Delta P)$. The model was used to calculate the resistance of the soil to soil-gas entry driven by steady indoor-outdoor pressure differences. To determine this resistance, we simulated the soil-gas entry rate caused by a 1 Pa steady indoor-outdoor pressure difference. The inverse of this entry rate defines the resistance of the soil to steady-state soil-gas entry. Since the equations which govern soil-gas flow are linear, this resistance defines the soil-gas entry rate caused by any steady indoor-outdoor pressure difference.

$$Q_S(\Delta P)=\frac{\Delta P}{R} \tag{6.13}$$

where R is the resistance of the soil to steady-state soil-gas entry ($Pa\ s\ m^{-3}$), and ΔP is the magnitude of the steady indoor-outdoor pressure difference. Table 6.2 lists the values of R for each combination of soil properties.

To estimate the component of the total soil-gas flow rate caused by atmospheric pressure fluctuations, we employ the finite-element model to simulate the step-response function. The step-response function is the soil-gas entry rate caused by a unit-step change in atmospheric pressure (see Chapters 3 and 4 for more details on the simulation of a step-response function). Using the step-response function, Q_{step} ($m^3\ s^{-1}\ Pa^{-1}$), and Duhamel's Theorem (Carslaw and Jaeger, 1959) we calculate the gas flow rate into and out of the basement caused by any atmospheric pressure fluctuations.

$$Q_{APF}(t) = \int_{-\infty}^{t} Q_{step}(t-\theta)\, P'_{atm}(\theta)\, d\theta \qquad (6.14)$$

where P'_{atm} is the time-rate-of-change of atmospheric pressure (Pa s^{-1}), and θ is a dummy variable indicating integration over time (s).

Once we have determined the gas flow rate into and out the basement, the advective radon entry is defined by

$$S_A(t,\Delta P) = I_u Q(t,\Delta P) \quad \text{if } Q > 0 \text{ (soil gas flows into the basement)} \qquad (6.15a)$$

$$S_A(t,\Delta P) = 0 \quad \text{if } Q < 0 \text{ (indoor air flows into the soil)} \qquad (6.15b)$$

where I_u is the undisturbed radon concentration of soil gas immediately underneath the basement floor (Bq m^{-3}), Q is the gas flow rate into and out of the basement ($m^3\ s^{-1}$). Gas flow out of the basement does not transport any radon because indoor radon concentrations are generally several orders of magnitude less than the undisturbed soil-gas radon concentration, I_u.

Theoretical Evaluation of Indoor-Outdoor Pressure Differences

A simplified version of the LBL infiltration model (Sherman, 1980) is used to calculate indoor-outdoor pressure differences. The indoor-outdoor pressure at the level of the basement floor, ΔP_f, is commonly associated with the advective entry of soil gas into buildings. The model considers the contribution of wind and the stack effect to this pressure difference,

$$\Delta P_f = \Delta P_w + \Delta P_s \tag{6.16}$$

The term ΔP_s is the stack, i.e. temperature, induced indoor-outdoor pressure difference at the floor level

$$\Delta P_s = \rho_a g \Delta h \frac{(T_{out} - T_{in})}{T_{in}} \tag{6.17}$$

where ρ_a is the density of air (kg m^{-3}), g is the gravitational acceleration (m s^{-2}), Δh is the distance between the basement floor and the neutral pressure level (m), T_{in} is the indoor temperature (K), and T_{out} is the outdoor temperature (K). The neutral pressure level is the height at which the indoor and outdoor pressure are equal.

The term ΔP_w is the wind-induced indoor-outdoor pressure difference,

$$\Delta P_w = C_p \frac{1}{2} \rho_a v^2 \tag{6.18}$$

where C_p is the pressure coefficient (-), and v is the wind velocity (m s^{-1}). The pressure coefficient depends on the building geometry, orientation, shielding, and distribution of leakage area. Table 6.3 lists the values of the parameters used to evaluate ΔP_f. For this analysis, we have assumed that the only depressurizes the interior of the structure; we are ignoring the effect of ground-surface pressures created by wind interaction with the building super-structure (Riley et al., 1996).

Meteorological Data

Two sources of meteorological data are used as inputs for the analysis described in this chapter. First, 112 days of atmospheric pressure measurements collected during the experiments described in Chapters 3 and 5 are analyzed using eqn. (6.14) to estimate the gas flow rate into and out of the basement driven by atmospheric pressure fluctuations. These measurements were made at 5-s intervals. The time-rate-of-change of atmospheric pressure is estimated using a central-difference scheme. Second, outdoor temperature and wind speed data from the Typical Meteorological Year data base (NOAA, 1981) are analyzed using eqns. (6.17) and (6.18) to estimate the seasonal variation of typical indoor-outdoor pressure differences. These data were collected at hourly intervals. We analyzed data from four cities, Newark NJ, Spokane WA, Tucson AZ, and Jacksonville FL. These cities were chosen from the four different census regions in order to illustrate the variation in indoor-outdoor pressure difference across the United States.

RESULTS AND DISCUSSION

An Upper Bound on Radon Entry

An estimate of the enhancement in the long-term radon entry rate caused by atmospheric pressure fluctuations is shown in Figs. 6.3 and 6.4. The word enhancement refers to the percent increase in the total radon entry rate due to atmospheric pressure fluctuations. For example, an enhancement of 100% indicates that atmospheric pressure fluctuations drive the same amount of radon entry as both diffusion and indoor-outdoor pressure differences. In other words, such fluctuations would increase the long-term radon entry rate by a factor of 2.

The largest enhancement in the long-term radon entry rate due to atmospheric pressure fluctuations occurs at neutral pressure conditions, that is, when there is no indoor-outdoor pressure difference. Under these conditions, Figs. 6.3 and 6.4 indicate that atmospheric pressure fluctuations can drive more than 5 times more entry than diffusion. Steady indoor-outdoor pressure differences reduce the contribution of atmospheric pressure fluctuations to the long-term radon entry rate by creating an offset in the soil-gas entry rate. This offset decreases the total volume of gas pumped into and out the structure by atmospheric pressure fluctuations --- the smaller this volume, the smaller the radon entry rate.

Fig. 6.3a indicates that the contribution of atmospheric pressure fluctuations to the long-term radon entry rate depends strongly on the permeability of the soil. At neutral pressure conditions, atmospheric pressure fluctuations drive more radon entry into houses built in high permeability soils than low permeability soils. However, slight indoor-outdoor pressure differences dramatically alter the relationship between soil permeability and the contribution of atmospheric pressure fluctuations to the long-term radon entry rate. For houses located at sites with high permeability soils, Fig. 6.3a shows that these pressure differences dramatically reduce the contribution of atmospheric pressure fluctuations to the long-term radon entry rate. In contrast, sustained indoor-outdoor pressure differences have relatively little effect on radon entry driven by atmospheric pressure fluctuations into houses built on low-permeability soils.

The effect of changes in permeability on the long-term radon entry driven by atmospheric pressure fluctuations can be explained in terms of the relationship between permeability and soil-gas flow. Under neutral pressure conditions, the soil-gas entry rate depends only on the soil-gas response to atmospheric pressure fluctuations. As described in Chapter 4, this response depends strongly on the characteristic response time of the soil gas. High permeability soils have a short characteristic response time. A short response time maximizes the volume of soil-gas pumped into and of a basement by atmospheric pressure fluctuations. Low permeability soils have a long characteristic response time. A long characteristic response time attenuates the soil-gas entry rate caused by high-frequency fluctuations in atmospheric pressure. This attenuation reduces the total volume of soil-gas pumped into and out a basement.

In the presence of indoor-outdoor pressure differences, the magnitude of the soil-gas entry rate depends on both the magnitude of this pressure difference and the soil-gas response to changes in atmospheric pressure. Since soil-gas flow caused by steady indoor-outdoor pressure differences varies linearly with permeability, the larger the permeability of the soil the larger the offset in the soil-gas entry rate caused by a given indoor-outdoor pressure difference and the smaller the relative contribution of atmospheric pressure fluctuations to the long-term radon entry rate. When the offset in the soil-gas flow rate is greater than the largest soil-gas flowrate caused by atmospheric pressure fluctuations, then these fluctuations have no effect on the radon entry rate.

Fig. 6.3b indicates that changes in air-filled porosity have relatively little effect on the enhancement of the long-term radon entry rate caused by atmospheric pressure fluctuations. Based on the analysis of soil-gas flow described in Chapter 4, we had expected that the radon entry rate driven by atmospheric pressure fluctuations should increase almost linearly with porosity. However, eqn. (6.3) indicates that soil-gas radon concentration varies inversely with porosity. The results shown in Fig. 6.3b suggests that these two effects caused by changing porosity offset one another.

Increasing the distance between the basement and the water table (or some other impermeable layer) increases the contribution of atmospheric pressure fluctuations to the long-term radon entry rate. For example, Fig. 6.3c indicates that increasing water-table depth from 3 to 18 m more than doubles the contribution of atmospheric pressure fluctuations to the long-term radon entry rate. The effect of changes in water-table depth on radon entry driven by atmospheric pressure fluctuations can be explained in terms of their effect on soil-gas flow. A described in Chapter 4, increasing the water-table depth increases the volume soil gas pumped into and out of the basement by atmospheric pressure fluctuations.

The presence of a high permeability subslab gravel layer dramatically increases the radon entry rate driven by atmospheric pressure fluctuations. Fig. 6.3 shows results for a basement without a subslab gravel layer; Fig. 6.4 presents results for a basement with a high-permeability subslab gravel layer. A comparison of these figures reveals that for the basement configuration considered here, a high permeability subslab gravel layer increases the radon entry rate due to atmospheric pressure fluctuations by a factor of ~ 4. The presence or absence of a high permeability subslab gravel layer does not alter the relative relationship between radon entry driven by atmospheric pressure fluctuations and soil permeability, air-filled porosity, and water-table depth.

Typical Indoor-Outdoor Pressure Differences

As the results shown in Figs. 6.3 and 6.4 demonstrate, indoor-outdoor pressure differences can dramatically reduce the contribution of atmospheric pressure fluctuations to the long-term radon entry rate. Therefore, to assess the importance of these fluctuations as a mechanism for driving long-term radon entry, we must examine the magnitude of typical indoor-outdoor pressure differences. Table 6.4 summarizes calculations of indoor-outdoor pressure differences for Jacksonville FL, Newark NJ, Spokane WA, and Tucson AZ. We report seasonal averages because the health effects associated with human exposures to indoor radon are caused by long-term exposures. Seasonal averages quantify the potential of indoor-outdoor pressure differences for driving long-term radon entry.

The results shown in Table 6.4 indicate a strong seasonal variation in indoor-outdoor pressure differences. These values were determined by averaging hourly estimates of indoor-outdoor pressure difference. During the winter, average indoor-outdoor pressure differences range between -2 and -5 Pa, whereas during the summer these pressure differences fall within -1 and -2 Pa. The majority of this seasonal variation is caused by changes in the contribution of the stack effect to the total indoor-outdoor pressure difference. In the summer, when indoor-outdoor temperature differences are small, the stack effect contributes relatively little to total indoor-outdoor pressure differences. In the winter, the stack effect can substantially increase the total indoor-outdoor pressure difference, especially for houses built in cities with cold climates such as Newark and Spokane. Since indoor-outdoor pressure differences are generally smaller during the summer than the winter, the results shown in Figs. 6.3 and 6.4 suggest that atmospheric pressure fluctuations will produce a relatively larger fraction of the total radon entry rate during the summer than during the winter.

Table 6.4 also reveals some regional variation in typical indoor-outdoor pressure differences. As expected, Table 6.4 indicates that houses located in cities which experience cold winters, e.g. Spokane and Newark, have larger indoor-outdoor pressure differences during the winter than houses built in more temperate climates, e.g. Jacksonville and Tucson. This variation is due to relatively greater contribution of the stack effect to the total indoor-outdoor in colder climates. During the summer, temperature effects can pressurize the interior of the basement of an air-conditioned building located in an area with a hot climate such as Tucson and Jacksonville. Note that this analysis is based on a prototypical house with a basement, houses built in warm climates frequently do not have basements.

The estimates shown in Table 6.4 are consistent with the few reported measurements of long-term average indoor-outdoor pressure differences. Nazaroff et al. (1985) measured an average indoor-outdoor pressure difference of -3.7 Pa during the winter in a one-story house in Chicago. Time series of indoor-outdoor pressure differences measured in several houses in New Jersey exhibit large seasonal variation (Revzan et al., 1988; Revzan, 1989). In these houses indoor-outdoor pressure differences ranged between -2 and -6 Pa during the winter and 0 and -2 Pa during the summer.

This analysis did not consider the contribution of heating, ventilation and air conditioning (HVAC) systems to indoor-outdoor pressure differences. Field studies have shown that in some houses the operation of HVAC systems can significantly affect these pressure differences. Leaky return air ducts caused a forced-air furnace to depressurize the basement of a house in New Jersey by as much as 10 Pa (Turk et al., 1989). Operation of an air conditioner in a slab-on-grade house pressurized the interior of a house relative to the atmosphere (Kozik et al., 1992).

How Important is Radon Entry Driven By Atmospheric Pressure Fluctuations?

By combining the estimates of typical indoor-outdoor pressure differences with the radon entry results shown in Figs. 6.3 and 6.4, we can assess the importance of atmospheric pressure fluctuations as a mechanism for driving radon entry. For this analysis, we have chosen to focus on houses built in Jacksonville and Spokane. Of the four cities considered in our analysis of indoor-outdoor pressure differences, a house in Jacksonville has the smallest annual-average indoor-outdoor pressure difference, -1.9 Pa, and a house in Spokane experiences the largest, -3.5 Pa.

Table 6.5 and 6.6 summarizes predictions of the total long-term radon entry rate (annual time-averaged radon entry rate), and the fraction of this entry caused by atmospheric pressure fluctuations. Table 6.5 presents results for a house located in Spokane, and Table 6.6 shows results for a houses located in

Jacksonville. These results quantify the fraction of the long-term radon entry for the entire range of soil properties and water-table depths considered in this study.

Tables 6.5 and 6.6 indicate that atmospheric pressure fluctuations contribute the largest fraction of the long-term radon entry rate, as much as 51%, into buildings at sites with a soil permeability of 10^{-12} m^2. Fig. 6.5 indicates that at this permeability, the contribution of atmospheric pressure fluctuations to the long-term radon entry rate is maximized relative to the contribution of indoor-outdoor pressure differences. The highest total radon entry rate occurs at sites with high permeability soils, $k = 10^{-10}$ m^2. At these sites, atmospheric pressure fluctuations drive only 1 to 6% of the total long-term radon entry rate.

The fraction of the long-term radon entry driven by atmospheric pressure fluctuations increases almost linearly with increases in air-filled porosity. However, increasing the porosity while holding the other parameters constant reduces the total radon entry rate. As expected from our analysis of soil-gas entry described in Chapter 4, increasing the water-table depth linearly increases the fraction of the total radon entry rate driven by atmospheric pressure fluctuations. Changes in water-table depth affect radon entry produced by atmospheric pressure fluctuations, but have essentially no effect on entry caused by diffusion and indoor-outdoor pressure differences.

Atmospheric pressure fluctuations drive a much larger fraction of the long-term radon entry into houses with a high-permeability subslab gravel layer in comparison to houses without such a gravel layer. The results in Tables 6.5 and 6.6 suggest that the addition of a subslab gravel layer increases the fraction of the long-term radon entry driven by atmospheric pressure fluctuations typically by a factor of 2 to 3.

To help put the results shown in Tables 6.5 and 6.6 in perspective, Figs. 6.5-6.6 show the contribution of diffusion, indoor-outdoor pressure differences, and atmospheric pressure fluctuations to the total radon entry rate. Fig. 6.5 shows predictions for a house in Spokane, and Fig. 6.6 presents results for a house in Jacksonville. These figures indicate that for a house with a subslab gravel layer atmospheric pressure fluctuations drive essentially the same amount of radon entry as diffusion. For a house without a gravel layer, these fluctuations cause less radon entry than diffusion.

Indoor Radon Concentration

Ultimately the importance of atmospheric pressure fluctuations as a mechanism for driving radon entry must be judged in terms of its impact on indoor radon concentration. Since indoor radon concentrations depend on both the radon entry rate and the building ventilation rate, we can draw an important distinction between advective entry caused by atmospheric pressure fluctuations and advective entry driven by indoor-outdoor pressure differences. Atmospheric pressure fluctuations drive advective radon entry but do not affect building ventilation rates. Therefore, under steady-state conditions, doubling entry driven by atmospheric pressure fluctuations will double indoor radon concentrations for a given building ventilation rate. In contrast, indoor-outdoor pressure differences drive both radon entry and building ventilation. Consequently, the effect of increases in entry driven by these pressure differences on indoor radon concentrations are partially offset by increases in building ventilation rate (Nazaroff et al., 1988).

We employ a simple steady-state mass balance to examine the contribution of atmospheric pressure fluctuations to long-term indoor radon concentrations, I (Bq m^{-3}),

$$I = \frac{S}{V \lambda_v} \tag{6.19}$$

where S is the long-term-average radon entry rate (Bq s^{-1}), V is the volume of the interior of the building (m^3), and λ_v is the building ventilation rate (s^{-1}). Eqn. (6.19) ignores the effect of radon decay and assumes that the interior of the house is well-mixed. Using eqn. (6.19) we can estimate the average radon entry rate required to maintain a house at the geometric mean of US indoor radon concentrations, ~35 Bq m^{-3} (Marcinowski et al., 1994). Assuming a building ventilation rate of 1 hr^{-1} and an interior volume of 200 m^3, eqn. (6.19) indicates that an average radon entry rate of ~2 Bq s^{-1} is required to create an long-term indoor radon concentration of 35 Bq m^{-3}. This estimate indicates the magnitude of the radon entry rate into a typical house. Figs. 6.5 and 6.6 indicate that atmospheric pressure fluctuations contribute at most 1 Bq s^{-1} to the long-term radon entry rate. Therefore, we can conclude that radon entry driven by atmospheric pressure fluctuations will not results in houses with greatly elevated indoor radon concentrations.

CONCLUSIONS

Under neutral pressure conditions, atmospheric pressure fluctuations can drive as much as 5 times more radon entry than diffusion. Consequently, advective radon entry caused by atmospheric pressure fluctuations is a plausible explanation for previously observed elevated indoor-radon concentration during periods of small indoor-outdoor pressure differences (Hernandez et al., 1984; Holub et al., 1985; Turk et al., 1989; Hintenlang and Al-Ahmady, 1992).

Indoor-outdoor pressure differences reduce the contribution of atmospheric pressure fluctuations to the long-term radon entry rate. Typical long-term indoor-outdoor pressure differences range from -1 to -5 Pa depending upon the season. Since indoor-outdoor pressure differences are generally smaller during the summer than the winter, atmospheric pressure fluctuations produce a relatively larger fraction of the total radon entry rate during the summer.

The contribution of atmospheric pressure fluctuations to the long-term radon entry rate depends strongly on the permeability of the soil. At sites with high permeability soils, $k = 10^{-10}$ m^2, atmospheric pressure fluctuations drive less than 5% of the long-term radon entry rate. On the other hand, these fluctuations typically produce more than 20% of the long-term radon entry rate at sites with a soil permeability less than $k = 10^{-11}$ m^2. Atmospheric pressure fluctuations generate the largest component (up to 50%) of the long-term radon entry rate at sites with a soil permeability of 10^{-12} m^2.

The air-filled porosity of the soil, the distance between the basement and an impermeable layer, and the presence or absence of a high permeability subslab gravel layer all affect the contribution of atmospheric pressure fluctuations to long-term entry. The percentage of long-term radon entry increases almost linearly with increases in air-filled porosity and the distance between the basement and an impermeable layer. For the basement configuration considered here, the addition of a subslab gravel layer increases the contribution of atmospheric pressure fluctuations to the long-term radon entry rate by a factor of more than 2.

In summary, this chapter indicates that over the long-term, atmospheric pressure fluctuations drive approximately the same amount of entry as diffusion. Consequently, radon entry produced by these fluctuations will not commonly cause houses to have long-term elevated indoor radon concentrations. However, these fluctuations drive a substantial portion of the total radon entry at sites with low permeability soils. Therefore, in relative terms, this entry causes increased health risks for occupants of houses at these sites.

REFERENCES

Allen C. (1984) Wind pressure data requirements for air infiltration calculations. Technical Note AIC-13, Air Infiltration Center, Bracknell, Berkshire, Great Britain RG12 4AH.

Carslaw H. S. and Jaeger J. C. (1959) *Conduction of Heat in Solids*. Clarendon Press, Oxford.

Hernandez T. L., Ring J. W. and Sachs H. M. (1984) The variation of basement radon concentrations with barometric pressure. *Health Phys.* **46**, 440-445.

Hintenlang D. E. and Al-Ahmady K. K. (1992) Pressure differentials for radon entry coupled to periodic atmospheric pressure variations. *Indoor Air* **2**, 208-215.

Holub R. F., Droullard R. F., Borak T. B., Inkret W. C., Morse J. G. and Baxter J. F. (1985) Radon-222 and ^{222}Rn progeny concentrations measured in an energy-efficient house equipped with a heat exchanger. *Health Phys.* **49**, 267-277.

Kozik A. C., Oppenheim P. and Schneider D. (1992) The effect of interior door position and methods of handling return air on differential pressures in a Florida house. The 1992 International Symposium on Radon and Radon Reduction Technology. Minneapolis, MN, U.S. Environmental Protection Agency, Air and Energy Environmental Research Laboratory, Research Triangle Park NC 27711.

Loureiro C. O., Abriola L. M., Martin J. E. and Sextro R. G. (1990) Three-dimensional simulation of radon transport into houses with basements under constant negative pressure. *Environ. Sci. Technol.* **24**, 1338-1348.

Marcinowski F., Lucas R. M. and Yeager W. M. (1994) National and regional distributions of airborne radon concentrations in United-States homes. *Health Phys.* **66**, 699-706.

Nazaroff W. W. (1988) Entry by pressure-driven flow or molecular diffusion? A reassessment of ^{222}Rn concentrations measured in an energy efficient house. *Health Phys.* **55**, 1005-1009.

Nazaroff W. W. (1992) Radon transport from soil to air. *Rev. Geophys.* **30**, 137-160.

Nazaroff W. W., Feustel H., Nero A. V., Revzan K. L., Grimsrud D. T., Essling M. A. and Toohey R. E. (1985) Radon transport into a detached one-story house with a basement. *Atmos. Environ.* **19**, 31-43.

Nazaroff W. W., Moed B. A. and Sextro R. G. (1988) Soil as a source of indoor radon: Generation, migration, and entry. In Nazaroff W. W. and Nero A. V. (Ed.) *Radon and Its Decay Products in Indoor Air*, John Wiley and Sons, New York, 57-112.

Nazaroff W. W. and Sextro R. G. (1989) Technique for measuring the indoor ^{222}Rn potential of soil. *Environ. Sci. Technol.* **23**, 451-458.

NOAA (1981) TMY user's manual. National Climatic Data Center, Asheville, NC 28801.

Revzan K. L. (1989) Radon entry, distribution, and removal in two New Jersey houses with basements. LBL-26830, Lawrence Berkeley National Laboratory, Berkeley CA 94720.

Revzan K. L., Fisk W. J. and Gadgil A. J. (1991) Modeling radon entry into houses with basements: Model description and verification. *Indoor Air* **1**, 173-189.

Revzan K. L., Turk B. H., Harrison J., Nero A. V. and Sextro R. G. (1988) Parametric modeling of temporal variations in radon concentrations in homes. LBL-24179, Lawrence Berkeley National Laboratory, Berkeley CA 94720.

Riley W. J., Gadgil A. J., Bonnefous Y. C. and Nazaroff W. W. (1996) The effect of steady winds on radon-222 entry into houses. *Atmos. Environ.* **30**, 1167-1176.

Scott A. G. (1988) Preventing radon entry. In Nazaroff W. W. and Nero A. V. (Ed.) *Radon and Its Decay Products in Indoor Air*, John Wiley and Sons, New York, N.Y., 407-433.

Sherman M. H. (1980) Air Infiltration in Buildings. LBL-10712, Lawrence Berkeley Laboratory.

Turk B. H., Prill R. J., Sextro R. G. and Harrison J. (1989) Intensive radon mitigation research: lessons learned. The 1988 International Symposium on Radon and Radon Reduction Technology. U.S. Environmental Protection Agency, Air and Energy Environmental Research Laboratory, Research Triangle Park NC 27711.

Table 6.1 Soil and concrete properties used to estimate diffusive radon flux into basement, and soil-gas radon concentration. These values are representative of the properties of common soils and concretes (Nazaroff, 1992).

Parameter	Symbol	Value
^{222}Rn decay constant	λ	2.1×10^{-6} s^{-1}
Soil Properties:		
radium content	A_{Ra}	30 Bq kg^{-1}
emanation coefficient	f	0.35
soil-grain density	ρ	2650 kg m^{-3}
air-filled porosity	ε	see Table 6.2
interstitial diffusivity	D	3×10^{-6} m^2 s^{-1}
Concrete Properties:		
radium content	$A_{Ra,c}$	30 Bq kg^{-1}
emanation coefficient	f_c	0.2
soil-grain density	ρ_c	2650 kg m^{-3}
air-filled porosity	ε_c	0.2
interstitial diffusivity	D_c	5×10^{-8} m^2 s^{-1}

Table 6.2 Values for the diffusive radon entry rate into and the undisturbed radon concentration underneath the prototypical basement. Values of the soil resistance to steady-state soil gas entry, R, are listed for a basement with and without a high permeability subslab gravel layer. L is the distance between basement floor and the water table, bedrock, or some other impermeable boundary.

case	k (m^2)	ε (-)	L (m)	I_u ($Bq\ m^{-3}$)	S_D ($Bq\ s^{-1}$)	Gravel R ($Pa\ min\ L^{-1}$)	No Gravel R ($Pa\ min\ L^{-1}$)
1	10^{-10}	0.4	8	40,000	0.52	0.12	0.37
1	10^{-11}	0.4	8	40,000	0.52	1.1	3.7
1	10^{-12}	0.4	8	40,000	0.52	11	37
1	10^{-13}	0.4	8	40,000	0.52	110	370
2	10^{-11}	0.2	8	98,000	0.91	1.1	3.7
2	10^{-11}	0.3	8	60,000	0.65	1.1	3.7
2	10^{-11}	0.4	8	40,000	0.52	1.1	3.7
2	10^{-11}	0.5	8	27,000	0.44	1.1	3.7
3	10^{-11}	0.4	3	40,000	0.52	1.4	4.0
3	10^{-11}	0.4	8	40,000	0.52	1.1	3.7
3	10^{-11}	0.4	13	40,000	0.52	1.1	3.7
3	10^{-11}	0.4	18	40,000	0.52	1.1	3.7

Table 6.3 Parameters used to estimate indoor-outdoor pressure differences created by wind and stack effects.

Parameter	Symbol	Value
Density of air	ρ_a	1.2 kg m^{-3}
Indoor temperature	T_{in}	20 °C
Outdoor temperature	T_{out}	TMY data base
Distance between basement floor and neutral plane	Δh	3 m
Pressure coefficient	C_p	-0.2[a]
Wind speed	v	TMY data base

[a] (Allen, 1984)

Table 6.4 Average indoor-outdoor pressure difference (Pa) due to wind and stack effects. Negative pressure difference indicates interior pressure less than atmospheric pressure. Summer is defined as May, June, July, August, September, October. Winter is defined as November, December, January, February, March, April.

	Summer			Winter		
	Wind	Stack	Total	Wind	Stack	Total
Jacksonville	-1.8	+0.6	-1.2	-1.8	-0.6	-2.5
Newark	-1.3	-0	-1.3	-2.9	-2.0	-4.9
Spokane	-1.5	-0.5	-2.0	-2.6	-2.4	-5.0
Tucson	-2.2	+0.7	-1.5	-1.8	-0.8	-2.6

Table 6.5 Long-term, time-averaged total radon entry rate into a house in Spokane. Percent APF is the percentage of the long-term radon entry rate that is driven by atmospheric pressure fluctuations. The average annual indoor-outdoor pressure difference for a house in Spokane is -3.5 Pa. The column "Variable" indicates the value of the parameter which is varied. The complete set of soil properties for each case is listed in Tables 6.1 and 6.2. L is the distance between basement floor and the water table, bedrock, or some other impermeable boundary.

		Basement with a Gravel Layer		Basement without a Gravel Layer	
Case	Variable	S_T (Bq s^{-1})	Percent APF	S_T (Bq s^{-1})	Percent APF
1	$k = 10^{-10}$ m^2	21.	2%	6.8	1%
1	$k = 10^{-11}$ m^2	3.2	19%	1.3	9%
1	$k = 10^{-12}$ m^2	1.3	46%	0.7	20%
1	$k = 10^{-13}$ m^2	0.8	35%	0.6	11%
2	$\varepsilon = 0.2$	6.7	11%	2.5	5%
2	$\varepsilon = 0.3$	4.5	15%	1.7	7%
2	$\varepsilon = 0.4$	3.2	19%	1.3	9%
2	$\varepsilon = 0.5$	2.4	22%	1.0	11%
3	L = 3 m	2.7	13%	1.2	4%
3	L = 8 m	3.3	17%	1.3	9%
3	L = 13 m	3.6	22%	1.3	13%
3	L = 18 m	3.9	27%	1.4	17%

Table 6.6 Long-term, time-averaged total radon entry rate into a house in Jacksonville. Percent APF is the percentage of the long-term radon entry rate that is driven by atmospheric pressure fluctuations. The average annual indoor-outdoor pressure difference for a house in Jacksonville is -1.9 Pa. The column "Variable" indicates the value of the parameter which is varied. The complete set of soil properties for each case is listed in Tables 6.1 and 6.2. L is the distance between basement floor and the water table, bedrock, or some other impermeable boundary.

		Basement With a Gravel Layer		Basement Without a Gravel Layer	
Case	Variable	S_T (Bq s^{-1})	Percent APF	S_T (Bq s^{-1})	Percent APF
1	$k = 10^{-10}$ m^2	12	6%	3.9	3%
1	$k = 10^{-11}$ m^2	2.5	35%	1.0	17%
1	$k = 10^{-12}$ m^2	1.3	51%	0.7	22%
1	$k = 10^{-13}$ m^2	0.8	36%	0.6	11%
2	$\varepsilon = 0.2$	4.7	24%	1.9	11%
2	$\varepsilon = 0.3$	3.3	30%	1.3	15%
2	$\varepsilon = 0.4$	2.5	35%	1.0	17%
2	$\varepsilon = 0.5$	1.9	38%	0.8	19%
3	L = 3 m	1.9	27%	0.9	9%
3	L = 8 m	2.5	35%	1.0	17%
3	L = 13 m	2.8	41%	1.1	23%
3	L = 18 m	3.1	47%	1.2	28%

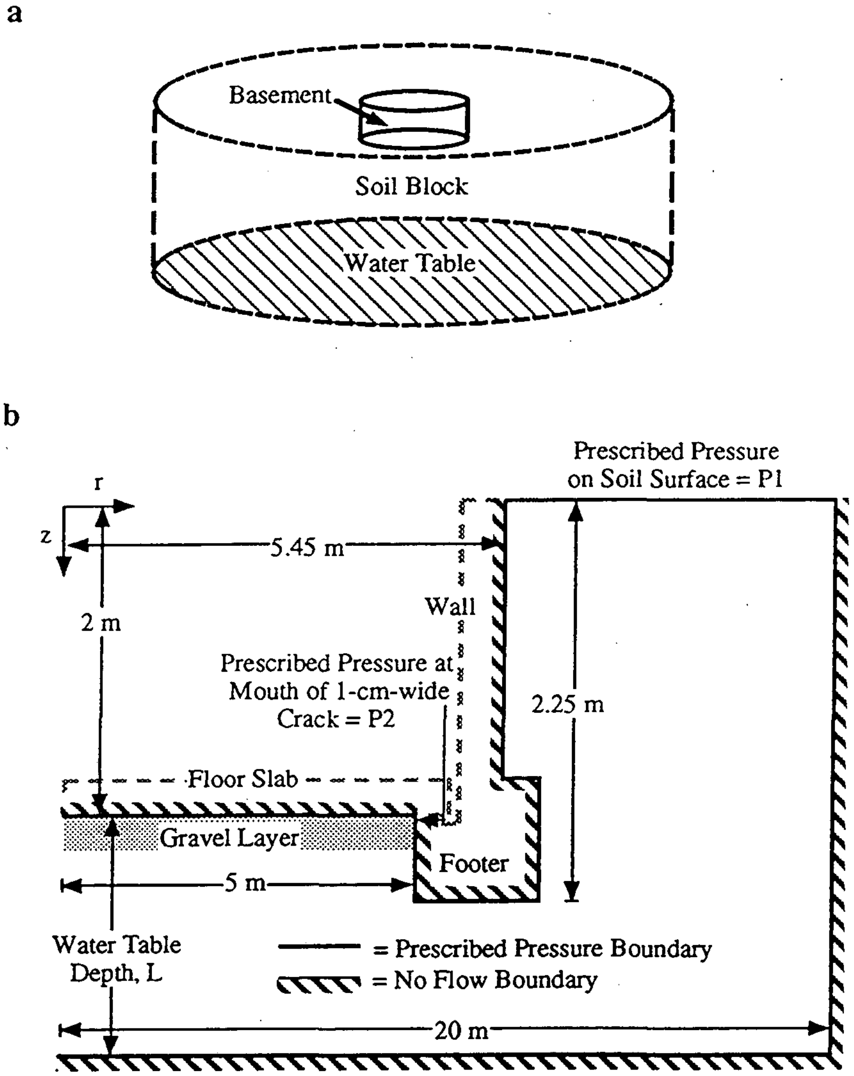

Fig. 6.1 Schematic of (a) the cylindrical basement and soil block, and (b) cross-section of model basement and soil block. Due to axial-symmetry only half the cylinder is shown. The boundary conditions used to simulate the flow of radon-laden soil gas into the basement are shown in (b). For this simulation, the finite-element model calculates the soil-gas pressure and velocity inside the region bounded by the heavy black line. The dashed lines indicate the interior edges of the walls of the structure. These lines are intended for visual guidance only. The figure is not drawn to scale.

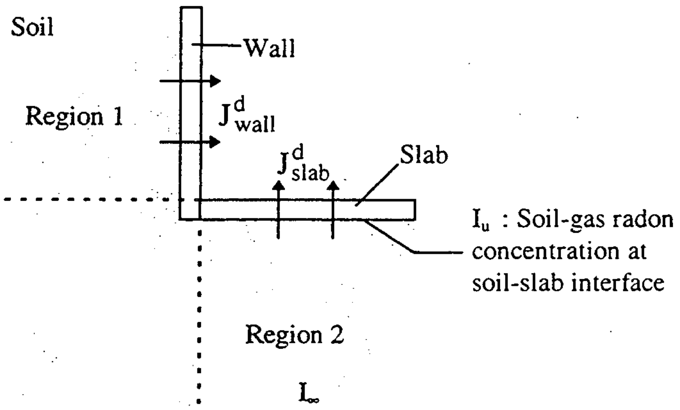

Fig. 6.2 Regions used to evaluate the soil-gas radon concentration and diffusive entry rate. I_u is the radon concentration of the soil-gas advected into the basement.

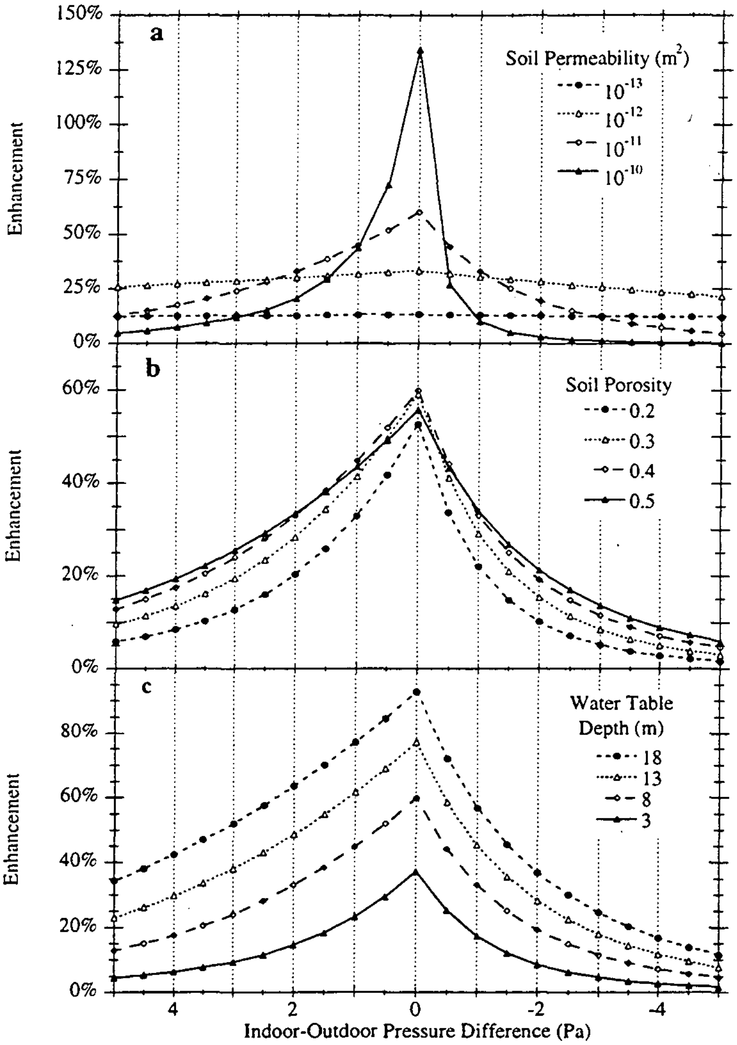

Fig. 6.3 Enhancement in long-term radon entry rate into a basement without a high permeability subslab gravel layer caused by atmospheric pressure fluctuations as a function of (a) soil permeability (Case 1, Table 6.2), (b) air-filled porosity (Case 2, Table 6.2), and (c) water table depth (Case 3, Table 6.2). An enhancement of 100% indicates that atmospheric pressure fluctuations drive the same amount of radon entry as both diffusion and indoor-outdoor pressure differences; i.e., these fluctuations increase the long-term radon entry rate by a factor of 2. A negative pressure difference indicates that the interior of the basement is depressurized relative to the ambient atmosphere.

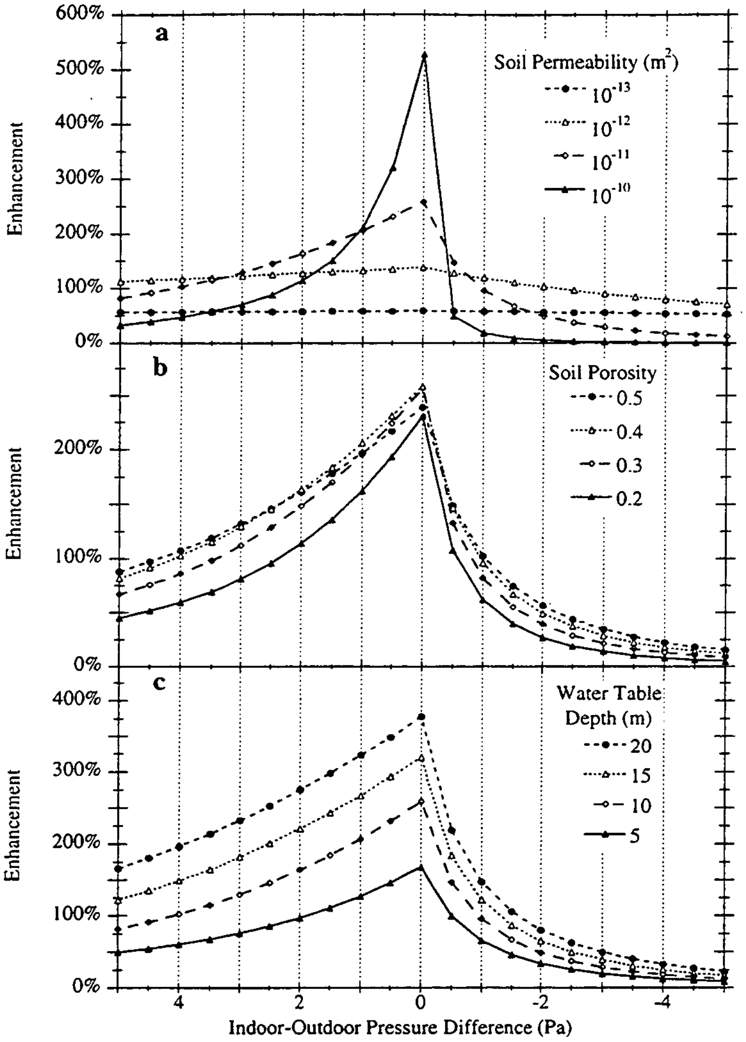

Fig. 6.4 Enhancement in long-term radon entry rate into a basement with a high permeability subslab gravel layer due to atmospheric pressure fluctuations as a function of (a) soil permeability (Case 1, Table 6.2), (b) air-filled porosity (Case 2, Table 6.2), and (c) water table depth (Case 3, Table 6.2). An enhancement of 100% indicates that atmospheric pressure fluctuations drive the same amount of radon entry as both diffusion and indoor-outdoor pressure differences; i.e., these fluctuations increase the long-term radon entry rate by a factor of 2. A negative pressure difference indicates that the interior of the basement is depressurized relative to the ambient atmosphere.

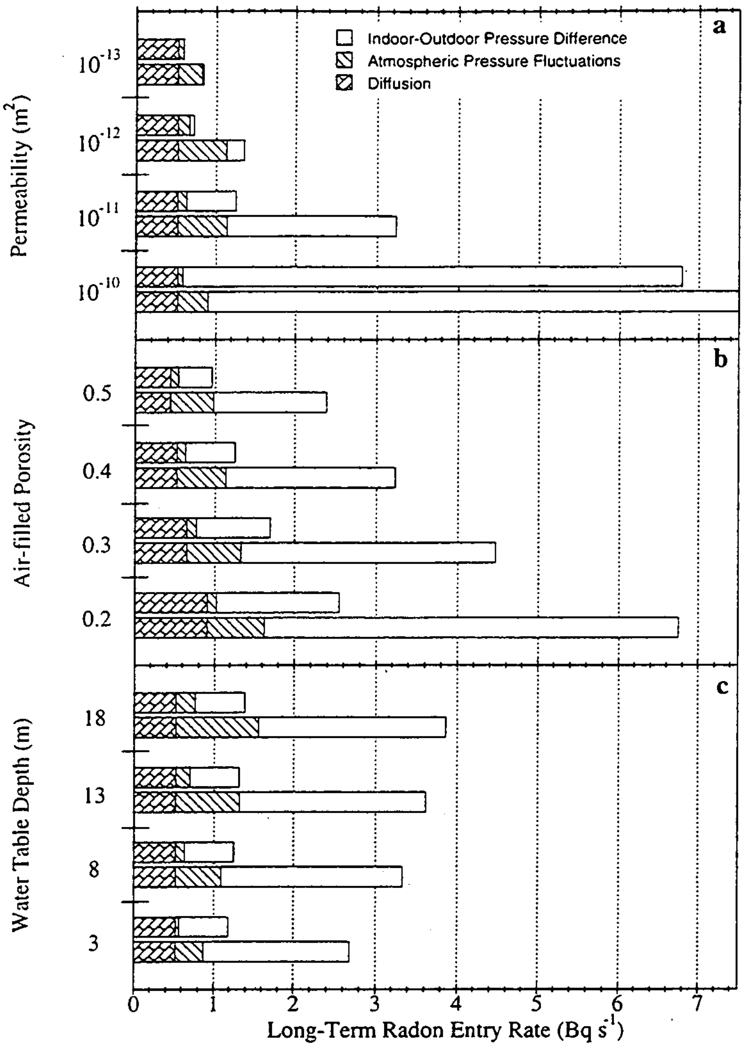

Fig. 6.5 Total radon entry rate as a function of (a) soil permeability, (b) air-filled porosity, and (c) water table depth. These predictions are for a house located in Spokane WA (annual average $\Delta P = -3.5$ Pa). For each case, the top bar indicates the house without a subslab gravel layer; the bottom bar indicates the house with a gravel layer. To increase the resolution of the figure, the bar indicating long-term radon entry into a basement with a high permeability subslab gravel layer and $k = 10^{-10}$ m^2 has been truncated. The end of this bar should read ~ 21 Bq s^{-1}.

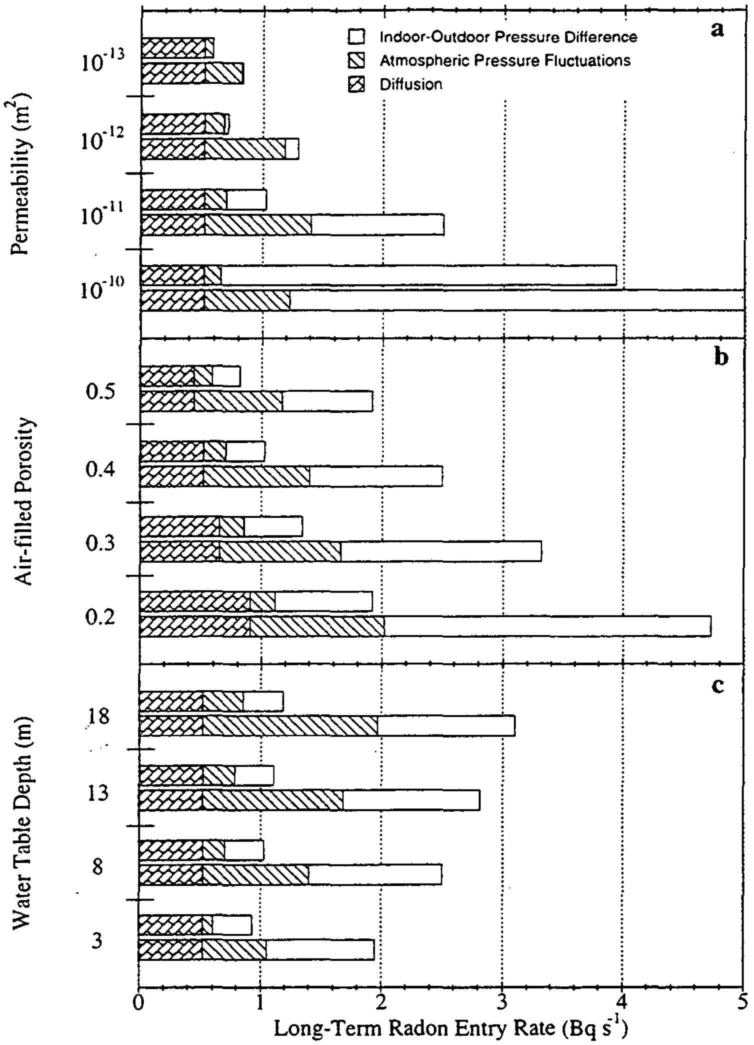

Fig. 6.6 Total radon entry rate as a function of (a) soil permeability, (b) air-filled porosity, and (c) water table depth. These predictions are for a house located in Jacksonville FL (annual average $\Delta P = -1.9$ Pa). For each case, the top bar indicates the house without a subslab gravel layer; the bottom bar indicates the house with a gravel layer. To increase the resolution of the figure, the bar indicating long-term radon entry into a basement with a high permeability subslab gravel layer and $k = 10^{-10}$ m^2 has been truncated. The end of this bar should read ~ 12 Bq s^{-1}.

Chapter 7

CONCLUSIONS

OVERVIEW

This chapter summarizes the contributions of this dissertation to our understanding of the mechanisms that drive and the factors that control radon entry into houses. These contributions fall into three areas: the effect of a high permeability subslab gravel layer on advective radon entry, the dynamics of radon entry driven by atmospheric pressure fluctuations, and the development and validation of theoretical models to predict radon entry. The chapter concludes with a discussion of future research directions.

SUMMARY OF RESULTS

The Influence of a Subslab Gravel Layer

The results described in this dissertation demonstrate that the presence of a high permeability subslab gravel layer can dramatically increase advective radon entry into a house. Since advective entry of radon-laden soil gas is the primary cause of elevated indoor radon concentrations, this finding has important implications to the development of radon mitigation techniques and to the design of radon-resistant houses. Chapter 2 considered the impact of a subslab gravel layer on radon entry driven by steady indoor-outdoor pressure differences.

Chapters 4 and 6 examined the influence of a subslab gravel layer on transient soil-gas and radon entry driven by atmospheric pressure fluctuations.

A subslab gravel layer dramatically changes the interaction of a building with the surrounding soil. Measurements reported in Chapter 2 indicate that a subslab gravel layer couples the openings in the basement floor together, enabling very small openings to effectively depressurize the entire gravel layer to the same magnitude as the interior of the basement. Once this occurs, the radon entry rate through openings in the floor is maximized. In contrast, openings in the floor of a basement without a high-permeability subslab gravel layer act relatively independently of each other. Therefore, an increase in open area in the floor of a basement without a gravel layer increases the radon entry rate, while beyond a minimum size, an increase in the open area in the floor over a gravel layer has no significant effect on radon entry.

Theoretical analysis in Chapters 4 and 6 indicates that a subslab gravel layer dramatically increases transient soil-gas and radon entry caused by atmospheric pressure fluctuations. The response time of a subslab gravel layer to a changes in pressure is several orders of magnitude shorter than the response time of the soil. Consequently, the gravel layer creates a plenum underneath a basement which maximizes transient soil-gas and radon entry.

These results help explain the ineffectiveness of sealing by itself as a radon mitigation technique. In houses with a subslab gravel layer one must seal essentially all of the openings to significantly reduce radon entry. In addition, these findings have implications for building codes which require the inclusion of a subslab gravel layer for homes constructed in high radon areas to improve the effectiveness of a passive subslab ventilation system (EPA, 1994). If the passive mitigation system is inadequate or if an active mitigation system is not installed or functioning properly, the gravel layer can greatly enhance the radon entry rate, potentially increasing indoor radon concentrations.

Radon Entry Driven by Atmospheric Pressure Fluctuations

Measurements reported in Chapter 5 demonstrate that atmospheric pressure fluctuations draw radon-laden soil gas into houses. These fluctuations drive radon entry without requiring the sustained indoor-outdoor pressure differences commonly associated with the advective transport of radon laden soil gas into houses. In fact, atmospheric pressure fluctuations can drive advective radon entry even when the interior of a building is slightly pressurized relative to the ambient atmosphere.

Chapter 5 describes an intensive study to quantify the effect of atmospheric pressure fluctuations on the long-term radon entry rate into an experimental structure. In the absence of a steady indoor-outdoor pressure difference, atmospheric pressure fluctuations drive 1.5 more radon entry than diffusion into the experimental basement. Pressurizing or depressurizing the interior of the structure relative to the ambient atmosphere diminishes the contribution of atmospheric pressure fluctuations to the long-term radon entry rate. At indoor-outdoor pressure differences with magnitudes greater than 1.5 Pa, atmospheric pressure fluctuations have essentially no effect on the long-term radon entry rate into the experimental structure.

Chapters 4 and 6 present results from a parametric study of the influence of soil properties, water table depth, and a high permeability subslab gravel layer on soil-gas and radon entry driven by atmospheric pressure fluctuations. This study suggests that under neutral pressure conditions, atmospheric pressure fluctuations drive several times more radon entry than diffusion into buildings located at sites with relatively permeable soils, $k \geq 10^{-11}$ m^2. Therefore, radon entry caused by these fluctuations is a possible explanation for elevated indoor radon concentration observed during periods when indoor-outdoor pressure differences were small (Hernandez et al., 1984; Holub et al., 1985; Turk et al., 1989; Hintenlang and Al-Ahmady, 1992).

Indoor-outdoor pressure differences reduce contribution of atmospheric pressure fluctuations to the long-term radon entry rate. Analysis of meteorological data indicates that neutral pressure conditions are uncommon. Typical long-term indoor-outdoor pressure differences range from -1 to -5 Pa depending upon the season. For pressure differences of this magnitude, the theoretical analysis described in Chapter 6 indicates that atmospheric pressure fluctuations drive less than 5% of the long-term entry at sites with a soil permeability greater than 10^{-10} m^2. On the other hand, these fluctuations produce between 20% and 50% of the total long-term radon entry rate at sites with a soil permeability less than 10^{-11} m^2. Atmospheric pressure fluctuations generate the largest component (up to 50%) of the long-term radon entry rate at sites with a soil permeability of 10^{-12} m^2.

In addition to soil permeability, other factors such soil porosity, the distance between the basement and an impermeable layer, and the presence or absence of a high permeability subslab gravel layer also affect the contribution of atmospheric pressure fluctuations to the long-term radon entry rate. The fraction of long-term radon entry caused by these fluctuations increases almost linearly with increases in air filled porosity and the distance between the basement and an impermeable layer. For the basement geometry considered in Chapter 6, a high permeability subslab gravel layer the increased contribution of atmospheric pressure fluctuations to the long-term radon entry by more than a factor of 2.

Although soil permeability, air-filled porosity, the distance between the basement and an impermeable layer and a subslab gravel layer all affect the magnitude of radon entry driven by atmospheric pressure fluctuations, over the long-term these fluctuations drive approximately the same amount of entry as diffusion. Consequently, radon entry produced by these fluctuations will probably not cause long-term elevated indoor radon concentrations. However, for houses built in low permeability, high-porosity soils ($k \leq 10^{-11}$ m^2, $\varepsilon \geq 0.4$), atmospheric pressure fluctuations typically drive between 20% and 50% of the total long-term radon entry. Therefore, in relative terms, advective radon entry driven by atmospheric pressure fluctuations causes increased health risks for occupants of houses at these sites.

Model Development and Validation

Chapter 3 describes a theoretical framework for predicting transient soil-gas flow into houses. This framework, which is based on the linearity of the soil-gas response to changes in pressure, represents a significant advance in our ability to evaluate and predict transient advective transport of soil-gas contaminants.

In Chapters 3 and 4, we applied this framework to the problem of soil-gas entry caused by atmospheric pressure fluctuations. Examination of gain and phase functions estimated from measured soil-gas flows provided valuable insight into the soil-gas response to atmospheric pressure. Utilizing the principle of superposition, we derived an analytical model to predict transient soil-gas entry into a house driven by atmospheric pressure fluctuations. From a dimensional analysis of this model, we identified two scaling parameters which characterize soil-gas response to changes in atmospheric pressure fluctuations. These scaling parameters indicate how changes in soil permeability, air-filled porosity, and the distance between the basement and an impermeable layer affect transient soil-gas entry. The shorter the characteristic response time and the larger the capacitance of the soil, the larger the soil-gas flow rate caused by a given atmospheric pressure fluctuation.

This dissertation also examined the performance of several mathematical models which simulate radon and soil-gas entry into houses. All of the models are based on Darcy's law with regionally-defined soil parameters. Chapter 2 compared detailed measurements of soil-gas and radon entry driven by steady indoor-outdoor pressure differences to predictions of a finite-difference model. This model predicted the relative effects of a subslab gravel layer and open area on advective radon entry driven by steady indoor-outdoor pressure differences, but underpredicted the magnitude of the soil-gas and radon entry by a factor of 1.5. Chapter 3 compared detailed measurements of soil-gas entry driven by atmospheric pressure fluctuations to predictions of a transient finite-element model and an analytical model. The finite-element model accurately predicted both the magnitude and the dynamics of the observed soil-gas flows. The analytical model correctly predicted the dynamics of the observed flow, but underpredicted the magnitude of the flow by a factor of 2.

DIRECTIONS FOR FUTURE RESEARCH

The work described in this dissertation suggests several directions for future research. First, the results of this dissertation are directly applicable to the transport of other gas-phase soil contaminants into houses. Recent theoretical (Little et al., 1992) and experimental (Wood and Porter, 1987; Hodgson et al., 1992; Fischer et al., 1995) studies suggest that contaminated soil can be an important source of indoor volatile contaminants. Although little research has been done to determine the magnitude of this source, the understanding of the processes affecting radon entry into houses can be used as a basis for understanding the transport of volatile contaminants into houses and for estimating the associated health risk.

Unlike radon, other soil-gas contaminants may have health effects associated with acute exposures. Because atmospheric pressure fluctuations intermittently drive large soil-gas entry rates into buildings, these fluctuations may contribute significantly to peak indoor concentrations of these contaminants. To examine the effect of atmospheric pressure fluctuations on peak indoor pollutant concentrations, the theoretical framework for predicting radon entry driven by atmospheric pressure fluctuations developed in this dissertation should be combined with a building ventilation model (e.g. Sherman, 1980).

The linearity and spectral techniques used to examine and predict transient soil-gas flow developed in this dissertation can be applied to a wide range of contaminant transport problems. An example of such a problem is the effects of transient winds on soil-gas and radon entry into houses. Wind interaction with the building superstructure creates ground surface pressures which can have a large effect on advective radon entry (Riley et al., 1996). Comparing gain and phase functions of the soil-gas response to changes in wind speed with wind speed power spectra (e.g. van der Hoven, 1957) may yield valuable insight into the effects of fluctuating winds on contaminant transport into houses.

The spectral techniques described in Chapter 3 can also be used to characterize soil permeability to air. The first step in such an analysis is to calculate gain and phase functions to describe the soil-gas response to changes in atmospheric pressure. The analytical model described in Chapter 3 could then be fit to these gain and phase functions to yield estimates of the permeability and air-filled porosity of the soil. Several researchers (Weeks, 1978; Rojstaczer and Tunks, 1995; Shan, 1995) have used time series measurements of soil-gas and atmospheric pressure to estimate soil permeability to air. However, these analyses only consider the soil-gas response to the changes in atmospheric pressure at one frequency, not over the entire spectrum.

Finally, the understanding of the physics underlying soil-gas flow caused by atmospheric pressure fluctuations developed in this dissertation also applies to problem of predicting the flux of soil-gas contaminants and trace gases from an uncovered soil. Soil-atmosphere fluxes of trace gases such as CO_2, N_20, and CH_4

are currently a topic of active research because of their role in global climate change (e.g. Batjes and Bridges, 1992). To date, most modeling of these fluxes has been based on molecular diffusion (Amundson and Davidson, 1990; Batjes and Bridges, 1992). Improved understanding of the mechanisms that control these fluxes may help explain the heterogeneous field measurements, and establish guidelines for conducting field investigations.

REFERENCES

Amundson R. G. and Davidson E. A. (1990) Carbon dioxide and nitrogenous gases in the soil atmosphere. *Journal of Geochemical Exploration* **38**, 13-41.

Batjes N. H. and Bridges E. M. (1992) A review of soil factors and processes that control fluxes of heat, moisture and greenhouses gases. International Soil Reference Information Centre: Wageningen, The Netherlands.

EPA (1994) Model standards and techniques for control of radon in new residential buildings. *Federal Register Notices* **59**, 13402-13416.

Fischer M. L., Bentley A. J., Dunkin K. A., Hodgson A. T., Nazaroff W. W., Sextro R. G. and Daisey J. M. (1995) Factors affecting indoor air concentrations of volatile organic compounds at a site of subsurface gasoline contamination. LBL-37768, Lawrence Berkeley National Laboratory, Berkeley CA 94720.

Hernandez T. L., Ring J. W. and Sachs H. M. (1984) The variation of basement radon concentrations with barometric pressure. *Health Phys.* **46**, 440-445.

Hintenlang D. E. and Al-Ahmady K. K. (1992) Pressure differentials for radon entry coupled to periodic atmospheric pressure variations. *Indoor Air* **2**, 208-

215.

Hodgson A. T., Garbesi K., Sextro R. G. and Daisey J. M. (1992) Soil-gas contamination and entry of volatile organic compounds into a house near a landfill. *J. Air Waste Mange. Assoc.* **42**, 277-283.

Holub R. F., Droullard R. F., Borak T. B., Inkret W. C., Morse J. G. and Baxter J. F. (1985) Radon-222 and ^{222}Rn progeny concentrations measured in an energy-efficient house equipped with a heat exchanger. *Health Phys.* **49**, 267-277.

Little J. C., Daisey J. M. and Nazaroff W. W. (1992) Transport of subsurface contaminants into buildings: An exposure pathway for volatile organics. *Environ. Sci. Technol.* **26**, 2058-2066.

Riley W. J., Gadgil A. J., Bonnefous Y. C. and Nazaroff W. W. (1996) The effect of steady winds on radon-222 entry into houses. *Atmos. Environ.* **30**, 1167-1176.

Rojstaczer S. and Tunks J. P. (1995) Field-Based Determination Of Air Diffusivity Using Soil Air and Atmospheric Pressure Time Series. *Wat. Resour. Res.* **31**, 3337-3343.

Shan C. (1995) Analytical Solutions For Determining Vertical Air Permeability In Unsaturated Soils. *Wat. Resour. Res.* **31**, 2193-2200.

Sherman M. H. (1980) Air Infiltration in Buildings. LBL-10712, Lawrence Berkeley Laboratory.

Turk B. H., Prill R. J., Sextro R. G. and Harrison J. (1989) Intensive radon mitigation research: lessons learned. The 1988 International Symposium on Radon and Radon Reduction Technology. U.S. Environmental Protection Agency, Air and Energy Environmental Research Laboratory, Research Triangle Park NC 27711.

Weeks E. P. (1978) Field Determination of Vertical Permeability to Air in the Unsaturated Zone. U.S. Geological Survey Professional Paper 1051, United States Government Printing Office, Washington, DC.

van der Hoven I. (1957) Power spectrum of horizontal wind speed in the frequency range from 0.0007 to 900 cycles per hour. *Journal of Meteorology* **14**, 160.

Wood J. A. and Porter M. L. (1987) Hazardous pollutants in Class II landfills. *J. Air. Pollut. Control Assoc.* **37**, 609-615.

Appendix A

MEASURED SOIL PROPERTIES AT THE STRUCTURE SITE

The soil at the structure site has been extensively characterized (Brimhall and Lewis, 1992; Flexser et al., 1993; Garbesi et al., 1993; Garbesi et al., 1996). This appendix summarizes the results of permeability measurements by Garbesi (1996) and new porosity measurements made at the structure site. These results are used for the theoretical analyses described in Chapters 2, 3, and 5.

SOIL PERMEABILITY

Garbesi et. al (1996) report on an intensive investigation of soil permeability to air at the experimental site. Their measurements indicate that the permeability of the undisturbed soil at this site is scale dependent. To illustrate this result, measurements of soil permeability as a function of sampling scale from the study by Garbesi et. al (1996) are reproduced in Fig. A.1. Fig. A.1 indicates that the effective soil permeability increases by more than an order of magnitude when the measurement scale increases from 0.1 to 3.5 m. Although the length scale of our system is ~ 6.5 m (see Chapter 3), Fig. A.1 suggests that the horizontal permeability of the undisturbed soil approaches an asymptote of ~ 3×10^{-11} m^2 at length scales greater than 3 m. Therefore, we use this value to characterize the effective permeability of the soil at the experimental site.

The permeability measurements shown in Fig. A.1 were made in the top 2 m of the soil profile. However, soil-gas entry driven by atmospheric pressure fluctuations depends largely on the permeability of the soil underneath the structure, depths greater than 2 m (see Fig. 3.2). Are the permeability measurements summarized in Fig. A.1 applicable to the region underneath the structure? Fig. A.2 shows measurements of permeability made around both structures as a function of depth. These measurements suggest that there is no correlation between permeability and depth. Based on this evidence, we assumed that the asymptote of $k \sim 3 \times 10^{-11}$ m^2 shown in Fig. A.1 accurately characterizes the effective permeability of the entire unsaturated zone.

AIR-FILLED POROSITY

Fig. A.3 shows results of porosity measurements at the experimental site. These results are taken from two different studies. The first set of measurements are indicated by the open circles in Fig. A.3. These measurements were made by Brimhall and Lewis (1992) and are based on the analysis of soil samples taken from a 3-m-deep trench dug ~ 10 m from the experimental structure. We made the second set of measurements, indicated by the solid-diamond symbols in Fig. A.3, using gravimetric analysis (Danielson and Sutherland, 1986) of soil cores taken by Flexser et al. (1993). These cores were taken from bore holes drilled between the two experimental structures. The porosity measurements made from these cores are listed in Table A.1.

The soil cores taken by Flexser et al. (1993) show a sharp transition in porosity between 1.6 and 2.2 m. This change corresponds to the transition between the organic surface soil and the underlying sapprolite. Such a sharp transition does not appear in the results reported by Brimhall and Lewis (1992). We hypothesize that the back hoe used to dig the trench may have disturbed the soil on the walls of the trench from which Brimhall and Lewis took their soil samples.

We used the results from our analysis of the soil cores taken by Flexser et al. (1993) to estimate the average porosity profile for the experimental site. This profile is indicated by the solid line in Fig. A.3. We calculated this profile by separately averaging the measurements made in the organic soil and the sapprolite. To connect these averages, we assumed that the porosity changes linearly in the transition region between the organic soil and the sapprolite. The air-filled porosity profile, indicated by the dashed line in Fig. A.3, was calculated from the estimated porosity profile using soil moisture measurements made with a time domain reflectrometer device (Trace System 1, Soil Moisture Equipment Corp., Santa Barbara, CA). Although soil-moisture measurements are made in the top 1.5 m of the soil profile at the structure site we assume that it is independent with depth. The average soil moisture at the site was ~ 20%.

REFERENCES

Brimhall G. H. and Lewis C. J. (1992) Differential element transport in the soil profile at the Ben Lomond small structure radon site: A geochemical mass balance study. University of California at Berkeley, Dept. of Geology and Geophysics, Berkeley CA 94720.

Danielson R. E. and Sutherland P. L. (1986) Porosity. In Black C. A. (Ed.) *Methods of Soil Analysis, Part 1. Physical and Mineralogical Methods*, American Society of Agronomy, Madison, WI, 443-450.

Flexser S., Wollenberg H. A. and Smith A. R. (1993) Distribution of radon sources and effects on radon emanation in granitic soil at Ben Lomond, California. *Environ. Geol.* **22**, 162-177.

Garbesi K., Sextro R. G., Fisk W. J., Modera M. P. and Revzan K. L. (1993) Soil-gas entry into an experimental basement: Model-measurement comparisons and seasonal effects. *Environ. Sci. Technol.* **27**, 466-473.

Garbesi K., Sextro R. G., Robinson A. L., Wooley J. D., Owens J. 'A. and Nazaroff W. W. (1996) Scale dependence of soil permeability to air: Measurement method and field investigation. *Wat. Resour. Res.* **32**, 547-560.

Table A.1 Measured total porosity as a function of depth at the structure site. Values determined by gravimetric analysis (Danielson and Sutherland, 1986) of soil cores taken by Flexser et al. (1993). These results are also presented in Fig. A.3.

Depth (m)	Porosity
0.66	0.59
1.3	0.61
1.4	0.53
2.5	0.36
2.7	0.36
2.8	0.29
3.0	0.37
3.2	0.42
3.3	0.37
3.5	0.34
3.6	0.43
3.7	0.32
3.9	0.46
4.1	0.40
4.3	0.41
4.4	0.40
4.9	0.33
5.0	0.39

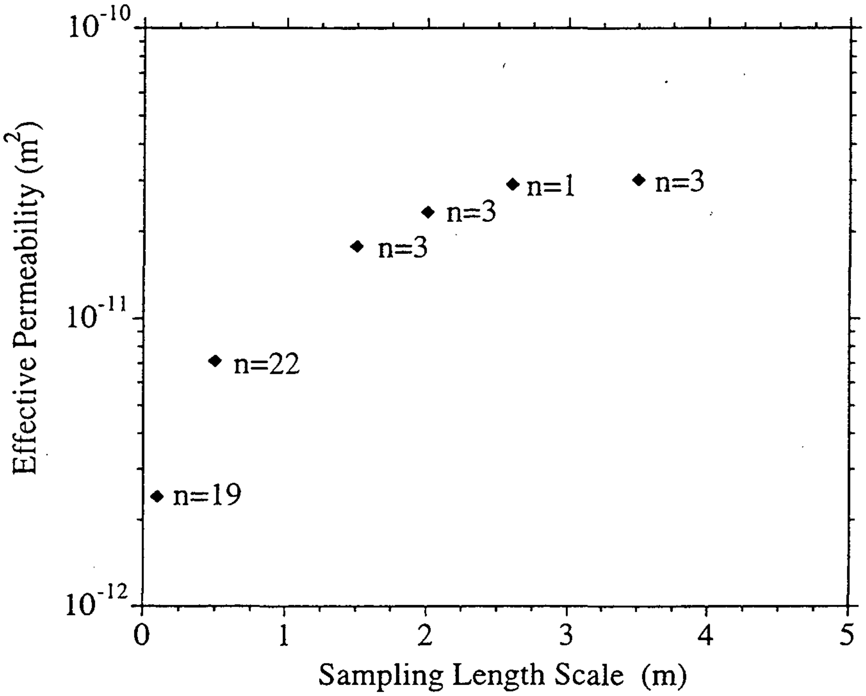

Fig. A.1 Effective permeability as a function of sampling scale. Symbols indicate the geometric mean value of *n* measurements made at a given scale. This figure is based on results reported by Garbesi et al. (1996).

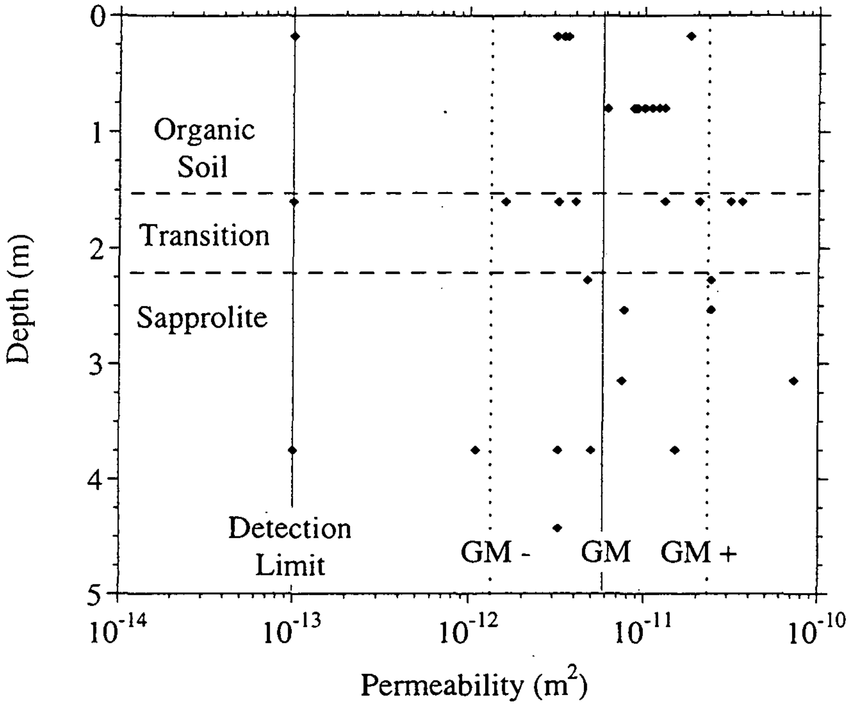

Fig. A.2 Permeability as a function of depth. The label "GM" indicates geometric mean of measurements; the label "GM +" indicates the geometric mean times the geometric standard deviation; the label "GM -" indicates the geometric mean divided by the geometric standard deviation. These measurements were made at the 0.5-m sampling scale. The technique used to make these measurements is described by Garbesi et al. (1993).

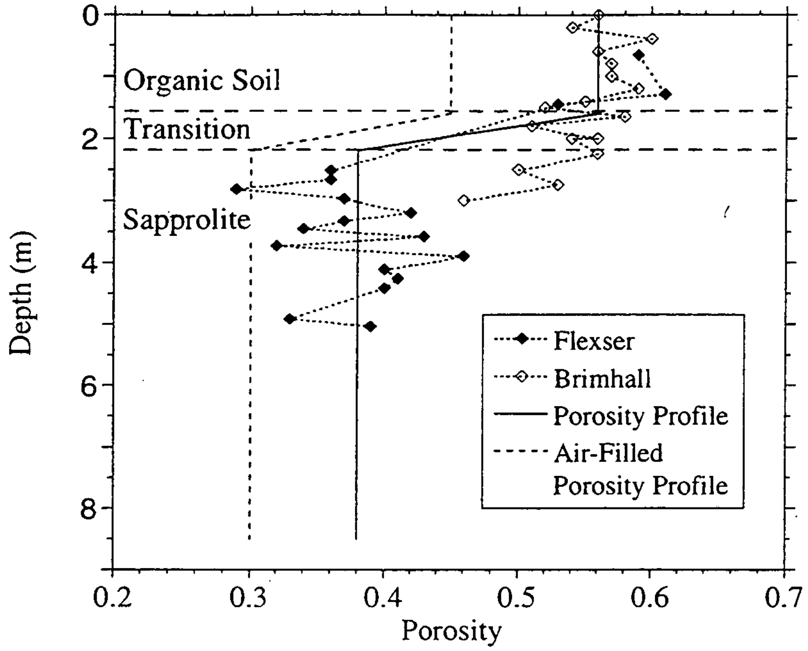

Fig. A.3 Porosity as a function of depth. Open diamonds indicate measurements made by Brimhall and Lewis (1992). Solid diamonds indicate results of gravimetric analysis of soil cores taken by Flexser et al. (1993). The porosity profile was estimated from the measurements indicated by solid diamonds. The air-filled porosity profile was calculated from the porosity profile and the measured soil moisture content, ~ 20%. We have extrapolated these profiles to 8.5 m, the measured depth of the water table below the soil surface.

Appendix B

FLOW SENSOR THEORY AND CALIBRATION

This appendix describes the theory and calibration of the U-shaped flow sensor developed to measure the magnitude and direction of the gas flow into and out of the experimental structure driven by atmospheric pressure fluctuations. We employed this sensor for the experiments described in Chapters 3 and 5.

A schematic of the flow sensor is shown in Fig. B.1. The sensor incorporates two omnidirectional hot-film velocity transducers (TSI model 8470) mounted in a U-shaped tube (1.9-cm ID). The sensor measures the magnitude and direction of gas flows down to 0.15 L min^{-1}. Two velocity transducers are required to determine the direction of the gas flow.

THEORY

We briefly describe the theory behind the operation of a hot-film velocity transducer to explain how the U-shape flow sensor determines the direction of the flow. A hot-film velocity transducer determines gas velocity by measuring the heat transfer rate from a small sphere which is maintained at a constant temperature difference above the surrounding gas. At air large velocities, the heat transfer rate from the sphere only depends on the velocity of the air flow past the sphere. This condition is commonly referred to as forced convection. If there is no external flow, the heat transfer rate from the sphere depends only on the buoyancy-driven flow induced by the heating of the sphere. This condition is commonly referred to as free convection. In between these two limits is the mixed convection regime in which both external and buoyancy-driven flow contribute significantly to the heat-transfer rate. In this regime, the heat transfer rate from the sphere depends on both the velocity of the air flow past the sphere and orientation of this flow with respect to gravity. This dependence of the heat-transfer rate on the orientation of the flow with respect to gravity in the mixed convection regime enables us to determine the direction of the flow through the sensor tube.

To demonstrate this directional dependence, we will derive an expression for the heat transfer rate from the spherical sensing element of the velocity transducer in the mixed convection regime. The heat transfer rate, q (W), from a sphere can be expressed as

$$q = \bar{h}A(T_S - T_\infty) \qquad \text{(B.1)}$$

where $\bar{h}$ is the average convection coefficient for the sphere (W K^{-1} m^{-2}), A is the surface area of the sphere (m^2), T_S is the temperature of the surface of the sphere (K), and T_∞ is the temperature of the ambient air (K). In heat transfer, $\bar{h}$ is commonly expressed in terms of the non-dimensional parameter, the Nusselt number,

$$\overline{\mathrm{Nu}}=\frac{\overline{\mathrm{h}}\mathrm{d}}{\mathrm{k}} \tag{B.2}$$

where d is the diameter of the sphere (m), and k is the thermal conductivity of air ($\mathrm{W\,K^{-1}\,m^{-1}}$). For mixed convection, $\overline{\mathrm{Nu}}$ depends on the orientation of the external flow with respect to gravity.

Semi-empirical correlations have been developed for $\overline{\mathrm{Nu}}$ for a sphere in mixed convection flow (Chen and Armaly, 1987). For assisting flows (external flow opposite to the direction of gravity),

$$\overline{\mathrm{Nu}}=\left(\mathrm{Nr}^{3.5}+\mathrm{Ng}^{3.5}\right)^{1/3.5}+2 \tag{B.3}$$

where

$$\mathrm{Nr}=0.493\,\mathrm{Re}^{1/2} \tag{B.4}$$

and

$$\mathrm{Ng}=0.392\,\mathrm{Gr}^{1/4}. \tag{B.5}$$

Re is the Reynolds number, and Gr is the Grashof number:

$$\mathrm{Re}=\frac{\mathrm{vd}}{\nu}, \qquad \mathrm{Gr}=\frac{g\beta(T_s-T_\infty)\,d^3}{\nu^2} \tag{B.6}$$

where v is the gas velocity ($\mathrm{m\,s^{-1}}$), ν kinematic viscosity of air ($\mathrm{m^2\,s^{-1}}$), g is the gravitational acceleration ($\mathrm{m\,s^{-2}}$), and β is the volumetric thermal expansion coefficient of air ($\mathrm{K^{-1}}$).

For opposing flows (external flow in the same direction as gravity),

$$\overline{\mathrm{Nu}} = \left(\mathrm{Nr}^3 - \mathrm{Ng}^3\right)^{1/3} + 2 \qquad \text{if } \mathrm{Ng}/\mathrm{Nr} < 1 \qquad \text{(B.7a)}$$

or

$$\overline{\mathrm{Nu}} = \left(\mathrm{Ng}^6 - \mathrm{Nr}^6\right)^{1/6} + 2 \qquad \text{if } \mathrm{Ng}/\mathrm{Nr} > 1. \qquad \text{(B.7b)}$$

Using the physical properties listed in Table B.1 and eqns. (B.1), (B.2), (B.3), and (B.7) we calculated the heat transfer rate from the spherical sensing element of the velocity transducer as a function of external flow velocity. Results from these calculations are shown in Fig. B.2. Fig. B.2 indicates that for gas velocities between 1 and 10 cm s^{-1}, the heat transfer rate of the spherical sensing element depends significantly on the orientation of the flow with respect to gravity. At a gas velocity of 5 cm s^{-1}, the heat transfer rate from the sphere in an assisting flow is more than 35% larger than the heat loss rate in an opposing flow. This difference in heat transfer rate causes a hot-film velocity transducer to report different values for the velocity for the same external flow depending on the orientation of this flow with respect to gravity. If the flow is against gravity, the transducer will report a higher velocity than if the flow is with gravity. This phenomenon enables us to determine the direction of the flow.

CALIBRATION

The U-shaped flow sensor was calibrated using the experimental apparatus shown in Fig. B.3. A pump and needle valve assembly was used to control the flow rate in the U-shaped tube. The flow rate through the sensor tube was measured with a bubble flowmeter. For each flow rate the velocity reported by each transducer was recorded. A calibration curve was then generated based on the velocity measured by the upward velocity transducer and the flow rate through the tube. The upward velocity transducer is the transducer in the tube in which the gas flow is against gravity (assisting flow). The flow through the U-shaped sensor is then reversed and the calibration procedure is repeated. Each U-shaped flow sensor has two calibration curves: one for gas flow into the structure, and one for gas flow out of the structure.

The response time, accuracy, and resolution of the flow sensor are 2 s, 5% of reading, and 0.02 L min^{-1} respectively. The accuracy of the flow sensor depends on both the accuracy of the bubble flowmeter used for the calibration and the repeatability of calibrations. Each sensor was regularly calibrated; there was less than 5% variation between each of these calibration runs.

OPERATION

To illustrate the operation of the U-shaped flow sensor, results from one calibration run are shown in Fig. B.4. Fig. B.4 indicates that the detection limit of the flow sensor is ~ 0.15 L min^{-1}. As the flow rate increases above the detection limit, the upward velocity sensor begins to measure flow. As previously mentioned, the velocity reported by the upward transducer is used to determine the flow rate through the tube. This transducer reports a higher velocity than the downward transducer until the flow rate in the tube approaches ~ 1.5 L min^{-1}.

Fig. B.4 indicates that at flow rates greater than ~ 1.5 L min^{-1} the directional distinction disappears. Notice that a flow rate of 1.5 L min^{-1} corresponds to a velocity of 15 cm s^{-1}. Fig. B.2 indicates that at velocities greater than 15 cm s^{-1} the heat transfer rate from the spherical sensing element does not depend on the orientation of the flow with respect to gravity.

Since the directional distinction disappears at high flow rates, the sampling frequency of the flow sensor must be much more rapid than the changes in flow direction. Rapid sampling allows us to determine the direction of the flow by recording the lower velocities that accompany these changes. This condition is easily satisfied for studies of soil-gas flow driven by atmospheric pressure fluctuations because more than 99% of the total power of the atmospheric pressure power spectrum occurs at frequencies less than 1000 day^{-1}. The response time of the flow sensor is ~ 2 s which permits fluctuations up to ~ 10,000 day^{-1} to be monitored.

REFERENCES

Chen T. S. and Armaly B. F. (1987) Mixed convection in external flow. In Kakaç S., Shah R. K. and Aung W. (Ed.) *Handbook of Single-Phase Convective Heat Transfer*, John Wiley & Sons, New York, 14-1 -- 14-35.

Table B.1 Physical properties used to estimate heat-transfer rate from spherical sensing element.

Property	Symbol	Value
Air:		
Kinematic viscosity	ν	1.5×10^{-5} m^2 s^{-1}
Volumetric expansion coefficient	β	3.2×10^{-3} K^{-1}
Thermal conductivity	k	2.6×10^{-2} W m^{-1} K^{-1}
Ambient temperature	T_∞	293 K
Sphere:		
Temperature	T_S	T_∞ + 30 K
Diameter	d	3.175×10^{-3} m
Surface area	A	3.2×10^{-5} m^2
Grashof number	Gr	130
Gravitational acceleration	g	9.8 m s^{-2}

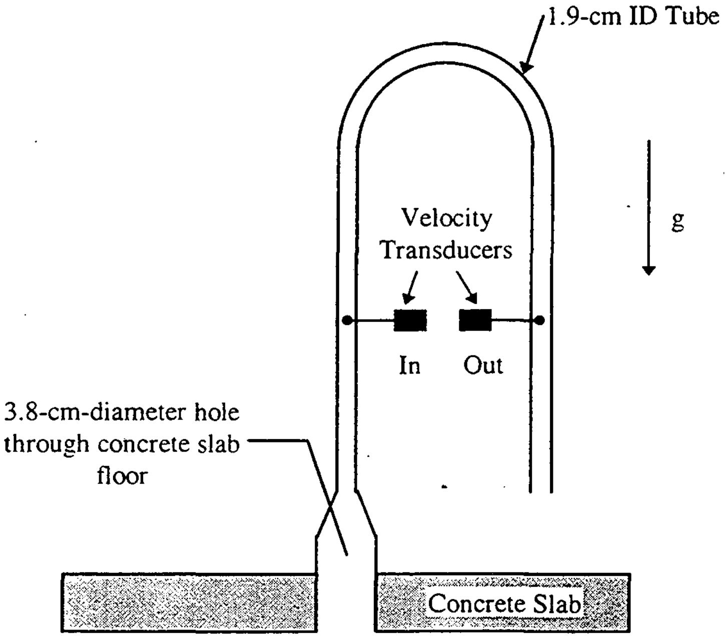

Fig. B.1 Schematic of U-shaped flow sensor. A 80-cm high flow sensor was used in Chapter 3. A 40-cm high flow sensor was used in Chapter 5. We decreased the height of the flow sensor to reduce the resistance of the sensor tube to gas flow.

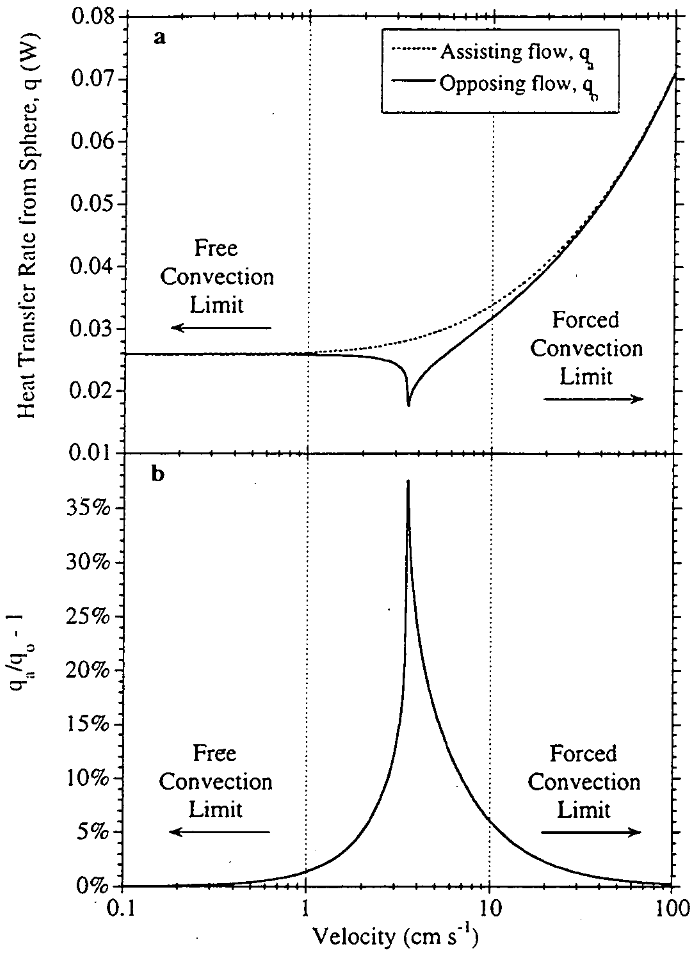

Fig. B.2 (a) Heat transfer rate from 3.175-mm-diameter sphere as a function of air flow rate. (b) Percent difference between heat-transfer rate from a sphere in an assisting flow and an opposing flow. An assisting flow is in the opposite direction to gravity. An opposing flow is in the same direction as gravity.

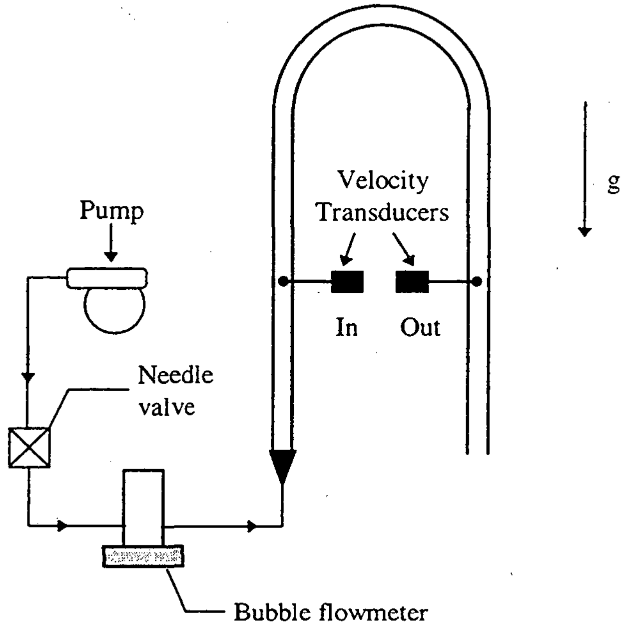

Fig. B.3 Flow sensor calibration system.

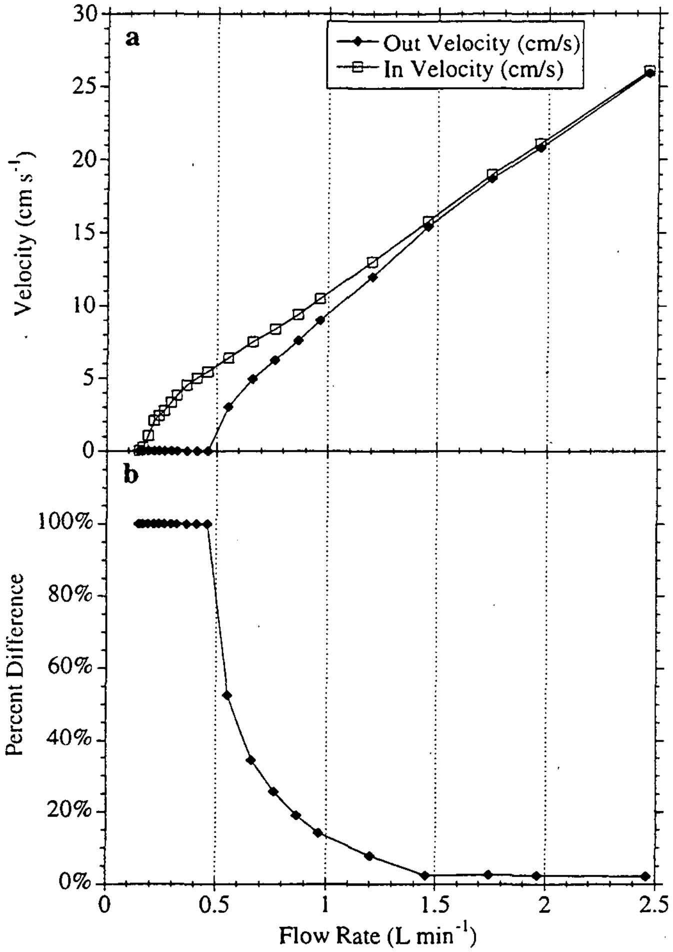

Fig. B.4 Performance of U-shaped flow sensor: (a) calibration curve for both velocity transducers; (b) percent difference in velocity reported by velocity transducers.

Appendix C

MODIFICATIONS OF RN3D

A finite-element model was used in Chapters 3, 4, and 6 to simulate soil-gas entry into a basement. This model is based on a public domain transient finite-element model called RN3D (Holford, 1994). RN3D was developed to simulate gas flow and radon transport in variably saturated, non-isothermal porous media. The model is based on Darcy's law and the standard Galerkin method. Holford (1994) describes the mathematics, numerics, and physics of RN3D. In this appendix, we describe the modifications made to RN3D in order to simulate soil-gas flow around a basement.

The original code only simulates regularly shaped geometries; we have written a preprocessor to generate a two-dimensional mesh with an irregularly shaped boundary required for simulating soil-gas flow around a basement. An example of such a mesh is shown in Fig. C.1. This irregularly shaped mesh was used to simulate the soil-gas flow around the experimental structure described in Chapter 3. The introduction of an irregularly shaped mesh substantially increases the flexibility of RN3D, but it does not change the underlying mathematics or physics of the model. However, in order to run simulations with an irregular flexible two-dimensional geometry, all of the subroutines in the original code which handle boundary conditions had to be rewritten. Tsang and Li (1995) have also modified

RN3D to simulate radon and soil-gas entry into basement. They first proposed the use of an external mesh generator in conjunction with RN3D to simulate more flexible two-dimensional geometries.

In addition to adapting RN3D to simulate more flexible geometries, we discovered two errors in the original code. The first error involves the calculation of volume integrals in cylindrical coordinates. Application of the finite-element method to an axisymetric cylindrical problem requires the evaluation of integrals of the following form,

$$\int_{\Re} \frac{\partial N_I}{\partial z}\frac{\partial N_J}{\partial z} 2\pi r\,dr\,dz \tag{C.1}$$

where $\Re$ defines the region of integration (an element), N_I and N_J are linearly independent basis functions, r is the radial coordinate, and z is the vertical coordinate. To evaluate integrals of the form shown in eqn. (C.1), RN3D assumes that

$$\int_{\Re} \frac{\partial N_I}{\partial z}\frac{\partial N_J}{\partial z} 2\pi r\,dr\,dz = 2\pi \bar{r} \int_{\Re} \frac{\partial N_I}{\partial z}\frac{\partial N_J}{\partial z}\,dr\,dz \tag{C.2}$$

where $\bar{r}$ is the centroidal radius of the element $\Re$. However, eqn. (C.2) is valid only if integrand on the right-hand side of eqn. (C.2) is ***not*** a function of r. Since RN3D uses bilinear basis functions (linear quadrilateral elements), the integrand on the right-hand side of eqn. (C.2) depends on r, and eqn. (C.2) is not correct (e.g. Reddy and Gartling, 1994). We have modified RN3D so that all volume integrals of the form indicated by eqn. (C.1) are correctly evaluated.

The second error involves the calculation of the mass flux across a boundary. The original version of RN3D incorrectly calculates this flux. We discovered this problem by applying a mass balance to the entire computational domain. For the case of steady-state soil-gas flow driven by a steady indoor-outdoor pressure difference, the mass flux of soil-gas into the basement must be balanced by the mass flux of air across the soil surface. However, because of the way in which the original version of the RN3D calculated the mass flux across a boundary, the flux into a basement was frequently 10 to 20% less than the mass flux across the soil surface. We corrected this problem by calculating the mass flux across the boundary using the method described by Reddy and Gartling (1994).

REFERENCES

Holford D. J. (1994) RN3D: A finite element code for simulating gas flow and radon transport in variably saturated, nonisothermal porous media: User's manual, version 1.0. PNL-8943, Pacific Northwest Laboratory, Richland WA 99352.

Reddy J. N. and Gartling D. K. (1994) *The Finite Element Method in Heat Transfer and Fluid Dynamics*. CRC Press, Boca Raton.

Tsang Y. W. and Li J. (1995) A numerical model to simulate the effects of atmospheric pressure fluctuations on soil-gas and radon entry into basements. LBL 37793, Lawrence Berkeley National Laboratory, Berkeley CA 94720.

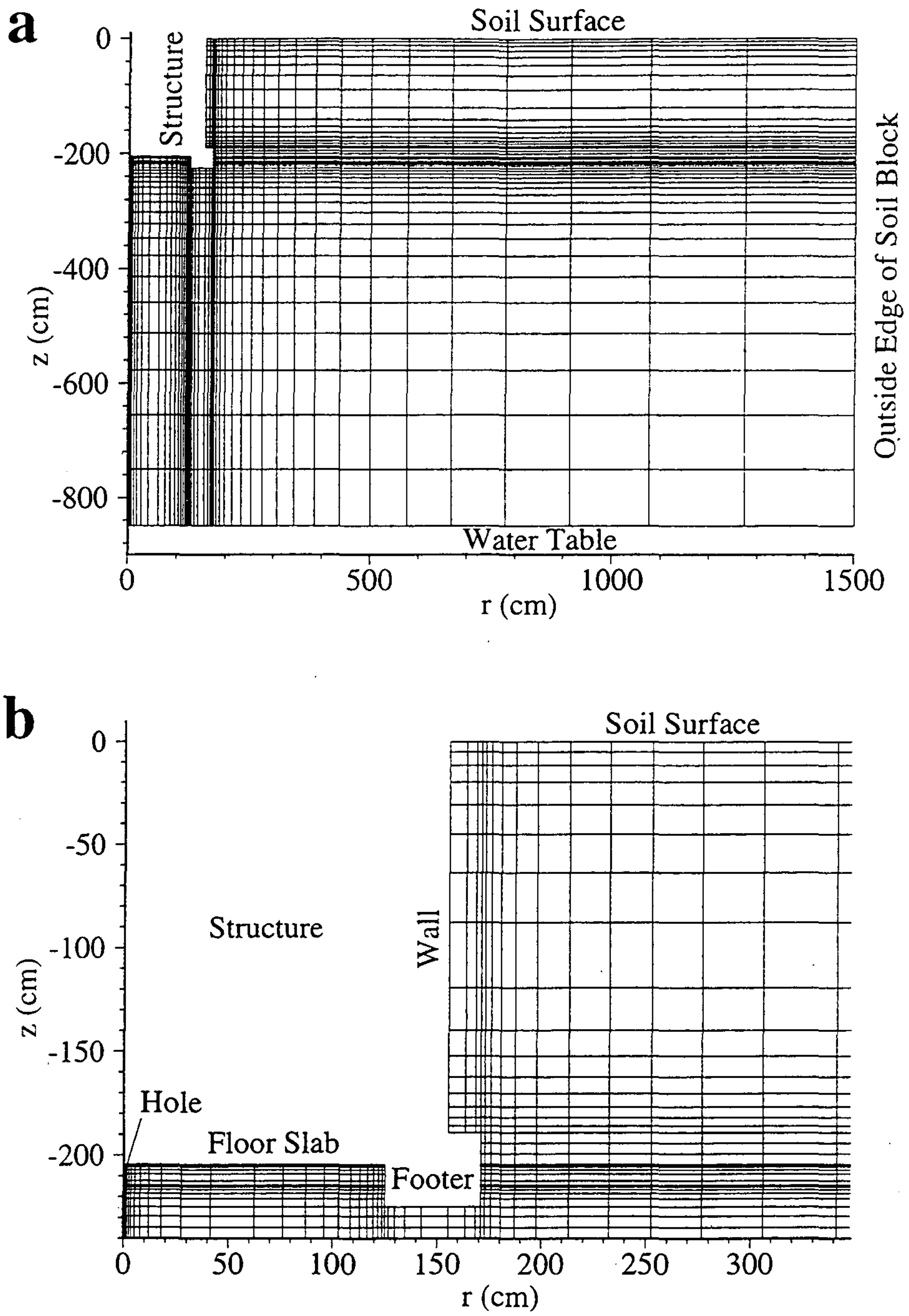

Fig. C.1 Finite element mesh used to simulate soil-gas flow around the experimental structure: (a) entire soil block, (b) region around the structure.

Appendix D

THE PERFORMANCE OF A LOW-VOLUME, LOW-FLOW CONTINUOUS RADON MONITOR

This appendix describes the calibration and performance of the low-volume, low-flow continuous radon monitors (CRMs) used for the radon entry measurements reported in Chapter 5. Fig. D.1 shows a schematic of a low-volume, low-flow CRM. Gas samples are drawn at a constant flow rate of 66 cm^3 min^{-1} and passed through a 33 cm^3 scintillation cell. To reduce the effects of ^{220}Rn on the measurements, the samples were drawn through an 11-m-long tube to provide a 3-min delay before being delivered to the CRM. A computer-controlled data acquisition system was used to record the α-decays detected by the photomultiplier tube. Counts were recorded at 1-min intervals.

To determine the radon concentration of the gas sample inside the scintillation cell, the counts from each CRM were interpreted using the algorithm described by Busigin et al. (1979). The Busigin algorithm is a forward-marching data analysis procedure that considers the production, deposition, and decay of radon progeny as a function of time. Use of this algorithm significantly improves the temporal resolution of a CRM. We estimated the statistical uncertainty associated with the Busigin algorithm using the method described by Modera and Bonnefous (1993).

Application of the Busigin algorithm requires two calibration coefficients, ξ and η. These coefficients represent the detection efficiency of a radon α-decay and the α-decay of radon's short-lived progeny, ^{218}Po and ^{218}Po, respectively. Table D.1 lists the values of ξ and η for the low-volume, low-flow CRMs used for the experiments described in Chapter 5. These coefficients were determined by following the procedure described by Busigin et al. (1979).

Laboratory experiments were conducted to examine the performance of these low-volume, low-flow CRMs. A schematic of the experimental configuration is shown in Fig. D.2. By alternatively activating and deactivating the three-way solenoid shown in Fig. D.2, the CRM is exposed to a square-wave radon concentration. Such a signal simulates the large, rapid fluctuations in radon concentration associated with soil-gas and radon entry driven by atmospheric pressure fluctuations. To illustrate the performance of the low-volume, low-flow CRM, results from one test run are shown in Fig. D.3. In this test, we exposed the CRM to a square-wave alternating between 65,000 and 0 Bq m^{-3} with a 20 min total period. Fig. D.3 indicates that the low-volume, low-flow CRM in combination with the Busigin algorithm accurately measures large, rapid fluctuations in radon concentration.

REFERENCES

Busigin A., van der Vooren A. W. and Phillips C. R. (1979) Interpretation of the response of continuous radon monitors to transient radon concentrations. *Health Phys.* **37**, 659-667.

Modera M. P. and Bonnefous Y. (1993) Statistical uncertainties associated with multiplexed sampling with a continuous radon monitor. *Health Phys.* **64**, 291-299.

Table D.1 Low-volume, low-flow CRM calibration coefficients.

Description	Symbol	U-Tube CRM	Gravel CRM
Steady-state counting efficiency: (Bq m^{-3})/(countst min^{-1})		221	230
Busigin coefficients:			
Radon alpha counting efficiency	ξ	0.75	0.75
Decay-product alpha counting efficiency	η	0.77	0.72

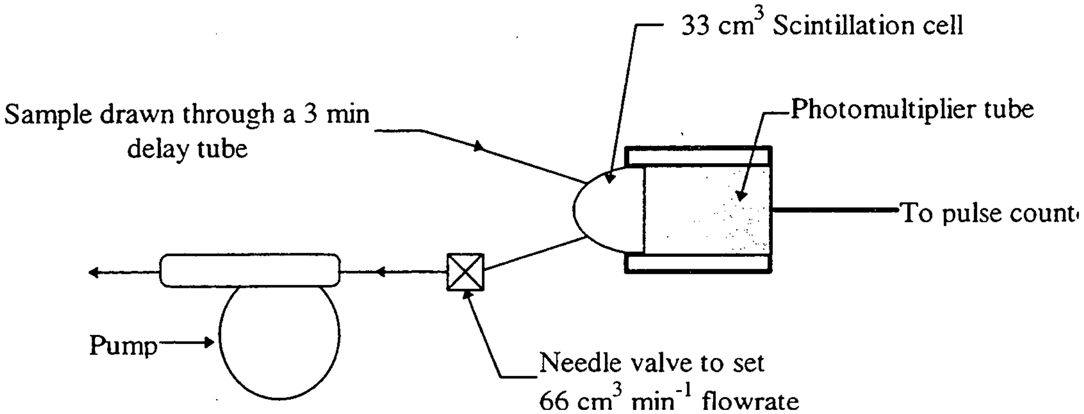

Fig. D.1 Schematic of low-volume, low-flow CRM.

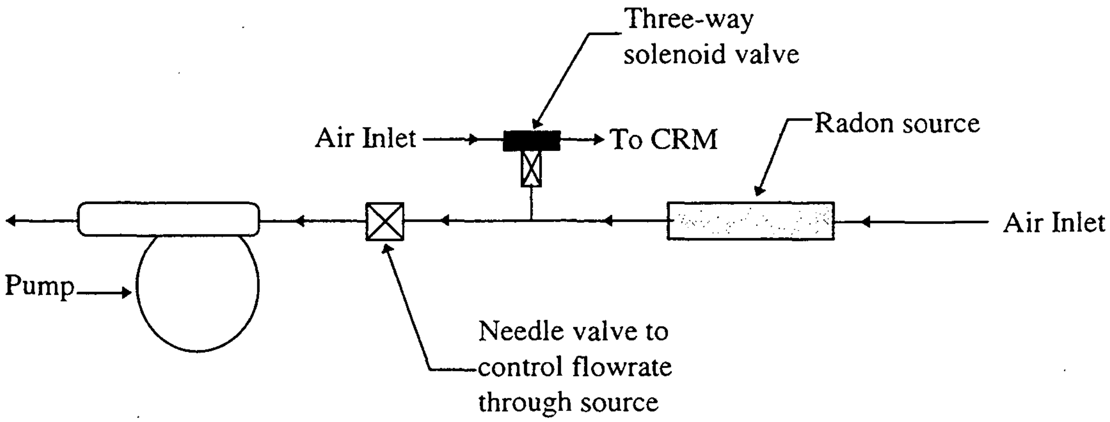

Fig. D.2 Experimental apparatus used to test the performance of low-volume, low-flow CRM. To create a square wave, the three-way solenoid valve switches between the "air inlet" and the tube connected to the radon source. The "common" side of the solenoid is connected to the CRM. The flow-through radon gas source is Pylon model RN-1025 which is made by Pylon Electronic Development Co., Ottawa, Canada.

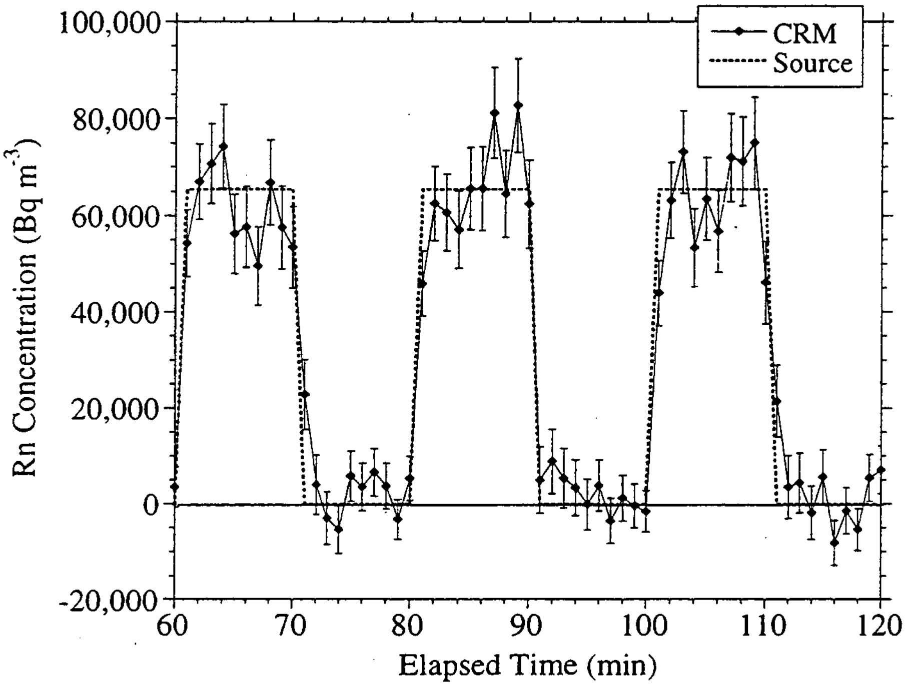

Fig. D.3 Results from a performance test of a low-volume, low-flow CRM. CRM count data were interpreted using the Busigin algorithm (Busigin et al., 1979). The measured radon concentration has been shifted 3-min to account for the effects of the delay tube (assuming plug flow). The vertical bars indicate the statistical uncertainty of the measurements.

ERNEST ORLANDO LAWRENCE BERKELEY NATIONAL LABORATORY
ONE CYCLOTRON ROAD | BERKELEY, CALIFORNIA 94720

Prepared for the U.S. Department of Energy under Contract No. DE-AC03-76SF00098